

**PROPAGATION OF MICROWAVES IN THE
TROPOSPHERE WITH POTENTIAL APPLICATION TO
GPS BASED NAVIGATION AND METEOROLOGY WITH
EMPHASIS ON INDIAN REGION**

Thesis Submitted to
Cochin University of Science and Technology

*In partial fulfillment of the requirements
for the award of*

Doctor of Philosophy
in
Physics
Under the Faculty of Sciences

by
KORAK SAHA

**Space Physics Laboratory
Vikram Sarabhai Space Centre
Indian Space Research Organisation
Thiruvananthapuram
INDIA**

July 2008

When you are solving a problem, *don't worry*. Now, *after* you have solved the problem, then *that's the time to worry*".

Richard Feynman

To
Baba, Ma
Mam, Shalini
and Dr. Suresh Raju

Declaration

This is to declare that the work presented in this thesis is original and no part of it has been submitted for the award of any degree or diploma of any other university or institution.

July - 2008



**KORAK SAHA
(Reg. No. 2994)**

भारत सरकार
अंतरिक्ष विभाग
विक्रम साराभाई अंतरिक्ष केन्द्र
तिरुवनन्तपुरम-695 022
केरल, भारत
फोन : (0471) 2563663
फैक्स : (0471) 2706535
तार/Gram:




Government of India
Department of Space
Vikram Sarabhai Space Centre
Thiruvananthapuram-695 022
Kerala, INDIA
Telephone : (0471) 2563663.
Fax : (0471) 2706535
SPACE

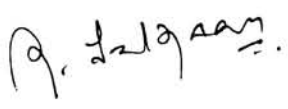
SPACE PHYSICS LABORATORY

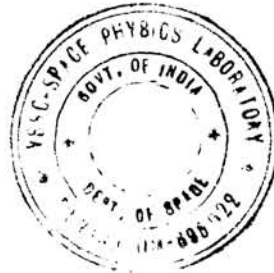
CERTIFICATE

Certified that the thesis entitled “**Propagation of Microwaves in the Troposphere with Potential Application to GPS based Navigation and Meteorology with emphasis on Indian region**” submitted by Mr. Korak Saha, to Cochin University of Science and Technology, Cochin, embodies the original results of the investigations carried out at the Space Physics Laboratory, Vikram Sarabhai Space Centre, Thiruvananthapuram, under my guidance. The work presented in this thesis has not been submitted for the award of any other degree or diploma to any other university or institution.

July-2008


Dr. K. Parameswaran
(Thesis Supervisor)


Countersigned
Prof. R. Sridharan
Director
Space Physics Laboratory



भारतीय अंतरिक्ष अनुसंधान संगठन



Indian Space Research Organisation

ACKNOWLEDGEMENT

A law of Physics says that the mechanical work between two points depends on the chosen path. Writing a thesis involves certainly some mechanical work and thus it obeys this law; it does matter the path you opt for, the story behind it, the people you meet, you work with, their support and commitment. Many people have walked along with me and have helped me to choose the right direction during the last five years. The final words of my thesis are dedicated to them.

Foremost, I would like to thank my supervisor, Dr. K. Parameswaran, who shared with me a lot of his expertise and research insight. He quickly became for me the role model of a successful researcher in the field. Thank you Sir, for helping me whenever I needed it, for believing in me, for nourishing my interest for research with your dedication, enthusiasm, optimism and creativity.

It is difficult to overstate my appreciation to Dr. Suresh Raju, who first brought me into the world of microwaves and with whom I began to learn about mathematical logic and theoretical computation. Not only a great mentor and colleague, he has also been a cornerstone in my professional development. I am indebted to him for his inexhaustible, reassuring and terrific patience he showed while dealing with me.

I am greatly indebted to Prof. R. Sridharan, Director, SPL, for his constant encouragement and the facilities provided. I have been benefited by his constructive suggestions and inspirations.

My word of thanks goes also to Dr. K. Krishna Moorthy, Head, ATA, for his encouraging and valuable suggestions. I thank you sir, for critically evaluating my thesis work, as a member of the research committee.

I would like to acknowledge Prof. Robert W. King (Bob) of MIT for providing the GAMIT support. I am also thankful to Prof. Arthur Niell, Dr. J. Boehm, Dr. Jens Wickhert, Prof. J. van Baelen and all the peer reviewers of my published papers for their innumerable discussions and healthy comments towards my work.

acknowledgement

My gratitude to IMD Pune, for providing me with the radiosonde and surface atmospheric data, NCEP/NCAR for providing data of reanalyzed atmospheric parameters, and COSPAR for the CIRA-86 model.

Special thanks to the whole GAGAN team especially Dr. M. R. Sivaraman, Mr. K. Bandopadhyay of SAC. My gratitude to Dr. Surendra Pal of ISAC, Dr. S. V. Kibe and Shri. K. N. S. Rao of ISRO HQ, Shri. P. Soma of ISTRAC, and all others associated with the Indian Satellite Based Navigation Programs for their technical support, providing GPS data, for fruitful discussions, critical reviews and supporting us in their own capacity.

I would also like to thank Dr. Tarun K. Pant, Dr. K. Rajeev, Dr. Anil Bhardwaj and Dr. K. Kishore Kumar for the numerous scientific discussions which helped me a lot to strengthen my basics of atmospheric physics. No wonder all of you showed a lot of patience while dealing with my nuttiest queries.

Thanks to Dr. D. Balasubramanium, Dr. Sijikumar, Dr. Suresh Babu, Dr. Prabha K. Nair, Dr. Radhika Ramchandran, Dr. N. V. P. Kiran Kumar, Dr. S. V. Sunil Kumar and all other scientific staff of SPL for various critical suggestions and discussions.

Special thanks to Members of my academic committee (Dr. Mannil Mohan, Dr. Anil Bhardwaj, Dr. Sudha Ravindran, Dr. K. Rajeev, Dr. Geetha Ramkumar, Dr. P. K. Kunhikrishnan) for correcting me wherever I was incorrect. Their scholarly advice in palpable form benefited the thesis a lot.

Dear Vins, Anto, Susa, Rani, thanks mates, for your support whenever I needed it, for your humor and friendship at SPL. Along with them I would also like to thank all my colleagues at SPL (Bittol, Deba, Nasu, Sandy, Sreeja, Marina, Vijay, Smitha, Mukunda, Denny, Meenu, Sonal, Jai, Sumodh, Prejith, Liji, Lijo, Veena, Sumod, Prejith, Raghu, Anish, Sherine, Mishra ji, Mushi da) for their remarkable company.

I also thank my Research Committee members (Dr. C. K. Rajan, Dr. V. C. Kuriakose, Dr. K. Mohan Kumar, Prof. L. Godfrey, Dr. V. Unnikrishnan Nair) for their encouragement, valuable suggestions and timely advice.

Acknowledgement

Thanks are also due to all Office staff of Space Physics Laboratory (Mr. S. Jayakumar, Ms. P. R. Suseela, Ms. C. Geetha, Mr. Hari Krishna Kishore M., Mr. Ashokan, Mr. Watson, Mr. Jithas to mention a few) and administrative staff of Cochin University of Science and Technology for their whole hearted support.

My close friends, those who always stood by my side asking over and over again "When will you get it done? Next week? Next Month? When?". To mention a few, Thanks to Harry, Ajay, Tango, Anshul (dallu), Gauti, Sharad, Ruchi, Gagan, Vickie, Yogi, Kirori.

Thanks to Yogesh (Guptaji), Shashank, Chaitanya (Babas), Arvind and Tara babhi, the Bhandaris (Navdeep, Manisha and Vedant), the Pants (Tarun sir, Pratibha bhabhi and Chesta), the Palodhis (Kanik, Semanti and Rangeen), the Jashs (Shamik and Rakhi), the Ahmeds (Maq sir, Seema bhabhi, Khushboo and Aman), the Bhardwajs (Anil sir, Preeti bhabhi, Anusha and Misha), the Gogois (Mukunda and Mitali), for being my extended family and making me feel home away from home in God's own country.

Thanks to my Baba (Shri. Shyamal Saha) and Ma (Smt. Mania Saha), not the least, for the indulgence, investment, and encouragement without end. Dear sister, Mam, thank you very much for your support and good luck for your future.

I would also like to thank my parents-in-law, Shri. Shiv Kumar Agarwal and Smt. Padma Rani Agarwal, for their support. Lots of thanks to Nikhil (Montu), Shivani, Nitin (Jijaji), Rudraksh and Pari for trusting me and endowing me with all their love and care.

I must thank my wife Shalini for putting up with my late hours, my spoiled weekends, my bad temper, but above all for putting up with me and surviving the ordeal. With all the 'cells' passing in this world it is a fortune that ours 'collided'.

CONTENTS

Preface	I
List of Acronyms	V
List of Symbols	IX
Publications in Referred International Journal	XIII

1. Global Positioning System in Navigation and Meteorology

1.0 History of Navigation Systems	1
1.1 Inertial Navigation	2
1.2 Radio Navigation	4
1.2.1 GPS Overview	4
1.2.2 GPS Ranging Signal	6
1.2.3 GPS Ranging using Time of Arrival Measurements	7
1.2.3.1 Two-dimensional position determination	7
1.2.3.2 Three-dimensional position determination	8
1.3 Different Constellations for Satellite Navigation	10
1.4 Navigation Requirements and Differential GPS (DGPS)	11
1.4.1 Required Navigation Performance (RNP)	12
1.4.2 Differential GPS	14
1.4.2.1 Satellite-based augmentation system (SBAS)	15
1.4.2.2 Ground-based augmentation system (GBAS)	17
1.5 Errors in GPS Signal	18
1.5.1 Satellite Clock Error	20
1.5.2 Ephemeris Error	20
1.5.3 Multipath	20
1.5.4 Receiver Noise	21
1.5.5 GPS Signal Propagation Errors	21
1.5.5.1 Microwave propagation in the atmosphere	22
1.5.5.2 Ionospheric contribution to atmospheric delay	23
1.5.5.3 Contribution of neutral atmosphere to atmospheric delay	26
1.6 A Review of Different Models for Estimating Tropospheric Delay	28
1.6.1 Linear Models for ZHD and ZWD	28
1.6.2 Hopfield Model for ZHD and ZWD	30
1.7 Projecting the Zenith Tropospheric Delay to Slant Direction	34

1.7.1 Herring Mapping Function	35
1.7.2 Niell Mapping Function	36
1.7.3 Global Mapping Function	38
1.8 GPS for Water Vapor Estimation Studies	39
1.9 Motivations of this Study	41
2. Estimation of Tropospheric Delay in Microwave Propagation	
2.0 Introduction	44
2.1 Effect of Neutral Atmosphere in the Propagation of Microwave	46
2.2 Ray tracing	48
2.2.1 Geometry of Ray propagation	48
2.2.2 Estimation of Tropospheric Range Error (ΔR)	51
2.3 Mean Neutral Atmospheric Models over the Indian Region	52
2.3.1 The COSPAR International Reference Atmosphere (CIRA) Model	56
2.3.2 A Reference Atmosphere for Indian Equatorial Zone from 0-80 km	57
2.4 Altitude Profiles of Dry and Wet Refractivity	59
2.4.1 Relative Contribution of Refraction Delay with Altitude	60
2.5 Zenith Tropospheric Delay and its Spatial and Temporal Variability	61
2.6 Summary	69
3. Development of Tropospheric Delay Models	
3.0 Introduction	71
3.1 Site-Specific Surface Models for Indian Subcontinent	72
3.2 Adaptation of Hopfield Model for the Indian Region	78
3.2.1 Dependence of h_D and h_W on Surface Temperature	86
3.3 A Unified Model for the Indian Subcontinent	90
3.3.1 Unified Surface Model	90
3.3.2 Unified Model in terms of Precipitable Water vapor	92
3.3.3 Unified Hopfield Model (Characteristic Height Parameters)	93
3.4 Validation of Surface Models	93
3.4.1 Validation of Site-Specific Models by Comparing with Ray-Traced Values	93
3.4.2 Validation of Unified Models using Ray-Tracing	95

3.5	Variability in Zenith Tropospheric Delay and its Deviation from Model Derived Values for Different Stations	98
3.6	Summary	105
4.	A Regional Tropospheric Delay Model for Tropics with Emphasis to the Indian Region	
4.0	Introduction	107
4.1	The WAAS Tropospheric Delay (WTD) Model	109
4.2	Indian Region-specific Tropospheric Delay (IRTD) model	114
4.3	Evaluation of IRTD and WTD model for the Indian subcontinent	116
4.4	Validation of IRTD Model by Comparing it with True ZTD	124
4.5	Summary	125
5.	Tropospheric Delay from Ground Based GPS and Comparison with Model Estimates	
5.0	Introduction	126
5.1	Processing of GPS Data	127
5.1.1	Optimization of IGS Stations in GAMIT Analysis	130
5.1.2	Estimation of ZTD from GPS Data	132
5.1.3	Comparison of GAMIT Derived ZTD with the IGS Operational Product	133
5.2	Comparison of ZTD Derived from GPS Measurements with those Estimated using Unified Models	135
5.3	A Comparison of ZTD Derived from GPS Data with those Estimated from IRTD and WTD models	138
5.4	Periodic Variations in ZTD	143
5.4.1	Mean Diurnal Variations of ZTD in Different Months for Bangalore and Hyderabad	144
5.4.2	Month-to-month (Seasonal) Variation in ZTD	146
5.4.3	Atmospheric Oscillations in GPS Derived ZTD	147
5.4.4	ISO and other Planetary Oscillations in ZTD _{GPS}	150

5.5	Summary	151
6.	Mapping Function for Tropospheric Delay	
6.0	Introduction	153
6.1	Slant Tropospheric Delay and True Mapping Function	154
6.2	Modified Chi Function for Troposphere	157
6.2.1	The Asymptotic Expansion for $Ch(X, \chi)$	160
6.2.2	Development of Mapping Function using the Chi Function	161
6.3	Validation and Comparison of Modified Chi Function	163
6.4	Assessment of the Estimated Tropospheric Delay using Various Models and Mapping Functions for Navigation Purpose	170
6.5	Summary	171
7.	Retrieval of Atmospheric Columnar Water Vapor Content from Ground Based GPS	
7.0	Introduction	172
7.1	Linear Model of PW in terms of ZWD	173
7.2	Adaptation of Bevis model for Indian region	174
7.3	Estimation of PW from GPS data at Bangalore	179
7.4	Estimation of PW from GPS Data at Hyderabad	186
7.5	Summary	188
8.	Summary and Future Scope	191
	References	194

PREFACE

Aircraft navigation systems today need globally interoperable navigational infrastructure that delivers benefits in safety, efficiency and capacity for the aircraft navigation, on global basis with highest level of accuracy. This kind of navigational structure has been aimed while conceptualizing the Global Navigation Satellite System (GNSS) based on Global Positioning System (GPS). The GPS with its high integrity, continuous availability and reliability, has revolutionized the navigation system. With four or more GPS satellites in view, a stand-alone GPS receiver can find its location anywhere over the globe with accuracy of few meters. High accuracy (within centimeters, or even millimeters) is often achieved by correcting the GPS signal with external augmentation system. The use of satellites for critical application like navigation has become a reality through the development of the augmentation systems like US based WAAS, Russian SDCM and European EGNOS *etc.*, with a primary objective of providing essential integrity information needed for navigation service in their respective regions. Apart from these, many countries have initiated developing space-based regional augmentation systems like GAGAN and IRNSS of India, MSAS and QZSS of Japan, COMPASS of China, *etc.* In future, these regional systems will operate simultaneously under GNSS to support a broad range of activities in the global navigation sector. Under this scenario, these regional augmentation systems will be an important component of GNSS. The need of the hour is to interlace these regional satellite navigation (SatNav) systems to provide a global coverage with unrestricted access to navigational position information. GNSS is the ideal navigation infrastructure platform to allow full exploitation of the global benefits to be gained for the Required Navigation Performance (RNP). Once fully operational, the GNSS is envisaged for providing CAT-I precision approach landing guidance requirement. Subsequently, this system will be improved upon to achieve the stringent criteria set for the CAT-II and CAT-III landing guidance requirements.

Among different types of error sources in the GPS precise positioning, the propagation delay due to the atmospheric refraction is a limiting factor on the achievable accuracy using this system. The Wide Area Differential GPS (WADGPS), aimed for accurate positioning over a large area though broadcasts different errors involved in GPS ranging including ionospheric and tropospheric errors, the use of these broadcasted tropospheric corrections are not sufficiently accurate due to the large temporal and spatial variations in different atmospheric parameters

especially in lower atmosphere (troposphere). This necessitated the estimation of tropospheric error based on realistic values of tropospheric refractivity. Different methodologies, that are presently available for the estimation of tropospheric delay, have been developed mostly based on the atmospheric data and GPS measurements from the mid-latitude regions, where the climate is entirely different from that over the tropics. Such methodologies over the tropical region are non-existent. The major drawback of these methodologies are that they neglect the seasonal variation of the delay for near-equatorial stations (for stations $\leq 15^\circ\text{N}$, the whole Indian peninsular region) and at the higher latitudes underestimates the delay. In this context, this study is a first and major step towards the development of models for tropospheric delay over the Indian region which is a prime requisite for future space based navigation programs (GAGAN and IRNSS). Apart from such models based on the surface measured parameters a model independent of measured parameter, exclusively for the tropical region is also developed, which is crucial for estimation of delay in zenith direction when measured parameters are not available. This zenith component of delay is then mapped towards the line-of-sight of the GPS satellite to estimate the actual slant delay towards the satellite. In practical situations this is achieved by developing an analytical function known as mapping function. In this study a new mapping function for the hydrostatic component of delay is developed by modifying the well known Chi function and is found to be superior to the existing global mapping functions. For the wet component of mapping function all the existing global mapping functions are equally good.

Water vapor is one of the most significant minor constituents of the atmosphere. It plays a significant role in weather and climate as well as transport of heat in the atmosphere. Water vapor is also a greenhouse gas that plays a critical role in the global climate system, not only confining to absorption and radiation of energy in the atmosphere, but also influencing the formation of clouds and aerosols (atmospheric chemistry) in the lower atmosphere. Large variability of atmospheric water vapor content in short spatial and/or temporal scales makes its measurement rather involved and expensive. A local network of GPS receivers is an effective tool for water vapor remote sensing over the land. This recently developed technique proves to be an effective tool for measuring Precipitable Water (PW), (the height of the liquid water column when the entire water vapor in a vertical column of the atmosphere is condensed). In fact the error (or noise) due to the lower atmosphere in GPS based navigation, acts as information on water vapor for the atmospheric scientists and meteorologists. In this study

potential of using GPS to estimate water vapor in the atmosphere at all-weather condition and with high temporal resolution is attempted. A good network of GPS could be a major source of water vapor information for Numerical Weather Prediction models and could act as surrogate to the data gap in microwave remote sensing for water vapor over land.

This thesis is composed of eight chapters, as summarized below

An overview of GPS and its various applications are given in **Chapter 1**. This includes fundamental aspects relating to GPS satellite, various augmentation systems for the GPS based navigation, the errors involved in GPS ranging and the ways to mitigate them. A review on the existing global tropospheric delay models, mapping functions are also described.

Chapter 2 details about the fundamentals of the delay due to microwave propagation (in GPS frequencies) through neutral atmosphere. In-house developed Ray tracing algorithm is used to estimate the true neutral atmospheric (tropospheric) delay. This is used to study the spatial and temporal variability of the tropospheric delay over the Indian sub-continent.

Chapter 3 deals with the development of conventional models relating the Tropospheric delays (both ZHD and ZWD) with easily measurable atmospheric parameters at the surface. These models include Site-Specific as well as Regional models for the Indian region. These models are developed using atmospheric data from the Indian region and is validated with the true values of tropospheric delay estimated by Ray tracing technique.

Chapter 4 deals with the development of an Indian Region-specific Tropospheric Delay (IRTD) model, which is independent of any measured atmospheric parameters. This model is validated extensively over the Indian subcontinent and is found to perform much better than the currently available global models.

Chapter 5 details with the processing of the GPS data for estimating the zenith tropospheric delay (ZTD) using the GAMIT10.2 software. The two-hourly values of ZTD thus obtained are further used to validate the models (presented in Chapter 3 and Chapter 4). The GPS estimated ZTD is also used to study the periodic variations in it. The variations in ZTD

have been shown to be important for developing higher order terms in the parameter independent models (IRTD, WTD) for navigation purpose.

Chapter 6 deals with the development of a new hydrostatic mapping function. This new mapping function is developed by modifying the Chi function and is validated by comparing with the true value of mapping function along with the existing global mapping functions.

Chapter 7 deals with the estimation of column integrated water vapor from GPS. As the wet delay derived from the GPS data (ZWD_{GPS}) depends primarily on the atmospheric water vapor content, this parameter could be used for estimating the PW in the atmosphere. The temperature dependence of atmospheric water vapor content over the Indian region is studied through deriving a parameter called the weighted mean temperature (T_m), which is the water vapor weighted vertically averaged temperature. T_m is modeled with surface temperature (T_s), which is used to estimate PW from GPS derived ZWD (in the Indian context).

A summary of major findings in this study is presented in **Chapter 8**. An outline of the future research scope in this area is also included.

LIST OF ACRONYMS

AMSU-A	Advanced Microwave Sounding Unit-A
AMSU-B	Advanced Microwave Sounding Unit-B
APV	APproach for Vertical guidance
AS	Antispoofing
BADC	British Atmospheric Data Centre
BAI	Bevis Adapted for Indian region
BoB	Bay of Bengal
C/A	Coarse/Acquisition
CAT I (II, III)	Category I (II, III) type of precision approach
CDMA	Code Division Multiple Access
Chi	Chapman Function (<i>see</i> Ch(X, χ) <i>in list of symbols</i>)
CIRA	COSPAR International Reference Atmosphere
CODE	Center of Orbit Determination in Europe
CRPL	Central Radio Propagation Laboratory
C-WAAS	Canadian WAAS
DGNSS	Differential GNSS
DGPS	Differential GPS
DH	Decision Height
DIAL	Differential Absorption LIDAR
DoD	Department of Defense
<i>drms</i>	distance root mean square
ECEF	Earth-Centered Earth-Fixed
ECMWF	European Centre for Medium-range Weather Forecast
EGNOS	European Geo-stationary Navigation Overlay System
EM	Electro Magnetic
ERA40	40 years of ECMWF reanalysis data
ESA	European Space Agency
EU	European Union
EUPOS	European Position Determination System
FAA	Federal Aviation Administration
GAGAN	GPS Aided Geo Augmented Navigation
GALILEO	European Global Satellite Navigation System
GBAS	Ground Base Augmentation System
GDOP	Geometric Dilution of Precision
GEOs	Geostationary Satellites
GLONASS	GLObal'naya NAVigatsionnaya Sputnikovaya Sistema
GM	Gauss-Markov

GMF	Global Mapping Function
GMF _h	Global MF hydrostatic
GMF _w	Global MF wet
GNSS	Global Navigation Satellite System
GPS	Global Positioning System
GST	GPS Standard Time
HAL	Horizontal Alert Limit
IAG	International Association of Geodesy
ICAO	International Civil Aviation Organization
IGS	International GPS service
IM	Integrity Monitor
IMD	India Meteorological Department
IMF	Isobaric Mapping Function
IMU	Inertial Measurement Unit
INLUS	Indian Land Uplink Station
INMCC	Indian Master Control Centre
INRES	INdian REference Station
INS	Inertial Navigation System
IRNSS	Indian Radio Navigation Satellite System
IRTD	Indian Region-specific Tropospheric Delay
IRU	Inertial Reference Unit
ISO	Intra Seasonal Oscillations
IST	Indian Standard Time
ITRF	International Terrestrial Reference Frame
IWV	Integrated (columnar) Water Vapor
JPL	Jet Propulsion Laboratory
LAAS	Local Area Augmentation System
LADGPS	Local Area Differential GPS
LIDAR	LIght Detection And Ranging
LORAN-C	LOng RANge Navigation
LOS	Line Of Sight
LS	Least-Squares
M1	Lunar diurnal period
M2	Lunar semi-diurnal period
MDGPS	Marine Differential GPS
MF	Mapping Function
MIT	Massachusetts Institute of Technology
MJO	Madden-Julian Oscillation
MSAS	MTSAT Satellite Augmentation System
MSIS	Mass Spectrometer and Incoherent Scatter

MSL	Mean Sea Level
MTSAT	Multifunctional Transport SATellite
NATO	North Atlantic Treaty Organization
NDGPS	Nationwide Differential GPS
NMF	Niell Mapping Function
NMF _h	Niell MF hydrostatic
NMF _w	Niell MF wet
NPA	Non Precision Approach
NSSDC	National Space Science Data Center
NWP	Numerical Weather Prediction
P(Y)	Precision/Protected (Y)
PL	Pseudolites
PPS	Precise Positioning Service
PR	Pseudorange
PRN	Pseudo Random Noise
PW	Precipitable Water vapor
QZSS	Quasi-Zenith Satellite System
RIM	Range Integrity and Monitoring
RINEX	Receiver Independent Exchange
RNP	Required Navigation Performance
RS	Reference Station
RSS	Root-Sum-Squared
RTCA	Radio Technical Commission for Aeronautics
RTCM SC-104	Radio Technical Commission for Maritime Services Study Committee-104
RVR	Runaway Visual Range
S/A	Selective Availability
SAGE II	Stratospheric Aerosol and Gas Experiment - III
S1	Solar diurnal tide
S2	Solar semi-diurnal tide
SAAS	Saastamoinen model 1972
SARPS	Standard And Recommended Practices
SBAS	Satellite Based Augmentation System
SDCM	System of Differential Corrections and Monitoring
SHD	Slant Hydrostatic Delay
SIO	Scripps Institute of Oceanography
SNAS	Satellite Navigation Augmentation System
SPS	Standard Positioning Service
SS-86	Sasi Sengupta Reference Atmosphere 1986
SSM/I	Special Sensor Microwave/Imager
STD	Slant Total Delay

SWD	Slant Wet Delay
TEC	Total Electron Content
TIROS	Television Infra-Red Observation Satellite
TMI	TRMM Microwave Imager
TOA	Time Of Arrival
TOVS	TIROS Operational Vertical Sounder
TRMM	Tropical Rainfall Measuring Missions
USERE	User Equivalent Range Error
UNB	University of New Brunswick
UTC	Coordinated Universal Time
VAL	Vertical Alert Limit
VDOP	Vertical Dilution of Precision
VLBI	Very Long Baseline Interferometry
VMF1	Vienna Mapping Function 1
VPE	Vertical Position Error
WAAS	Wide Area Augmentation System
WADGPS	Wide Area Differential GPS
WGS-84	World Geodetic System 1984
WMO	World Meteorological Organization
WTD	WAAS Tropospheric Delay
WVMR	Water Vapor Microwave Radiometer
ZHD	Zenith Hydrostatic Delay
ZHD _m	ZHD estimated by Unified model
ZTD	Zenith Tropospheric Delay
ZTD _{GAMIT}	ZTD derived using GAMIT 10.2
ZTD _{GPS}	ZTD derived from GPS data
ZTD _{IGS}	ZTD estimated by IGS
ZTD _{IRTD}	ZTD from IRTD model
ZTD _{TRUE}	ZTD estimated by ray-tracing
ZTD _{WTD}	ZTD estimated by WTD model
ZWD	Zenith Wet Delay
ZWD _{GPS}	ZWD derived from the GPS
ZWD _m	ZWD estimated by Unified model

LIST OF SYMBOLS

PR_A^i	Pseudorange between receiver 'A' and satellite 'i'
S_A^i	Geometric distance between receiver 'A' and satellite 'i'
c	Speed of light (in vacuum, $c = 299792458$ m/s)
δ_A	Receiver clock error
δ^i	Satellite clock error
$\delta_{A[ION]}^i$	Ionospheric propagation delay
$\delta_{A[TROP]}^i$	Tropospheric propagation delay
N_A^i	Integer Ambiguity
λ_C	Carrier wavelength (~ 19 cm for L_1)
M_A^i	Multipath errors
ϵ_{PR}	Code phase measurement errors
ϵ_φ	Carrier phase measurement errors
ϕ_A^i	Carrier phase between receiver 'A' and satellite 'i'
v	Velocity of electromagnetic wave in a medium (in m/s)
n	Refractive index of the medium
μ	Permeability of the medium
μ_0	Permeability of free space
ϵ	Dielectric constant of the medium
ϵ_0	Dielectric constant of free space
R	Apparent range
Δt	Time taken by ray to travel from satellite to receiver (in ns)
ΔR	Estimated range error (in m)
f	Frequency of propagating radio waves (in GHz)
n_p	Index of refraction for the phase propagation
n_g	Refractive index for group propagation
n_e	Electron number density
v_p	Phase velocity
v_g	Group velocity
ΔR_{iono}	Ionospheric range error (in m)
O_F	Obliquity factor
L_1	L-band ($f = 1.57542$ GHz)

L_2	L-band ($f = 1.2276$ GHz)
ρ_{L_1}	Pseudorange observations at L_1
ρ_{L_2}	Pseudorange observations at L_2
ΔR_{tropo}	Tropospheric range error (in m)
N	Refractivity
g	Acceleration due to gravity (in m/s^2)
h	Height (in m)
ρ	Density of air (in kg/m^3)
H_g	Geopotential height (in m)
P	Pressure (in hPa)
T	Temperature (in K and $^{\circ}\text{C}$)
e	Water vapor partial pressure (in hPa)
P_S	Surface Pressure (in hPa)
T_S	Surface Temperature (in K and $^{\circ}\text{C}$)
e_S	Surface water vapor partial pressure (in hPa)
g_m	Weighted mean acceleration due to gravity (in m/s^2)
R_d	Gas constant for dry air ($= 287 \text{ J kg}^{-1} \text{ K}^{-1}$)
N_D	Dry component of refractivity
N_W	Wet component of refractivity
k_1	Hydrostatic refractivity constant ($= 77.6 \text{ K/hPa}$)
M_d	Apparent molecular weight of dry air ($= 28.97 \text{ kg/kmol}$)
R^*	Universal gas constant ($= 8314.3 \text{ J kmol}^{-1} \text{ K}^{-1}$)
φ	Ellipsoidal latitude
h_C	Height of the center of atmospheric column above ellipsoid (in km)
N_S	Surface refractivity
β	Temperature lapse rate ($= -6.81 \text{ K/km}$)
ρ_d	Density of dry air
ρ_w	Density of water vapor
M_w	Molecular weight of water ($= 18.016 \text{ kg/kmol}$)
h_{0D}	Characteristic height of dry atmosphere for $T = 0^{\circ}\text{C}$ (in km)
h_D	Characteristic height of dry atmosphere (in km)
N_{SD}	Surface dry refractivity
N_{SW}	Surface wet refractivity
h_W	Characteristic height of wet atmosphere (in km)
χ	Zenith angle
H_o	Height above sea level

MF_h	Hydrostatic mapping function
MF_w	Non-hydrostatic (wet) mapping function
doy	Day of the year
P	Electric Polarization
M	Molecular weight
A_N	Avogadro's number ($= 6.022 \times 10^{26} \text{ kmol}^{-1}$)
γ	Induced dipole moment per unit applied field
γ_p	Permanent dipole moment of the molecules
K	Boltzmann constant ($= 1.381 \times 10^{-23} \text{ J K}^{-1} \text{ molecule}^{-1}$)
ω	Angular frequency ($= 2\pi f$)
τ	Relaxation time
P_d	Pressure of dry air (in hPa)
k_2	Hydrostatic refractivity constant ($= 64.79 \text{ K hPa}^{-1}$)
k_3	Hydrostatic refractivity constant ($= 3.776 \times 10^5 \text{ K}^2 \text{ hPa}^{-1}$)
r_e	Radius of earth (in km)
$\Delta\Psi$	Total angular deviation
D_{si}	Effective path length
D	Geometric distance
S	Actual path traveled by ray
ds	Infinitesimal path distance
$d\tau$	Infinitesimal time
T_D	Dew point temperature (in K)
ΔR_W	Wet range error (in m)
ΔR_D	Dry range error (in m)
$\Delta\Psi_D$	Dry component of angular deviation
$\Delta\Psi_W$	Wet component of angular deviation
δ_{ZHD}	Month-to-month variability in ZHD
δ_{ZWD}	Month-to-month variability in ZWD
ρ_s	Surface water vapor density (in kg m^{-3})
I_s	Columnar integrated water vapor (in kg m^{-2})
λ	Water vapor lapse rate (unitless)
k_{hyd}	Hydrostatic scaling factor
k_{wet}	Wet scaling factor
P_{msl}	Pressure at MSL (in hPa) (<i>see MSL in List of Acronyms</i>)
T_{msl}	Temperature at MSL (in K)
e_{msl}	Water vapor pressure at MSL (in hPa)
P_o	Annual mean value of P_{msl} (in hPa)
T_o	Annual mean value of T_{msl} (in K)
e_o	Annual mean value of e_{msl} (in hPa)

β_0	Mean value of β (in K/km)
λ_0	Mean value of λ
P'	Annual amplitude of P_{msl} (in hPa)
T'	Annual amplitude of T_{msl} (in K)
e'	Annual amplitude of e_{msl} (in hPa)
β	Annual amplitude of β (in K/km)
λ	Annual amplitude of λ
d_0	Phase offset epoch (in day number)
\mathbf{p}	Vector of observations in GPS phase measurements
\mathbf{A}	Observations' matrix
$\ddot{\mathbf{O}}_{xyz}$	Vector of unknown parameters
\emptyset	Measured white noise
\mathbf{B}	Measurement noise of covariance matrix
H	Atmospheric scale height
$\text{Ch}(X, \lambda)$	Chapman (or Chi) function
σ_{abs}	Absorption cross-section
ζ	Atmospheric column depth
T_m	Water vapor weighted mean temperature (in K)
R_v	Gas constant for water vapor ($= 461 \text{ J kg}^{-1} \text{ K}^{-1}$)
ρ_l	Density of liquid water (in kg m^{-3})
Π	Proportionality coefficient connecting PW with ZWD

PUBLICATIONS IN REFERRED INTERNATIONAL JOURNAL

1. **Korak Saha**, K. Parameswaran and C. Suresh Raju, 2007: Tropospheric Delay in Microwave Propagation for Tropical Atmosphere Based on Data from the Indian Subcontinent. *J. Atmos. Solar. Terr. Phys.*, **69**, 875 – 905.
2. Suresh Raju, **Korak Saha**, Bijoy V. Thampi and K. Parameswaran, 2007: Empirical Model for Mean Temperature for Indian Zone and Estimation of Precipitable Water Vapor from Ground Based GPS Measurements. *Ann. Geophys.*, **25**, 1935 – 1948.
3. Parameswaran, K., **Korak Saha** and C. Suresh Raju, 2008: Development of a Regional Tropospheric Delay Model for GPS-based Navigation with Emphasis to the Indian Region. *Rad. Sci.* (**in press**), **43**, doi:10.1029/2007RS003782.

Chapter 1

GLOBAL POSITIONING SYSTEM IN NAVIGATION AND METEOROLOGY

1.0 History of Navigation Systems

Navigation is a very ancient skill or art of planning, reading, and controlling the movement of a craft or vehicle from one place to another. The word *navigate* is derived from the Latin roots *navis* meaning "ship" and *agere* meaning "to move" or "to direct". All navigational techniques involve locating the navigator's position compared to known locations or patterns. Fundamental navigation skill requires usage of our eyes, good judgment ability and landmarks for moving from one place to another. However, in some cases where a more accurate knowledge of our position, intended course, or transit time to a desired destination is required, navigation aids other than landmarks are used. Methods of navigation have changed through history. Each new method has enhanced the navigator's ability to complete his voyage. One of the most important judgments the navigator must make is the best method to use. A few types of navigation methods are listed below:

1. *Pilotage*: Essentially relies on recognizing landmarks to know the position. It involves navigating in restricted waters with frequent determination of position relative to geographic and hydrographic features.
2. *Dead reckoning*: Relies on a prior position, along with some form of heading information and some estimate of speed.
3. *Celestial navigation*: Uses time and the angles between local vertical and celestial objects (e.g., sun, moon, or stars). It involves reducing celestial measurements to lines of position using tables, spherical trigonometry, and almanacs.
4. *Radio navigation*: Uses radio waves (from artificial source) to determine position by either radio direction finding systems or hyperbolic systems, such as Decca, Omega and LORAN-C. The latest satellite based radio navigation includes the Global Positioning System (GPS).

5. *Inertial navigation*: Relies on the information on initial position, velocity and attitude; thereafter measures the real time attitude and accelerations. A brief account of this system is presented in the next section.

1.1 Inertial Navigation

Inertial Navigation System (INS) operates on the basis of Newton's laws of motion. Newton's first law of motion states that a body will continue to be in the state of rest or moving with uniform velocity unless acted by an external force (inertia). The sensors used in this system makes use of the property of inertia to measure accelerations and turn rates in a fixed reference frame (an inertial reference frame) in which Newton's laws of motion are valid. Once the acceleration is measured, it would be possible to calculate the change in velocity and position by performing successive integrations of the acceleration *w.r.t.* time. Since only changes in position and velocity are obtained using measurements, the determination of initial position and velocity are very crucial in accurate navigation by INS. The inertial sensors measure the vector-valued variables, rotation rate and acceleration, using:

- (a) Gyroscopes: These are sensors for measuring rotation; *e.g.* rate gyroscopes measure rotation rate, and displacement gyroscopes measure rotation angle.
- (b) Accelerometers: These are sensors for measuring acceleration. However, accelerometers cannot measure gravitational acceleration.

Broadly, INS consists of two sections:

- (a) An inertial measurement unit (IMU) or inertial reference unit (IRU) containing a cluster of sensors: accelerometers (usually three) and gyroscopes (also three in number). These sensors are rigidly mounted to a common base to maintain the same relative orientations.
- (b) Navigation computers (one or more) which calculate the gravitational acceleration (not measurable by accelerometers) and doubly integrate the net acceleration to maintain an estimate of the position of the host vehicle.

The two systems of IMU are Gimbals and Strapdown for the INS. Gimbals have been used for isolating gyroscopes from rotations of their mounting bases since the time of Foucault. They have been used for isolating an inertial sensor cluster in a gimbaled IMU since about 1950. At least three gimbals are required to isolate a subsystem from the host vehicle rotations about three axes, roll, pitch, and yaw. A fourth gimbal is required for

vehicles with full freedom of rotation about all three axes: such as high-performance aircraft. In Strapdown type of INS, the inertial sensor cluster is “strapped down” to the frame of the host vehicle, without using intervening gimbals for rotational isolation. Strapdown INS generally requires more powerful navigation computers than their gimballed counterparts as this system computer must integrate the full (six degree of freedom) equations of motion to estimate the position.

The main advantages of INS over other navigation systems are, (1) it is autonomous and does not rely on any external aids or on visibility conditions, (2) it can operate in tunnels or underwater as well as any where else, (3) it is inherently well suited for integrated navigation, guidance, and control of the host vehicle, (4) its IMU measures the derivatives of the variables to be controlled (*e.g.* position, velocity, and attitude) and (5) it is immune to jamming and inherently stealthy, because it neither receives nor emits detectable radiation and requires no external antenna which could be detected by radar.

The disadvantages of INS are that the mean-squared navigation errors increase with time. The Acquisition, Operation and Maintenance costs for INS are order of magnitude larger than that in radio navigation aids like GPS. The INS weight which is generally high has a multiplying effect on vehicle system design, because it requires increased structure and propulsion weight as well. The power requirements are much larger than the GPS receivers. The heat dissipation, which is proportional to and shrinks with high power consumption is also a limitation of INS. The relatively high cost of INS was one of the major factors that lead to the development of Global Positioning System or GPS. The synergism of GPS and INS has improved the INS performance, and also made it cost effective. The use of integrated GPS/INS for mapping the gravitational field near the earth’s surface has also enhanced INS performance by providing more detailed and accurate gravitational models. INS also benefits GPS performance by carrying the navigation solution during loss of GPS signals and allowing rapid reacquisition when signals become available. Some of the applications of GPS/INS integrated systems could be performed neither by GPS nor by INS stand-alone *e.g.* the low-cost systems for precise automatic control of vehicles operating at the surface of the earth, including automatic landing systems for aircraft, and autonomous control of surface mining equipment, surface grading equipment, and farm equipment.

1.2 Radio Navigation

Various types of radio navigation aids that exist today are either ground-based or space-based systems. For most part, the accuracy of ground-based radio navigation aids is proportional to their operating frequency. Highly accurate systems generally transmit at relatively short wavelengths, and the user must remain within the line of sight (LOS), whereas systems broadcasting at lower frequencies (longer wavelengths) are not limited to LOS and are less accurate navigation systems.

1.2.1 GPS Overview

Satellite based navigation was born when U.S. Navy decided in the early 1960s to create a system for the purpose of precise navigation. Early space-based systems *e.g.* **TRANSIT** of U.S. Navy and **TSIKADA** of Russian system provided two dimensional high-accuracy positioning service. The limitations of both these systems were that each position fixing required approximately 10 to 15 minutes of receiver data processing for estimating the user's position. Though these attributes were well suited for ship navigation because of its low velocities, it was not suitable for aircraft and high-dynamic platform. This led to the development of the Global Positioning System (**GPS**) by U.S., which presently is a synonym to the satellite based navigation. Subsequently in the early 1970s, development of this satellite system for three-dimensional positioning was initiated with the following aims:

1. Global coverage
2. Continuous/all weather operation
3. Ability to serve as a precise dynamic platform (high precision and reliable accuracy).

The first operational GPS prototype satellite was launched in February 1978. The operational GPS system of today is virtually identical to the one proposed in 1970s. In fact now they have expanded their functionality to support additional military capabilities; the satellite orbits are slightly modified, but the receiver designed to work with the original four satellites still performs the function. Presently there are 24(+6 in back up) GPS satellites, each continuously transmits navigation signal for positioning purpose.

The fundamental navigation technique using GPS is to accomplish one-way ranging from the GPS satellites which are broadcasting their estimated positions. A minimum of four satellites which are simultaneously available in the field of view are used for this purpose by matching the incoming signal (generated using atomic clocks) with a user-generated replica

signal and measure the difference phase of the incoming signal against the user's crystal clock. With four satellites and appropriate geometry, the four unknowns (typically, latitude, longitude, altitude and a correction to the user's clock) are determined from these measurements. Subsequent position of each satellite is informed (and regularly updated) from the range measurements carried out at five monitoring stations located at Colorado Springs, Ascension Island, Diego Garcia, Kwajalein, and Hawaii. Using sophisticated prediction algorithms, these master control stations estimate the satellite location, and subsequently make necessary corrections for the satellite clock. With these closed loop corrections, the satellite positions are inferred within an average *rms* error of 2-3 m [Parkinson–Spilker *et al.*, 1996].

The Global Positioning System consists of three segments: the space segment, the control segment, and the user segment, as shown in Figure 1.1. The space segment consists of 24(+6) satellites, each of which is continuously transmitting a ranging signal that includes navigation message stating its current position and time correction. The control segment tracks each satellite and periodically uploads to the satellite its prediction of future position and clock time corrections. These predictions are then continuously transmitted by the satellite to the user as a part of the navigation message. The user receiver tracks the ranging signals of selected satellites and calculates three-dimensional position and local time.

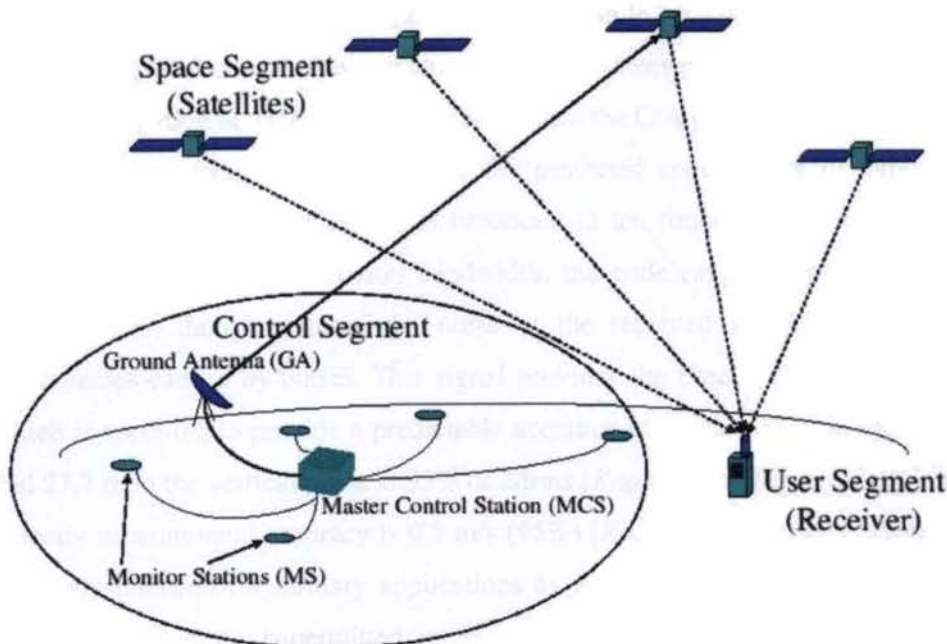


Figure 1.1: Pictorial representation of the three segments in the GPS based navigation system

1.2.2 GPS Ranging Signal

The GPS ranging signal is broadcasted at two frequencies: a primary signal (L_1) at 1.57542 GHz and a secondary broadcast (L_2) at 1.2276 GHz. On these two carrier frequencies the satellites broadcast the ranging codes and navigation data using a modulation technique called Code Division Multiple Access (CDMA). Thus each satellite transmits on these frequencies, but with different ranging codes than those employed by other satellites. These codes are selected because they have low cross-correlation properties with respect to one another. Each satellite generates a short code referred to as the coarse/acquisition or C/A code and a long code denoted as the precision or P(Y) code.

The C/A code is a short Pseudo Random Noise (PRN) code in the primary signal (L_1) that broadcast at a bit rate of 1.023 MHz. This is the principal civilian ranging signal, and it is always broadcasted in unencrypted form. The positioning attained using this signal is called the Standard Positioning Service (SPS). Although moderately degraded, the SPS is always available to all the users worldwide free of cost without any restrictions on its usage. This service is specified to provide accuracy better than 13 m in the horizontal plane and 22 m in the vertical plane (global average) at 95% $2drms$ [Kaplan and Hegarty, 2006]. The term *drms* refers to distance root mean square which is a common measure used in navigation and $2drms$ refers to the radius of a circle which contains at least 95% of all possible fixes that can be obtained with a system. However, to boost up GPS usage in future civilian navigation services, it is proposed to have the C/A code at some more frequencies.

The P(Y) code, sometimes called the protected code, is a very long code (actually segments of a 200-day code) that is broadcast at ten times the rate of C/A, 10.23 MHz. Because of its higher modulation bandwidth, the code ranging signal is somewhat more precise. This, though reduces the noise in the received signal does not improve the inaccuracies caused by biases. This signal provides the Precise Positioning Service (PPS), which is specified to provide a predictable accuracy of at least 22 m in the horizontal plane and 27.7 m in the vertical plane at 95% of $2drms$ [Kaplan and Hegarty, 2006]. The specified velocity measurement accuracy is 0.2 m/s (95%) [Kaplan and Hegarty, 2006]. This code is primarily intended for military applications as well as for the use of selected government agencies. Civilian use is permitted, but only with special approval of the U.S. Department of Defense (DoD). Because of this, the military has encrypted this signal to prevent the unauthorized users from accessing this information. This ensures that this unpredictable

code (to the unauthorized user) cannot be spoofed. This mechanism is called *antispoofing* (AS). When encrypted the P code becomes Y code, hence the name P(Y).

For managing certain critical situations, the accuracy of the C/A code is degraded intentionally by desynchronizing the satellite clock (*dithering*), or by incorporating small errors in the broadcast ephemeris (*epsilon*), which is called *selective availability* (S/A). However, the process of S/A has been discontinued since 1 May 2000 by the U.S. government.

1.2.3 GPS Ranging using Time of Arrival Measurements

The GPS uses the concept of time of arrival (TOA) ranging to determine the user position. This concept entails measuring the time taken by the transmitted signal (*e.g.*, from a foghorn, radio beacon, or satellite in case of GPS) from a known location to reach the user receiver. This time interval, referred to as the signal propagation time, is then multiplied by the speed of the signal to estimate the emitter-to-receiver distance.

1.2.3.1 Two-dimensional position determination

Consider the case of a ship vessel (receiver) trying to determine its position using a foghorn (transmitter). The ship should have an accurate clock and the mariner should have an approximate knowledge of the ship's location. The foghorn whistle is sounded precisely on the minute mark of the ship clock which is synchronized to foghorn clock. The mariner records the elapsed time from minute mark to the foghorn whistle being heard. This propagation time multiplied by speed of sound is the distance from foghorn to the ship. Based on measurement from one such foghorn, mariner's distance (D_1) to foghorn is calculated. With this the mariner can locate his position anywhere on the circle, as denoted in Figure 1.2a. If mariner simultaneously measured the time range from second foghorn in same way, assuming transmissions are synchronized to a common time base and mariner knows the transmission times, the ship will be at range D_2 from the foghorn 2 (see Figure 1.2b). Therefore, the ship relative to the foghorns is at one of the intersections of the range circles (point A and B). Since mariner has approximate knowledge of ship's location, the ambiguity between location A and B can be resolved. If not, then measurement from a third foghorn is needed (see Figure 1.2c). This method also known as "Triangulation" (or trilateration), is being used for navigation since time unknown.

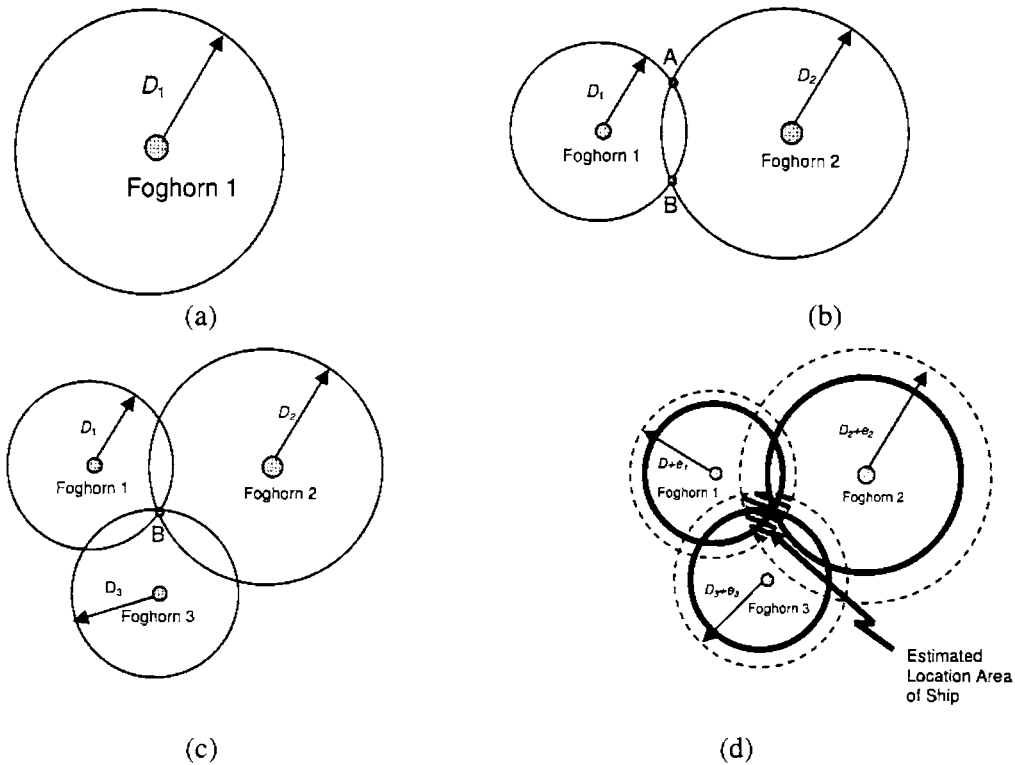


Figure 1.2: Triangulation method in two-dimensions

This development assumed that the ship was precisely synchronized with the foghorn time base. However, this might not be the case. Suppose the time offset for each of the measurements is e_1 , e_2 and e_3 (Figure 1.2d). Then the position of the ship is anywhere inside the shaded area, with highest precision at the dot in the centre, which could be achieved by compensating for the time offsets.

1.2.3.2 Three-dimensional position determination

Since the positioning in space using satellite is a three-dimensional problem, a three-dimensional trilateration technique is used in the present study. Fundamentally, three-dimensional trilateration is not much different from two-dimensional trilateration, but it's a little tricky to visualize. Imagine the radii from the examples in the previous paragraph going off in all directions. In that case, instead of a series of circles, one gets a series of spheres. If a receiver is known to be at $\sim 20,000$ km from satellite A in the sky, it could be anywhere on the surface of a huge, imaginary sphere with a 20,000 km radius (Figure 1.3a). If the same receiver is 25,000 km from satellite B, one can overlap the first sphere

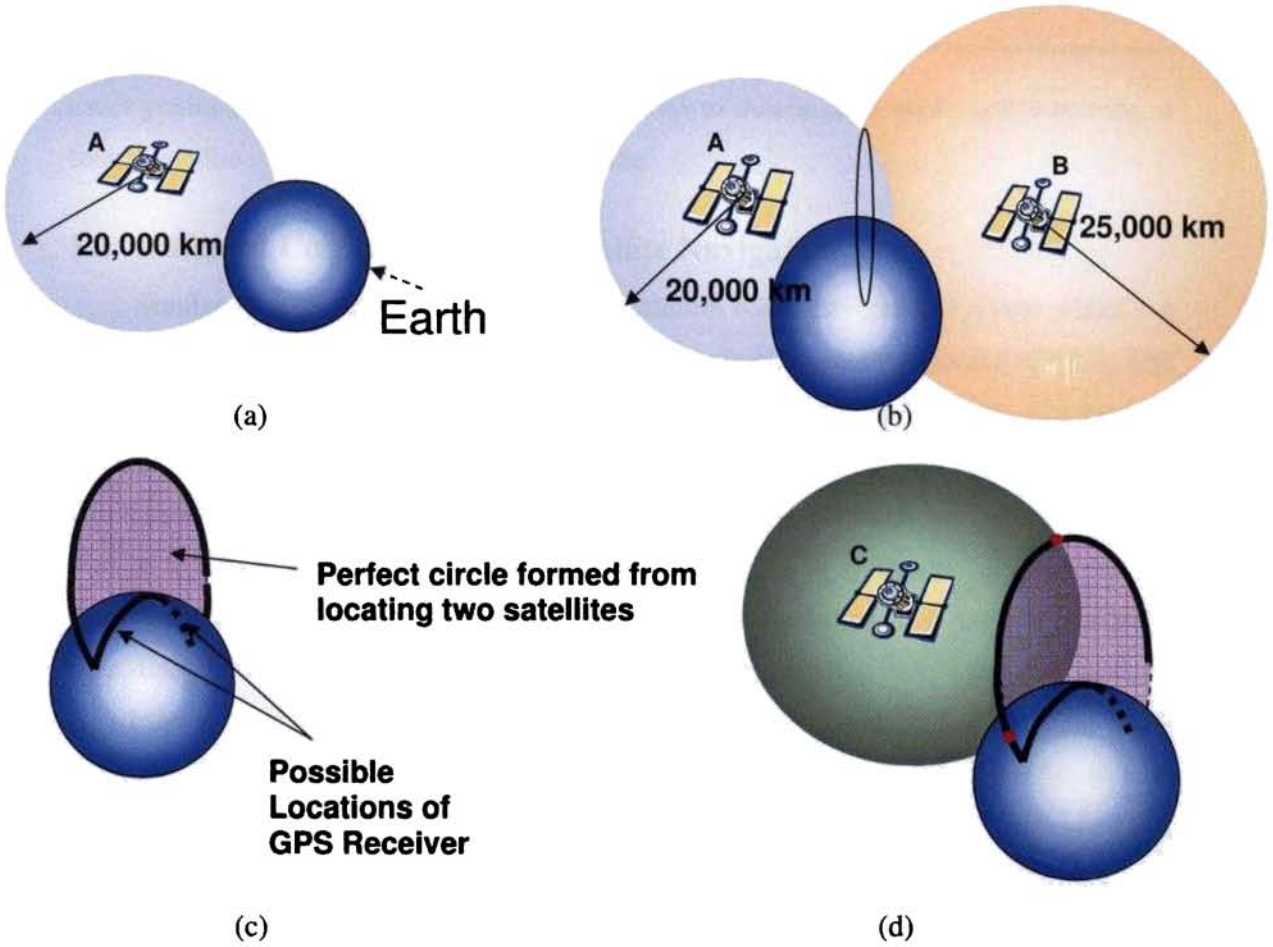


Figure 1.3: Triangulation method in three-dimensions

with another, larger sphere. The spheres intersect in a perfect circle and the circle of intersection implies that the GPS receiver lies somewhere in a partial ring on the earth (Figure 1.3b & c). With the help of a third satellite, one gets a third sphere, which intersects this circle at two points (Figure 1.3d). The Earth itself can act as a fourth sphere -- only one of the two possible points will actually be on the surface of the planet, so the point in the space can be eliminated. However, if the receiver is not on the earth surface then it generally looks for four or more satellites, to improve accuracy and provide precise altitude information. In order to make this simple calculation, the GPS receiver should know (1) the location of at least four satellites above the receiver and (2) the distance between receiver and each of those satellites. Thus GPS receiver measures the time taken by the transmitted signal from the different satellites (A, B, and C) to reach the receiver and triangulates for the

exact position. While three satellites are essential to determine latitude and longitude, a fourth satellite is necessary to determine altitude.

1.3 Different Constellations for Satellite Navigation

Similar to GPS, there are various other satellite based navigation systems which are either being developed or planned for the global navigation satellite system (GNSS). The pioneer among them is the Russian GLObal'naya NAVigatsionnaya Sputnikovaya Sistema (GLONASS), and the European Global Satellite Navigation System (GALILEO). GLONASS is currently operational and is maintained by Russian ministry of defense. Similar to the GPS, the GLONASS is a space based navigation system providing global, all weather access to precise position, velocity and time information to a properly equipped user. Each GLONASS satellite transmits two carrier frequencies in L-band. The primary (L_1) band ranges from 1.6025 GHz to 1.6155 GHz at an interval of 0.5625 MHz, while secondary (L_2) band from 1.2464 GHz to 1.2565 GHz at an interval of 0.4375 MHz (*i.e.* 24 channels are available in each band). Each frequency is modulated by 5.11 MHz precision (P-code) signal or 0.511 MHz C/A signal. Overall, same message code is modulated over different carrier frequencies for different satellites. As on 2003, out of the intended 24 satellites envisaged only eleven were operational. The twelfth satellite was added in December 2004 [Ramjee and Ruggieri, 2005]. Hence, this constellation is not operating with its full capability. However, India has recently agreed to launch a few of their future satellites [http://www.india.mid.ru/summits/old_07.html] to make the constellation fully operational.

Moving from ideas and concepts conceived in the 1990s, the European Union (EU) along with European Space Agency (ESA) intends to operate the GALILEO under international civil control. This constellation will have 27(+) satellites depending on the level of international cooperation, the associated ground infrastructure and regional augmentations. The first phase of launching for GALILEO was accomplished in December 2005 [<http://news.bbc.co.uk/2/hi/science/nature/4555298.stm>]. A detail comparison of GPS, GLONASS and GALILEO systems is presented in Table 1.1. Meanwhile, China has come out with COMPASS as their regional navigation system. The COMPASS will have a constellation of 30 non-geostationary satellites and five geo-stationary satellites (GEOs) at 58.75° E, 80° E, 110.5° E, 140° E, and 160° E [Hein *et al.* 2007]. In addition to the global

satellite based navigation systems already underway, two regional satnav systems are also being developed by Japan and India. These systems are Quasi-Zenith Satellite System (QZSS) of Japan and Indian Radio Navigation Satellite System (IRNSS) of India [Hein *et al.* 2007]. All these regional systems will be inter-operable and inter-compatible for the development of a fully operational GNSS.

Table 1.1: A Detail Comparison of the GPS, GLONASS and GALILEO Features

Item	GPS	GLONASS	GALILEO
Operator	Department of Defence, USA	Ministry of Defence, Russia	EU and ESA
Total no of satellites	30	24	27-30
Current status	31 satellites	14 satellites	1 satellites
Altitude	20,200 km	19,100 km	23,616 km
No. of Orbits	6	3	3
Orbit period	11 hr. 58 min.	11 hr. 15 min.	14 hr. 24 min.
Orbit inclination	55°	65°	56°
Operating frequencies (GHz)	L ₁ = 1.575 L ₂ = 1.227	L ₁ = 1.602-1.615 L ₂ = 1.246-1.256	1.164-1.1215 (E ₅) 1.260-1.300 (E ₆) 1.559-1.592 (E ₇ -L ₁ -E ₁)
Clock rate i) C/A code ii) P code	1.023 Mbits/sec 10.23 Mbits/sec	0.511 Mbits/sec 5.11 Mbits/sec	10 Mbits/sec 5.11 Mbits/sec 2.046 Mbits/sec 1.023 Mbits/sec
Coordinate system	WGS-84 ECEF	SGS-90 (PZ-90) ECEF	ITRF _{0x} (IERS)
Time	GPS time synchronized with UTC	GLONASS time synchronized with UTC	GST (TAI), UTC (TAI)
Service offered	C/A code: Civilian application. P-code: Military application.	Safety-of-life applications. Navigation service. Search and rescue. Sub-meter real time accuracy for mobile users	Open service. Safety-of-life service. Commercial service. Public regulated service. Search and Rescue service.

1.4 Navigation Requirements and Differential GPS (DGPS)

Navigation requirement is the performance of the navigation system, necessary for operation within a defined airspace. The required navigation performance (RNP) is a part of a broader concept called "Performance-based Navigation," a method of implementing routes and flight paths that differs from earlier concepts. This procedure not only has an associated performance specification which an aircraft must meet before the path is flown, but must also monitor the achieved performance and provide an alert in the event when this fails to

meet the specification. RNP equipped aircraft can safely operate routes with less separation than previously required which is significant because it increases the number of aircraft that can safely use a particular airspace and therefore accommodate the increasing demand for air traffic capacity.

1.4.1 Required Navigation Performance (RNP)

The International Civil Aviation Organization (ICAO) developed the RNP approach in early 1990s and it has become a standard for airspace utilization nowadays. The RNP is a statement of the navigation performance necessary for operation within a defined airspace. The main required navigation parameters defined in *RTCA* [1999] are the following:

- (a) **Accuracy**: It is the degree of conformance of the estimated or measured position and/or the velocity of a platform at a given time with its true position or velocity. Radio navigation performance accuracy is usually specified as “Predictable”, “Repeatable” and “Relative”.
- (b) **Integrity**: It is the ability of the system to provide timely warnings to the user when it should not be used for navigation purpose. To achieve this, the system has to provide an *alert limit*, defined as the maximum error allowable in the user computed position. This alert limit can be specified in horizontal (HAL) as well as in the vertical (VAL).
- (c) **Continuity**: This is the capability of the total system (including all the elements necessary to maintain aircraft position within the defined airspace) to perform its function without non-scheduled interruptions during the intended operations.
- (d) **Availability**: This is the percentage of time that a system is performing the required function under stated conditions. Signal availability is the percentage of time that navigation signals transmitted from external sources are available to the user.

As an example the required RNP parameters for a GNSS aviation operation are presented in Table 1.2. This table details about the ICAO requirements from en-route to Category III (CAT III) precision approach operations. All the four main parameters for RNP along with the alert limit and time-to-alert are provided for each phase of flight operation. The critical accuracy in vertical direction is not required until the aircraft reaches the Approach for Vertical Guidance (APV-I and II) operation. The APVs are new classes of less stringent vertically guided approaches, which have been defined to enable the full utility of the performance that near-term satellite based augmentation system (SBAS) can provide.

Table 1.2: ICAO GNSS Aviation Operational Performance Requirements [Ramjee and Ruggieri, 2005]

Operations	Accuracy (95%)	Integrity (1-Risk)	Alert Limit	Time-to-Alert	Continuity (1-Risk)	Availability
Oceanic	12.4 nm	$1 \cdot 10^{-7}$ / hr	12.4 nm [#]	2 min	$1 \cdot 10^{-5}$ / hr	0.99-0.99999
En route	2.0 nm	$1 \cdot 10^{-7}$ / hr	2.0 nm	1 min	$1 \cdot 10^{-5}$ / hr	0.99-0.99999
Terminal	0.4 nm	$1 \cdot 10^{-7}$ / hr	1.0 nm	30 sec	$1 \cdot 10^{-5}$ / hr	0.99-0.99999
NPA*	220 m	$1 \cdot 10^{-7}$ / hr	0.3 nm	10 sec	$1 \cdot 10^{-5}$ / hr	0.99-0.99999
APV [†] I	220 m (H) 20 m (V)	$1 \cdot 2 \cdot 10^{-7}$ / approach	0.3 nm (H) 50 m (V)	10 sec	$1 \cdot 8 \cdot 10^{-6}$ / 15 sec	0.99-0.99999
APV II	16 m (H) 8 m (V)	$1 \cdot 2 \cdot 10^{-7}$ / approach	40 m (H) 20 m (V)	6 sec	$1 \cdot 8 \cdot 10^{-6}$ / 15 sec	0.99-0.99999
CAT I	16 m (H) 4-6 m (V)	$1 \cdot 2 \cdot 10^{-7}$ / approach	40 m (H) 10-15 m (V)	6 sec	$1 \cdot 8 \cdot 10^{-6}$ / 15 sec	0.99-0.99999
CAT II	6.9 m (H) 2 m (V)	$1 \cdot 10^{-9}$ / 15 sec	17.3 m (H) 5.3 m (V)	1 sec	$1 \cdot 4 \cdot 10^{-6}$ / 15 sec	0.99-0.99999
CAT III	6.2 m(H) 2 m (V)	$1 \cdot 10^{-9}$ / 15 sec	15.5 m(H) 5.3 m (V)	1 sec	$1 \cdot 2 \cdot 10^{-6}$ / 30 sec (H) $1 \cdot 2 \cdot 10^{-6}$ / 15 sec (V)	0.99-0.99999

*Non-precision approach; [†] Approach for vertical guidance; [#] nautical miles

The precision approach channels for the various phases of landing aircraft are shown in Figure 1.4. Each of these landing categories is defined by the decision height (DH) at which the pilot or the aircraft must make the decision either to continue or abort the landing. This decision depends on the runway visual range (RVR) at the corresponding decision height.

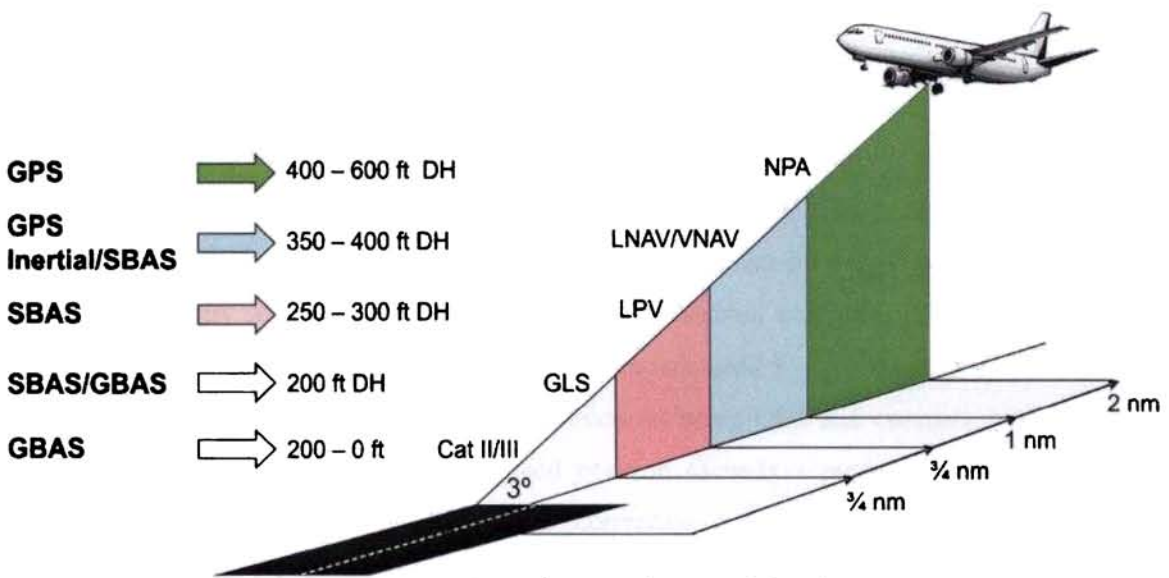


Figure 1.4: Precision approaches along with aircraft landing requirements

The three categories of most stringent approach and landings: CAT I, CAT II, and CAT III are achievable by ground based augmentation system (GBAS). For CAT I the corresponding values of DH and RVR are 200 ft and >2,400 ft respectively. The same for CAT II (CAT III) are 100 ft (50 ft) and >1200 ft (700 ft).

1.4.2 Differential GPS

A stand-alone GPS has limitations in providing the continuity, availability, integrity and accuracy to allow for its use as the sole means of navigation for all phases of flight. In order to meet the operational requirements, augmentation must be applied to basic GPS signals to eliminate the errors. In augmentation, a supplementary navigation method called Differential GPS (DGPS) is used to improve significantly the accuracy and integrity of the stand-alone GPS. The basic categories of augmentation proposed are Satellite-based augmentation system (SBAS) and Ground-based augmentation system (GBAS).

In the late 1980s, the United States Coast Guard started the development of a Marine DGPS (MDGPS) system to meet maritime navigation requirements in the United States. In 1989, radio-beacon located on Montauk Point, New York, was modified to broadcast DGPS corrections in the RTCM SC-104 (Radio Technical Commission for Maritime Services Study Committee-104) message format. By February 1997, fifty four radiobeacons were modified to provide DGPS correction for most of the U.S. coastal regions and inland waterways. In the same year, the coverage was further enhanced throughout the entire United States. This was named as Nationwide Differential GPS (NDGPS) system. The MDGPS essentially utilize the code-based Local area DGPS (LADGPS) techniques. The network for MDGPS/NDGPS includes Reference Stations (RS) to monitor GPS and generate differential corrections. Each RS has two GPS receivers for redundancy along with collocated Integrity Monitors (IM). Each IM includes another pair of GPS receivers and radiobeacon receivers to monitor the corrections broadcasted by the same site. The IM compute their positions and the differential corrections using GPS and compare with their known (surveyed) positions. If the computed position exceeds a preset tolerance, faulty satellite is removed from the differential correction calculation after notifying as “unhealthy” for the user. A frame relay network is used such that two central control stations, which are manned 24 hours a day, 7 days a week, can monitor the status of all the sites. The specified accuracy of the MDGPS/NDGPS systems is 10 m, *2drms*, within

coverage areas. Typical accuracies are much better (1 – 3 m). The specified availability is 99.9% for dual coverage areas and 99.7% for areas with single coverage. Later ICAO developed standards for the two types of code-based DGPS systems (SBAS and GBAS) for civil aircraft navigation applications.

1.4.2.1 Satellite-based augmentation system (SBAS)

A SBAS is a Wide area differential GPS (WADGPS) system that provides differential GPS corrections and integrity data using GEOs as the communication path. A unique feature of SBASs is that they provide DGPS data, using a single broadcast directly at the GPS L_1 frequency which can be used for ranging. The goal of SBASs is to meet the navigation requirements for civil aviation from the en-route phase of flight through vertically guided precision approach to a reasonably high precision landing (up to CAT I). A number of SBASs had been implemented or are planned for future (Figure 1.5). Such a system currently operational over the United States is the Wide Area Augmentation System (WAAS). The C-WAAS is the Canadian extension of WAAS, which is based on a network of reference stations located in the Canadian territory and linked to the Federal Aviation Administration (FAA) master stations in United States. Similarly the one that is being developed in Europe is the European Geo-stationary Navigation Overlay System (EGNOS) [ICG, 2006; Kaplan and Hegarty, 2006].

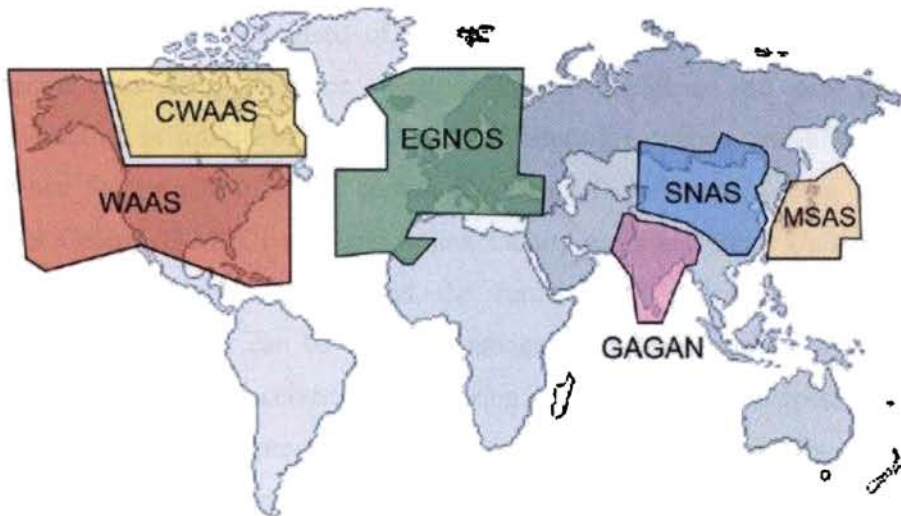


Figure 1.5: A Pictorial representations of different existing and upcoming SBAS systems

Japan is developing a SBAS based on its Multifunctional Transport Satellite (MTSAT), called the MTSAT Satellite Augmentation System (MSAS). The People's

Republic of China launched a series of experimental satellites, “Beidou”, for mastering the satellite based navigation technology. The Chinese SBAS strategy is encapsulated in the Satellite Navigation Augmentation System (SNAS) [Ramjee and Ruggieri, 2005]. India is also developing its own SBAS called GAGAN (GPS Aided Geo Augmented Navigation) and it is under the control of the Indian Space Research Organisation and the Airports authority of India [Kibe, 2003] with planned operational capability by 2009. The other upcoming regional augmentation systems are the Russian System of Differential Corrections and Monitoring (SDCM) and the IRNSS of India [ICG, 2006; Kaplan and Hegarty, 2006]. In years to come, these regional systems will operate simultaneously and emerge as a Global Navigation Satellite System to support a broad range of activities in the global navigation sector. Thus regional augmentation systems will have to play major role in GNSS. The potential of GNSS will be further enhanced through a focused attention on the coordination among these regional augmentation systems through maintaining its accuracy, integrity, reliability and inter-operability everywhere on the globe. Under the proposed framework for the real-time position determination with high accuracy ($\sim 0.2\text{-}0.5$ m), the EUPOS (European Position Determination System) is aimed using DGNSS (Differential GNSS) by maintaining huge network (~ 800 DGNSS reference stations with distance between them less than 100 km) of ground based stations [Rosenthal, 2007].

All SBAS systems are comprised of four major sub-elements, viz. the monitoring receivers, central processing facilities, satellite uplink facilities, and one or more geostationary satellite in orbit. For GAGAN the monitoring receivers are referred to as Indian Reference Station (INRES), the central processing facilities are known as Indian Master Control Centre (INMCC) and land uplink facility as Indian Land Uplink Station (INLUS). The GAGAN sub-elements and the functionality provided by them are summarized in Figure 1.6. As can be seen, the navigation signals received by the user, transmitted from GPS are also received by monitoring networks or INRES operated by the SBAS service providers. Each site within the monitoring networks generally includes a number of GNSS receivers (for redundancy) that provide L_1 C/A code and L_2 P(Y) code pseudorange and carrier-phase data to the central processing facilities or INMCC. At INMCC the data from the entire network are processed to develop estimates of each GPS satellite’s true position, associated clock error, corrections based on the differences between the networks estimates of these parameters and the values in the broadcast GPS navigation

data, and estimate of Ionospheric and Tropospheric delay error across the service area. These estimates and integrity information are then forwarded to the satellite up-link facilities

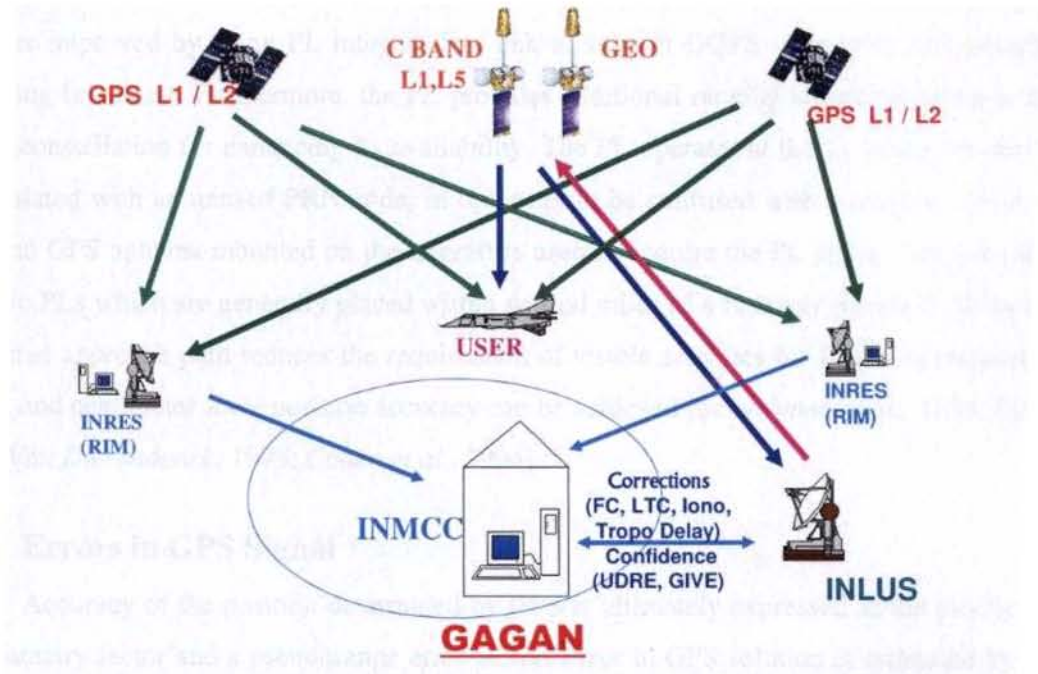


Figure 1.6: The GAGAN sub-elements and its functionality

(INLUS). From INLUS the signal is continuously transmitted to a geostationary satellite via C-band, which is further transmitted to the user at L_1 and L_5 frequencies. The timing of the signal is done in a very precise manner such that the signal appears as though it was generated on board the satellite as a GPS ranging signal.

1.4.2.2 Ground-based augmentation system (GBAS)

In a Ground-based augmentation system, SPS is augmented with a ground reference station to improve the performance of the navigation services in a local area. The only operational GBAS is the Large Area Augmentation System (LAAS) of the U.S. Federal Aviation Administration. This can support all phases of flight within its coverage area, including precision approach, landing, departure, and surface movement. In GBAS system, Pseudolites (PL) or integrity beacons (low-power ground based transmitters) are configured to emit GPS-like signals for improving accuracy, integrity, and availability of GPS [Parkinson and Spilker, 1996; Van Dierendonck, 1990; Elrod and Van Dierendonck, 1993; Elrod et al., 1994]. The improvement in accuracy can thus be obtained by enhancing the local geometry, measured according to a lower Vertical Dilution of Precision (VDOP) which

is very crucial for aircraft precision approach and landing. The accuracy and integrity is further improved by using PL integral data link to support DGPS operations and integrity warning broadcast. Furthermore, the PL provides additional ranging source to augment the GPS constellation for enhancing its availability. The PL operates at the L_1 frequency and is modulated with an unused PRN code, in order not to be confused with a satellite signal. A second GPS antenna mounted on the aircraft is used to acquire the PL signal. The presence of two PLs which are generally placed within several miles of a runway threshold along the nominal approach path reduces the requirement of visible satellites for DGPS operations to four, and centimeter-level position accuracy can be achieved [Schuchman *et al.*, 1989; Elrod and Van Dierendonck, 1993; Cohen *et al.*, 1994].

1.5 Errors in GPS Signal

Accuracy of the position determined by GPS is ultimately expressed as the product of a geometry factor and a pseudorange error factor. Error in GPS solution is estimated by the formula: (error in GPS solution) = (geometry factor) \times (pseudorange error factor). The pseudorange is the actually measured range which includes the errors that limit the GPS stand alone system to achieve the RNP up to the stringent CAT III condition. A detailed list of different sources of error in GPS ranging along with the range of these errors as well as the contribution from each error required to bring it down for navigation purpose (at CAT III level) is presented in Table 1.3. With appropriate assumptions, the pseudorange error factor is the satellite User Equivalent Range Error (UERE), which comprises of the components from all the three segments of the GPS system. The Space segment comprises of the satellite clock error and broadcasted ephemeris error. The ground segment has error contribution due to receiver noise and the multipath effect. The errors introduced by the propagation of GPS signal through the intervening atmosphere are the Ionospheric error and the Tropospheric (neutral atmospheric) error. All these errors are combined by root-sum-squared (RSS) to yield the UERE. The RSS addition for UERE is justified under the assumption that the errors can be treated as independent random such that the 1-sigma total error is the RSS of the individual 1-sigma values. The geometry factor, which expresses the composite effect of the relative satellite/user geometry on the GPS solution error, is generally known as the Geometric Dilution of Precision (GDOP). The GDOP value for a GPS system is 2.5, thus UERE value of 0.83 can achieve a CAT III level of position accuracy.

Table 1.3: A Table Showing the Error Budget in GPS

No.	Error Segment	Error Source	Range of Error (m)	1σ error required for Navigation (m)
1	Space	Satellite Clock Error	0.3-4	0.0
2	Segment	Satellite Ephemeris Error	1-6	0.8
3	Propagation	Ionospheric Error	5-45	0.1
4	Error	Tropospheric Error	2.5-30	0.2
5	Ground	Receiver Noise	0.5-5	0.1
6	Segment	Multipath	3-10	0.2
User Equivalent Range Error (UERE) or Total RSS				0.83
Navigation Accuracy = GDOP × UERE GDOP for GPS is 2.5				2.0 (CAT III)

The pseudorange or the measured distance between the satellite and the receiver can thus be obtained either by code and/or carrier-phase measurements. Following *Wübbena* [1991], the simplified observation equation for carrier wave L_1 which can be expressed in terms of pseudorange (PR) and carrier phase (ϕ) measurements is:

$$PR_{A[L_1]}^i = S_{A[L_1]}^i + c \cdot (\delta_A - \delta^i) + \delta S_{A[ION,L_1]}^i + \delta S_{A[TROP]}^i + M_A^i + \epsilon_{PR} \quad (1.1)$$

$$\phi_{A[L_1]}^i = S_{A[L_1]}^i + c \cdot (\delta_A - \delta^i) - \delta S_{A[ION,L_1]}^i + \delta S_{A[TROP]}^i + N_A^i \lambda + M_A^i + \epsilon_\phi \quad (1.2)$$

S_A^i = geometric distance between receiver antenna A and satellite i

c = speed of light (in vacuum, $c = 299\,792\,458$ m/s)

δ_A = receiver clock error

δ^i = satellite clock error

$\delta S_{A[ION]}^i$ = Ionospheric propagation delay

$\delta S_{A[TROP]}^i$ = Tropospheric propagation delay

N_A^i = Integer Ambiguity

λ_c = carrier wavelength (~ 19 cm for L_1)

M_A^i = Multipath errors

ϵ_{PR} = code phase measurement errors

ε_ϕ = carrier phase measurement errors

Understanding of the significance of these errors is important in applications that require very high accuracy. Each of these errors is briefly discussed in the following subsections.

1.5.1 Satellite Clock Error

The atomic clocks in GPS satellites, although highly accurate, are not perfect. The drift of these clocks from GPS system time, results in pseudorange error. The GPS time is a composite time scale derived from the times kept by clock at GPS monitoring stations along with the onboard satellite clock, which is used as the reference time. The GPS time which is set at 00h on 6th Jan 1980 and presently ahead of UTC by 14 seconds has not been perturbed by leap seconds. The atomic clocks stability is about 1 to 2 parts in 10^{13} over a period of one day. This means the satellite clock error is about 0.864 to 17.28 ns, which introduces around a 0.3-4 m error in ranging [Kaplan and Hegarty, 2006]. The Master control station determines the clock errors of each satellite and transmits clock correction parameters to the satellites for re-broadcasting to the user along with the navigation message.

1.5.2 Ephemeris Error

Ephemerides of all satellites are computed and up linked to the satellites along with other navigation data for re-broadcasting to the user. These ephemerides (in satellite navigation messages) are predicted from previous GPS observations at the ground control station. The satellite ephemeris error is the difference between the actual position and velocity of a satellite and those predicted by the broadcast ephemeris model. The residual satellite position error is in the range 1-6 m [Warren and Raquet, 2002].

1.5.3 Multipath

This refers to the phenomenon of a signal reaching the receiver antenna through two or more paths. Typically an antenna receives the direct signal along with one or more of its reflections from structures in the vicinity and also from ground. The reflected signal is delayed and usually weak compared to the direct signal. The multipath though affects the code as well as the carrier phase measurements; the magnitude of this error differs significantly. The error due to multipath effect is usually within 3-10 m [Kaplan and Hegarty, 2006]. A primary remedy for avoiding multipath is to place the antenna away from

reflectors, which may not be practical always. The affect of multipath can then be reduced by suitably designing the antenna consequently lowering the contribution from side lobes. In benign environments, such as open field, placing an antenna closer to the ground can decrease observed multipath errors because when the antenna is near to ground the signals experiences shorter excess path delays that tend to produce smaller multipath errors. Choke ring antennas are the special kind of antennas which are successful in mitigating the multipath arrivals from the ground or low-elevation scatterers.

1.5.4 Receiver Noise

The code and carrier phase measurements are affected by random noise, which is usually referred to as receiver noise. This includes the noise introduced by antenna, amplifiers cables and the receiver. The receiver noise varies with the signal strength, which in turn varies with the satellite elevation angle. The dominant source of error in pseudorange measurements is the thermal noise jitter and the effects of interference. The C/A code composite receiver noise and resolution error contribution are slightly larger than that for P(Y) code because the former has a smaller *rms* bandwidth than the latter.

1.5.5 GPS Signal Propagation Errors

The Microwaves as they propagate through the atmosphere undergo scattering, attenuation and refraction. As the GPS signal lies in the L-band of the Microwave frequency domain, the contribution of signal delay due to scattering and attenuation is negligible. So the delay in the GPS signal when it traverses through the atmosphere is mainly due to the refractive nature of the intervening atmosphere. However, the L-band is aptly chosen frequency band as the refractive effect of ionosphere is moderate, and that of neutral atmosphere is least, at these frequencies. For GPS application, the atmospheric regions of interest for error budget are mainly the neutral atmosphere and ionosphere. The effect of neutral atmosphere ranges from the surface of the earth up to approximately 100 km in altitude, where as that of the ionosphere ranges from 75 km and more. The delay caused by the ionized region of the atmosphere is called the Ionospheric delay and that by the neutral atmosphere is Tropospheric delay (as 98% of the neutral atmosphere is contained in the troposphere).

1.5.5.1 Microwave propagation in the atmosphere

The earth's atmosphere is a heterogeneous medium with significant variations of its physical parameters such as temperature, pressure and humidity, *etc.*, prominently in vertical direction. When microwave propagates through such a medium, it introduces a small retardation as well as bending of the ray path. The velocity (v) of an electromagnetic wave in a medium having a refractive index n , is written as $v = c/n$ where c is its velocity in vacuum. For most of the physical media, $n > 1$, which implies that the speed of the propagating electromagnetic (EM) wave is less than that in vacuum. The value of n is characterized by permeability (μ) and dielectric constant (ϵ) of the medium. The expression for v can then be written as $v = c/\sqrt{\mu\epsilon}$. If μ_0 and ϵ_0 are the permeability and dielectric constant of free space, respectively, then $c = \sqrt{\mu_0\epsilon_0}$. For a refractive medium ($\epsilon > \epsilon_0$), the wave propagates with a velocity which is less than that in free space (*i.e.* $v < c$).

In general, the index of refraction is a complex quantity with its real component representing the non-absorbing part of the medium and the imaginary part representing the attenuation of electromagnetic waves by the medium. In microwave domain the refractive index of air is a function of temperature, pressure and humidity. As all these three parameters decrease with increase in altitude, n also decreases with altitude. At standard temperature and pressure, $n \approx 1.0003$ [Petty, 2004]. It approaches unity with increasing altitude. As a result, the ray path bends towards the earth surface due to refraction. The decrease in velocity and bending of ray-path introduces an error in the measured range which is taken as the product of the velocity of the wave in free space and time taken by the wave to trace the in-between region. A typical illustration of the propagation of radio waves in the atmosphere from a transmitter in the satellite to the observer on the earth's surface is presented in Figure 1.7. As virtually there is no atmosphere above the ionosphere, the ray does not undergo any pronounced deviation in this region. Neglecting the horizontal variability, the atmosphere can be divided into a number of concentric layers each of thickness ds , with n_i as the refractive index for each layer. The time taken by a ray to travel from a distant satellite to receiver is equal to $\Delta t = 1/c \int n ds$ and the apparent range $R = c \times \Delta t$. The error in the estimated range (ΔR) due to extra time (Δt) incurred by the refraction

effect would be obtained by differencing the apparent range and the direct path (or geometric line of site distance, D)

$$\Delta R = \int n ds - D \quad (1.3)$$

As seen from eq. (1.3) a clear knowledge on the variation of n along the ray path is necessary for the calculation of range error.

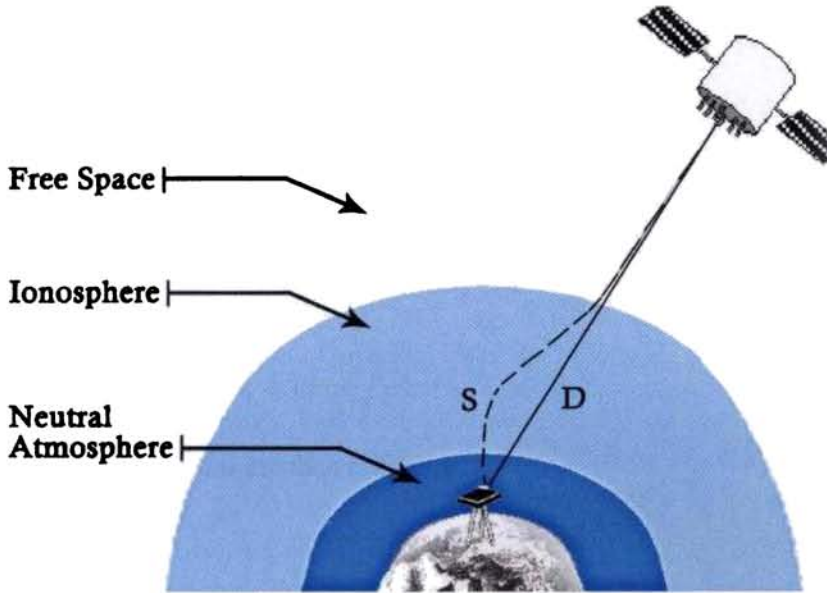


Figure 1.7: A pictorial illustration of the wave propagation at GPS frequencies in the atmosphere

1.5.5.2 Ionospheric contribution to atmospheric delay

The earth's atmospheric region above 75 km is partly ionized. This ionization influences the propagation of EM waves differently. On one hand, the layer can act as a mirror to radio wave in the short wave (10 – 100 meters wavelength) domain, it acts as a dispersive medium for the microwave frequencies. The index of refraction for the phase propagation (n_p) in the ionosphere is approximated as [Kaplan and Hegarty, 2006]

$$n_p = 1 + \frac{c_2}{f^2} + \frac{c_3}{f^3} + \frac{c_4}{f^4} \dots \quad (1.4)$$

where the coefficients c_2 , c_3 and c_4 are frequency independent as well as a function of the electron number density. The refractive index of the ionosphere depends on the frequency of the propagating wave (f), making the medium dispersive. The expression of refractive index for group propagation (n_g) can be written as

$$n_g = n_p + f \frac{dn_p}{df} \quad (1.5)$$

Substituting eq. (1.4) in eq. (1.5) n_g can be written as

$$n_g = 1 - \frac{c_2}{f^2} - \frac{2c_3}{f^3} - \frac{3c_4}{f^4} \dots \quad (1.6)$$

Neglecting the higher order terms one can write

$$n_p = 1 + \frac{c_2}{f^2} \quad n_g = 1 - \frac{c_2}{f^2} \quad (1.7)$$

The coefficient c_2 is estimated as $c_2 = -40.3 n_e \text{ Hz}^2$, where n_e is the electron number density. Then eq. (1.7) can be rewritten as

$$n_p = 1 - \frac{40.3 n_e}{f^2} \quad n_g = 1 + \frac{40.3 n_e}{f^2} \quad (1.8)$$

The phase and group velocities are then estimated as:

$$v_p = \frac{c}{1 - \frac{40.3 n_e}{f^2}} \quad v_g = \frac{c}{1 + \frac{40.3 n_e}{f^2}} \quad (1.9)$$

In case of microwave propagating through the ionosphere, it experiences a group retardation and phase advance, a phenomenon referred to as ionospheric divergence. The refractive index of the ionosphere varies inversely with the square of radio frequency and so ionospheric refraction is more significant at lower frequencies (below S-band) [Kaplan and Hegarty, 2006]. The range error associated with the microwave propagation through the ionosphere is

$$\Delta R_{\text{iono}} = -\frac{40.3}{f^2} \int n_e dl \quad (1.10)$$

where $\int n_e dl$ is the electron density along the path length, referred to as the total electron count (TEC). Since the TEC is generally referenced to the vertical direction through the ionosphere, for other elevation angles the ΔR_{iono} is to be multiplied by an obliquity factor (O_F) or mapping function given as

$$O_F = \left[1 - \left(\frac{r_e \cos \phi_e}{r_e + h_1} \right)^2 \right]^{-\frac{1}{2}} \quad (1.11)$$

where h_f is the height of maximum electron density (~ 350 km), r_e is the radius of earth and ϕ_e is the elevation angle. With addition of the O_F the path delay expression becomes

$$\Delta R_{\text{iono}} = -O_F \frac{40.3}{f^2} \text{TEC} \quad (1.12)$$

This dispersive behavior of ionosphere to microwave propagation is used for estimating the ionospheric delay by making the measurements at two frequencies say L_1 and L_2 . Differencing the pseudorange measurements made on both L_1 and L_2 frequencies enables the estimation of delays in both the L_1 and L_2 . Thus to account for the ionospheric delay one uses the following expressions for L_1 and L_2

$$\Delta R_{\text{iono,corr}_{L_1}} = \left(\frac{f_{L_2}^2}{f_{L_2}^2 - f_{L_1}^2} \right) (\rho_{L_1} - \rho_{L_2}) \quad (1.13a)$$

$$\Delta R_{\text{iono,corr}_{L_2}} = \left(\frac{f_{L_2}^2}{f_{L_2}^2 - f_{L_1}^2} \right) (\rho_{L_1} - \rho_{L_2}) \left[\frac{f_{L_1}^2}{f_{L_2}^2} \right] \quad (1.13b)$$

where ρ_{L_1} and ρ_{L_2} are the pseudorange observations at L_1 and L_2 . For various civilian applications including navigation, single-frequency receivers are used. Then it is obvious that one cannot use eq. (1.13) or the dual frequency technique to estimate the ionospheric delay. Consequently, models of the ionosphere are to be employed to correct for the ionospheric delay. One important example of such a model is the Klobuchar model, which removes (on average) about 50% of the ionospheric delay at mid-latitudes through a set of coefficients included in the GPS navigation message [Kaplan and Hegarty, 2006]. Another method of removing the ionospheric delay in a single frequency receiver for navigation is by providing near-real time TEC values from the reference stations (consisting of minimum three dual frequency receivers). These dual frequency receivers estimate the TEC for each reference station in-and-around the user and provide the TEC information to the user through broadcasting *via* a geostationary (communication) satellite link. To achieve this more efficiently, one has to have a dense network of reference stations.

Thus to summarize, the ionosphere is characterized by a large concentration of free electrons that cause a variation of the channel refractive index and, consequently, of the wave propagation velocity in the medium. In particular, the ionosphere effects on the GPS signals mainly result in 1) a combination of group delay and carrier phase advance, which varies with the paths and electron density encountered by the signal in crossing the

ionosphere, and 2) scintillation, which can bring the signal amplitude and phase to fluctuate rapidly at certain latitudes and even cause loss of lock. Other effects related to the ionosphere, such as Faraday's rotation and ray bending that changes the arrival angle, are not significant for the GPS frequencies. In the GPS frequency bands, the Ionospheric path delay in zenith direction might vary from 2-50 ns, in a diurnal fashion that is quite variable and unpredictable from day-to-day. At lower elevation angles, the delay might increase up to three times the value at the zenith. This implies that the Ionospheric error can contribute in the range of 5-45 m [Ramjee and Ruggieri, 2005]. The ionosphere being a dispersive medium (frequency dependent), dual (or multi) frequency observations helps to reduce this delay. Note that as the present study is focused only on the effect of neutral atmosphere in microwave ranging, the refraction effects in the ionosphere will not be considered in subsequent discussions.

1.5.5.3 Contribution of neutral atmosphere to atmospheric delay

Most of the neutral constituents in the atmosphere reside in the lower part of the earth's atmosphere. The neutral density decreases exponentially with increase in altitude following the hydrostatic equilibrium. Though the concentration of the major neutral constituents (N_2 , O_2 , Ar, etc) decreases with altitude almost all the water vapor and bulk of the dry gases are found in the troposphere which ranges from sea level (≈ 0 m) to $\sim 12 - 16$ km. In this region, the temperature in general decreases almost linearly with increase in altitude with a fixed lapse rate. The altitude extent of the troposphere varies with latitude. The region separating the troposphere from the atmosphere above it is known as tropopause where the temperature gradient is very small and approaches close to zero. The region above the tropopause, where the atmospheric temperature starts increasing with altitude, is referred to as stratosphere. In addition to the major constituents, the neutral atmosphere also contains significant amount of trace constituents like CO_2 , O_3 and water vapor. All these gases in the atmosphere, except water vapor are non-polar molecules, while water vapor is polar in nature. A polar molecule will have a permanent electric dipole moment and it aligns itself to the applied electromagnetic field, while a non-polar molecule do not have a permanent electric dipole moment and this will be induced when an external electromagnetic field is applied. While the non-polar gas molecules are well mixed in the atmosphere and obey the hydrostatic equations, water vapor is not well mixed.

As the refractive index of air is greater than unity, the wave propagation through this medium undergoes group retardation. In addition to that the ray-path is curved because of the refractive bending. The group retardation and bending of the ray affect the net apparent path length traveled by the wave and can be estimated as the integral of the refractive index (n) profile (eq. 1.3) along the curved path. If 'S' is the curved path and 'D' is the direct path length then the extra path length estimated through ranging is $\Delta R_{\text{tropo}} = \int_S n \cdot ds - D = \int_S (n-1) \cdot ds + [S-D]$. Considering the wave propagation in vertical, as there is no refractive bending 'S' will be identically equal to 'D'. Then the extra path encountered in the zenith direction, usually referred to as zenith tropospheric delay (ZTD) is $\int_0^{\infty} (n-1) \cdot ds$, where the integral is taken for the entire neutral atmosphere. The equation can be written in terms of the refractivity (N) of the air as $ZTD = 10^{-6} \times \int N \cdot ds = 10^{-6} \times [\int N_D \cdot ds + \int N_W \cdot ds]$ where N_D and N_W represents the hydrostatic (dry) and non-hydrostatic (wet) component of refractivity, respectively. The net tropospheric delay in the zenith direction thus has two parts, one governed by the non-polar gases (hydrostatic), which is usually referred to as zenith hydrostatic delay (ZHD) and the other contributed by water vapor which is referred to as the zenith wet delay (ZWD). While the hydrostatic (dry) component constitutes about 90% of the total delay, the non-hydrostatic (wet) part constitutes the remaining 10%. More details on tropospheric delay due to refraction and its estimation are presented in Chapter 2.

The refraction of the Microwaves at GPS frequencies as it passes through the entire neutral atmosphere is referred to as tropospheric delay [Misra and Enge, 2001; Barry and Chorley, 1998]. The GPS signals when it traverses through the troposphere it induces delay effects in the order of 2-30 m [Ramjee and Ruggieri, 2005]. These effects depend on the density of atmospheric gases as well as the zenith angle at which the ray propagates. Complete information on different atmospheric parameters like pressure (P), temperature (T) and water vapor partial pressure (e) is essential to estimate this delay. At GPS frequencies, the delay caused by troposphere is one order in magnitude less than that caused by the ionosphere. But this delay is almost the same for both L_1 and L_2 frequencies. Since it is not frequency dependent (non-dispersive), this effect cannot be eliminated using dual (or multi) frequency measurements. However, this can only be accounted for through modeling. The existing global models are successful in predicting the dry part of the delay with an accuracy of approximately 1 cm and the wet part with ~ 5 cm [Kaplan and Hegarty, 2006].

1.6 A Review of Different Models for Estimating Tropospheric Delay

Different empirical meteorological models are developed for the estimation of the ZHD and ZWD on a global basis. *Saastamoinen* [1972] evolved a simple relation between ZHD and surface pressure (P_S) taking into account the variation due to gravity and height for different latitudes. The claimed accuracy of the Saastamoinen model is within 0.4 km for all the latitudes and seasons. Later on *Davis et al.* [1985] and *Elgered et al.* [1991] proposed similar expressions for ZHD with a slightly different value for the coefficients. All these models are developed under the assumption that the dry atmosphere is in hydrostatic equilibrium and follows the equation of state. However, since water vapor does not follow the hydrostatic conditions and can remain heterogeneously distributed in the atmosphere, similar models for ZWD were not attempted until *Ifadis* [1986] and *Mendes and Langley* [1998] developed simple empirical relation connecting ZWD with P_S , surface temperature (T_S) and surface water vapor partial pressure (e_S). A slightly different model for ZHD and ZWD was arrived by *Hopfield* [1971], based on a different refractivity model. A brief outline of these models is presented in the following subsections.

1.6.1 Linear Models for ZHD and ZWD

Saastamoinen [1972] showed that although the refractivity at any point in a dry atmosphere depends on pressure and temperature, the height integral of this dry refractivity profile would be a simple linear function of surface pressure. The main assumption in this model is that the dry atmosphere is in hydrostatic equilibrium and the equation of state

$$dP = -g(h) \cdot \rho(h) \cdot dH_g \quad (1.14)$$

is true. Here the acceleration due to gravity (g) is a function of height (h), ρ is the density of the air and H_g is the geopotential height (in m) or the vertical coordinates with reference to earth's Mean Sea Level (MSL). If g is assumed to be a constant with a weighted mean value g_m then eq. (1.14) can be written as

$$\rho = -\frac{1}{g_m} \cdot \frac{dP}{dH_g} \quad (1.15)$$

This equation along with the ideal gas law ($P = \rho R_d T$) can be used to estimate the N_D value as

$$N_D = \left[k_1 \frac{P}{T} \right] = k_1 \cdot R_d \cdot \rho = -k_1 \cdot R_d \cdot \frac{1}{g_m} \cdot \frac{dP}{dH_g} \quad (1.16)$$

where $k_1 = 77.6 \text{ K/hPa}$, is hydrostatic refractivity constant [Bevis *et al.*, 1992], P is pressure (hPa), and R_d is gas constant of dry air ($\text{J kg}^{-1} \text{ K}^{-1}$). Then the ZHD can be written as

$$\begin{aligned} \text{ZHD} &= 10^{-6} \cdot \int_{h_s}^{\infty} N_D(h) \cdot dh = -10^{-6} k_1 \cdot R_d \cdot \frac{1}{g_m} \cdot \int_{P_s}^{\infty} \frac{dP}{dH_g} = -10^{-6} k_1 \cdot R_d \cdot \frac{1}{g_m} \cdot (P_{\infty} - P_s) \\ &= -10^{-6} k_1 \cdot R_d \cdot \frac{1}{g_m} \cdot (0 - P_s) = \frac{10^{-6} k_1 \cdot R^*}{M_d} \cdot \frac{P_s}{g_m} = 0.022275 \cdot \frac{P_s}{g_m} \end{aligned} \quad (1.17)$$

where R^* is the universal gas constant ($=8314.3 \text{ J kmol}^{-1} \text{ K}^{-1}$), M_d is the molecular weight of dry air ($=28.9644 \text{ kg/kmol}$) and the g_m is defined as

$$g_m = \frac{\int_{h_s}^{\infty} \rho(h) \cdot g(h) \cdot dh}{\int_{h_s}^{\infty} \rho(h) \cdot dh} \quad (1.18)$$

and can be interpreted as the gravity at the centroid of the atmospheric column [Saastamoinen, 1972]. The value of g_m depends on latitude through the relation [Davis *et al.*, 1985]

$$g_m = 9.8062 \cdot (1 - 0.00265 \cdot \cos 2\varphi - 0.00031 \cdot h_c) \quad (1.19)$$

where φ is the ellipsoidal latitude and the h_c is the height of the center of the atmospheric column above the ellipsoid (in km), which is linearly modeled by Saastamoinen as $h_c = 7.3 + 0.9 \times h$; where h is the height of the antenna site above the ellipsoid (km).

Substituting this in eq. (1.19) the expression for g_m can be written as

$$g_m = 9.784 \cdot (1 - 0.00266 \cdot \cos 2\varphi - 0.00028 \cdot h) \quad (1.20)$$

Then from eq. (1.17)

$$\text{ZHD} = \frac{0.0022767 \cdot P_s}{1 - 0.00266 \cdot \cos 2\varphi - 0.00028 \cdot h} \quad (1.21)$$

This model is very popular due to its simplicity. The *rms* error budget using Saastamoinen model [Elgered *et al.*, 1991] shows that the error in the refractivity constant contributes to about 2.4 mm in ZHD. The uncertainty in g_m has only a marginal influence of 0.2 mm and the uncertainty of the universal gas constant and the variability of the dry mean molar mass contributes approximately 0.1 mm in the estimation of ZHD. Thus, in this model along with surface pressure measurements the height of the station and its latitude are used for the computation of the gravity correction. Though a similar model was not tried for ZWD in the

earlier attempts mainly due to the heterogeneity of the distribution of water vapor in the atmosphere, later *Chao* [1972], *Berman* [1976], and *Saastamoinen* [1972] tried to develop models for the wet component but with obsolete value of refractivity constants. All these models were either station or season specific and had biases of up to 10-20 % depending on the site.

Ifadis [1986] proposed a model for the zenith wet delay as a function of P_s , T_s and e_s in the following form.

$$\begin{aligned} \text{ZWD} = & 0.554 \cdot 10^{-2} - 0.88 \cdot 10^{-4} \cdot (P_s - 1000) \\ & + 0.272 \cdot 10^{-4} \cdot e_s + 2.771 \frac{e_s}{T_s} \end{aligned} \quad (1.22)$$

Mendes and Langley [1998] derived a linear relation for ZWD in the form

$$\text{ZWD} = 0.122 + 0.00943 \cdot e_s \quad (1.23)$$

relating zenith wet delay and partial water vapor pressure at the surface using data from about 50 stations, most of which are located in USA and Canada.

Though meteorological parameters at surface are correlated reasonably well with the range error, these surface models are not efficient enough to account for the complete integral effect of atmospheric refraction in vertical direction [*Bock and Doerflinger*, 2000]. In case, if the required range is from a particular altitude in the atmosphere, the refraction effect for the altitude above, only need to be accounted for. In this context, *Hopfield* [1971] tried to develop a model accounting for the variation of atmospheric refractivity with altitude through an analytical function.

1.6.2 Hopfield Model for ZHD and ZWD

Hopfield [1969] developed an analytical model for the altitude profile of refractive index based on surface refractivity (N_s) and a term called the “characteristic height” which is different for the hydrostatic and non-hydrostatic component of refractivity. These characteristic heights are defined as the altitude above which the atmospheric refraction effect is negligible. This implies that the values of N_D and N_W become negligible above the respective characteristic heights. Once the mean annual pattern of characteristic height is modeled for a station, it is possible to estimate the range error directly from surface refractivity. These analytical relations are arrived based on following approach.

The equation for hydrostatic equilibrium (eq. 1.14) that follows from the ideal gas laws of Boyle-Mariotte and Gay-Lussac can be expressed in differential form by expressing the density as $\rho = \frac{P}{R_d \cdot T}$ in the form

$$dP = -g \cdot \frac{P}{R_d \cdot T} \cdot dh \Leftrightarrow \frac{dP}{P} = -\frac{g}{R_d \cdot T} \cdot dh \quad (1.24)$$

The altitude profile of the temperature in the troposphere can be approximated to be linear with a constant temperature lapse rate (β) in the form $T = T_s + \beta \cdot h$, where T_s is temperature at the surface (or antenna height), h is the height above MSL and T is a function of altitude. Substituting this in eq. (1.24) the differential equation takes the form

$$\frac{dP}{P} = -\frac{g}{R_d \cdot (T_s + \beta \cdot h)} \cdot dh \quad (1.25)$$

Integrating this equation for altitude region 0 to h where the atmospheric pressure decreases from P_s to P

$$\begin{aligned} \int_{P_s}^P \frac{dP}{P} &= -\frac{g}{R_d} \cdot \int_0^h \frac{1}{(T_s + \beta \cdot h)} dh \\ \Rightarrow \ln\left(\frac{P}{P_s}\right) &= \ln\left[\left(\frac{(T_s + \beta \cdot h)}{T_s}\right)^{-\frac{g}{R_d \cdot \beta}}\right] \\ \Rightarrow P &= P_s \cdot \left(\frac{(T_s + \beta \cdot h)}{T_s}\right)^{-\frac{g}{R_d \cdot \beta}} \end{aligned} \quad (1.26)$$

Now, let us recall the hydrostatic refractivity formula:

$$N_D = k_1 \cdot R_d \cdot \rho = \frac{k_1 \cdot R^* \cdot \rho}{M_d} \quad (1.27)$$

The total density of air, ρ is the sum of density of dry air (ρ_d) and that of water vapor (ρ_w) given as

$$\rho = \rho_d + \rho_w = \frac{P_d \cdot M_d}{R^* \cdot T} + \frac{e \cdot M_w}{R^* \cdot T} \quad (1.28)$$

where M_w is the molecular weight of water (=18.016 kg/kmol). If one considers that $P_d \gg e$ and $P_d \cdot M_d \gg e \cdot M_w$ then it is acceptable to approximate that $M_d \approx M_w$. Then the ρ becomes

$$\rho = \rho_d + \rho_w = \frac{P_d \cdot M_d}{R^* \cdot T} + \frac{e \cdot M_w}{R^* \cdot T} \approx \frac{P_d \cdot M_d + e \cdot M_d}{R^* \cdot T} = \frac{P \cdot M_d}{R^* \cdot T} = \frac{P}{R_d \cdot T} \quad (1.29)$$

Substituting this in eq. (1.27) the expression for N_D becomes

$$N_D = k_1 \cdot R_d \cdot \rho = k_1 \cdot R_d \cdot \frac{P}{R_d \cdot T} = k_1 \cdot \frac{P}{T} \quad (1.30)$$

Substituting for P and T

$$N_D = k_1 \cdot \frac{P}{T} = k_1 \cdot \frac{1}{T_s + \beta \cdot h} \cdot P_s \cdot \left(\frac{T_s + \beta \cdot h}{T_s} \right)^{-\frac{R}{R_d \cdot \beta}} \quad (1.31)$$

which can be further simplified to

$$\begin{aligned} N_D &= k_1 \cdot \frac{P}{T} = k_1 \cdot \frac{P_s}{T_s} \cdot \left(\frac{T_s}{T_s + \beta \cdot h} \right) \cdot \left(\frac{T_s + \beta \cdot h}{T_s} \right)^{-\frac{R}{R_d \cdot \beta}} \\ &= N_{SD} \cdot \left(\frac{T_s + \beta \cdot h}{T_s} \right)^{-\left(1 + \frac{g \cdot M_d}{R_d \cdot \beta}\right)} = N_{SD} \cdot \left(1 + \frac{\beta \cdot h}{T_s} \right)^\eta \end{aligned} \quad (1.32)$$

where $N_{SD} = k_1 \cdot \frac{P_s}{T_s}$. For a default temperature lapse rate of $\beta = -6.81$ K/km and a mean

gravity acceleration of $g = 9.806$ m/s² the exponent becomes $\eta = 4.02 \approx 4$ that is adopted for the Hopfield two-quartic model. Another modification is made by substitution of

$$\frac{\beta}{T_s} = \frac{1}{\frac{1}{\beta} \cdot T_s - h_{0D}} = -\frac{1}{h_{0D} - \frac{1}{\beta} \cdot T_s} = -\frac{1}{h_D} \quad (1.33)$$

where T_s is the surface temperature in °C; h_{0D} is the characteristic height of the dry atmosphere for temperature of 0°C (in km) and h_D is the characteristic height of the dry atmosphere (in km). The variation of h_D (in km) with T_s (in °C) is modeled from global radiosonde data as

$$h_D = 40.136 + 0.14872 \times T_s \quad (1.34)$$

As stated above employing a value of 4 for η , N_D is simplified as

$$N_D = N_{SD} \cdot \left(1 - \frac{h}{h_D} \right)^4 \quad (1.35)$$

eq. (1.32) can then be integrated analytically to yield ZHD as

$$\text{ZHD} = 10^{-6} \cdot N_{SD} \cdot \int_0^{h_D} \left(1 - \frac{h}{h_D}\right)^4 dh = 10^{-6} \cdot N_{SD} \cdot \frac{h_D}{5} \quad (1.36)$$

It is clear that a number of approximations lead to this simple formula. Apart from the fact that the air is treated as an ideal gas which is not too critical, the assumption of a constant temperature lapse rate is one important approximation that should be stressed as well as the fact that the gravity is not modeled in terms of its dependence on the height, as was done for Saastamoinen model.

Hopfield [1969] assumed that the non-hydrostatic component of N also follows the similar relationship but with a different value for the characteristic height. Thus in analogous to eq. (1.35) an expression for the non-hydrostatic component can be written as

$$N_w = N_{sw} \cdot \left(1 - \frac{h}{h_w}\right)^4 \quad (1.37)$$

where h_w is the wet characteristic height. The wet delay then can be written as

$$\text{ZWD} = 10^{-6} \cdot N_{sw} \cdot \int_0^{h_w} \left(1 - \frac{h}{h_w}\right)^4 dh = 10^{-6} \cdot N_{sw} \cdot \frac{h_w}{5} \quad (1.38)$$

Mendes and Langley [1998] found a relation between the surface temperature (in °C) and h_w (in km) of the form

$$h_w = 7.508 + 0.002421 \cdot \exp\left(\frac{T_s}{22.90}\right) \quad (1.39)$$

The estimation of the ZWD based on Hopfield method needs only the information about e_s and T_s [*Hopfield*, 1969]. As h_w is not well correlated with T_s , there will be some uncertainty in the estimation of ZWD using this model. Analysis shows that a 10% error in the value of h_w can introduce an error of < 1% in the estimated value of ZTD and hence can be neglected for application purpose.

Even though all these empirical models are considered as global, most of these are experimentally derived using the available radiosonde data from European and North American continents [*Satirapod and Chalermwattanachai*, 2005]. The accuracy of these empirical models has been assessed by comparing model output with true values estimated by ray-tracing the atmospheric profiles. It has been shown that ZHD models are typically accurate up to 2-3 mm at mid-latitudes [*Janes et al.*, 1991], and estimates of ZWD from surface meteorological data exhibit typical errors of up to 3-5 cm [*Askne and Nordius*, 1987;

Janes et al., 1991; *Elgered*, 1992] and up to 5-8 cm during the passage of weather fronts [*Elgered*, 1993; *Ichikawa*, 1995].

1.7 Projecting the Zenith Tropospheric Delay to Slant Direction

The tropospheric delay is shortest in zenith direction and increases with zenith angle. In many cases for the use of GPS in navigation and meteorology it becomes necessary to use the data from higher zenith angle mainly because of the fact that usage of a high zenith angle expands the observation geometry in navigation application while increases the amount of data availability in meteorological applications. Many investigators [*Ware et al.*, 1997; *Flores et al.*, 2000; *Braun et al.*, 2001; *Mac Donald and Xie*, 2000] have elaborately studied the effect of very high zenith angles in GPS slant observations in relation to meteorological applications. Studies have shown that though the tropospheric delay is ~ 2 m in the zenith direction, it increases to over ~ 20 m at high zenith angle [*Ramjee and Ruggieri*, 2005; *Dodson et al.*, 1999a], thus exceeds the criteria set for optimum positioning for civil navigation [*Kaplan and Hegarty*, 2006]. In general the tropospheric delay at a given zenith angle (χ), referred to as slant total delay (ΔR), which is related to zenith delay as

$$\Delta R = \text{ZHD} \times \text{MF}_h(\chi) + \text{ZWD} \times \text{MF}_w(\chi) \quad (1.40)$$

This projection of zenith path delay into a slant direction is performed by application of a mapping function (MF) or obliquity factor. The first part in eq. (1.40) is the hydrostatic component of slant delay (SHD) and the second part represents the non-hydrostatic component of slant delay (SWD). Thus the mapping functions are defined as

$$\text{MF}_h(\chi) = \frac{\text{SHD}}{\text{ZHD}} \quad (1.41a)$$

$$\text{MF}_w(\chi) = \frac{\text{SWD}}{\text{ZWD}} \quad (1.41b)$$

Tracing the ray-path through the refractivity profiles (derived from the radiosonde data) provides an estimate of mapping function [*Rocken et al.* 2001], which is also known as direct mapping function (or true value of MF). Simplest analytical function for MF is the cosecant function. The upper limit of use of this function for many applications is $\sim 60^\circ$ (zenith angle). In higher zenith angles, *Marini* [1972] showed that for a spherically symmetric atmosphere the MF can be approximated by a continued fraction, which was later on modified by *Herring* [1992], *Niell* [1996] etc. *Niell* [2000] also proposed an isobaric

hydrostatic mapping function (IMF) which uses only one meteorological input parameter (the height of the 200 hPa isobar). The most commonly used MF among the analysts is Niell mapping function (NMF) [Niell, 1996] the coefficients for which are determined from site coordinates and the day of the year using a look-up table. Recently, a Global Mapping Function (GMF), based on data from the global ECMWF numerical weather model was developed by *Boehm et al.* [2006a]. The coefficients of GMF were obtained from the expansion of the Vienna Mapping Function (VMF1) parameters [Boehm et al. 2006b] into spherical harmonics on a global scale. In the following section three of these global MFs are discussed in detail.

1.7.1 Herring Mapping Function

The curvature of the earth's atmosphere and non-linear variations of earth's atmosphere in vertical direction makes the development of MF very difficult. The complexity involved in developing a simple MF, is the reason why many (more-or-less similar) approximations are in use. However, the fractional expansion of *Marini* [1972] and *Marini and Murray* [1973] was found to be superior. It meets the following two boundary conditions: 1) The tropospheric mapping function is asymptotic in $\cos\chi$ for $\chi \rightarrow 0$ and 2) it is asymptotic in $1/\cos\chi$ for $\chi \rightarrow 90^\circ$. The continued fraction that is presented by *Herring* [1992] satisfies both conditions and can be truncated according to the accuracy requirements. This function is given as

$$MF(\chi) = \frac{\frac{1}{1 + \frac{a}{1 + \frac{b}{1 + c}}}}{\frac{1}{\cos(\chi) + \frac{a}{\cos(\chi) + \frac{b}{\cos(\chi) + c}}} \quad (1.42)$$

where χ is the zenith angle and a , b and c are the mapping function coefficients, to be determined. Herring [1992] derived coefficients for the mapping function by raytracing 10 years of rawinsonde data from North America. The surface temperature (T_s), latitude (ϕ) and height above the sea-level (H_o) are introduced to obtain the three hydrostatic coefficients as

$$\begin{aligned}
 a &= (1.2320 + 0.0139 \cdot \cos(\varphi) - 0.0209 \cdot H_o + 0.00215 \cdot (T_s - 10)) \cdot 10^{-3} \\
 b &= (3.1612 - 0.1600 \cdot \cos(\varphi) - 0.0331 \cdot H_o + 0.00206 \cdot (T_s - 10)) \cdot 10^{-3} \\
 c &= (171.244 - 4.293 \cdot \cos(\varphi) - 0.149 \cdot H_o - 0.0021 \cdot (T_s - 10)) \cdot 10^{-3}
 \end{aligned} \quad (1.43)$$

and three wet components as

$$\begin{aligned}
 a &= (0.583 - 0.011 \cdot \cos(\varphi) - 0.052 \cdot H_o + 0.0014 \cdot (T_s - 10)) \cdot 10^{-3} \\
 b &= (1.402 - 0.102 \cdot \cos(\varphi) - 0.101 \cdot H_o + 0.0020 \cdot (T_s - 10)) \cdot 10^{-3} \\
 c &= (45.85 - 1.91 \cdot \cos(\varphi) - 1.29 \cdot H_o + 0.015 \cdot (T_s - 10)) \cdot 10^{-3}
 \end{aligned} \quad (1.44)$$

1.7.2 Niell Mapping Function

Niell [1996] used the same continued fraction with an additional term for height correction to project the zenith hydrostatic delay into slant direction. This function is known as Niell hydrostatic mapping function (NMF_h) and is given as

$$MF_h(\chi) = \frac{1 + \frac{a_{hyd}}{1 + \frac{b_{hyd}}{1 + c_{hyd}}}}{\cos(\chi) + \frac{a_{hyd}}{\cos(\chi) + \frac{b_{hyd}}{\cos(\chi) + c_{hyd}}}} + \left[\frac{1}{\cos(\chi)} \frac{1 + \frac{a_{hgt}}{1 + \frac{b_{hgt}}{1 + c_{hgt}}}}{\cos(\chi) + \frac{a_{hgt}}{\cos(\chi) + \frac{b_{hgt}}{\cos(\chi) + c_{hgt}}}} \right] \cdot \frac{h}{1000} \quad (1.45)$$

Where a_{hgt} , b_{hgt} and c_{hgt} are the coefficients for height correction, h is the height of the station above mean sea level. The coefficients, a_{hyd} , b_{hyd} and c_{hyd} , are estimated for any given day-of-year by using a periodic function (of first harmonic) in the form,

$$a(\varphi, doy) = a(\varphi)_{avg} - a(\varphi)_{amp} \times \cos\left[\frac{2\pi(doy - doy_o)}{365.25}\right] \quad (1.46a)$$

for latitudes $|\varphi| \leq 15^\circ$ and $|\varphi| \geq 75^\circ$ and

$$\begin{aligned}
 a(\varphi, doy) &= a(\varphi)_{avg} + [a(\varphi_{i+1})_{avg} - a(\varphi_i)_{avg}] \cdot m \\
 &\quad - (a(\varphi)_{amp} + [a(\varphi_{i+1})_{amp} - a(\varphi_i)_{amp}] \cdot m) \times \cos\left[\frac{2\pi(doy - doy_o)}{365.25}\right]
 \end{aligned} \quad (1.46b)$$

for $15^\circ < |\varphi| < 75^\circ$, with doy_o being set to 28 days for the northern and 211 for the southern hemisphere. Again, the latitude dependent coefficients are interpolated linearly, but the seasonal variations are subtracted from the average values. The values for selected latitudes

are given in Table 1.4 below. The table for the latitudinal mean and amplitude of these parameters are created using data from the mid-latitude region.

Table 1.4: Values of Different Parameters in eq. (1.46) for the hydrostatic delay mapping function

Latitude (φ)	Average (a_{avg})		
	$a_{hyd} (\times 10^{-3})$	$b_{hyd} (\times 10^{-3})$	$c_{hyd} (\times 10^{-3})$
15	1.2769934	2.9153695	62.610505
30	1.2683230	2.9152299	62.837393
45	1.2465397	2.9288445	63.721774
60	1.2196049	2.9022565	63.824265
75	1.2045996	2.9024912	62.258455
Latitude (φ)	Amplitude (a_{amp})		
	$a_{hyd} (\times 10^{-5})$	$b_{hyd} (\times 10^{-5})$	$c_{hyd} (\times 10^{-5})$
15	0.0	0.0	0.0
30	1.2709626	2.1414979	9.0128400
45	2.6523662	3.0160779	4.3497037
60	3.4000452	7.2562722	84.795348
75	4.1202191	11.723375	170.37206
Height correction			
	a_{hgt}	b_{hgt}	c_{hgt}
	2.53×10^{-5}	5.49×10^{-3}	1.14×10^{-3}

For the Niell wet delay mapping function (NMF_w), a simplified form of eq. (1.46) is used to interpolate the parameter values extracted from Table 1.5 because there is no annual (seasonal) variation considered in this mapping function. The periodic function is

$$a(\varphi, doy) = a(\varphi)_{avg} + [a(\varphi_{i+1})_{avg} - a(\varphi_i)_{avg}] \cdot m \quad (1.47a)$$

For the latitude range $15^\circ < |\varphi| < 75^\circ$ and

$$a(\varphi, doy) = a(\varphi)_{avg} \quad (1.47b)$$

For latitudes $|\varphi| \leq 15^\circ$ and $|\varphi| \geq 75^\circ$.

Table 1.5: Values of Different Parameters in eq. (1.47) for the wet delay mapping function

Latitude (φ)	Average (a_{avg})		
	$a_{wet} (\times 10^{-4})$	$b_{wet} (\times 10^{-3})$	$c_{wet} (\times 10^{-2})$
15	5.8021897	1.4275268	4.3472961
30	5.6794847	1.5138625	4.6729510
45	5.8118019	1.4572752	4.3908931
60	5.9727542	1.5007428	4.4626982
75	6.1641693	1.7599082	5.4736038

As there is no height correction term in the wet delay the NMF_w reduces to

$$MF_w(\chi) = \frac{1 + \frac{a_{hyd}}{b_{hyd}}}{1 + \frac{a_{hyd}}{b_{hyd}} + c_{hyd}} \cdot \frac{\cos(\chi) + \frac{a_{hyd}}{b_{hyd}}}{\cos(\chi) + c_{hyd}} \quad (1.48)$$

1.7.3 Global Mapping Function

The Global mapping function (GMF), which uses the same continued fraction as that in NMF (eq. 1.45), is modeled with sufficient accuracy for zenith angles up to 87° . The parameters a , b and c , which are different for the hydrostatic and wet components are computed from Numerical Weather Models. Using a $15^\circ \times 15^\circ$ global grids of monthly mean profiles for pressure, temperature and humidity from 40 years' ECMWF (European Centre for Medium-range Weather Forecasts) reanalysis data (ERA40), the coefficients a_{hyd} and a_{wet} are determined. Taking pre-defined (empirical) expression for b_{hyd} , c_{hyd} , b_{wet} , and c_{wet} ; the coefficients a_{hyd} and a_{wet} are derived through a single ray-trace at 3.3° initial elevation angle (86.7° zenith angle) and by simply inverting the continued fraction form [Boehm *et al.* 2006a]. These hydrostatic coefficient (a_{hyd}) at surface are then scaled down to mean sea level (a_o) using the height correction given by Niell [1996]. The mean values of ' a_o ' and its amplitude are fitted using a periodic function (eq. 1.46a), to the time-series of the ' a ' parameters at each grid point. This global grid of the mean values, a_o , and of its amplitude, for both the hydrostatic and wet coefficients in the continued fraction form are expanded into special spherical harmonic coefficients up to degree and order 9 in a least square adjustment. This expansion is given as

$$a_o = \sum_{n=0}^9 \sum_{m=0}^n P_{mn}(\sin \varphi) \cdot [A_{nm} \cdot \cos(m \cdot \lambda) + B_{nm} \cdot \sin(m \cdot \lambda)] \quad (1.49)$$

The hydrostatic and wet coefficients of ' a ' for a given site coordinates and day-of-year can then be determined using eq. (1.46).

1.8 GPS for Water Vapor Estimation

Water vapor plays a major role in many of the atmospheric and geophysical phenomena, which include transfer of energy and formation of clouds and weather system. Weather forecast models demand water vapor information with high temporal resolution over a wide geographical region. Large variability of atmospheric water vapor content in short spatial and/or temporal scales makes its measurement rather involved and expensive. While direct measurement of water vapor content using Water Vapor Microwave Radiometer (WVMR) is very expensive, measurements using Radiosonde are time consuming. Satellite based microwave remote sensing, at its present state of art, proves to be an effective tool for this purpose because it can provide the information even over inaccessible regions like oceans, *etc.* However, revisit time of polar orbiting satellites limits the temporal resolution. Satellite based water vapor measurements over land is far more difficult because of the large heterogeneity of land surface features. The land surface also acts as a warm background for microwave remote sensing of atmosphere. As a result, most of the satellite-based measurements of atmospheric water vapor prove to be more useful over the oceanic regions. The details about the existing variety of platforms and sensors are summarized in Table 1.6 and shown in Figure 1.7.

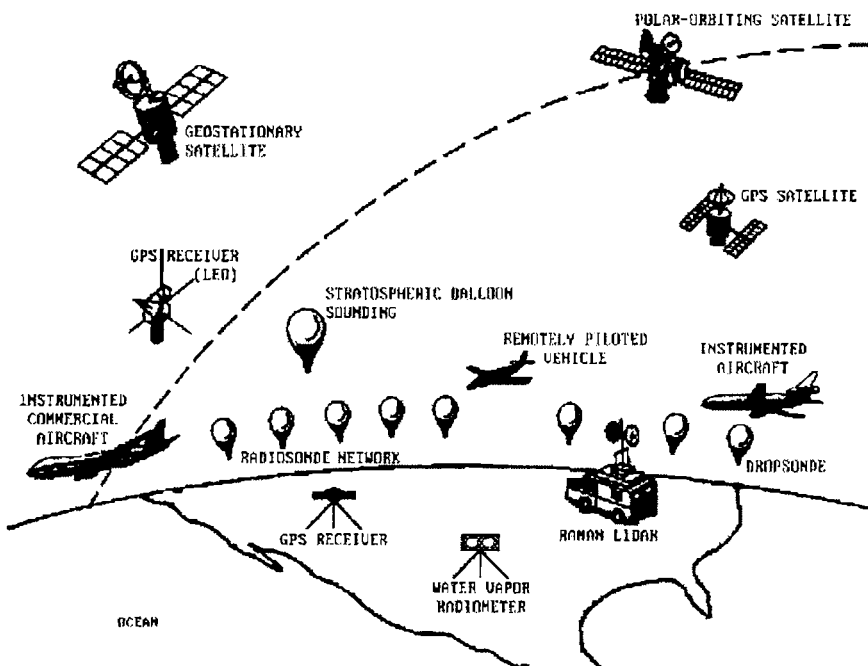


Figure 1.7: A pictorial representation of different methods used for measuring atmospheric water vapor content

Table 1.6: Characteristics of various water vapor observing systems

Observing Platforms	Measurement Systems	Advantages	Disadvantages
Satellites	IR sensors (e.g. TOVS) <i>Susskind et al. [1984]</i>	Provides total columnar water vapor and vertical profile information of water vapor over large areas	Data limited to cloud free region, can exhibit regional biases and error in lower Troposphere
	Microwave Sensors (e.g. SSM/I, TRMM/TMI, AMSUA, AMSUB)	Provides total columnar water vapor and its sounding over large area and not highly affected by cloud	Data is limited to Oceanic region. Land surface acts as warm background. Poor vertical/horizontal resolution
	Solar Occultation (e.g. SAGE II) <i>Rind et al. [1993]</i>	Global humidity data from Stratosphere and above. High accuracy and vertical resolution	Coverage limited by clouds and sampling poor in tropical region
	GPS Radio Occultation (GPS RO) <i>Kursinski [1997]</i>	Limb sounding provides P , T and e profiles with good resolution in upper troposphere (above 3 km)	Does not provide profiles from surface to first 2-3 km
Aircraft <i>Starr and Melfi [1991]</i>	Direct point and Lyman alpha Hygrometers, DIALs and Capacitive sensors	Research aircraft can make measurements at any location and time and Commercial aircraft will have global data coverage	Expensive and has limited data
Balloons	Daily Radiosonde sensors of WMO standards <i>Elliot and Gaffen [1991]; Olmans and Hofmann [1995]; Dabberdt et al. [1995]</i>	Large global network, Has good vertical resolution, Long database since 1930 is available, High quality observations is used for comparison with operational measurement systems	Data quality is variable in upper troposphere and poor in stratosphere, Highly time consuming, Quality of observation is poor at very high and low Humidity, Instrument is expensive, Data is available only twice over land.
Ground Based (Surface)	Meteorological observations using Wet- and Dry- bulb Psychrometer and dew point Hygrometer <i>Middleton and Spilhaus [1953]</i>	Long records of reasonably high quality global data are available and observations are made daily	Spatial coverage is non-uniform and data is only for earth's surface
	Ground based WVMR <i>Bevis et al. [1992]</i>	Precipitable Water Vapor (PW) measurements with high precision, continuously with short time interval	Expensive device, Poor horizontal resolution and no measurements during rainfall
	Raman LIDAR, DIALs	High quality data (good vertical and temporal resolution)	Expensive systems, require high skilled operators, Usefulness during nighttime and clear sky conditions
	Ground based GPS receivers (Present Study)	High precision PW using existing navigation GPS receivers. Has excellent temporal resolution. Gives data in all weather conditions	Horizontal resolution depends on tracking network infrastructure; Poor vertical resolution

A local network of GPS receivers is an effective alternative for water vapor remote sensing over the land [Businger *et al.*, 1996] and this recently developed technique proves to be very effective in measuring Precipitable Water vapor (PW), which is the height of the liquid water column when the entire water vapor in a vertical column of the atmosphere is condensed, as clouds and precipitation do not significantly affect the propagating GPS signals at 19 and 24 cm wavelengths. Rocken *et al.* [1993; 1995; 1997] demonstrated the capability of ground based GPS system for measuring PW with an accuracy of few millimeters. Emardson *et al.* [1998] and Tregoning *et al.* [1998] also have reported similar measurements of PW from GPS observations. However, most of these studies have been carried out over the mid-latitude regions where the average PW is <20 mm. This points the importance of PW measurements using GPS over tropical region, where the atmospheric water vapor content is relatively large and perpetual cloud cover and precipitation severely affect other remote sensing techniques.

The sensitivity of atmospheric refractivity to the presence of water vapor makes it possible for ground-based GPS receivers to provide time series data on PW above the receiver site. The wet component of propagation delay in microwaves, for a ground based GPS receiver, is nearly proportional to the total amount of the water vapor (integrated) along the signal path. In the case of liquid water and ice, the hydrogen bond between water molecules greatly reduces the contribution of the dipole moment to the delay [Schüler 2002]. Because of this, the presence of precipitation and cloud ice does not discernibly affect the GPS measurement of water vapor. If the position of the receiver is accurately known and the Ionospheric delay has been accounted with a fairly good accuracy, then it will be possible to estimate the altitude integrated columnar water vapor overlying the receiver from the GPS signals, making use of the data on surface pressure and temperature at the same location [Bevis *et al.* 1992, 1994; Rocken *et al.* 1993, 1995; Duan *et al.* 1996]. As the Integrated water vapor is a representative of the total latent heat available in the column, it can be used as a potential tool in numerical weather prediction (NWP) models [Kuo *et al.*, 1993, 1996] and weather analysis.

1.9 Motivations of this Study

Global Positioning System (GPS), with its high integrity, continuous availability and reliability, revolutionized the navigation system based on radio ranging. With four or more

GPS satellites in view, a GPS receiver can find its location anywhere over the globe with accuracy of few meters [Parkinson–Spilker *et al.*, 1996]. High accuracy – within centimeters, or even millimeters is achievable by correcting the GPS signal with external augmentation system. The use of satellite for critical application like navigation has become a reality through the development of these augmentation systems (like WAAS, SDCM, and EGNOS, *etc.*) with a primary objective of providing essential integrity information needed for navigation service in their respective regions. Apart from these, many countries have initiated developing space-based regional augmentation systems like GAGAN and IRNSS of India, MSAS and QZSS of Japan, COMPASS of China, *etc.* In future, these regional systems will operate simultaneously and emerge as a Global Navigation Satellite System or GNSS to support a broad range of activities in the global navigation sector.

Among different types of error sources in the GPS precise positioning, the propagation delay due to the atmospheric refraction is a limiting factor on the achievable accuracy using this system. The WADGPS, aimed for accurate positioning over a large area though broadcasts different errors involved in GPS ranging including ionosphere and troposphere errors, due to the large temporal and spatial variations in different atmospheric parameters especially in lower atmosphere (troposphere), the use of these broadcasted tropospheric corrections are not sufficiently accurate. This necessitated the estimation of tropospheric error based on realistic values of tropospheric refractivity. Presently available methodologies for the estimation of tropospheric delay are mostly based on the atmospheric data and GPS measurements from the mid-latitude regions, where the atmospheric conditions are significantly different from that over the tropics. No such attempts were made over the tropics. In a practical approach when the measured atmospheric parameters are not available analytical models evolved using data from mid-latitudes for this purpose alone can be used. The major drawback of these existing models is that it neglects the seasonal variation of the atmospheric parameters at stations near the equator. At tropics the model underestimates the delay in quite a few occasions. *In this context, the present study is a first and major step towards the development of models for tropospheric delay over the Indian region which is a prime requisite for future space based navigation program (GAGAN and IRNSS).* Apart from the models based on the measured surface parameters, a region specific model which does not require any measured atmospheric parameter as input, but depends on

latitude and day of the year was developed for the tropical region with emphasis on Indian sector.

Large variability of atmospheric water vapor content in short spatial and/or temporal scales makes its measurement rather involved and expensive. A local network of GPS receivers is an effective tool for water vapor remote sensing over the land. This recently developed technique proves to be an effective tool for measuring PW. *The potential of using GPS to estimate water vapor in the atmosphere at all-weather condition and with high temporal resolution is attempted. This will be useful for retrieving columnar water vapor from ground based GPS data. A good network of GPS could be a major source of water vapor information for Numerical Weather Prediction models and could act as surrogate to the data gap in microwave remote sensing for water vapor over land.*

Chapter 2

ESTIMATION OF TROPOSPHERIC DELAY IN MICROWAVE PROPAGATION

2.0 Introduction

The positioning accuracy achieved with GPS in geodesy, Navigation, *etc.*, is being continuously improved during the last two decades. Historically, the main sources of errors which are progressively being reduced are the orbital error, the antenna phase center modeling, signal multipath, scattering by the environment near by the receiver and the clock error, based on recent technological advances. These advances have limited applications or usage in mitigating the error due to the atmospheric refraction, which can be resolved only through accurate modeling of atmospheric refraction effect. Owing to the large variations of atmospheric properties in space and time, its modeling is rather complicated.

In most of the ranging applications it is assumed that the EM wave travels along straight line with speed equal to that in vacuum. But since the earth's atmosphere is a non-homogeneous medium with a significant variation in its physical properties such as pressure, temperature, humidity *etc.* with altitude, it introduces a corresponding variation in the index of refraction. An EM wave propagating through the atmosphere undergoes continuous refraction leading to bending of the ray path (from its direct line-of-sight) as well as group retardation because of the decrease in the group velocity (refractive index of the medium being >1). Thus, a refracting medium makes the propagating wave to travel a longer distance taking a longer time to reach the destination than that would have been in the absence of the atmosphere. As the range is inferred from the time-of-flight, this delay manifests as an error in estimated range (a pseudo range).

In general, the region of the earth's atmosphere which affects the propagation of microwaves in the GPS frequencies can be broadly classified into two; (i) the ionosphere and (ii) the neutral atmosphere. The ionosphere is a dispersive medium (*i.e.* the refractive index of the medium depends on the frequency of the EM wave traveling through it). As its index of refraction varies inversely with square of the frequency, by using higher frequencies (in GHz) and properly modeling the ionosphere or by making measurements in

dual (or multi) frequencies, the range error due to ionosphere can be reduced considerably. At present, in the state-of-art of GPS systems, the ionospheric contribution (in the zenith direction) is reduced to $< 1 - 5$ m.

As the neutral atmosphere is non-dispersive at the GPS frequencies, the delay due to neutral atmospheric refraction cannot be accounted through dual (or multi) frequency measurements. Estimation of this delay needs a strategy entirely different from that used for the ionized region. Since the bulk of the neutral atmosphere resides in the lower region (or Troposphere) and most of the delay caused by this comes from these altitudes, this is usually referred to solely as the “Tropospheric delay”. The geometry of radio refraction in the neutral atmosphere is shown in Figure 2.1. The points A and B in the figure denote the locations of the receiving station and radio beacon source, respectively. The D and α denote the true range and elevation angle of the beacon. If there were no atmosphere a radio signal starting from B would travel along the straight-line path D and reach the point A . Due to the presence of the atmosphere, the ray would be refracted and the path is curved along S . In this case, the angle of arrival of the radio signal at A is α' which is the apparent elevation angle. The apparent position of the beacon is then at P . Here AP is the apparent range that is greater than the true range (AB), since ray takes longer time to travel in the refracting medium than that in vacuum. If n is the refractive index, D is the direct path length and S is the curved path length, then range error is given by eq. (1.3).

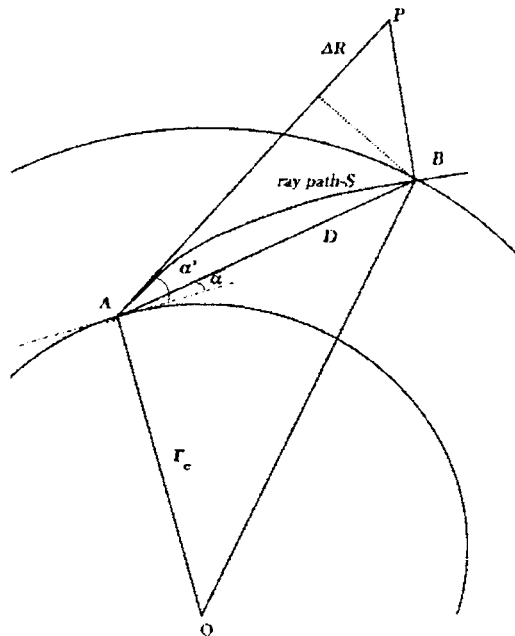


Figure 2.1: Schematic diagram showing the range error and angular deviation associated with radio ranging

2.1 Effect of Neutral Atmosphere in the Propagation of Microwave

The refraction of radio waves as they pass through the neutral atmosphere is generally referred to as tropospheric delay [Misra and Enge, 2001; Barry and Chorley, 1998]. Debye [1957] has considered the effect of an imposed electric field on the dielectric properties of both non-polar and polar molecules in a liquid. In the presence of an external electric field these molecules develop an induced dipole moment. In addition to that, the polar molecules develop an orientational polarization due to the alignment of the axes of permanent dipoles along the field direction. This adds up to the total induced dipole moment. The expression for the polarization (dipole moment per unit volume) of a polar liquid under the influence of a high frequency radio field as obtained by Debye [1957] can be applied to the case of gases with proper approximation. This polarization $\mathbf{P}(\omega)$ is given as

$$\mathbf{P}(\omega) = \frac{\epsilon - 1}{\epsilon + 2} \cdot \frac{M}{\rho} = \frac{4\pi A_N}{3} \left[\gamma_i + \frac{\gamma_p^2}{3KT} + \frac{1}{1 + i\omega\tau} \right] \quad (2.1)$$

where \mathbf{P} = Electric Polarization

ϵ = the dielectric constant of medium

M = the molecular weight

ρ = the density

A_N = Avogadro's number

γ_i = induced dipole moment per unit applied field

γ_p = permanent dipole moment of the molecules

T = Absolute temperature

K = Boltzmann constant

$\omega = 2\pi f$, where f is the frequency of the applied field

τ = Relaxation time required for external field induced orientations of the molecules to return to random distributions after the field is removed

Debye's analysis shows that for external fields with frequencies less than 100 GHz, $\omega\tau \ll$

1. In this case the above equation can be rewritten as

$$\frac{\epsilon - 1}{\epsilon + 2} \cdot \frac{M}{\rho} = \frac{4\pi A_N}{3} \left[\gamma_i + \frac{\gamma_p^2}{3KT} \right] \quad (2.2)$$

For gases, as ϵ is close to unity eq. (2.2) reduces to

$$\epsilon - 1 = \frac{\rho}{M} 4\pi A_N \left[\gamma_i + \frac{\gamma_p^2}{3KT} \right] \quad (2.3)$$

For non-polar gases $\gamma_p = 0$; In this case

$$\epsilon - 1 \approx \frac{\rho}{M} 4\pi A_N \gamma_i \quad (2.4)$$

Using the perfect gas law $P = \rho RT$, the above equation can be rewritten as

$$\epsilon - 1 \approx k'_1 \frac{P}{T} \quad (2.5)$$

where k'_1 is constant.

For polar gases the eq. (2.3) reduces to

$$\epsilon - 1 \approx k'_2 \frac{P}{T} [A_0 + B_0/T] \quad (2.6)$$

where k'_2 , A_0 and B_0 are constants. P and T are the pressure and temperature of the polar gas respectively. For a mixture of gases, Dalton's law of partial pressure is assumed to hold with the result that we can sum the effects of polar and non-polar gases. In troposphere, mainly the effects of dry air (non-polar gases) and water vapor (a polar gas) only ($P = P_d + e$) is to be considered in which case eq. (2.6) reduces to

$$\epsilon - 1 = k'_1 \frac{P_d}{T} + k'_2 \frac{e}{T} \left(A_0 + \frac{B_0}{T} \right) \quad (2.7)$$

where P_d is the pressure of dry air and e the partial pressure of water vapor. In case of air, the dielectric constant (ϵ) is related to the refractive index (n) through $n-1 \approx (\mu\epsilon - 1)/2$; where μ is the permeability which is assumed to be approximately unity for air. In this case, the above equation can be written in terms of the refractivity (N) of the air as [Smith and Weintraub, 1953; Thayer, 1974]

$$N = (n-1) \times 10^6 = k_1 \frac{P}{T} + k_2 \frac{e}{T} + k_3 \frac{e}{T^2} \quad (2.8)$$

Note here that P is the total atmospheric pressure. In eq. (2.8) P and e are expressed in hPa and T in K. The values of the constants k_1 , k_2 and k_3 as reported by Bevis *et al.* [1992] are, respectively, $77.604 \pm 0.014 \text{ K hPa}^{-1}$, $64.79 \pm 0.08 \text{ K hPa}^{-1}$ and $(3.776 \pm 0.004) \times 10^5 \text{ K}^2 \text{ hPa}^{-1}$. These constants in eq. (2.8) are considered to be good up to 0.5 percent of N in

frequencies up to 30 GHz for normally encountered ranges of pressure, temperature and humidity.

Radio refractivity in troposphere has two principal components, a hydrostatic (Dry) component (N_D) due to non-polar molecules (dry air) and a non-hydrostatic (Wet) component (N_W) due to polar component of water vapor. The nomenclatures 'dry' and 'wet' are to some extent misnomers as the dry component also has the contribution from non-polar component of water vapor. In spite of that these terms are very widely used among the GPS community. Thus, from eq. (2.8) the N_D and N_W can be written as

$$N_D = k_1 \frac{P}{T} \quad (2.9a)$$

$$N_W = k_2 \frac{e}{T} + k_3 \frac{e}{T^2} \quad (2.9b)$$

The constant k_3 of the wet term is much larger than that of the dry term. So, even a small amount of water vapor in dry air makes a large difference in the total refractivity. Using the altitude profiles of P , T and e the altitude profiles of N can be obtained. The range error ΔR then is estimated by tracing the ray-path considering the altitude variation of N given by this profile.

2.2 Ray Tracing

In order to examine the refraction effect of the microwaves in the atmosphere the ray-path is to be traced from the observer at the surface of the earth up to the satellite, taking into account the altitude variation of refractive index and the earth's curvature. In general, earth's curvature has a greater influence on path length due to atmospheric refraction for very low elevation angles (grazing incidence), as the wave spends more time in the lower layers where the refractive effects are significant.

2.2.1 Geometry of Ray Propagation

The earth's atmosphere is assumed to be divided into a series of concentric homogeneous spherical layers, each characterized by a mean refractive index. Applying the Snell's law for spherically stratified atmospheric layers allows the numerical integration of refractive effect. Consider the trajectory of a ray passing from 'A', the point on the surface of the earth (Figure 2.2), to the point 'B' at a height h from the surface of the earth with an initial zenith angle χ_0 to the local vertical. On reaching B the zenith angle becomes χ_m

because of the refraction. The total angular deviation is denoted as $\Delta\psi$.

If Z_i and Z_{i+1} are the lower and upper boundaries of a given layer, χ_i and χ_{i+1} are local zenith angles at these boundaries. At the height of Z_{i+1} the angle of refraction is χ_{i+1} and the angle of incidence is α_i , considering a triangular element OPQ

$$\frac{r_e + Z_i}{\sin \alpha_i} = \frac{r_e + Z_{i+1}}{\sin(180 - \chi_i)}$$

or

$$\sin \alpha_i = (r_e + Z_i) \frac{\sin \chi_i}{(r_e + Z_{i+1})} \quad (2.10)$$

where r_e is the Earth's radius.

Applying Snell's law at boundary Z_{i+1} , we have

$$n_i \sin \alpha_i = n_{i+1} \sin \chi_{i+1} \quad (2.11)$$

where n_i and n_{i+1} are the mean refractive indices of layers above Z_i and Z_{i+1} , respectively.

Substituting for $\sin \alpha_i$ in eq. (2.11)

$$n_i (r_e + Z_i) \sin \chi_i = n_{i+1} (r_e + Z_{i+1}) \sin \chi_{i+1}$$

or

$$\sin \chi_{i+1} = \frac{n_i (r_e + Z_i) \sin \chi_i}{n_{i+1} (r_e + Z_{i+1})} \quad (2.12)$$

Knowing the height profile of n_i , the angle of incidence at the upper layer χ_{i+1} can be estimated from the angle of incidence χ_i at the lower layer. This procedure can be repeated from the lower boundary at A (where $\chi_i = \chi_0$) to the upper boundary at B (where $\chi_{i+1} = \chi_m$) by dividing the in between region into small layers (like Z_i, Z_{i+1}) characterized with its own refractive index and thickness.

The angle κ_i subtended at the center of the earth by the ray path PQ within the layer between Z_i to Z_{i+1} is given by

$$\kappa_i = \chi_i - \alpha_i \quad (2.13)$$

where α_i is defined by eq. (2.11). The total angles subtended by the ray path at the center of the earth when traversing the atmosphere from A to B is

$$\kappa = \sum_1^{l-1} (\chi_i - \alpha_i) \quad (2.14)$$

where l is the number of segments between A and B . Now the total angular deviation of the trajectory can be estimated knowing the values of χ_m , χ_0 and κ . Considering the quadrilateral $ACBO$, the interior angles

$$\begin{aligned}
 \angle OAC &= 180 - \chi_0 \\
 \angle ACB &= 180 - \Delta\Psi \\
 \angle CBO &= \chi_m \\
 \angle OAC + \angle ACB + \angle CBO + \angle AOB &= 360^\circ \\
 \Delta\Psi &= \kappa + (\chi_m - \chi_0)
 \end{aligned}
 \tag{2.15}$$

where, $\Delta\Psi$ is the total angular deviation of the ray from the straight line path.

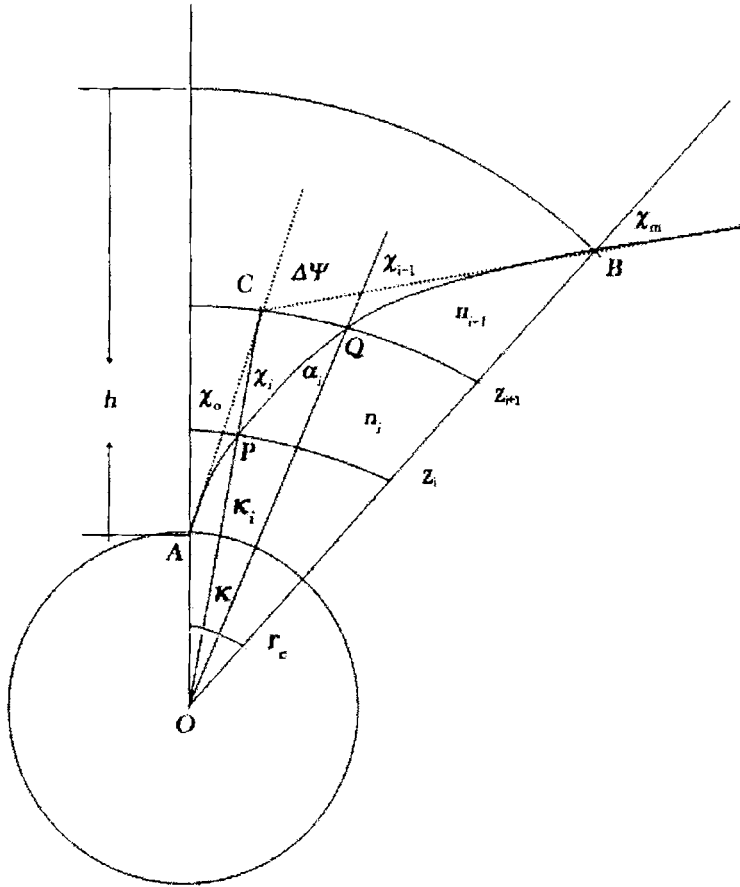


Figure 2.2: Schematic diagram of refracted ray path used for ray-tracing

The effective path length, D_{si} , between Z_i and Z_{i+1} is given by

$$\frac{D_{si}}{\sin \kappa_i} = \frac{(r_c + Z_{i+1})}{\sin \chi_i}
 \tag{2.16}$$

or

$$D_{si} = (r_e + Z_{i+1})(\sin \kappa_i / \sin \chi_i) \quad (2.17)$$

for $0^\circ < \chi < 180^\circ$ and $D_{si} = Z_{i+1} - Z_i$ for $\chi = 0^\circ$ or 180° . Now, the actual path length traversed by the wave from A to B is

$$S = \sum_1^{m-1} D_{si} \quad (2.18)$$

The direct path AB can be estimated by solving the triangle ABO . The geometrical distance AB , or D , is given by

$$D = \sqrt{r_e^2 + (r_e + h)^2 - 2r_e(r_e + h)\cos \kappa} \quad (2.19)$$

Equations (2.18) and (2.19) are used to estimate S and D later in eq. (2.24). As discussed in Section 2.1 (eq. 2.8) the refractive index of the neutral atmosphere is a function of P , T and e , to estimate a refractive index profile and further ΔR the vertical profiles of these parameters are to be known precisely. An easily available source for these data from a fixed location is the regular balloon sounding carried out by the India Meteorological Department (IMD) in accordance with WMO specifications.

2.2.2 Estimation of Tropospheric Range Error (ΔR)

As the refractive index of air is greater than unity, the wave propagating through this medium undergoes a group-retardation. In ranging applications the propagation time is transferred into range by using the velocity of electromagnetic wave in vacuum (c). Thus, delay in propagation introduces an error in the ranging. The other source of error is the refractive bending of ray path due to the spatial variability of the refractive index. Thus, wave takes a curved path through the atmosphere, which is always longer than the direct line-of-sight distance. Considering a wave propagating through a medium with refractive index of n , the time taken by the wave to travel an infinitesimal path distance, ds , is given as

$$d\tau = \frac{nds}{c} \quad (2.20)$$

where c is the velocity of light in free space.

The corresponding distance traveled in free space is then

$$cd\tau = nds \quad (2.21)$$

The total time taken by the wave to cover the path between the source and the destination (*e.g.*, satellite to GPS receiver on earth surface) is

$$\tau = \int d\tau = \frac{1}{c} \int n ds \quad (2.22)$$

The path length traveled by the wave is

$$G = \int n ds \quad (2.23)$$

The wave path length G is larger than the true geometric distance D , between source and receiver.

The total range error can then be written as

$$\Delta R = \int n ds - D$$

or

$$\Delta R = \int (n - 1) ds + \int ds - D$$

i.e.,

$$\Delta R = \int (n - 1) ds + [S - D]$$

or

$$\Delta R = 10^{-6} \times \int N ds + [S - D] \quad (2.24)$$

The first term in the right side of eq. (2.24) represents the error due to retardation of the wave as it traverses through the medium. The second term represents the extra distance traversed by the wave due to the bending of ray path. From eq. (2.9) it is clear that the tropospheric delay (ΔR) consists of two components the hydrostatic (or "dry") component, which accounts for approximately 90% of the delay and the "wet" component, which accounts for the remaining 10% of the delay. At nadir (when zenith angle is zero) the second term in eq. (2.24) tends to zero as there will not be any bending for normal incidence. The range error in this case is usually referred to as the Zenith Tropospheric Delay (ZTD). Priory knowledge on hydrostatic and non-hydrostatic refractivity profiles is necessary for tracing the ray path to estimate tropospheric range error, which requires atmospheric parameter profiles obtained from upper atmospheric soundings.

2.3 Mean Neutral Atmospheric Models over the Indian Region

The balloon soundings provide altitude profiles of atmospheric pressure (in hPa), air temperature (in °C) up to ~ 26 km, and dew point temperature (T_D in °C) up to ~ 12 km. However, depending on the atmospheric conditions this upper limit will vary slightly from

day-to-day. A major problem encountered in the measurement of T_D is the saturation effect of humidity sensor as well as the limitation in the sensitivity at higher altitudes where water vapor is very small. The T_D values are used to derive the water vapor partial pressure (e in hPa) using the relation

$$e(T) = 6.105 \exp \left[25.22 \left(\frac{T_D - 273.0}{T_D} \right) - 5.31 \ln \left(\frac{T_D}{273.0} \right) \right] \quad (2.25)$$

The radiosonde raw data is formatted in terms of pressure levels. The temperature and dew point temperature at these levels along with the corresponding altitude are tabulated along with the values of pressure, temperature and dew point temperature at the surface just before the balloon release. This data is reformatted in terms of altitude, to generate the altitude profiles of P , T , T_D and e . These altitude profiles, which are unequally spaced in altitude (as they are reformatted from the data at standard pressure level), are interpolated appropriately to generate suitable spaced profiles at 10 m interval from the surface to 5 km, at 200 m interval up to 20 km and 500 m beyond 20 km. A variable altitude resolution (close resolution at lower altitude where the values of these parameters and their variability is large) for the data is selected mainly to accomplish a fairly uniform accuracy for the derived parameters along the entire altitude region (up to 26 km for P and T and up to 12 km for e). Note that typical accuracies achievable in radiosonde measurements as quoted by *Bisagni* [1989] are, respectively, ~ 2.0 hPa for the barometric pressure, about $+ 0.4$ K for temperature and 4% for relative humidity.

For the present analysis, the radiosonde data from 18 IMD locations, fairly well distributed over Indian subcontinent representing all major climatic and geographical conditions prevailing over the subcontinent, are selected. A list of these stations along with geographical locations is presented in Table 2.1. As mentioned earlier, for all these stations, the altitude profiles of P , T , T_D and e will not be available up to the same level on all the days. However, the daily profiles of P , T , T_D and e in each month for five consecutive years from 1995 to 1999 are averaged to generate mean profiles for respective months for every station. The extent of day-to-day variability of these profiles is quantified in terms of the standard deviations at each altitude for different months. Meteorological data from the regular radiosonde observations made by the IMD at these locations (Table 2.1) for a period

Table 2.1: A List of IMD stations selected for the present study.

Station	Latitude °(N)	Longitude °(E)	Height from MSL (m)
Trivandrum	8.48	76.95	64.0
Portblair	11.66	92.71	79.0
Bangalore	12.96	77.58	921.0
Mangalore	12.95	74.83	31.0
Chennai	13.00	80.18	16.0
Goa	15.48	73.81	60.0
Hyderabad	17.45	78.46	545.0
Vishakhapatnam	17.70	83.30	66.0
Mumbai	19.11	72.85	14.0
Kolkata	22.65	88.45	6.0
Ahmedabad	23.06	72.63	55.0
Bhopal	23.28	77.35	523.0
Guwahati	26.10	91.58	54.0
Jodhpur	26.30	73.01	224.0
Lucknow	26.75	80.88	128.0
Delhi	28.58	77.20	216.0
Patiala	30.32	76.45	251.0
Srinagar	34.08	74.83	1587.0

of five years (1995-1999) are thus used to develop the site-specific monthly mean atmospheric models. As a typical example the monthly mean models for P , T and e for the three months of January, May and July (representative of three different seasons) for Trivandrum and Delhi are presented in Figure 2.3. For the near-equatorial coastal station Trivandrum these mean atmospheric parameters show less seasonal variation compared to that at a higher latitude inland station (like Delhi). While the temperature profile remains more-or-less similar throughout the year for Trivandrum it varies significantly for a station like Delhi. In case of water vapor, a clear seasonal variation of ~ 20 hPa (at surface) is seen over Delhi while for Trivandrum the profile is almost similar throughout the year. The surface water vapor pressure at Trivandrum is ~ 30 hPa which decreases almost exponentially with increase in altitude. Beyond 4 km the amount of water vapor is very low and does not show any pronounced seasonal variation at both these stations. One primary limitation of atmospheric data obtained from radiosonde is that it does not reach beyond 20 hPa or ~ 26 km in altitude, even though the prominence of neutral atmosphere extends up to ~ 100 km is to be considered for GPS related applications.

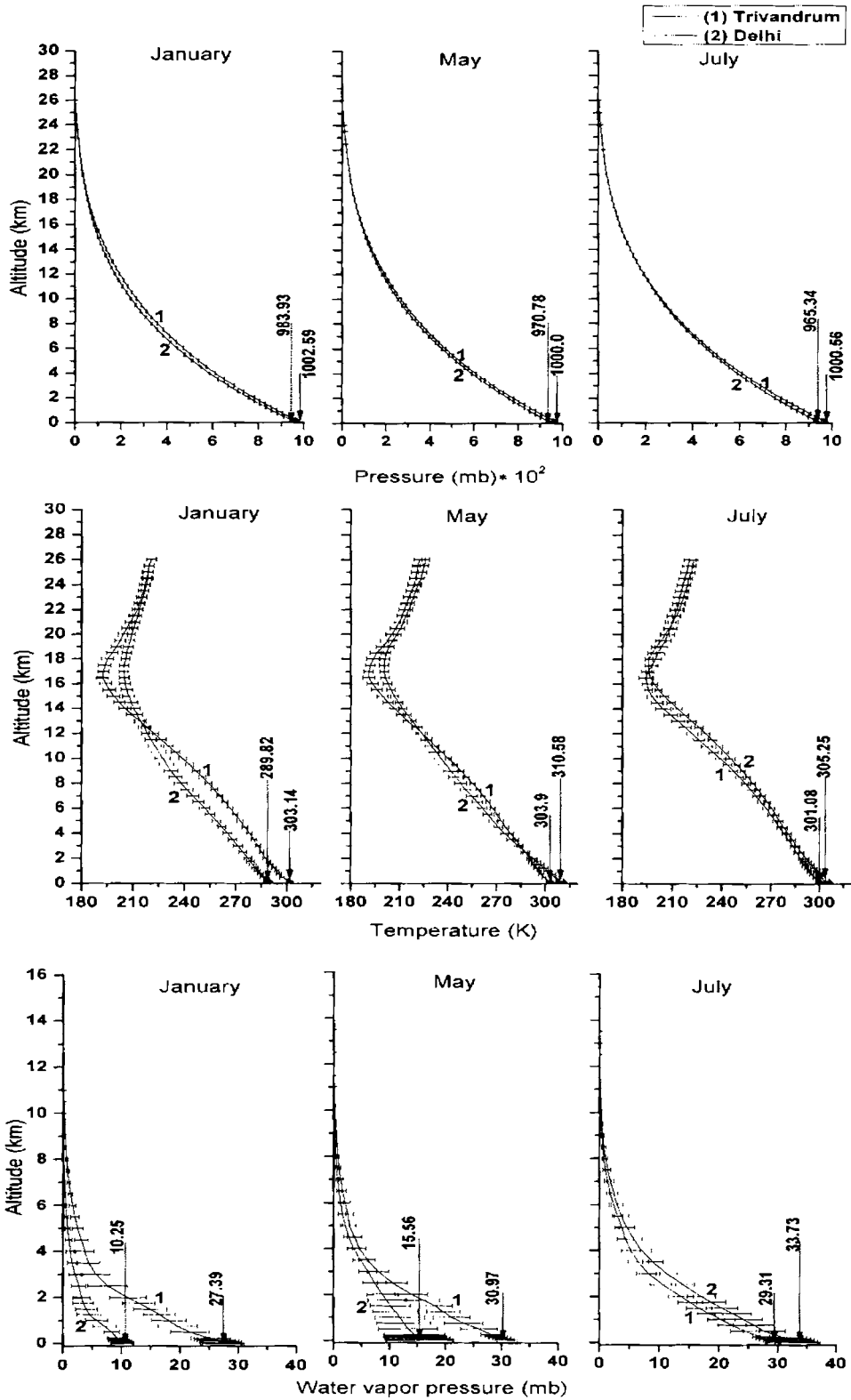


Figure 2.3: Altitude profiles of monthly mean P , T and e for three seasons at Trivandrum (1) and Delhi (2). The corresponding surface value of these parameters are also marked in each frame

To achieve this, the upper air data from COSPAR International Reference Atmosphere (CIRA) is incorporated.

2.3.1 The COSPAR International Reference Atmosphere (CIRA) Model

The CIRA provides empirical models of atmospheric temperature and densities as recommended by the Committee on Space Research (COSPAR). Since the early sixties different editions of CIRA have been published and CIRA-86 is the latest revised version of this model [CIRA, 1986]. Above 100 km CIRA-86 compares well with the MSIS model, which is available from NSSDC (MI-91E). In the lower region below 120 km, CIRA-86 consists of tables of the monthly mean values of temperature and zonal wind with almost global coverage (80°N – 80°S). Two sets of files are available, one in pressure coordinates including also the geopotential heights, and the other is in height coordinates generated from several global data compilations including ground-based and satellite (Nimbus 5, 6, 7) measurements [Oort, 1983; Labitzke et al., 1985]. This model reproduces most of the characteristic features of the atmosphere such as the equatorial wind and the general structure of the tropopause, stratopause, and mesopause. Table 2.2 lists all the parameters their vertical coordinates, spatial ranges and resolutions in detail Fleming et al. [1988].

Table 2.2: A List of Different Parameters (vertical coordinates, spatial ranges and resolutions of the zonal mean data) Contained in CIRA Model

	Parameter	Vertical Coordinate	Vertical Range; Resolution	Latitudinal Range; Resolution
A	Temperature	Altitude	0-120 km; 5 km	80°S-80°N; 10°
B	Pressure	Altitude	20-120 km; 5 km	80°S-80°N; 10°
C	Temperature	Log-pressure	1013-0.000025 hPa; 0.5 sh*	80°S-80°N; 10°
D	Geopotential height	Log-pressure	1013-0.000025 hPa; 0.5 sh	80°S-80°N; 10°
E	Zonal wind	Log-pressure	1013-0.000025 hPa; 0.5 sh	80°S-80°N; 10°

* sh = $-\ln(p/p_0)$; where $p_0 = 1013$ hPa

For the present study P and T profiles from the CIRA model are used from 20 km to 100 km. As radiosonde data is available up to ~ 26 km the CIRA profiles in the overlapping region 20 to 26 km are scaled appropriately to match with the observed radiosonde profiles in this region. Once this is accomplished the modified CIRA profile up to 100 km is combined with the radiosonde data to develop the full profile. The confidence on this profile is further confirmed by comparing with the SS-86 model [Sasi and Sengupta, 1986] developed exclusively for near equatorial stations, viz. Trivandrum.

2.3.2 A Reference Atmosphere for Indian Equatorial Zone from 0-80 km

The SS-86 model is considered as a 'reference atmosphere' valid for Indian Equatorial Zone in the altitude range of 0 (surface) to 80 km and widely used in many atmospheric studies. This model was evolved incorporating radiosonde data from surface to 20 km from four equatorial IMD stations (Chennai, Portblair, Trivandrum, Minicoy) and the M-100 rocket data in the altitude region 20 to 80 km from Trivandrum for a sufficiently long period of 11 years (from 1971 to 1982).

Water vapor in the atmosphere is mostly confined to the troposphere much below the tropopause for which the profiles from radiosonde measurements can be effectively used as no other more reliable measurements are available for this parameter. A comparison of SS-86, CIRA-86 and radiosonde profiles for January at Trivandrum is shown in Figure 2.4(a-c). In Figure 2.4(a) P values from radiosonde are available from surface to 26 km, and for CIRA-86 it is plotted from ~ 20 km to 100 km. The SS-86 model values for P are also plotted in the same figure from 0 – 80 km. The mean absolute difference between the SS-86 and CIRA-86 P values is $\sim 0.5 \pm 0.4$ hPa and the maximum absolute deviation is ~ 1.3 hPa. Figure 2.4 (b) shows a comparison of the T profile obtained from SS-86, radiosonde and CIRA-86 model. The CIRA-86 profile matches reasonably well with the radiosonde (up to 26 km) profile. The mean absolute difference between radiosonde and CIRA-86 is $\sim 4.5 \pm 3.5$ K, where as that between SS-86 and CIRA-86 is $\sim 1.95 \pm 1.9$ K. The maximum deviations are of the order of 13.34 K and 11.32 K, respectively. Figure 2.4 (c) shows a comparison of dry refractivity (N_D) from all the three sources. The mean absolute difference in N_D between SS-86 and CIRA-86 model is $\sim 1.24 \pm 0.8$ while the maximum deviation is ~ 3 . The Zenith range error values calculated from the above models are, 2.315 m for SASI-86 where as it is 2.294 m for CIRA-86, with a deviation of ~ 2 cm corresponding to an

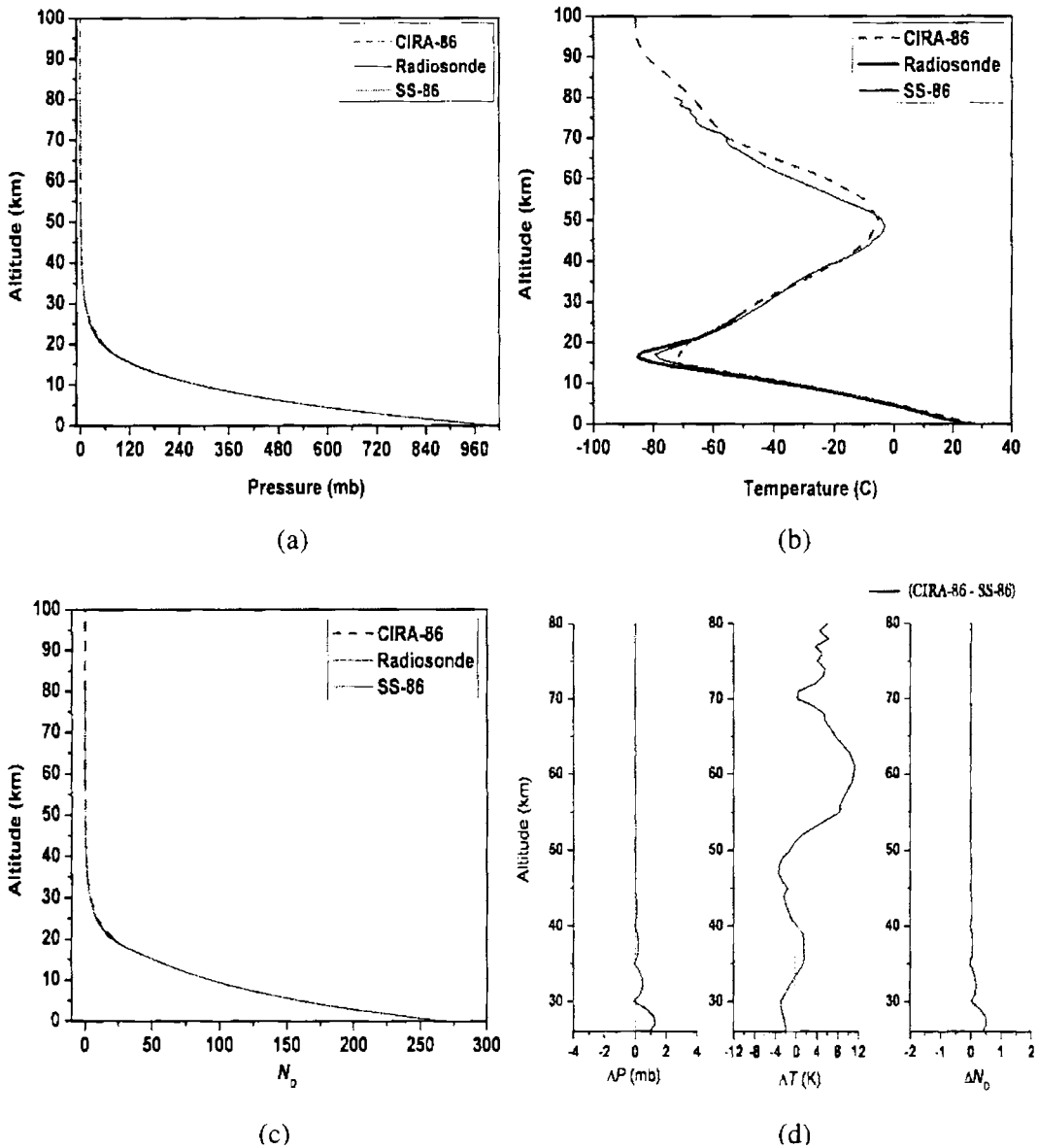


Figure 2.4: A Comparison of SS-86, Radiosonde and CIRA-86 monthly mean profiles of Pressure (a), Temperature (b) and Dry component of Refractivity (c) at Trivandrum; along with a plot showing the differences between CIRA-86 and SS-86 model for all the three parameters (d)

uncertainty of $\sim 0.01\%$. Figure 2.4(d) shows the difference between the SS-86 and CIRA-86 model values of P , T and N_D . The CIRA-86 data used for this analysis are downloaded from <http://badc.nerc.ac.uk/data/cira/acquiring.html>, the British Atmospheric Data Centre (BADC) website. To estimate the P and T values at the particular stations latitudes (ϕ) from the zonal mean values for every 10 degree latitude available from the website the following formula are used

$$P(\varphi, h) = P(\varphi_1, h) - [P(\varphi_1, h) - P(\varphi_2, h)] \left(\frac{\varphi - \varphi_1}{\varphi_2 - \varphi_1} \right)$$

$$T(\varphi, h) = T(\varphi_1, h) - [T(\varphi_1, h) - T(\varphi_2, h)] \left(\frac{\varphi - \varphi_1}{\varphi_2 - \varphi_1} \right) \quad (2.26)$$

where φ_1 and φ_2 are, respectively, the values of the latitudes just above and below the latitude (φ) for which the data is to be retrieved. Following this procedure the mean altitude profiles of P and T up to 120 km are obtained for all the eighteen stations listed in Table 2.1.

2.4 Altitude Profiles of Dry and Wet Refractivity

The refractive index profiles are generated from the monthly profiles of P , T and e using equations (2.9a) and (2.9b). As an example, the dry and wet refractivity for the month of June is presented in Figure 2.5 (a) and (b), respectively, for Trivandrum and Delhi. The horizontal bars indicate the standard deviation representing the amount of day-to-day variability. The value of N_w is largest near the surface (~ 130 units) and decreases almost exponentially with increase in altitude. Because of this, the refraction effects will be more at lower altitudes and decreases with increase in altitude. The dry component, N_D , is much larger in magnitude than N_w . The day-to-day variability of N_D is significantly small compared to that of N_w . Note that though significant contribution of N comes from N_D the large variability in N_w contributes significantly for the day-to-day variation of N .

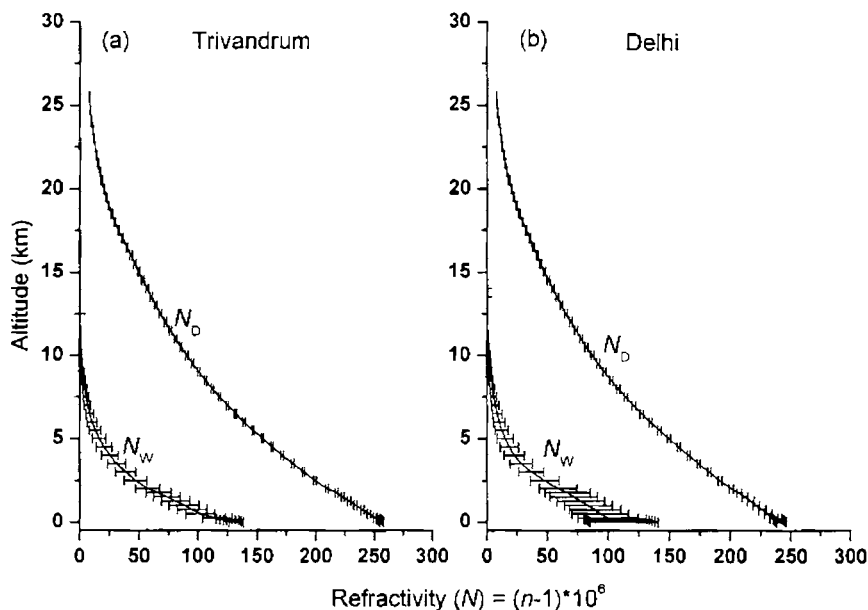


Figure 2.5: Typical altitude profiles of N_D and N_w for Trivandrum (a) and Delhi (b) in June

2.4.1 Relative Contribution of Refraction Delay with Altitude

The refractivity of atmosphere is maximum near the surface and decreases with increasing altitude. It should be worth in this context to examine the relative contribution to total range error and bending angle from different altitudes. The cumulative contribution

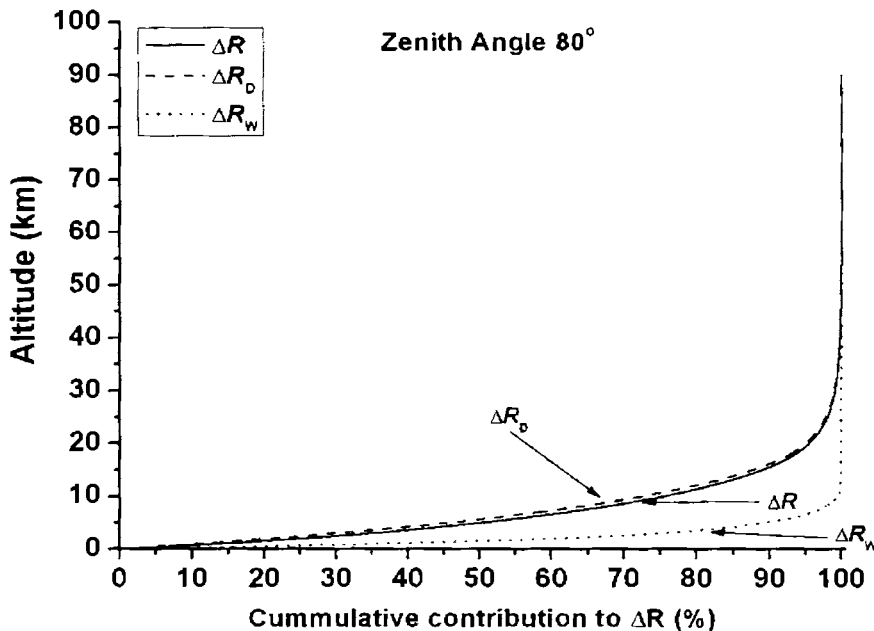


Figure 2.6: Curves showing the relative contribution (percentage of the total effect due to the entire atmospheric column) from different altitude regions (starting from surface) to the total range error (ΔR). The contribution of dry (-----) and wet (.....) components are also shown separately along with that of the total delay (——)

from different altitudes (in percentage) to ΔR and $\Delta \Psi$ estimated through ray-tracing for a zenith angle of 80° is presented in Figures 2.6 and 2.7, respectively. The cumulative contribution to wet range error (ΔR_W) up to 2 km is about 60% and is about 90% for altitudes below 5 km. The atmospheric region below 9 km contributes $\sim 98\%$ of the total ΔR_W . For the dry component (ΔR_D), the atmosphere below 6 km contributes about 50% of total dry range error and atmosphere below 16 km contributes nearly 90%. In case of total range error (ΔR), which includes both dry and wet components, about 98% of contribution comes from the altitude region below 25 km.

Figure 2.7 shows the percentage of cumulative contribution of $\Delta \Psi$ along with its dry and wet components ($\Delta \Psi_D$ and $\Delta \Psi_W$ respectively) at different altitudes. The lower atmosphere below 5 km significantly contributes for $\Delta \Psi_W$ and atmosphere below 15 km for $\Delta \Psi_D$. The atmosphere up to 26 km contributes around 98% of total $\Delta \Psi$. According to the

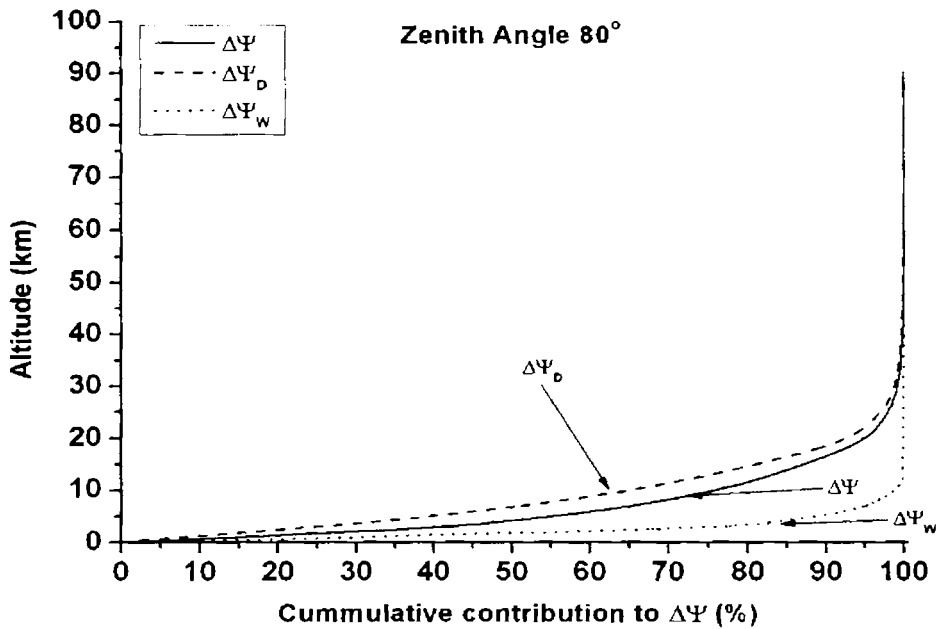


Figure 2.7: Curves showing the relative contribution (percentage of the total effect due to the entire atmospheric column) from different altitude regions (starting from surface) to the total range error ($\Delta\Psi$). The contribution of dry (-----) and wet (.....) components are also shown separately along with that of the total delay (———)

above analysis, the atmosphere up to 26 km altitude contributes about 98% of the total range error caused by entire neutral atmosphere. However, for GPS-based aircraft navigation, even the remaining 2% error is significant. Taking account of this fact, the neutral atmosphere up to 100 km is considered for estimating ΔR and $\Delta\Psi$.

2.5 Zenith Tropospheric Delay and its Spatial and Temporal Variability

The Zenith Tropospheric Delay (ZTD) comprises of two components *viz.*, the Zenith Hydrostatic Delay (ZHD) and Zenith Wet Delay (ZWD) [Saastamoinen, 1972], which can be written as

$$\text{ZTD} = \text{ZHD} + \text{ZWD} = 10^{-6} \cdot \int_{h_s}^{\infty} N(h) \cdot dh \quad (2.27)$$

where

$$\text{ZHD} = 10^{-6} \cdot \int_{h_s}^{\infty} N_d(h) \cdot dh, \quad \text{ZWD} = 10^{-6} \cdot \int_{h_s}^{\infty} N_w(h) \cdot dh$$

and h_s is the user altitude (it is the altitude of the GPS receiver antenna position). The mean altitude profile of N along with amount of its day-to-day variability (due to the day-to-day variations of P , T and e)

represented by the respective standard deviations σ_P , σ_T and σ_e , respectively, are estimated for different months applying the error propagation formula [Ku, 1966]. The day-to-day variability in N_D and N_W is quantified separately based on the respective standard deviations. Thus the standard deviation of N is estimated as,

$$\sigma_N^2 = \left(\frac{\partial N}{\partial P}\right)^2 \frac{\sigma_P^2}{n_P} + \left(\frac{\partial N}{\partial T}\right)^2 \frac{\sigma_T^2}{n_T} + \left(\frac{\partial N}{\partial e}\right)^2 \frac{\sigma_e^2}{n_e} \quad (2.28)$$

Where n_P , n_T and n_e are the number of daily values of Pressure, Temperature and water vapor partial pressure at a given altitude. The $\frac{\partial N}{\partial P}$, $\frac{\partial N}{\partial T}$ and $\frac{\partial N}{\partial e}$ are the partial derivative of N , about its mean values, which are generated by

$$\frac{\partial N}{\partial P} = \frac{k_1}{T} \quad (2.29)$$

$$\frac{\partial N}{\partial T} = -\frac{1}{T^2} \left[k_1 P + k_2 e + 2k_3 \frac{e}{T} \right] \quad (2.30)$$

$$\frac{\partial N}{\partial e} = \frac{k_2}{T} + \frac{k_3}{T^2} \quad (2.31)$$

where k_1 , k_2 and k_3 are the coefficients as given in eq. (2.8).

For each month the mean values of ZTD, ZHD and ZWD are estimated separately using the three respective profiles of $N(h)$ along with those of $N(h) + \sigma_N(h)$ and $N(h) - \sigma_N(h)$. The difference between upper and lower limits represents the standard deviation of ZHD and ZWD. Figure 2.8 shows the month-to-month variation of mean ZHD for the eighteen stations along with the standard deviations (vertical bars) representing the amount of day-to-day variability. The annual mean of ZHD is around 2.3 m for all these stations, except for Srinagar, Bangalore, Hyderabad, Bhopal, Jodhpur and Patiala (Table 2.3). At Srinagar, which is situated at an altitude of ~1600 m above MSL, the annual mean value of ZHD is ~1.92 m and for Bangalore, which is situated at an altitude of ~930 m above MSL, it is ~2.08 m. Hyderabad and Bhopal are higher-latitude stations with altitude of ~ 500 m above MSL where as Jodhpur and Patiala are mid-latitude stations with altitude ~ 250 m above MSL. The ZHD for all these stations are ~ 2.1 m. The amplitude of the annual variation in ZHD is very small for all the three tropical stations and increases with increase in latitude.

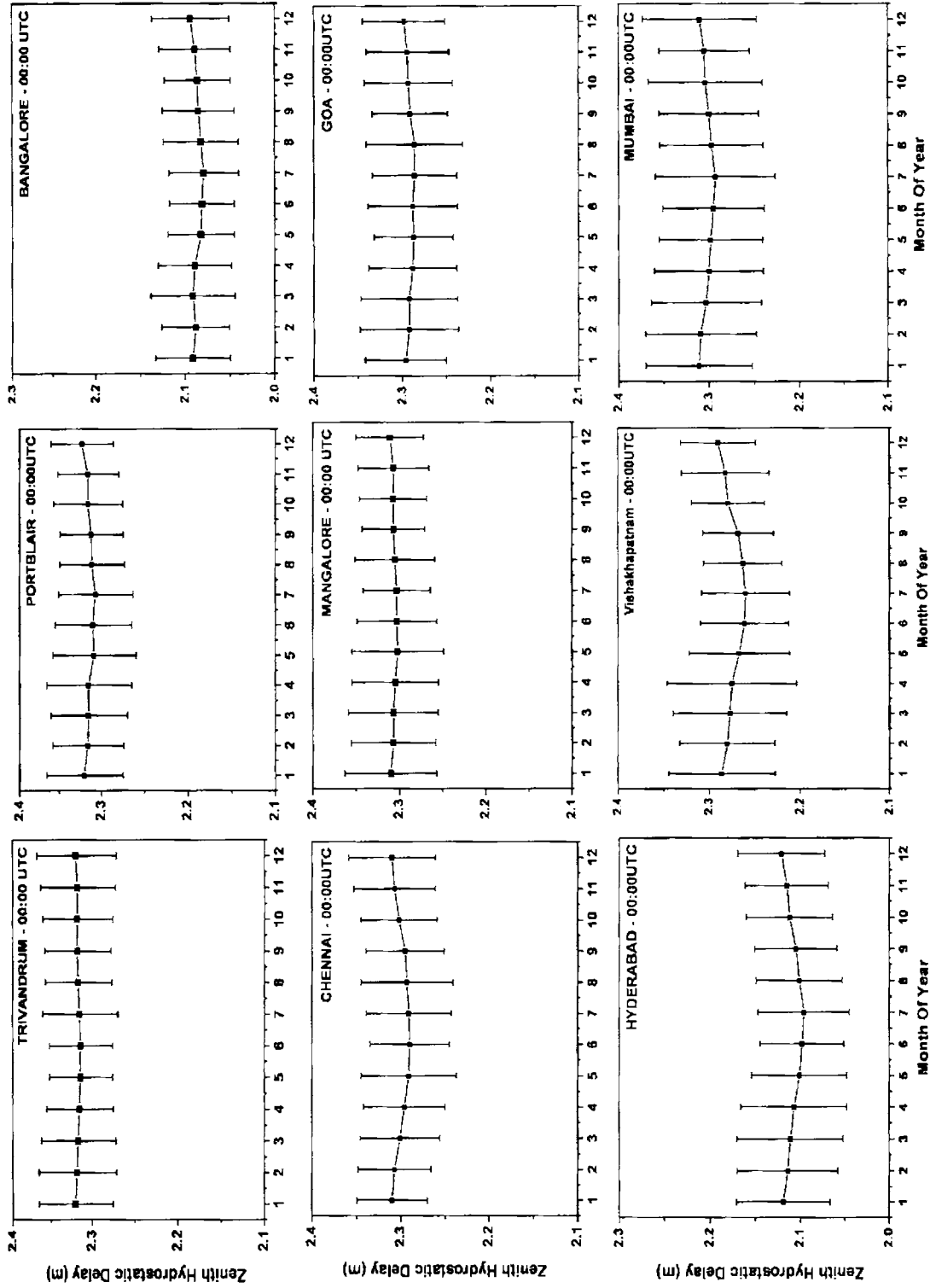


Figure 2.8a: Month to month variation of ZHD for Trivandrum, Chennai, Bangalore, Mangalore, Goa, Hyderabad, Vishakhapatnam and Mumbai. Same ordinate scale is used for all plots to illustrate the variation of mean level from one station to the other

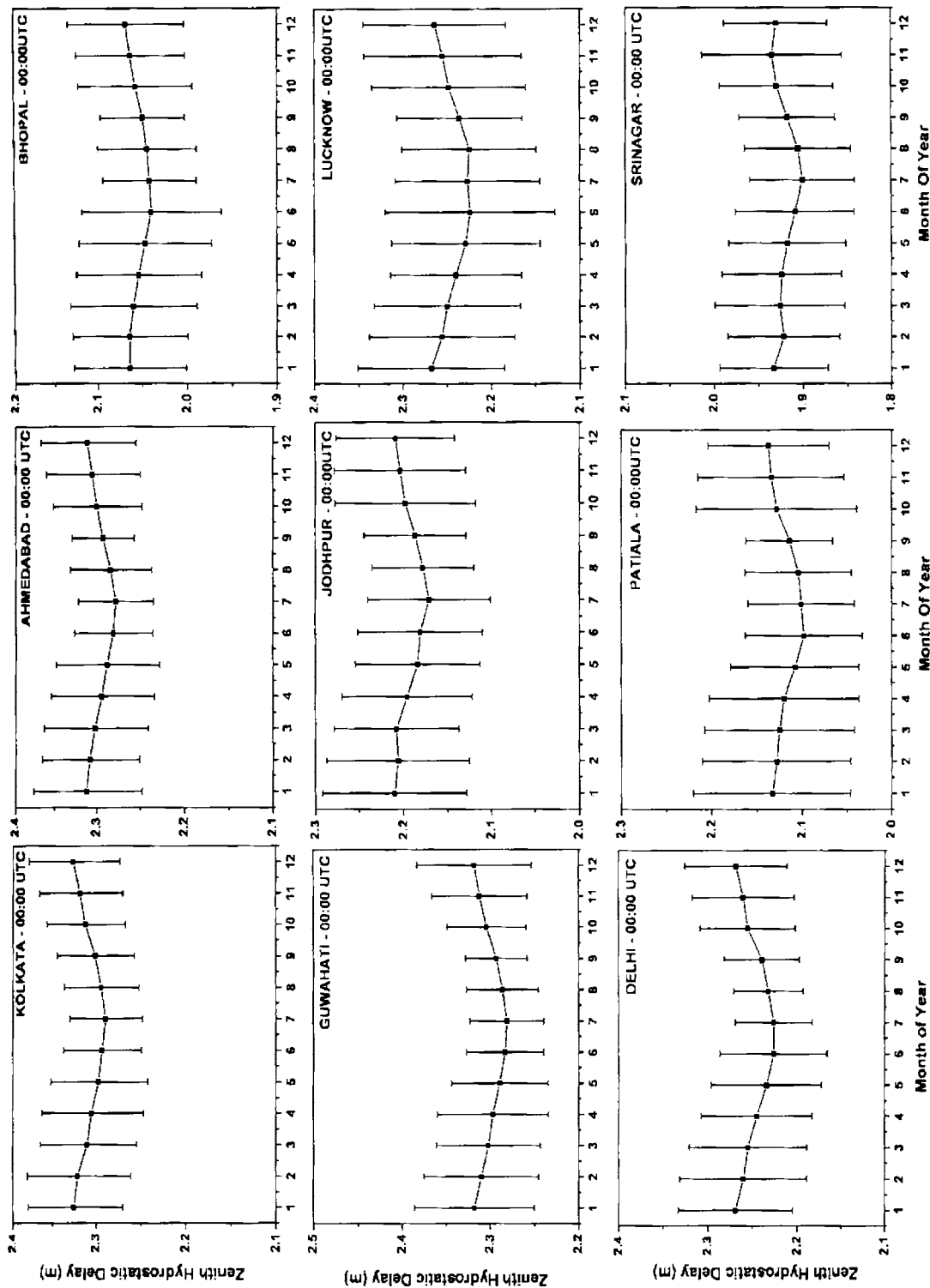


Figure 2.8b: Month to month variation of ZHD for Kolkata, Ahmedabad, Bhopal, Guwahati, Jodhpur, Lucknow, Patiala, and Srinagar. Same ordinate scale is used for all plots to illustrate the variation of mean level from one station to the other

Maximum annual variation is observed at the high latitude stations beyond Guwahati, with a prominent maximum during the period Dec-Jan with an amplitude of ≤ 15 cm. While the amplitude of the annual variation of mean ZHD for Trivandrum is about 0.34 cm and that for Delhi is ~ 1.5 cm, the day-to-day variability of ZHD in a month is around 7.0 cm indicating that in all the cases, the amplitude of the annual variation of mean ZHD is smaller than the day-to-day variability in each month. Note that, a large ZHD variation up to ~ 5.0 cm, is reported to be quite common [Bock and Doerflinger, 2000] during synoptic-scale and meso-scale disturbances.

Figure 2.9 shows the month-to-month variation of the ZWD for different stations, with vertical bars representing the standard deviation indicating the amount of day-to-day variability caused by the corresponding variations in the atmospheric water vapor. The value of ZWD is small for the dry period (December to February) and large during the monsoon (July and August) period. Amplitude of the annual variation of ZWD is small for the tropical coastal/island stations (Trivandrum and Portblair) compared to that for Delhi, Kolkata, Ahmedabad and Guwahati *etc.* Note that the absolute values of ZWD at Trivandrum and Portblair are much larger than the corresponding values at other stations during the winter period. At Bangalore and Srinagar, the mean value of ZWD as well as the amplitude of its annual variation is small.

The monthly mean values of ZWD vary in the range ~ 27 cm to 37 cm at Trivandrum and ~ 25 cm to 40 cm at Portblair, while for the higher latitude stations like Delhi, Guwahati, Ahmedabad and Kolkata, the lowest value of ZWD ranges from 10 cm to 15 cm, and the highest value exceeds 40 cm. This difference in the annual variation of ZWD at these stations is mainly caused by the large annual variability in atmospheric water vapor content at these stations [Parameswaran and Krishna Murthy, 1990]. It may be noted that at Trivandrum and Portblair as the temperature values are much larger than those at the higher latitude stations during the winter period, the atmosphere can hold relatively more water vapor, leading to much larger values of ZWD than those the other high latitude stations. During July-August period as the air temperature is relatively large at the higher latitude stations the atmosphere can hold relatively more water vapor (compared to near equatorial stations). Over and above the temperature effects, the massive synoptic system, “South-West monsoon”, which sets in at the southern tip of the Indian peninsula around first week of June and steadily advances towards north reaching Delhi within a time span of around 20

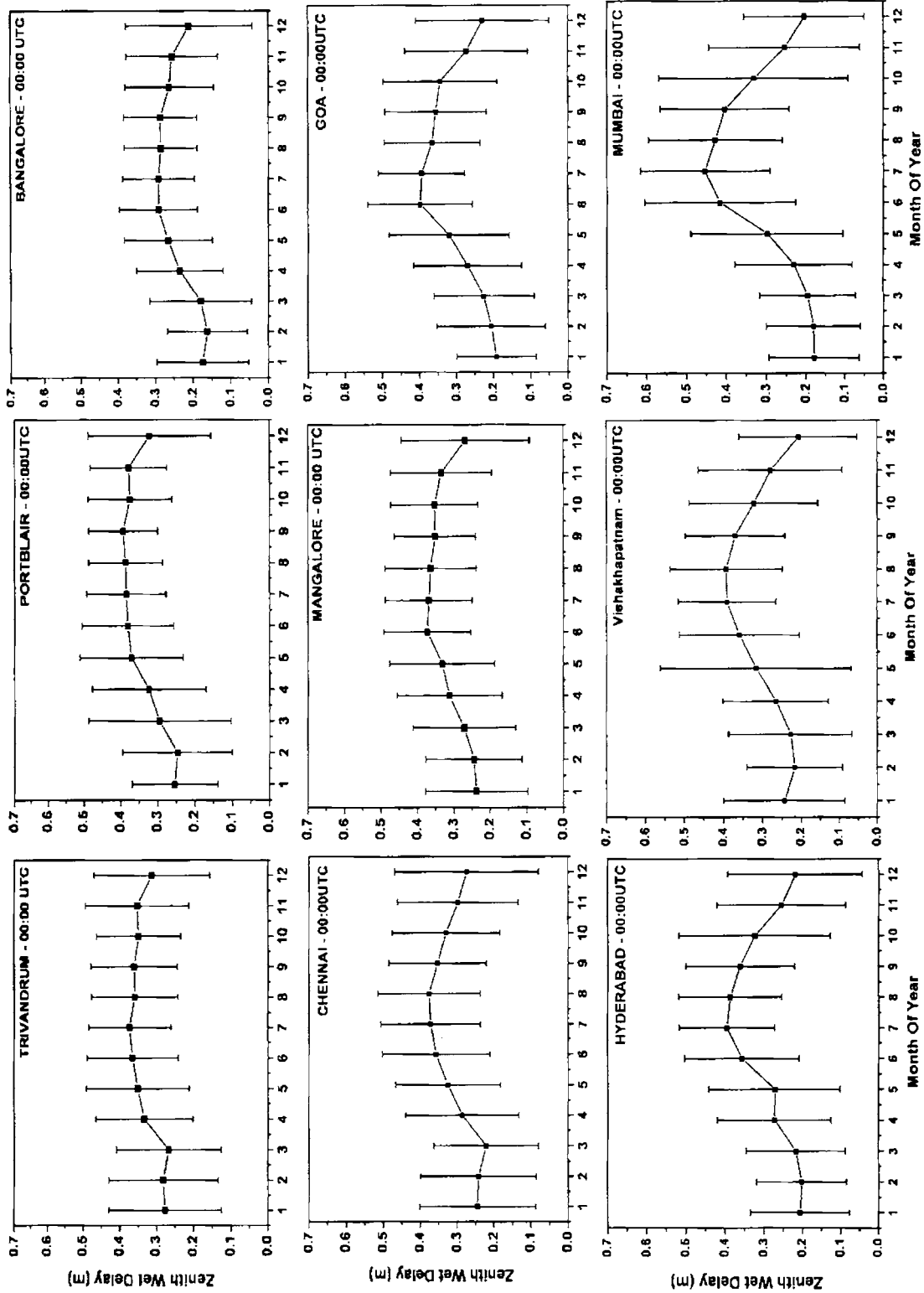


Figure 2.9a: Month to month variation of ZWD for Trivandrum, Portblair, Bangalore, Chennai, Mangalore, Goa, Hyderabad, Vishakhapatnam and Mumbai. Same ordinate scale is used for all plots to illustrate the variation of mean level from one station to the other

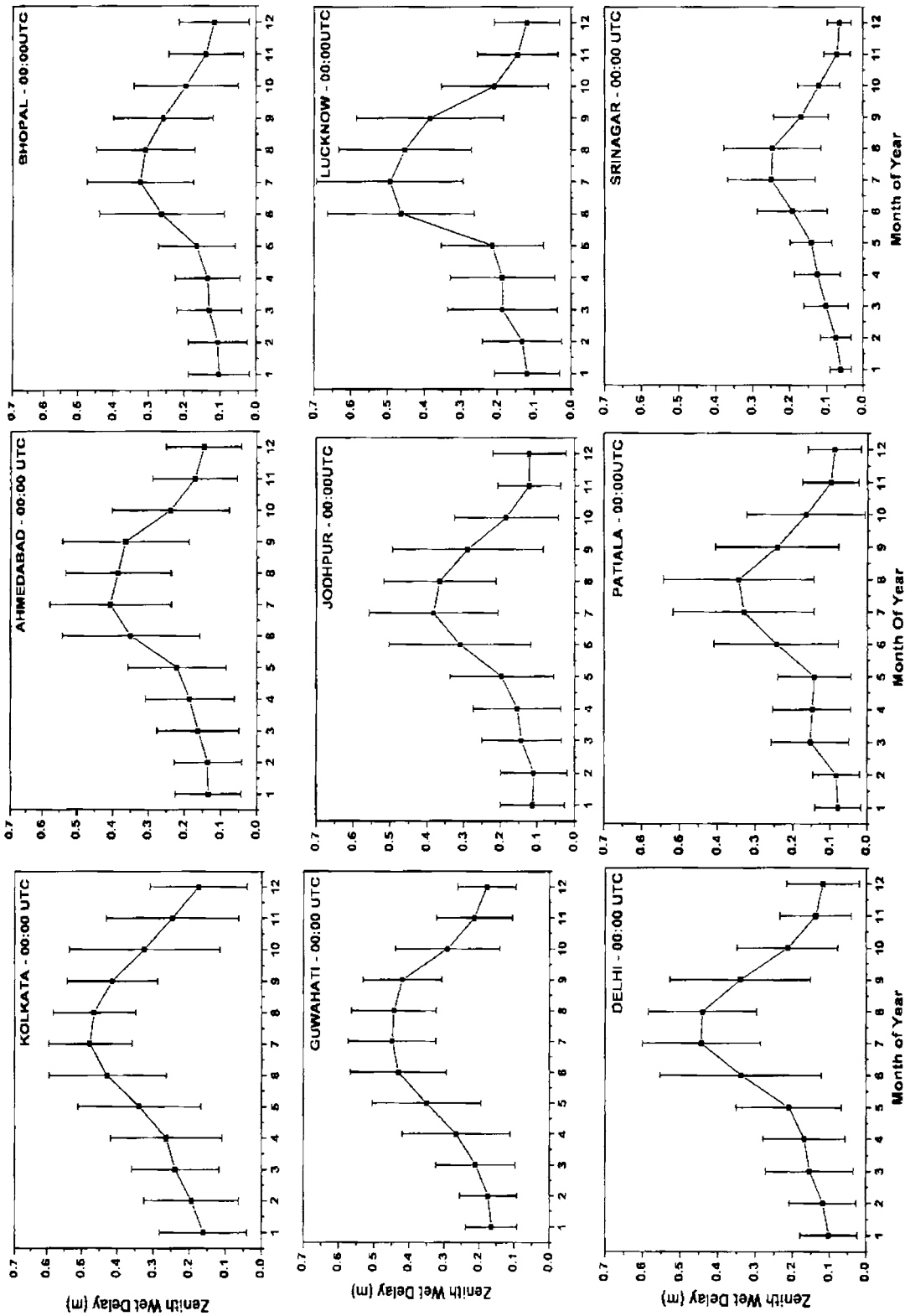


Figure 2.9b: Month to month variation of ZWD for Kolkata, Ahmedabad, Bhopal, Guwahati, Jodhpur, Lucknow, Delhi, Patiala, and Srinagar. Same ordinate scale is used for all plots to illustrate the variation of mean level from one station to the other

days, is characterized by cool moist air, advecting from the Arabian Sea and spreading over the entire subcontinent, bringing abundant water vapor over to the continent. Advection of the moist air from the ocean to the heated continental atmosphere causes further increase in the atmospheric water vapor content, especially at the higher latitude stations. This adds to further enhancement in the value of ZWD at these stations during June-September period. The value of ZWD thus depends very much on the capacity of atmosphere to hold water vapor (without precipitating) as well as the supply of water vapor. The picture is quite different for high altitude stations where the atmosphere is relatively dry. At Bangalore the minimum value of ZWD is about 15 cm. Even though the value of ZWD increases during June-August period because of the increase in columnar water vapor, it remains less than 30 cm. Similar is the case for Srinagar, which is located at still higher altitude where the minimum value of ZWD is around 5 cm and the maximum seldom exceeds 25 cm, indicating that the value of ZWD decreases with increase in (station) altitude. At Bangalore the mean ZWD shows a broad peak during June to September while at Srinagar it shows a sharp peak during the July and August. The ZWD varies roughly from 0 to 30 cm between the poles and the equator and from a few cm to about 20 cm during the year at mid-latitudes [Elgered, 1993]. The 2nd and 3rd column of Table 2.3 shows the annual mean values of ZHD and ZWD along with the extent of its month-to-month variation within parenthesis.

As can be seen from this table, the month-to-month variability for both the delays is small for the two tropical stations than those for the other stations. Maximum month-to-month variability in ZHD (δ_{ZHD}) is ≤ 3.8 cm and that of ZWD (δ_{ZWD}) is 13.7 cm (which is almost one order of magnitude larger). The 4th and 5th columns in Table 2.3 show the amount of mean day-to-day variability (mean of standard deviation in each month), which varies from 4.0 cm to 8.5 cm for ZHD and from 7.2 cm to 15.8 cm for ZWD. Considering the day-to-day values of ZTD over a year, it varies by 31.4 cm over the tropics and by 63.6 cm over the mid-latitudes. This variation is quite significant as far as GPS based navigation is concerned. Table 2.3 also shows the maximum and minimum values of ZHD (6th and 7th columns) and ZWD (8th and 9th columns), for each station. Except for the two high altitude stations, the maximum value of ZWD varies from 43 cm (Patiala) to 64 cm (Kolkata) and the minimum value varies from 6.5 cm (Delhi) to 24 cm (Trivandrum). The range of variability of ZHD is relatively small compared to that of ZWD. As seen from the Table 2.3, the day-to-day variability of tropospheric range error due to variations in the atmospheric

parameters could be as large as 15 cm, which is quite significant for navigation and hence calls for the development of fairly accurate empirical models based on easily measurable atmospheric parameters.

Table 2.3: Table Summarizing the Annual Mean Value of ZHD and ZWD for Different Indian Stations along with its Possible Deviation (Standard Deviation) from Month-to-Month. To Illustrate the Maximum Possible Deviation on a Day-to-Day Basis, the Maximum and Minimum Values of ZHD and ZWD Encountered during the Course of an Year is presented in the Last Four Columns

Station	ZHD (δ_{ZHD}) (cm)	ZWD (δ_{ZWD}) (cm)	Standard deviation of daily ZHD (cm)	Standard deviation of daily ZWD (cm)	Maximum and minimum values of daily ZHD calculated over a period of one year		Maximum and minimum values of daily ZWD calculated over a period of one year	
					Max. (cm)	Min. (cm)	Max. (cm)	Min. (cm)
Trivandrum	231.4 (0.3)	34.1 (3.2)	4.5	13.6	232.8	230.3	52.8	23.9
Portblair	231.3 (0.5)	34.5 (5.0)	4.3	12.7	232.1	229.0	50.0	16.9
Bangalore	208.6 (0.5)	24.2 (4.8)	4.0	11.7	209.5	207.1	38.4	20.4
Chennai	230.2 (0.7)	30.7 (7.9)	4.5	15.1	231.7	221.0	51.7	17.3
Mangalore	230.4 (0.4)	31.7 (5.1)	4.4	13.4	231.3	222.0	56.3	22.1
Goa	229.2 (0.6)	29.9 (7.3)	4.9	14.5	231.7	228.6	47.9	18.0
Hyderabad	211.0 (0.8)	28.5 (7.1)	5.1	14.8	219.7	204.0	55.6	14.9
Vishakhapatnam	227.3 (1.1)	30.5 (6.6)	5.1	15.8	229.0	225.6	39.3	20.7
Mumbai	230.3 (0.8)	30.0 (10.1)	5.5	15.8	231.0	228.8	45.3	17.0
Kolkata	230.7 (1.3)	31.1 (11.4)	5.0	14.6	233.2	226.6	63.8	17.9
Ahmedabad	229.4 (1.2)	24.4 (10.1)	5.5	13.5	231.4	224.9	55.0	10.0
Bhopal	205.4 (0.9)	19.3 (7.9)	6.4	11.9	207.2	200.0	51.5	10.6
Guwahati	229.6 (1.3)	30.7 (11.2)	5.3	11.8	231.8	223.4	54.7	15.2
Jodhpur	217.8 (3.8)	20.6 (9.8)	7.3	13.2	228.9	197.0	58.0	11.9
Lucknow	224.4 (1.5)	25.4 (13.7)	8.5	15.0	226.9	222.0	51.5	11.9
Delhi	224.6 (1.6)	23.5 (12.2)	5.7	13.1	228.2	218.0	59.9	6.5
Patiala	211.8 (1.35)	17.7 (9.3)	7.4	12.2	223.0	209.2	42.7	12.8
Srinagar	191.8 (1.1)	13.5 (6.4)	7.2	7.2	192.5	179.8	38.0	11.7

2.6 Summary

When microwave propagates through the neutral atmosphere, it undergoes refraction depending on the real component of the refractive index of the medium and attenuation

depending on the imaginary part. For GPS based aircraft navigation employing microwave ranging, the delay of wave propagation (caused by the wave) due to refraction and subsequent error in positioning is a major challenging task. The delay due to neutral atmosphere consists of two components. While the hydrostatic (dry) component, which depends primarily on atmospheric pressure and temperature, accounts for approximately 90% of the total delay, the wet component, which purely depends on the moisture content of the atmosphere, accounts for the remaining part. The delay caused by the neutral atmosphere depends on the geographical location as well as prevailing climatic conditions. Most accurate estimation of the Tropospheric delay could be achieved by ray-tracing employing the altitude profiles of neutral atmosphere refractivity which is a function of P , T and e . The tropospheric range error in the zenith direction as well as its spatial and temporal variabilities over the Indian sub-continent is examined by selecting eighteen appropriately located stations. It is also observed that hydrostatic component (ZHD) and non-hydrostatic component (ZWD) of tropospheric range error at all these stations have shown pronounced day-to-day variation (~ 4.0 cm to ~ 8.5 cm for ZHD and ~ 7.0 cm to ~ 15.8 cm for ZWD). While the month-to-month variations of mean ZHD ranges ~ 0.5 cm to ~ 3.8 cm that of ZWD is about ~ 5.0 cm to ~ 14 cm. Even though the tropospheric range error can be estimated within reasonable accuracies through ray tracing, the information on the altitude profiles of the atmospheric parameters may not be easily available for many places at any given time. To resolve this problem, it is highly essential to develop simple models based on the geographical location and time of the year and/or based on easily available atmospheric parameters at the surface in line with global efforts.

Chapter 3

DEVELOPMENT OF TROPOSPHERIC DELAY MODELS

3.0 Introduction

Neutral atmosphere being non-dispersive in nature, the only way to mitigate the tropospheric delay is to estimate it from the refractivity profiles, accomplishing a priori knowledge of which to incorporate in operational model is rather difficult. Then it becomes essential to develop conventional models relating the Tropospheric delay (both ZHD and ZWD) with easily measurable atmospheric parameters at the surface. Though a typical mean value of ~ 2.3 m for ZHD and 20 to 40 cm for ZWD can generally be taken as a “rule of thumb”, the day-to-day variability in atmospheric parameters can introduce a variation up to ± 15 cm about this mean value, as far as tropospheric range error is concerned. Because of this, conventional models [Saastamoinen, 1972; Davis *et al.*, 1985; Ifadis, 1986; Mendes and Langley, 1998] for ZHD and ZWD are developed in terms of atmospheric parameters at the surface, such as surface pressure (P_s), surface temperature (T_s) and surface water vapor pressure (e_s).

Saastamoinen [1972] developed a simple relation between ZHD and P_s for different latitudes taking into account the altitude variation also, which is fairly accurate up to 0.4 km for different seasons. Later Davis *et al.* [1985] and Elgered [1991] proposed similar models for ZHD with a slightly different value for the relevant coefficients. All these models are developed under the assumption that the dry atmosphere is in hydrostatic equilibrium and follows the equation of state. However, since water vapor need not be in hydrostatic equilibrium and is heterogeneously distributed in the atmosphere, similar models were not attempted for ZWD until Ifadis [1986] who developed simple empirical relation between ZWD and P_s , T_s and e_s . Later Mendes and Langley [1998] also proposed a simple empirical relation for ZWD using e_s and T_s . A slightly different model for ZHD and ZWD are evolved by Hopfield [1971], following a different approach based on refractivity profile.

A brief outline of these models is summarized in Chapter 1 Section 1.8. It would be worth in this context to note that all these empirical models are developed based on meteorological data from European and North American continents [Satirapod and

Chalermwattanachai, 2005]. The accuracies of these models, assessed by comparing with the true estimates obtained from ray-tracing, are typically < 3 mm for ZHD [Janes *et al.* 1991], and < 5 cm for ZWD [Askne and Nordius, 1987; Janes *et al.*, 1991; Elgered, 1992] with a maximum deviation extending up to ~ 8 cm during abnormal weather events [Elgered, 1993; Ichikawa, 1995]. However, no such studies are reported till date over the tropical/subtropical region. Taking note of this fact, empirical models applicable for the tropical region are developed based on the meteorological data from different locations situated at distinct climatic conditions over the Indian subcontinent. These models are validated by comparing with the true range error (estimated by ray-tracing).

3.1 Site-Specific Surface Models for Indian Subcontinent

The relationship between zenith tropospheric delay and the atmospheric parameters at surface are examined for different stations located at different climatic zones over the Indian subcontinent. A simple linear relationship is established for ZHD in terms of surface pressure through regression analysis. The true value of ZHD is estimated by applying the integral (eq. 2.39) to the monthly mean atmospheric models described in Section 2.6 and an empirical linear model connecting ZHD with P_S is developed in the following form

$$\text{ZHD} = a_D \cdot P_S \quad (3.1)$$

Figure 3.1 shows typical scatter plot of ZHD estimated through ray tracing with P_S (in hPa) for eight among the eighteen stations selected for this analysis (Table 2.1). These stations represent the major climatic zones over the Indian region and also have the location in proximity to major airports, considered in the GAGAN project. These stations are grossly referred to as the Range Integrity and Monitoring (RIM) stations. The regression analysis is performed keeping the value of intercept as zero and the resulting slope (a_D) and correlation coefficient are listed in the respective scatter plots. For all these stations, the value of correlation coefficient lies between 0.82 and 0.99. The standard error of a_D for each station is $< 0.024\%$ which corresponds to about 0.05 cm in delay. The standard deviation (SD) of the correlation also is listed in these plots. The values of coefficients a_D thus estimated for all the stations are presented in column 2 of Table 3.1.

Following a similar approach linear models are established for ZWD on a monthly mean basis for different stations with different surface humidity parameters such as surface

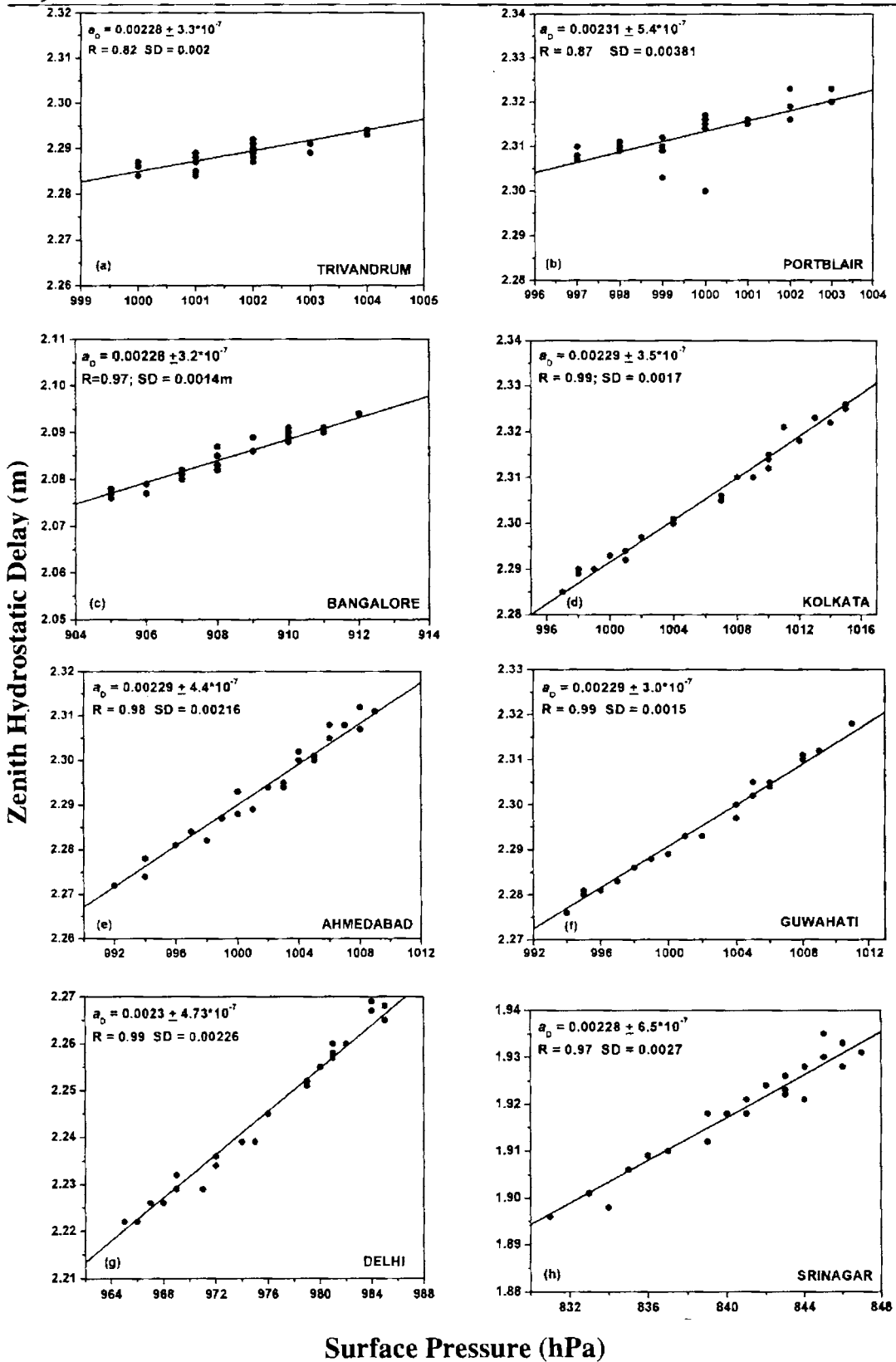


Figure 3.1: Scatter plots along with the regression line showing the variation of ZHD with P_s for different stations located at different climate zones over the Indian subcontinent and adjoining oceanic region

Table 3.1: Coefficients of Site-Specific Surface Models for Different Indian Stations

Station	Dry		Wet	
	ZHD (m) = $a_D \times P_S$	ZWD (m) = $a_W \times e_S$	ZWD (m) = $b_W \times \rho_S$	ZWD (m) = $c_W \times PW$
	$a_D \times 10^{-3}$	a_W	b_W	$c_W \times 10^{-3}$
Trivandrum	2.280 ± 3.3E-4 (0.82; 0.002)	0.01199 ± 1.5E-4 (0.77; 0.0217)	16.595 ± 0.233 (0.72; 0.023)	6.45 ± 5.6E-3 (0.99; 0.0015)
Portblair	2.310 ± 5.4E-4 (0.87; 0.0038)	0.01212 ± 1.8E-4 (0.93; 0.025)	16.753 ± 0.255 (0.91; 0.025)	6.45 ± 4.3E-3 (0.99; 0.0011)
Bangalore	2.280 ± 3.2E-4 (0.97; 0.0014)	0.0122 ± 2.48E-4 (0.86; 0.025)	16.703 ± 0.384 (0.81; 0.0278)	6.53 ± 7.1E-3 (0.99; 0.0013)
Mangalore	2.280 ± 3.4E-4 (0.89; 0.0017)	0.0113 ± 2.2E-4 (0.85; 0.030)	15.628 ± 0.316 (0.85; 0.032)	6.35 ± 7.7E-3 (0.99; 0.0019)
Chennai	2.290 ± 2.7E-4 (0.98; 0.0013)	0.0111 ± 3.1E-4 (0.58; 0.042)	15.409 ± 0.443 (0.54; 0.043)	6.33 ± 7.8E-3 (0.99; 0.0019)
Goa	2.280 ± 6.6E-4 (0.81; 0.0032)	0.0109 ± 2.9E-4 (0.92; 0.040)	15.047 ± 0.40 (0.92; 0.040)	6.34 ± 7.1E-3 (0.99; 0.0017)
Hyderabad	2.230 ± 3.0E-4 (0.98; 0.0014)	0.0142 ± 2.5E-4 (0.94; 0.026)	19.577 ± 0.413 (0.90; 0.030)	6.42 ± 5.6E-3 (0.99; 0.0013)
Vishakhapatnam	2.270 ± 3.4E-4 (0.99; 0.0017)	0.0107 ± 2.8E-4 (0.81; 0.039)	15.477 ± 0.87 (0.41; 0.089)	6.39 ± 7.8E-3 (0.98; 0.0200)
Mumbai	2.290 ± 3.7E-4 (0.97; 0.0017)	0.0117 ± 3.8E-4 (0.92; 0.049)	16.267 ± 0.56 (0.90; 0.051)	6.33 ± 5.5E-3 (0.99; 0.0013)
Kolkata	2.290 ± 3.5E-4 (0.99; 0.0017)	0.0119 ± 3.01E-4 (0.94; 0.0408)	16.43 ± 0.427 (0.94; 0.0418)	6.43 ± 9.2E-3 (0.99; 0.0023)
Ahmedabad	2.290 ± 4.4E-4 (0.98; 0.0022)	0.0119 ± 2.27E-4 (0.97; 0.0245)	16.627 ± 0.315 (0.97; 0.0243)	6.43 ± 1.1E-2 (0.99; 0.0022)
Bhopal	2.160 ± 6.1E-4 (0.97; 0.0028)	0.0112 ± 2.5E-4 (0.96; 0.023)	15.394 ± 0.38 (0.95; 0.025)	6.37 ± 3.7E-3 (0.99; 0.0060)
Guwahati	2.290 ± 3.0E-4 (0.99; 0.0015)	0.0127 ± 2.7E-4 (0.97; 0.0338)	17.520 ± 0.399 (0.97; 0.036)	6.46 ± 1.1E-2 (0.99; 0.0027)
Jodhpur	2.230 ± 7.1E-4 (0.98; 0.0032)	0.0122 ± 2.0E-4 (0.98; 0.018)	16.847 ± 0.30 (0.98; 0.019)	6.34 ± 0.2E-3 (0.99; 0.0028)
Lucknow	2.260 ± 5.2E-4 (0.98; 0.0025)	0.0126 ± 4.5E-4 (0.95; 0.048)	17.418 ± 0.66 (0.95; 0.051)	6.25 ± 0.3E-3 (0.99; 0.0069)
Delhi	2.300 ± 4.7E-4 (0.99; 0.0023)	0.0128 ± 2.3E-4 (0.99; 0.023)	17.539 ± 0.373 (0.98; 0.0274)	6.44 ± 1.4E-2 (0.99; 0.0024)
Patiala	2.200 ± 9.4E-4 (0.95; 0.0044)	0.0101 ± 8.4E-4 (0.70; 0.084)	13.929 ± 1.15 (0.70; 0.083)	6.00 ± 1.13E-1 (0.99; 0.0069)
Srinagar	2.280 ± 6.5E-4 (0.97; 0.0027)	0.0118 ± 1.5E-4 (0.99; 0.0093)	15.934 ± 0.172 (0.99; 0.0078)	6.61 ± 2.5E-2 (0.99; 0.0027)

water vapor pressure (e_s in hPa), surface water vapor density (ρ_s , in kg m^{-3}) and the columnar integrated water vapor (I_s in kg m^{-2}) also known as Precipitable Water vapor (PW in mm). As a typical example the scatter plots of ZWD estimated through ray tracing, with e_s for the eight RIM stations are presented in Figure 3.2. A linear relationship was sought analogous to that of the dry component through regression analysis keeping the value of intercept as zero in the following form

$$\text{ZWD} = a_w \times e_s$$

$$\text{ZWD} = b_w \times \rho_s$$

$$\text{ZWD} = c_w \times \text{PW} \quad (3.2)$$

values of the coefficients thus estimated are presented in columns 3, 4 and 5 of Table 3.1 for all the eighteen stations. The quantities shown inside the parenthesis in each cell are the correlation coefficient and its standard deviation, respectively. A perusal of Figure 3.1 along with Figure 3.2 shows that the deviation of points from the mean line is relatively large in the latter case, the effect of which is also observable in the standard error associated with the regression coefficients. This shows that, in general, the uncertainty in the prediction of ZWD is larger than that of ZHD. The regression coefficients connecting ZWD with e_s , ρ_s and PW are also examined by removing the imposed condition of “zero intercept”. The values of regression coefficient are rearranged in a more convenient form as shown below and the coefficients a_0 , b_0 , c_0 , e_0 , ρ_0 , and PW_0 are estimated.

$$\text{ZWD} = a_0 \times (e_s - e_0) \quad \text{for } e_s > e_0$$

$$\text{ZWD} = b_0 \times (\rho_s - \rho_0) \quad \text{for } \rho_s > \rho_0$$

$$\text{ZWD} = c_0 \times (\text{PW} - \text{PW}_0) \quad \text{for } \text{PW} > \text{PW}_0 \quad (3.3)$$

The values of these coefficients along with their respective standard error are summarized in Table 3.2. The respective values of the correlation coefficient and its standard deviation are presented within the parenthesis just below the corresponding coefficients. The values of a_0 , and b_0 are marginally greater than corresponding values of a_w , and b_w for all the 18 stations except Chennai, Hyderabad, Vishakhapatnam, Bhopal, Jodhpur, Patiala and Srinagar where the values of e_s , ρ_s and PW are relatively small. The values of c_0 and c_w for different stations are more or less comparable. As these models are developed for each station separately based on the monthly mean atmospheric models and surface meteorological parameters from respective stations, they are termed as “**Site-Specific surface models**” in

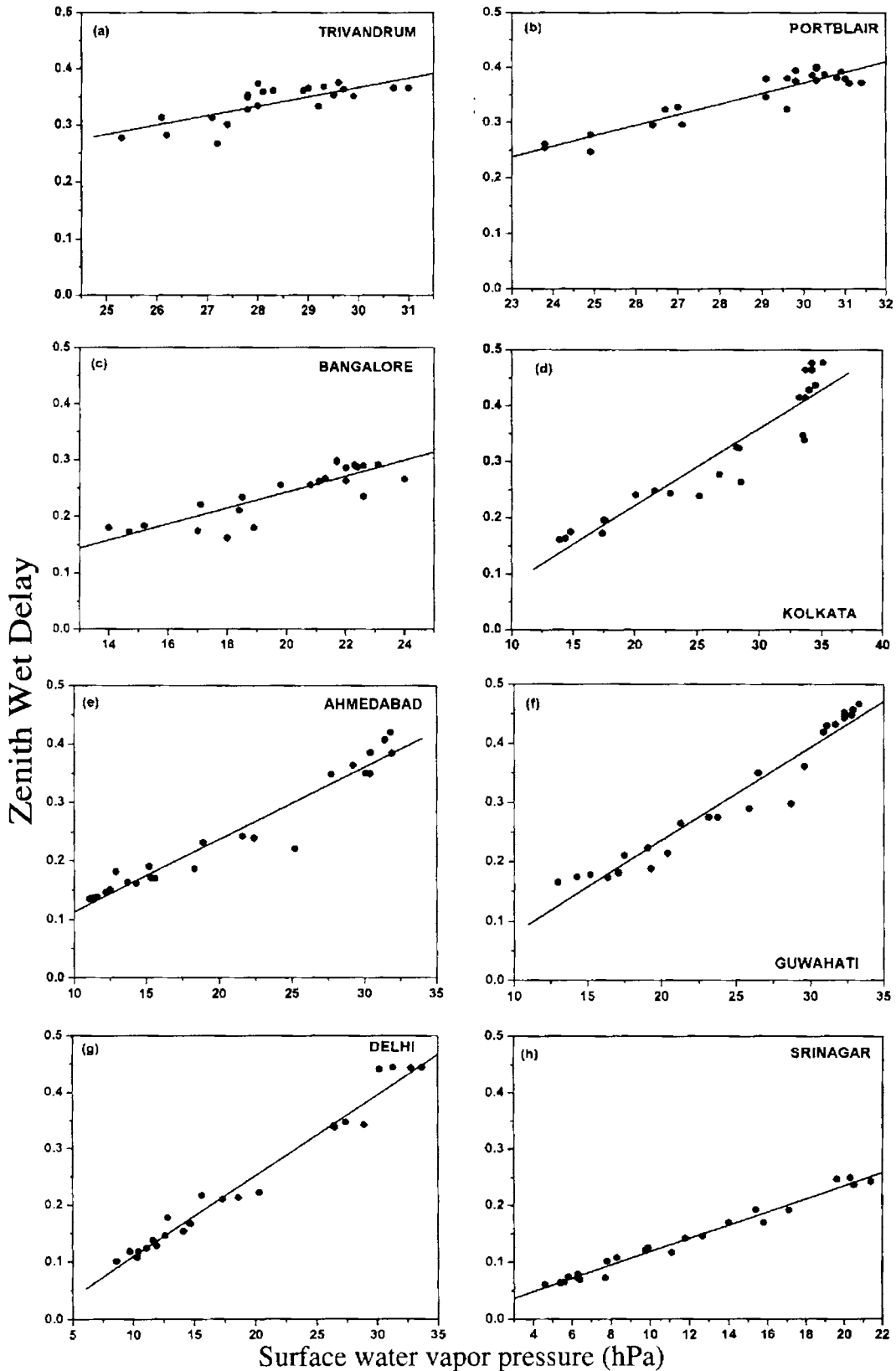


Figure 3.2: Scatter plots along with the regression line showing the variation of ZWD with e_s for different stations located at different climate zones over the Indian subcontinent and adjoining oceanic region

Table 3.2: The Regression Coefficients Connecting ZWD with e_s , ρ_s and PW, Removing the Imposed Condition of "Zero Intercept"

Station	Wet range error					
	ZWD (m) = $a_0 \times (e_s - e_0)$		ZWD (m) = $b_0 \times (\rho_s - \rho_0)$		ZWD (m) = $c_0 \times (PW - PW_0)$	
	$(a_0 \pm \Delta a_0) \times 10^{-3}$	$e_0 \pm \Delta e_0$	$b_0 \pm \Delta b_0$	$(\rho_0 \pm \Delta \rho_0) \times 10^{-3}$	$(c_0 \pm \Delta c_0) \times 10^{-3}$	$PW_0 \pm \Delta PW_0$
Trivandrum	15.11 ± 2.7 (0.77;0.019)	7.82 ± 0.08	21.39 ± 4.5 (0.71;0.02)	5.98 ± 4.5	6.35 ± 0.05 (0.99;0.001)	0.19 ± 2e-3
Portblair	19.17 ± 1.5 (0.93;0.018)	10.59 ± 0.04	24.47 ± 2.3 (0.91;0.021)	6.58 ± 2.3	6.46 ± 0.03 (0.99;0.001)	0.07 ± 1.6e-3
Bangalore	14.13 ± 1.8 (0.86;0.024)	2.80 ± 0.04	17.65 ± 2.7 (0.81;0.028)	0.806 ± 2.7	6.56 ± 0.04 (0.99;0.001)	0.174 ± 1.4e-3
Mangalore	17.34 ± 2.3 (0.85;0.027)	9.9 ± 0.06	25.69 ± 3.4 (0.85;0.027)	8.03 ± 3.4	6.47 ± 0.04 (0.99;0.002)	1.00 ± 2.2e-3
Chennai	11.95 ± 3.6 (0.58;0.043)	2.07 ± 0.10	15.99 ± 5.4 (0.54;0.044)	0.73 ± 5.4	6.30 ± 0.05 (0.99;0.002)	0.27 ± 2.3e-3
Goa	18.81 ± 1.7 (0.92;0.030)	11.89 ± 0.05	25.69 ± 2.4 (0.92;0.030)	8.5 ± 2.35	6.42 ± 0.03 (0.99;0.002)	0.567 ± 1.3e-3
Hyderabad	15.53 ± 1.2 (0.94;0.026)	1.77 ± 0.03	21.22 ± 2.1 (0.91;0.030)	1.18 ± 2.1	6.40 ± 0.02 (0.99;0.001)	0.15 ± 1.1e-3
Vishakhapatnam	11.45 ± 1.8 (0.81;0.039)	1.95 ± 0.05	12.3 ± 5.94 (0.40;0.090)	5.43 ± 5.9	6.85 ± 0.30 (0.98;0.019)	3.6 ± 1.5e-2
Mumbai	16.71 ± 1.6 (0.92;0.041)	8.14 ± 0.04	23.10 ± 2.4 (0.91;0.044)	5.78 ± 2.4	6.33 ± 0.02 (0.99;0.001)	0.07 ± 1.0e-3
Kolkata	13.80 ± 1.0 (0.94;0.038)	3.92 ± 0.03	19.81 ± 1.5 (0.94;0.038)	3.53 ± 1.5	6.34 ± 0.02 (0.99;0.002)	0.79 ± 1.0e-3
Ahmedabad	12.37 ± 0.6 (0.97;0.025)	0.86 ± 0.01	16.98 ± 0.9 (0.97;0.025)	0.35 ± 0.8	6.37 ± 0.03 (0.99;0.002)	0.45 ± 1.1e-3
Bhopal	11.08 ± 0.7 (0.96;0.023)	0.13 ± 0.01	15.16 ± 1.1 (0.95;0.025)	0.22 ± 1.0	6.13 ± 0.08 (0.99;0.005)	1.42 ± 2.7e-3
Guwahati	15.69 ± 0.8 (0.97;0.027)	4.96 ± 0.02	22.44 ± 1.5 (0.97;0.027)	4.19 ± 1.2	6.34 ± 0.02 (0.99;0.001)	1.05 ± 0.8e-3
Jodhpur	12.12 ± 0.5 (0.98;0.018)	0.04 ± 0.01	17.42 ± 0.8 (0.98;0.019)	0.50 ± 0.7	6.22 ± 0.02 (0.99;0.002)	0.82 ± 0.9e-3
Lucknow	15.59 ± 1.0 (0.95;0.041)	4.59 ± 0.02	21.96 ± 1.6 (0.95;0.044)	3.60 ± 1.6	6.05 ± 0.05 (0.99;0.005)	1.72 ± 2.1e-3
Delhi	14.30 ± 0.5 (0.98;0.019)	2.34 ± 0.01	20.20 ± 0.7 (0.98;0.022)	2.14 ± 0.8	6.34 ± 0.01 (0.99;0.002)	0.76 ± 0.7e-3
Patiala	9.90 ± 2.2 (0.70;0.086)	0.43 ± 0.05	14.11 ± 3.2 (0.70;0.085)	0.21 ± 3.2	5.50 ± 0.20 (0.99;0.016)	4.15 ± 6.2e-3
Srinagar	11.70 ± 0.4 (0.98;0.009)	0.15 ± 0.01	16.58 ± 0.4 (0.99;0.007)	0.39 ± 0.4	6.39 ± 0.03 (0.99;0.001)	0.87 ± 0.6e-3

further discussions. However, the accuracy of these models in general depends on the accuracy of the surface atmospheric parameters [Bock and Doerflinger, 2000].

3.2 Adaptation of Hopfield Model for the Indian Region

The surface models provide integrated range error all the way from top of the atmosphere to the surface. Whenever the prediction of tropospheric range error is required from an elevated platform, a priori knowledge of the altitude dependences of the relevant coefficients is to be accounted through an appropriate correction factor [Baby et al., 1988]. Taking this factor into account, the *Hopfield* [1969] model (which addressed the altitude dependence in range error) is adapted for the Indian region. As detailed in Section 1.5.4, in this model the integral effect of refractive index parameter above the user altitude alone is considered. The altitude variation of refractivity is modeled through the semi-analytical relations connecting the surface refractivity with the characteristic height parameter. Correspondingly two characteristic height parameters evolve, one for the hydrostatic component (h_D) and the other for the non-hydrostatic component (h_W). The altitude profile of dry component of refractivity (N_D) when $h \leq h_D$ can be expressed as,

$$N_D = N_{SD} \left[\frac{(h_D - h)}{(h_D - h_S)} \right]^\eta \quad (3.4)$$

where h_D (in km) is the “characteristic height” for dry refractivity profile, h_S is the altitude of the station above MSL and N_{SD} is the value of N_D at the surface (where $h = h_S$). The equation for dry component is obtained by analytically solving the gas law equations applicable for the atmosphere [Hopfield, 1969]. As the temperature lapse rate varies with geographic latitude as well as to certain extent with altitude also, η also varies accordingly. Even though, no such analytical form can be arrived in the case of the wet component (N_W), *Hopfield* [1969] in his formulation assumed that the water vapor also follows a similar law with same value of η but different value of characteristic height (h_W). With this assumption the altitude variation of wet component of refractivity (N_W), when $h \leq h_W$, is modeled as

$$N_W = N_{SW} \left[\frac{(h_W - h)}{(h_W - h_S)} \right]^\eta \quad (3.5)$$

where h_W (in km) is the ‘characteristic height’ for wet refractivity profile and N_{SW} is the value of N_W at the surface. In the above formulations, it is implicitly assumed that the effect

of N_D above h_D and that of N_W above h_W is insignificant. As the zenith delay is obtained by integrating the atmospheric refractivity along the altitude between h_S and top of the atmosphere, ZHD and ZWD can be estimated by analytically integrating eq. (3.4) and eq. (3.5) respectively, replacing the upper limits by the respective characteristic heights. If we consider the altitude profiles of N_D and N_W starting from the surface, for any location h_S can be treated as zero. The expression for zenith range errors can then be written as.

$$\text{ZHD} = \int_0^{h_D} N_D dh = N_{SD} \frac{h_D}{(\eta + 1)} \quad (3.6a)$$

and

$$\text{ZWD} = \int_0^{h_W} N_{wet} dh = N_{SW} \frac{h_W}{(\eta + 1)} \quad (3.6b)$$

The above equations are strictly valid only when the integrals are taken up to the respective characteristics height.

If we consider the mean sea level values of the dry and wet components of the refractivity (N_{0D} and N_{0W} , respectively), then N_{SD} and N_{SW} at the surface ($h = h_S$) can be written in terms of their MSL values as

$$N_{SD} = N_{0D} \left(\frac{h_D - h_S}{h_D} \right)^\eta \quad (3.7a)$$

and

$$N_{SW} = N_{0W} \left(\frac{h_W - h_S}{h_W} \right)^\eta \quad (3.7b)$$

Then eq. (3.6a) and eq. (3.6b) can be rewritten accordingly in terms of N_{0D} and N_{0W} . Following a similar approach, eq. (3.7a) and eq. (3.7b) both can be extrapolated for any given altitude by replacing h_S with that altitude. In case if one is interested in using the surface values N_{SD} and N_{SW} , same procedure can be followed by replacing N_{0D} and N_{0W} in eq. (3.7a) and eq. (3.7b), respectively, by N_{SD} and N_{SW} . In this case h_S should be replaced by the height of the location above the surface (h_P).

However, this method requires a priori knowledge of the characteristic height parameters and atmospheric refractive index at the surface. The characteristic height is derived by equating the numerical integral of refractive index profile to the theoretically estimated value of integrated refraction effect given in eq. (3.6a) and eq. (3.6b). In this

process β decides the value of η and hence the denominator of the eq. (3.6). Even though using different temperature lapse rate will change the value of η , the value of h_D estimated through eq. (3.6a) using the new lapse rate also will change correspondingly in such a way that the ratio of $h_D/(\eta+1)$ remains the same. This is true in case of h_W also. However, in the present study the temperature lapse rate is taken as 6.7 K/km as was done by *Hopfield* [1971] and the values of h_D and h_W derived for all the stations are based on this lapse rate.

Implementation of this model, however, involves modeling of the characteristic height parameters for different stations. Substituting the true range error estimated by integrating the refractivity profiles obtained from the monthly mean atmospheric models in eq. (3.6a) and eq. (3.6b) respectively; the dry and wet characteristic heights are estimated at each station for different months. The month-to-month variation of h_D estimated for 00:00 UTC and 12:00 UTC (corresponding to 05:30 IST and 17:30 IST, respectively) for all the eighteen stations used for the present study are presented in Figure 3.3(a-r). Similarly, Figure 3.4(a-r) shows the month-to-month variation of h_W for these stations. The vertical lines in these figures show the respective standard deviations in each month (representing the day-to-day variability) estimated by applying the error propagation formula [*Ku*, 1966] appropriately. While the month-to-month variation (seasonal) of h_D is small for the tropical stations ($< \pm 0.5$ km), it is large for the high-latitude stations (~ 5 km). While the mean value of h_W varies between ~ 11 km to ~ 14 km for the tropical stations it varies in the range 8 km to 16 km for the high latitude stations. Significant annual variation in h_W is observable for the high-latitude stations (with amplitude as large as ~ 9 km). A distinct morning to evening difference is observable in the values of h_D for all these stations with the evening values consistently being larger than the corresponding morning values, even though such a trend does not emerge for h_W . However, in most of the cases the evening values of h_W are larger than the morning values. The annual mean values of h_D and h_W for the eighteen stations are presented in Table 3.3 along with the respective standard deviations, within parenthesis (indicating the extent of mean monthly variations). While the observed mean values of h_D and h_W are quite large and fairly constant for the near equatorial stations (Trivandrum, Portblair and Bangalore), a prominent annual variation is observable for the other stations particularly in case of h_D . The characteristic height for different months can be used as a look up table for each station for estimating the range error employing eq. 3.6(a) and eq. 3.6(b) by incorporating the respective values of surface refractivity.

Table 3.3: Mean Value of h_D and h_W along with the Maximum Month-to-month Variability (within parenthesis)

Stations	h_D (km)	h_W (km)
Trivandrum	44.610 (0.39)	13.32 (0.88)
Portblair	44.580 (0.25)	13.34 (1.10)
Bangalore	43.890 (0.70)	13.28 (1.59)
Mangalore	44.270 (0.43)	12.69 (1.16)
Chennai	44.363 (0.52)	12.61 (1.81)
Goa	44.258 (0.46)	12.06 (1.67)
Hyderabad	43.098 (0.75)	15.99 (1.93)
Vishakhapatnam	43.904 (0.39)	12.96 (3.90)
Mumbai	44.278 (0.58)	12.79 (2.12)
Kolkata	44.063 (0.79)	12.83 (1.60)
Ahmedabad	44.323 (1.30)	13.25 (1.46)
Bhopal	41.509 (1.02)	12.76 (2.22)
Guwahati	43.750 (0.77)	13.41 (1.71)
Jodhpur	42.814 (1.19)	14.02 (1.41)
Lucknow	43.282 (1.08)	13.29 (3.04)
Delhi	43.910 (1.17)	13.34 (1.80)
Patiala	41.673 (1.15)	12.14 (9.92)
Srinagar	41.960 (1.32)	12.08 (0.95)

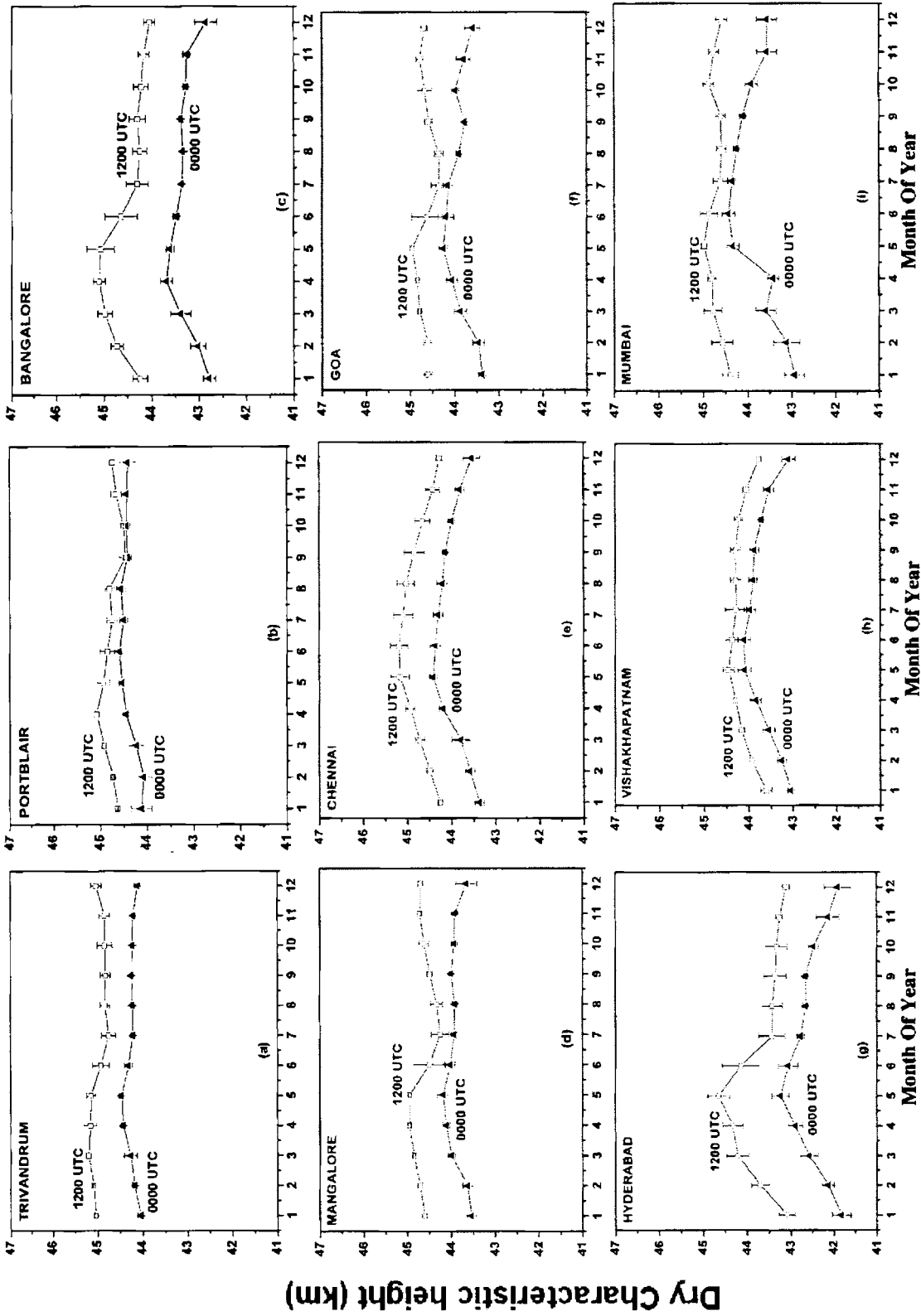


Figure 3.3(a-i): Month-to-month variation of h_0 for Trivandrum, Portblair, Bangalore, Mangalore, Chennai, Goa, Hyderabad, Vishakhapatnam, and Mumbai. continuous lines with solid triangle represent the variations for 00:00 UTC and the same with open square for 12:00 UTC

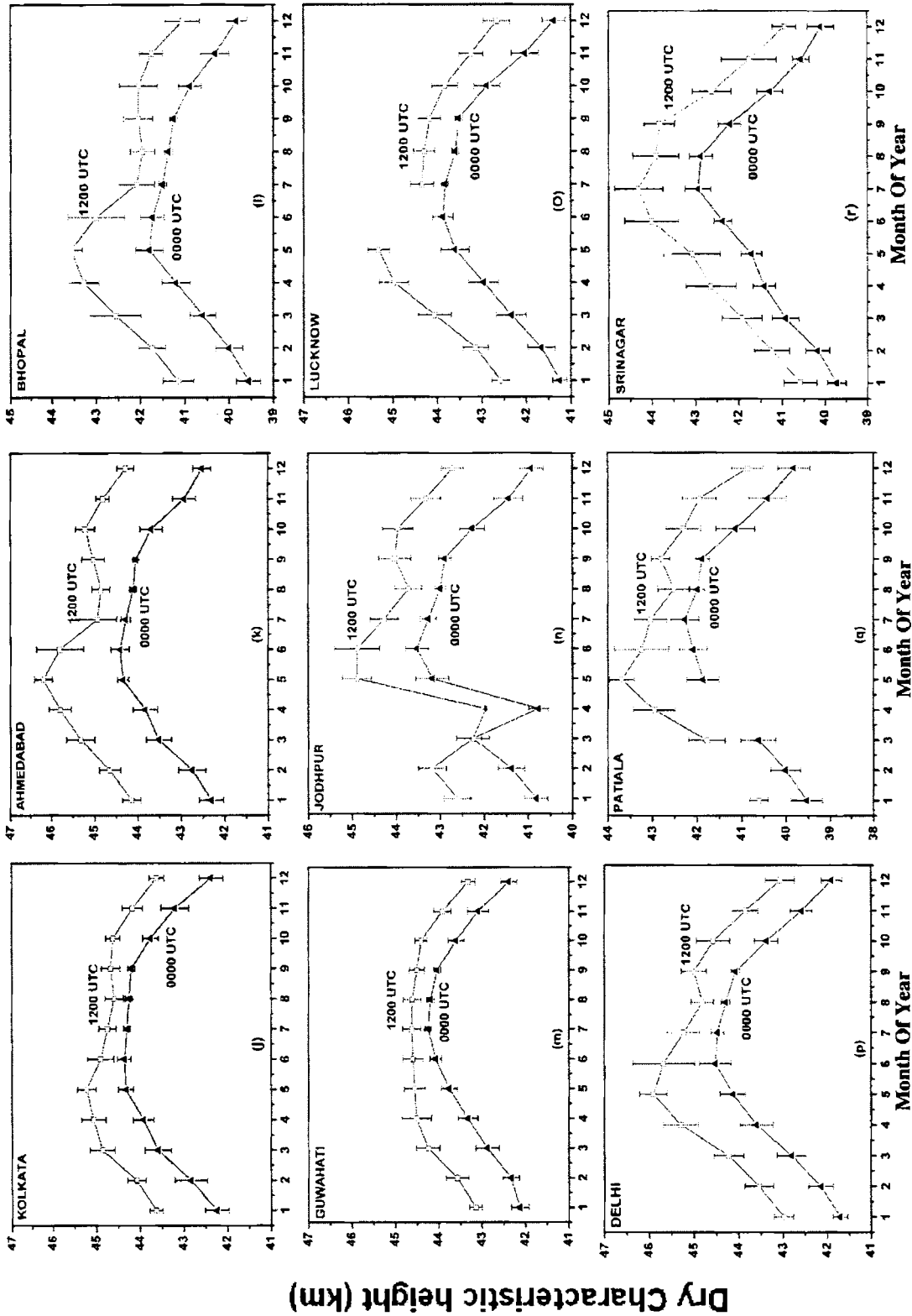


Figure 3.3(j-r): Month-to-month variation of h_D for Kolkata, Ahmedabad, Bhopal, Guwahati, Jodhpur, Lucknow, Delhi, Patiala, and Srinagar. continuous lines with solid triangle represent the variations for 00:00 UTC and the same with open square for 12:00 UTC

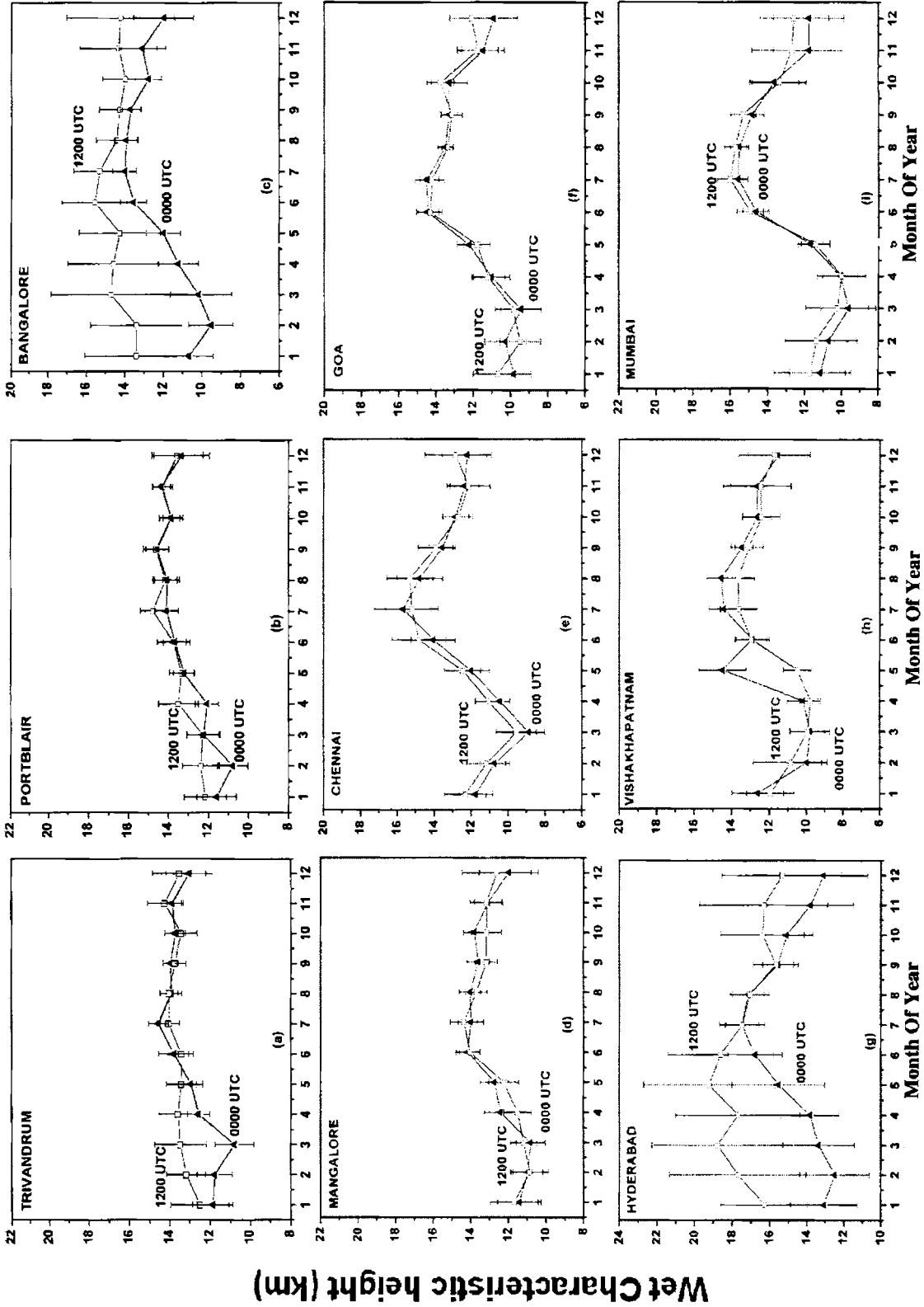


Figure 3.4(a-j): Month-to-month variation of h_w for Trivandrum, Portblair, Bangalore, Chennai, Goa, Hyderabad, Vishakhapatnam, and Mumbai. continuous lines with solid triangle represent the variations for 00:00 UTC and the same with open square for 12:00 UTC

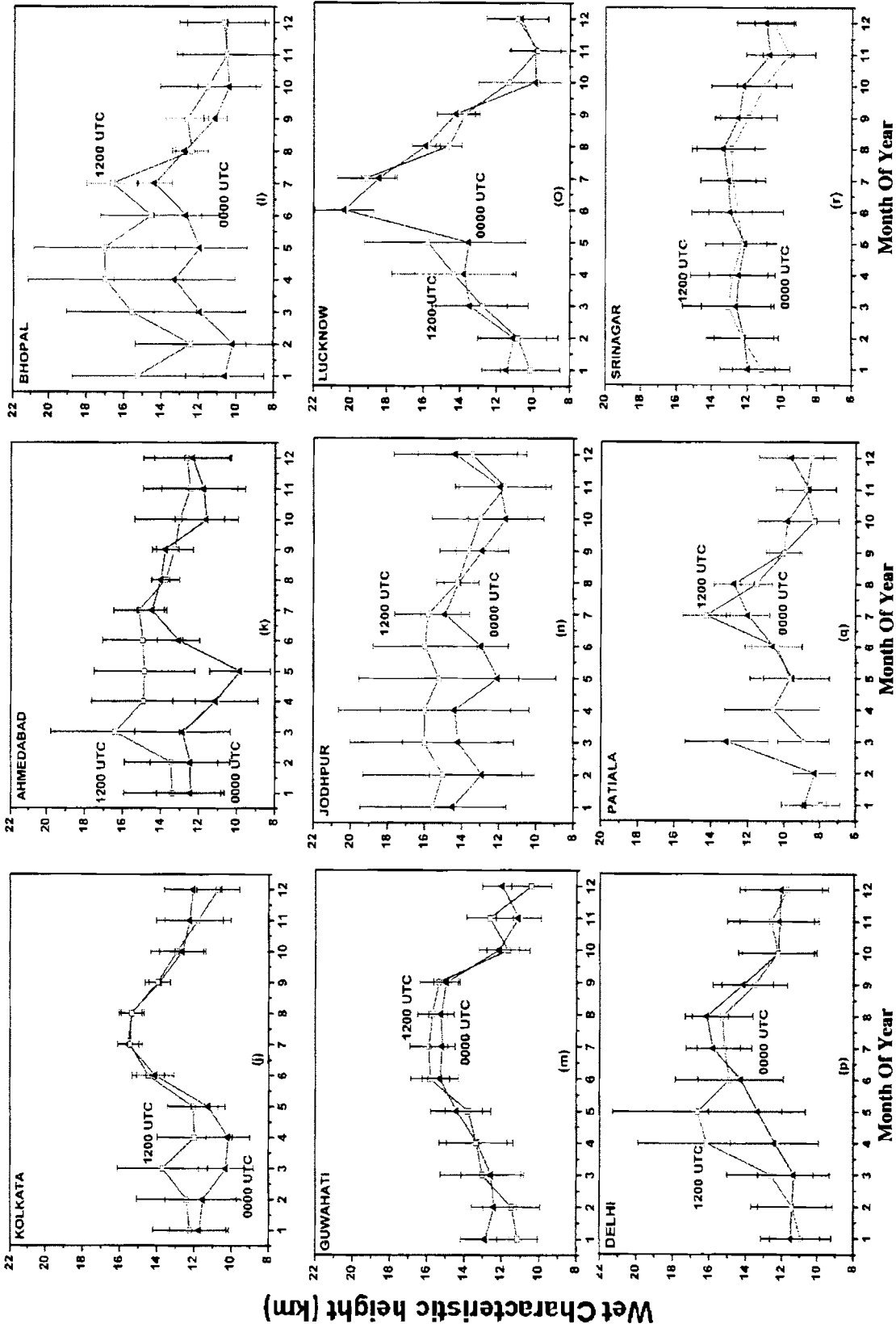


Figure 3.4(j-r): Month-to-month variation of h_w for Kolkata, Ahmedabad, Bhopal, Guwahati, Jodhpur, Lucknow, Delhi, Patiala, and Srinagar. continuous lines with solid triangle represent the variations for 00:00 UTC and the same with open square for 12:00 UTC

3.2.1 Dependence of h_D and h_W on Surface Temperature

The morning to evening difference in characteristic heights could be attributed mainly to the corresponding changes in the atmospheric temperature. While this dependence is distinctly observable for h_D , the dependence is rather weak for h_W . Then it would be possible to generate an empirical relation for h_D in terms of surface temperature which will be useful for the application even on a day-to-day basis. Though a systematic morning to evening difference is not observable for h_W , it would be convenient to treat this also analogous to h_D keeping in mind that eq. (3.5) was also proposed on these lines. The only additional input required in this case would be the value of surface temperature. Once the necessary inputs for the model *viz.* surface pressure, water vapor partial pressure and surface temperature are fed, the parameters N_{SD} , N_{SW} , h_D , and h_W can directly be generated using the appropriate relationships. With this motivation empirical models for h_D and h_W are developed based on linear regression. Figure 3.5 shows a scatter plot depicting the temperature dependence of h_D for different RIM stations along with the best fit line obtained through the regression analysis in the following form

$$h_D = h_{D0} + g_D T_S \quad (3.8)$$

The values of h_{D0} and g_D for all the 18 stations are presented in Table 3.4. The values of h_{D0} are around 40 km and are fairly constant for all the stations. The values of g_D , the temperature gradient of h_D is around 0.14 for all these stations.

Following a similar procedure, the empirical relation connecting h_W with T_S is established based on the observed dependencies as depicted in Figure 3.6. As can be seen from this figure, the scatter of points is relatively large, and the correlation of h_W with T_S is inferior. This could be attributed to the fact that water vapor is not well mixed in the atmosphere and its altitude variation is not exactly similar to that of the other major gas-constituents in the atmosphere, notwithstanding the fact that higher atmospheric temperature is conducive even for holding more water vapor and extending the profile to higher altitude. Large-scale advection of water vapor during the monsoon period is another factor responsible for the observed low correlation between h_W and T_S .

Note that, in developing a quartic model for N_W , no theoretical justification was provided by Hopfield for adopting such a relationship. It was just adapted analogous to that for hydrostatic component mainly for the convenience in modeling. Keeping these factors

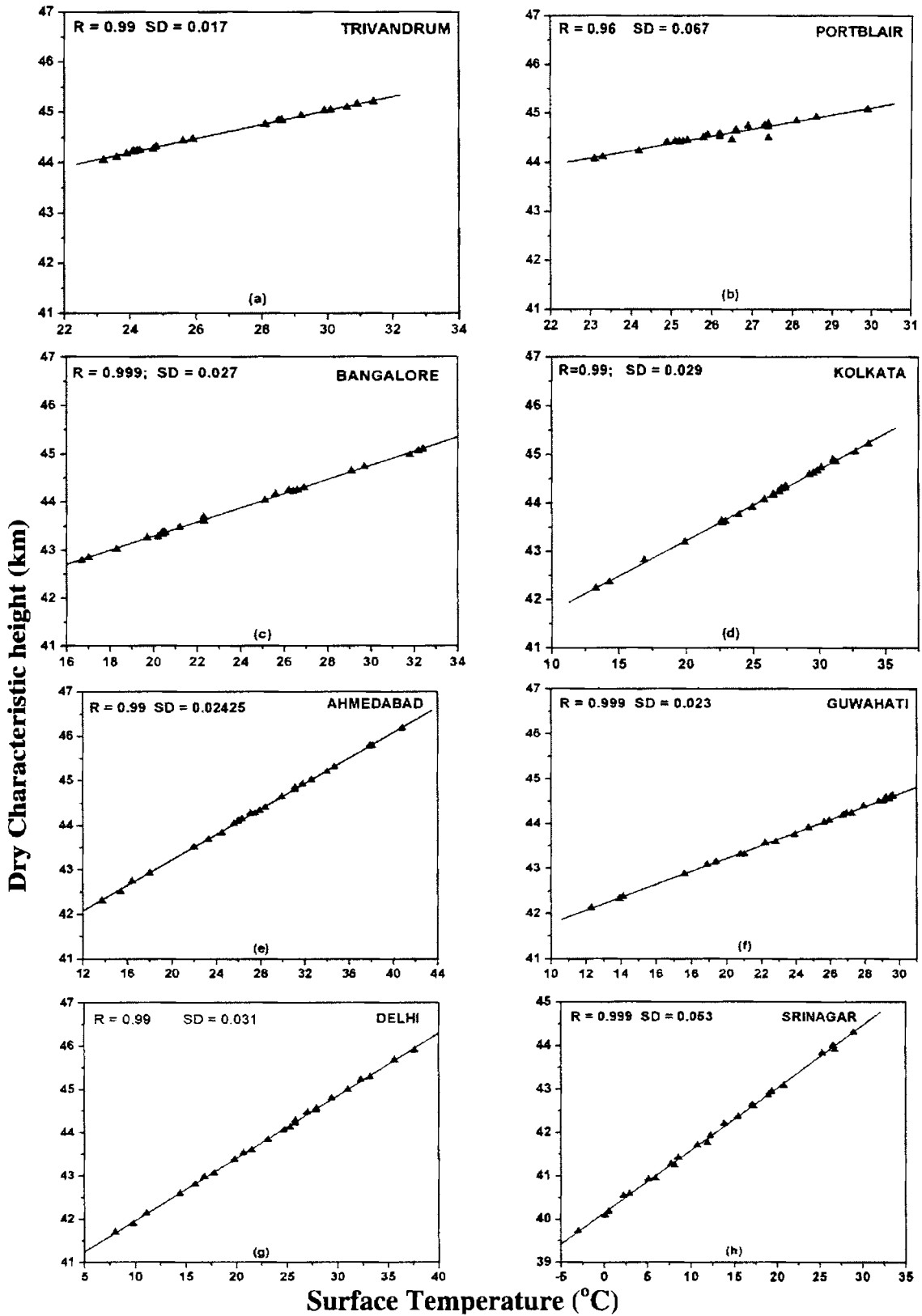


Figure 3.5: Scatter plots along with best-fit regression line showing the surface temperature dependence of dry characteristic height (h_D)

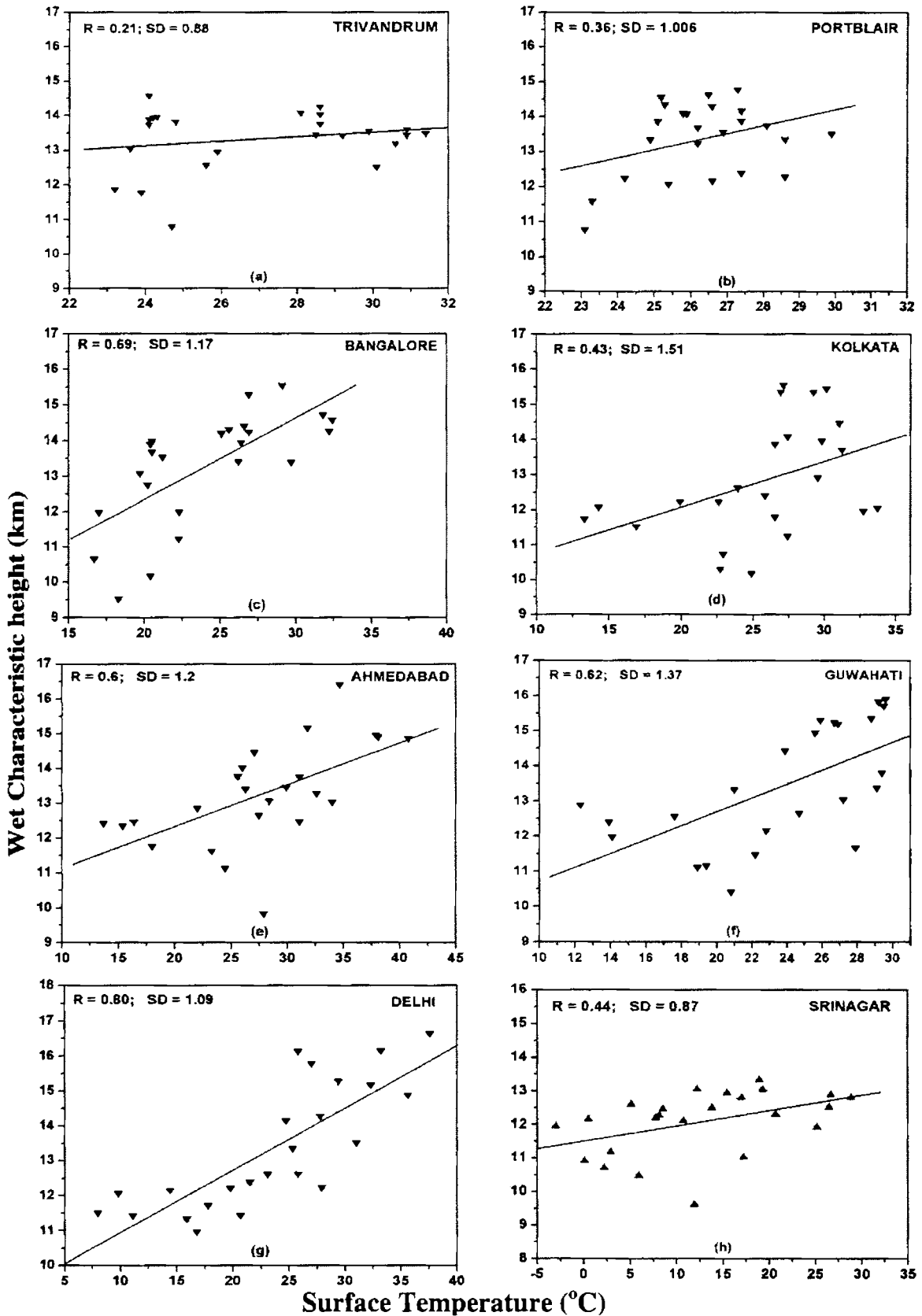


Figure 3.6: Scatter plots along with best-fit regression line showing the surface temperature dependence of wet characteristic height (h_w)

Table 3.4: Empirical Relations Representing the Temperature Dependencies for the Dry and Wet Characteristic Height Parameters (h_D and h_W) for Different Stations

Station Name	Model for h_D $h_D = h_{D0} + g_D T_S$		Model for h_W $h_W = h_{W0} + g_W T_S$	
	h_{D0} (km)	g_D	h_{W0} (km)	g_W
Trivandrum	40.86 (0.03)	0.140 (0.001)	11.58 (1.75)	0.065 (0.064)
Portblair	40.74 (0.02)	0.146 (0.008)	7.355 (3.46)	0.229 (0.13)
Bangalore	40.37 (0.03)	0.146 (0.001)	7.746 (1.25)	0.230 (0.051)
Mangalore	40.46 (0.05)	0.141 (0.002)	14.42 (2.18)	0.063 (0.080)
Chennai	40.28 (0.04)	0.146 (0.001)	7.583 (2.84)	0.180 (0.101)
Goa	40.33 (0.11)	0.145 (0.004)	10.23 (3.03)	0.068 (0.111)
Hyderabad	39.36 (0.02)	0.141 (6e-4)	7.792 (1.07)	0.311 (0.039)
Vishakhapatnam	39.83 (0.06)	0.151 (0.002)	9.737 (3.42)	0.092 (0.125)
Mumbai	40.23 (0.17)	0.148 (0.006)	8.642 (3.17)	0.152 (0.115)
Kolkata	40.28 (0.03)	0.147 (0.001)	9.457 (1.53)	0.131 (0.058)
Ahmedabad	40.36 (0.02)	0.143 (7e-4)	9.923 (1.00)	0.120 (0.035)
Bhopal	37.92 (0.03)	0.144 (0.001)	6.978 (1.15)	0.233 (0.044)
Guwahati	40.34 (0.02)	0.144 (9e-4)	8.730 (1.29)	0.198 (0.050)
Jodhpur	39.59 (0.49)	0.121 (0.018)	12.10 (0.94)	0.072 (0.033)
Lucknow	39.75 (0.04)	0.146 (0.001)	7.371 (1.82)	0.244 (0.072)
Delhi	40.52 (0.02)	0.144 (8e-4)	9.150 (0.7)	0.178 (0.028)
Patiala	38.41 (0.06)	0.140 (0.002)	8.312 (1.05)	0.076 (0.042)
Srinagar	40.14 (0.02)	0.144 (0.001)	11.50 (0.306)	0.046 (0.020)

into account in order to facilitate the modeling, an empirical relation is established for the variations of h_W with T_S similarly that for h_D as,

$$h_W = h_{W0} + g_W T_S \quad (3.9)$$

The coefficients estimated through linear regression for each station relating h_W to T_S is included in Table 3.4. While for the dry characteristic height the value of intercept (h_{D0}) is fairly constant for all the stations (about 40.5 ± 0.24 km) with a mean slope of 0.144 ± 0.002 km $^{\circ}$ C, for wet characteristic height the mean intercept (h_{W0}) is about 9.43 km with a slope of 0.14 km $^{\circ}$ C. The variability of the intercept and slope in the case of h_W for different stations is large compared to that of h_D . However, this is not a major constraint because even with these limitations the above relationship can provide fairly good prediction of h_W . These models for different stations are referred to as “**Site-specific Hopfield model**” in further discussions.

Both the Site-Specific Surface model and Hopfield model estimate the zenith tropospheric delay in terms of surface meteorological parameters. The essential difference between these two models is that while the former provides this in terms of surface

hydrostatic pressure and water vapor partial pressure, the latter includes the effect of surface temperature also.

3.3 A Unified Model for the Indian Subcontinent

3.3.1 Unified Surface Model

A close examination of empirical relations derived based on the surface model and Hopfield model for the individual stations show that the variability of the coefficients connecting the range error with meteorological parameters is rather small. This prompted development of a Unified Model (each for surface model and Hopfield model) applicable for all these stations which hence will be applicable for the entire region encompassing these stations. Though such unified models could be inferior to the site-specific models, its potential increases because of the fact that one simple equation will be sufficient for the entire region. Following the same methodology adopted for individual stations, the relation between surface meteorological parameters and dry component of range error is sought by pooling together the data from all the eighteen stations. Figure 3.7a shows the scatter plot of surface pressure with zenith dry range error, considering all the stations. A simple linear relation is established based on linear regression (keeping zero intercept) and the slope is estimated. This yields a simple linear relation termed as the “**Unified Surface model**” as in the form

$$\text{ZHD} = (0.00228 \pm 2.25 \times 10^{-6}) \times P_S \quad (3.10)$$

with a correlation coefficient of 0.97. In eq. (3.10) P_S is expressed in hPa and ZHD is obtained in meters. Following a similar approach, a linear relation connecting ZWD and e_S also is established for the whole subcontinent. A scatter plot of ZWD, with the corresponding values of e_S is shown in Figure 3.7b. The linear relation of the form

$$\text{ZWD} = A_0 + A_1 \times e_S \quad (3.11)$$

is established between the two through regression analysis and evaluated the coefficients A_0 and A_1 . The values of A_0 and A_1 are, respectively, -0.01978 ± 0.0057 m and $0.01288 \pm 2.4 \times 10^{-4}$ m hPa⁻¹. As can be seen from Figure 3.7b, when e_S is very large (>30 hPa) the range error estimated through the relation (shown by thin straight line) is consistently lower than the true range error obtained from ray-tracing (marked points). Similarly a higher altitude station like Srinagar has lower values of e_S compared to near sea-level stations

(Trivandrum and Portblair). In order to distinguish the values corresponding to Srinagar, these are plotted in Figure 3.7b with a different symbol (∇).

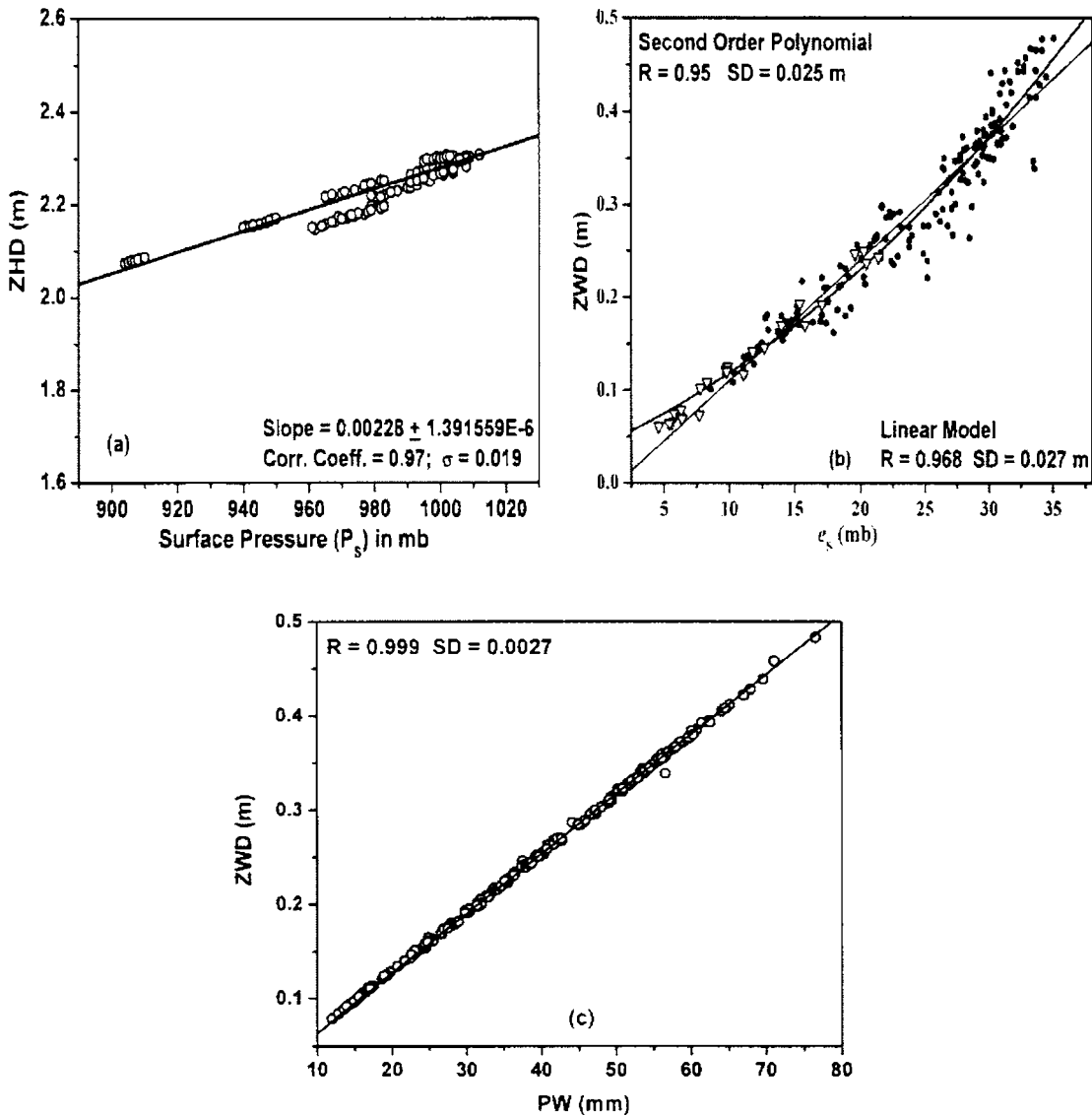


Figure 3.7: Regression analysis showing the dependence of dry and wet components of tropospheric zenith range on relevant surface atmospheric parameters considering all the eighteen stations together for generating a unified model: Variation of dry range error with surface pressure (a), Variation of wet range error with surface water vapor partial pressure (b) and variation of wet range error with columnar (precipitable) water vapor (c)

A careful examination of Figure 3.7b shows that the points in this scatter plot are more aligned to a non-linear increase of ZWD with e_s . Considering this aspect the applicability of a second order polynomial is examined to relate ZWD with e_s , which yielded a relationship of the form

$$\text{ZWD} = (0.0391 \pm 0.013) + (0.00636 \pm 0.001) \times e_s + (1.58 \times 10^{-4} \pm 3.75 \times 10^{-5}) \times e_s^2 \quad (3.12)$$

The nonlinear variation of ZWD by this relationship is shown in Figure 3.7b with the thick line.

3.3.2 Unified Model in terms of Precipitable Water Vapor

As seen in Section 3.1, a linear model relating PW with ZWD will be more appropriate for predicting ZWD than similar models based on surface values of water vapor partial pressure, or water vapor density at surface, as far as individual stations are concerned. However, it should be noted in this context that it will not be possible to get values of PW at any location whenever prediction of ZWD is required. On the contrary it will be easier to get values of e_s or ρ_s from many places at almost all the time. Hence from the application point of view such models (relating ZWD with e_s or ρ_s) will be more useful even though the error associated with them will be comparatively larger. One of the ways for estimating PW is by using a sun-photometer working on the principle of differential attenuation (of water vapor and other atmospheric species at two optical wavelengths). This instrument operates only during day time under clear sky conditions and requires regular calibration. Ground based microwave radiometer, which can work in all weather condition (except heavy precipitation) though is another potential instrument for measuring PW, is very expensive. The estimation of PW from radiosonde is not only expensive (recurring expenditure when ever launched) but also has a poor temporal and spatial resolution (considering the time taken for each sounding and the balloon drift). The satellite based microwave radiometers though are very useful over the oceanic regions they will not be available quite frequently. A GPS network could be a good source of PW especially over the land (not too expensive). This can be operated in all weather conditions with a very good temporal resolution and does not require any calibration. In this case, a Unified Model to estimate ZWD from PW will be useful.

Figure 3.7c shows a scatter plot of PW with true zenith wet delay (estimated from refractivity profiles derived from radiosonde) clubbing all the eighteen stations. A linear model was developed based on the regression analysis, which yielded a relationship of the form

$$\text{ZWD} = (0.0064 \pm 4.4 \times 10^{-6}) \times \text{PW} \quad (3.13)$$

with correlation coefficient close to unity. As can be seen directly from Figure 3.7c, this model is significantly superior to the other three models. The mean absolute difference for different stations is presented in the last column of Table 3.7 along with the corresponding standard deviation. A similar model was also used by *Bevis et al.* [1992] for deriving ZWD from ground based GPS measurements. In his global model, *Bevis et al.* [1992] evolved a value of 0.00666 as the ratio of ZWD/PW which varies as much as 20% with location, season and weather condition [*Bevis et al.*, 1994].

3.3.3 Unified Hopfield Model (Characteristic Height Parameters)

Following a very similar approach a unified empirical model is developed for zenith tropospheric delay based on the Hopfield method. This essentially involves deriving a unified model for dry and wet characteristic height parameters in terms of T_S by grouping the data from all the eighteen stations. The temperature dependence of h_D and h_W are established incorporating the data from all the 18 stations by linear regression which is of the form

$$h_D = (40.209 \pm 0.045) + (0.154 \pm 0.002) \times T_S \quad (3.14a)$$

$$h_W = (10.474 \pm 0.29) + (0.111 \pm 0.01) \times T_S \quad (3.14b)$$

A typical scatter plot of h_D (in km) with T_S (in °C) and h_W (in km) and T_S (in °C) obtained by combining all the stations is presented in Figure 3.8a and Figure 3.8b along with the best fitted line represented by eq. 3.14a and eq. 3.14b, respectively. The correlation coefficient for h_D and h_W are 0.98 and 0.56, respectively. Comparing the values of these regression coefficients with those presented in Table 3.4 (site-specific surface model), it can be seen that the present value of slope is slightly larger than the corresponding values in Table 3.4 while the value of the intercept is slightly small.

3.4 Validation of Surface Models

3.4.1 Validation of Site-Specific Models by Comparing with Ray-Traced Values

The site-specific models are validated by comparing the model predictions with the true range errors for the respective station obtained through ray tracing employing the altitude profiles of refractivity. Sufficient care is taken to ensure that the daily

meteorological data have water vapor profile extending up to or beyond 10 km altitude, and the temperature and pressure profiles extending up to at least 25 km. The comparison is quantified by estimating the absolute difference between true and model predicted zenith delays, a summary of which is presented in Table 3.5. The data for RIM stations are highlighted with bold face. The mean of the absolute differences are presented along with the standard deviations. While the mean value indicates the average deviation of the model, the standard deviation indicates the amount of variability. The accuracy of surface model based on P_S is comparable to that of the Hopfield model in predicting ZHD. The mean deviation is lowest for Trivandrum and highest for Jodhpur.

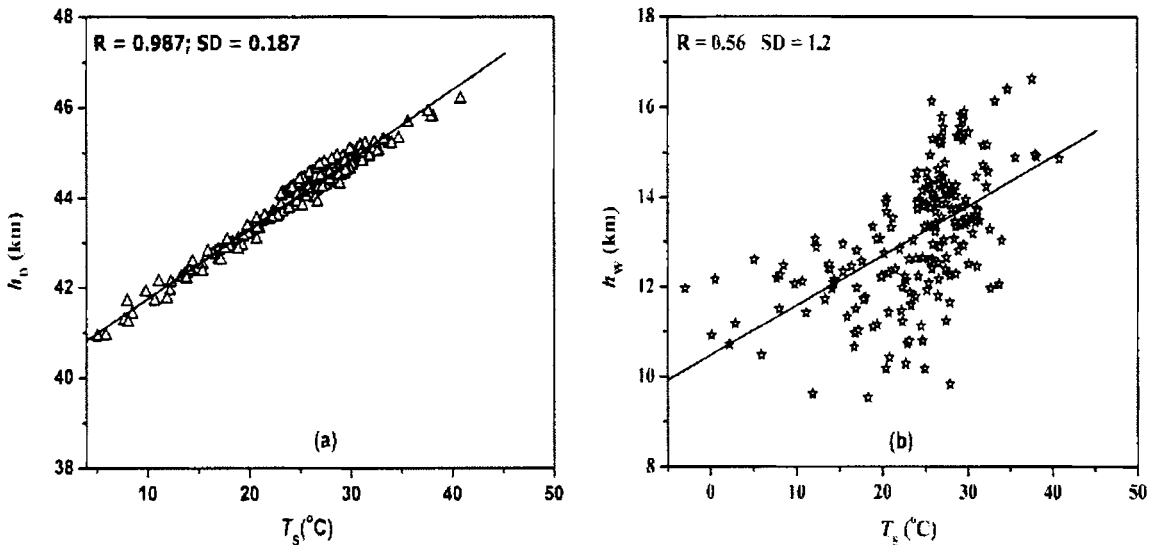


Figure 3.8: Regression analysis showing the dependence of dry (h_D) and wet (h_W) characteristic heights on surface temperature (T_S) considering all the eighteen stations together

The deviation of Site-Specific models, in case of ZWD, based on e_S and T_S is about 5-6 cm for most of the stations. For a few stations like Vishakhapatnam, Mumbai, Jodhpur and Lucknow the deviation is > 6 cm. Srinagar (being high altitude station) shows minimum mean absolute difference about ~ 2 cm for ZWD. Among all the RIM stations considered, Kolkata shows maximum deviation of ~ 6 cm. The best estimate of wet delay comes from model based on Precipitable Water vapor. The mean absolute difference for this model is ~ 0.3 cm except at Patiala and Lucknow. By combining the surface models based on P_S and the wet range error model based on PW, the best estimate of ZTD (with an error < 6 cm) can be achieved for almost all the stations. As an alternative (when PW is not

available) the surface models based on e_s or Hopfield model based on e_s and T_s (which are more easily available) could be considered, even though the involved accuracies are rather inferior. Note that, the accuracy achieved by these models also meets basic requirement of satellite based navigation system discussed in Chapter 1.

Table 3.5: Mean Absolute Difference and the standard deviation of Site-specific Models (from true zenith range error) for Different Stations (RIM stations in Bold), for the Hydrostatic and Non-hydrostatic Components

Station	Hydrostatic delay (ZHD)		Non-hydrostatic delay (ZWD)		
	Mean abs. Diff (cm)		Mean abs. Diff (cm)		
	Surface model based on P_s	Hopfield model	Surface model based on e_s	Hopfield model	Surface model based on PW
Trivandrum	0.17 (0.1)	0.15 (0.1)	5.2 (3.7)	5.1 (3.6)	0.17 (0.1)
Portblair	0.36 (0.3)	0.49 (0.4)	4.5 (3.5)	4.6 (3.6)	0.16 (0.1)
Bangalore	0.45 (0.2)	0.2 (0.2)	4.0 (3.0)	4.2 (3.0)	0.16 (0.1)
Mangalore	2.3 (1.9)	2.5 (2.5)	4.9 (3.6)	6.3 (4.3)	0.64 (0.3)
Chennai	4.5 (2.7)	4.4 (2.7)	6.1 (4.5)	5.9 (4.4)	0.6 (0.3)
Goa	2.4 (0.5)	1.5 (0.5)	5.4 (3.5)	5.7 (3.9)	0.5 (0.23)
Hyderabad	3.7 (2.0)	3.5 (2.0)	6.7 (4.6)	6.1 (4.4)	0.4 (0.26)
Vishakhapatnam	3.5 (2.6)	3.6 (2.7)	7.6 (6.3)	7.5 (6.2)	0.3 (0.2)
Mumbai	3.18 (2.8)	3.12 (2.7)	6.9 (4.3)	7.5 (4.5)	0.51 (0.27)
Kolkata	0.35 (0.2)	0.32 (0.3)	6.0 (4.2)	6.4 (4.3)	0.21 (0.1)
Ahmedabad	0.34 (0.3)	0.33 (0.2)	5.2 (4.0)	5.3 (4.0)	0.24 (0.2)
Bhopal	1.25 (1.2)	1.35 (1.25)	6.5 (5.1)	5.8 (4.6)	0.66 (0.3)
Guwahati	0.24 (0.2)	0.25 (0.2)	4.4 (3.3)	5.0 (3.6)	0.20 (0.1)
Jodhpur	11.2 (6.2)	10.0 (5.5)	9.5 (8.1)	9.4 (8.1)	0.4 (0.3)
Lucknow	5.7 (5.7)	5.7 (5.8)	8.8 (12.9)	8.6 (12.7)	1.1 (1.3)
Delhi	0.27 (0.2)	0.27 (0.2)	4.0 (3.0)	4.5 (3.6)	0.20 (0.2)
Patiala	2.7 (2.3)	3.4 (2.6)	4.1 (3.0)	5.6 (3.8)	2.0 (0.4)
Srinagar	1.80 (1.7)	1.09 (1.8)	2.0 (2.0)	1.9 (1.6)	0.19 (0.1)

3.4.2 Validation of Unified Models using Ray-Tracing

The accuracy of unified model is also examined by comparing the estimated delays with those obtained by ray tracing as well as with other global models based on surface parameters [Saastamoinen, 1972; Hopfield, 1971; Ifadis, 1986; Mendes and Langley, 1998]. The mean of the absolute difference of the deviations for each station is presented in Table 3.6. These values are larger than those for site-specific surface models presented in Table 3.5, especially for Trivandrum and Ahmedabad. For the case of ZWD, the comparison of

Table 3.6: Mean Absolute Difference and the standard deviation of Unified Model and Global Model from True Zenith Range Error for Different Stations, for the Hydrostatic Component

Station Code	Hydrostatic delay		
	Mean abs. Diff (cm)		
	SAAS (1972) P_s	Surface Model P_s	Hopfield model
Trivandrum	2.66 (0.2)	1.01 (0.2)	1.24 (0.27)
Portblair	2.57 (0.4)	0.94 (0.4)	1.10 (0.40)
Bangalore	1.03 (0.3)	0.45 (0.2)	0.30 (0.20)
Mangalore	2.33 (2.13)	2.29 (1.88)	2.87 (2.66)
Chennai	4.09 (2.5)	3.84 (2.35)	5.15 (2.83)
Goa	2.10 (0.47)	2.40 (0.47)	1.00 (0.43)
Hyderabad	2.28 (2.45)	2.23 (2.25)	3.08 (2.75)
Vishakhapatnam	4.70 (2.80)	4.33 (2.75)	5.90 (2.84)
Mumbai	2.86 (2.50)	2.79 (2.26)	3.39 (3.15)
Kolkata	0.84 (0.4)	0.97 (0.4)	0.80 (0.4)
Ahmedabad	0.70 (0.4)	1.10 (0.4)	0.99 (0.5)
Bhopal	12.10 (1.73)	11.70 (1.73)	13.25 (1.71)
Guwahati	0.85 (0.6)	0.79 (0.5)	0.93 (0.8)
Jodhpur	16.02 (6.68)	15.66 (6.66)	17.25 (6.83)
Lucknow	7.40 (6.26)	7.08 (6.19)	8.45 (6.45)
Delhi	1.90 (0.3)	0.28 (0.2)	0.47 (0.25)
Patiala	7.76 (3.11)	7.44 (3.03)	8.81 (3.40)
Srinagar	2.40 (2.6)	3.20 (2.0)	2.90 (2.0)
All stations together	2.90 (3.60)	2.90 (3.4)	2.98 (4.15)

both linear (eq. 3.11) and second order (eq. 3.12) models are presented in Table 3.7. In case of ZWD the deviation of unified model is comparable to that of Site-Specific model. Among different models suggested for ZWD, the second order polynomial Unified model yields a better prediction. Considering all the eighteen stations together the mean of the absolute difference for SAAS and Unified model from the true value is ~ 2.9 cm. In the case of wet delay, the Unified models developed in the present analysis are much superior to the currently available models [Ifadis, 1986 and Mendes and Langley, 1998]. The mean absolute difference of the Unified model based on e_s varies from about 4 cm to 9 cm whereas that in case of other two global models is in the range 5 cm to 15 cm. This study indicates the region specific models (for tropics) are superior to the available global models developed

Table 3.7: Mean Absolute Difference and the standard deviation of Unified Models and Global Models from True Zenith Range Error for Different Stations, for the Non-hydrostatic Component

Non-hydrostatic delay						
Mean abs. Diff (cm)						
	Mendes (1997)	Ifadis (1986)	Surface Model - e_s	2 nd order Model - e_s	Hopfield Model	Surface Model - PW
Trivandrum	8.15 (4.7)	9.18 (4.8)	5.1 (3.6)	4.8 (3.7)	4.98 (3.5)	0.17 (0.17)
Portblair	7.51 (5.2)	8.49 (5.3)	4.5 (3.5)	4.4 (3.5)	4.40 (3.3)	0.16 (0.13)
Bangalore	8.12 (3.8)	8.08 (3.8)	4.3 (2.9)	4.9 (2.8)	4.20 (2.8)	0.57 (0.21)
Mangalore	7.97 (4.62)	9.08 (4.82)	4.2 (3.4)	4.12 (3.27)	5.25 (3.93)	0.37 (0.23)
Chennai	8.70 (5.14)	9.98 (5.40)	5.4 (4.0)	5.20 (3.88)	4.35 (3.25)	0.26 (0.20)
Goa	7.27 (4.84)	8.18 (5.46)	4.9 (3.0)	4.76 (2.86)	4.86 (2.67)	0.22 (0.17)
Hyderabad	15.53 (5.90)	16.24 (5.91)	11.3 (5.6)	10.92 (5.53)	11.11 (5.55)	0.52 (0.29)
Vishakhapatnam	8.96 (6.98)	9.81 (7.41)	7.2 (5.6)	6.92 (5.47)	6.90 (5.44)	0.26 (0.20)
Mumbai	10.81 (5.38)	12.07 (5.77)	6.0 (3.9)	5.45 (3.83)	6.20 (3.99)	0.18 (0.13)
Kolkata	11.21 (5.9)	12.44 (6.2)	5.9 (4.1)	5.06 (4.0)	5.70 (4.0)	5.70 (4.0)
Ahmedabad	7.62 (5.6)	8.58 (5.8)	4.8 (3.7)	4.8 (3.9)	5.00 (3.9)	5.00 (3.9)
Bhopal	7.54 (6.71)	8.07 (6.91)	6.18 (4.5)	6.14 (4.47)	6.03 (4.58)	6.03 (4.58)
Guwahati	11.87 (5.7)	12.92 (5.9)	6.1 (4.1)	4.3 (3.7)	5.90 (4.0)	5.90 (4.0)
Jodhpur	14.32 (8.45)	15.51 (8.63)	9.8 (8.3)	9.73 (8.50)	9.97 (8.06)	9.97 (8.06)
Lucknow	14.08 (13.33)	15.26 (13.53)	9.28 (14.2)	9.27 (13.08)	9.54 (13.00)	9.54 (13.00)
Delhi	9.18 (6.7)	9.96 (6.9)	5.0 (3.9)	4.0 (3.1)	4.90 (3.9)	4.90 (3.9)
Patiala	4.43 (3.29)	5.13 (3.50)	7.35 (4.7)	5.88 (4.06)	5.23 (3.75)	5.23 (3.75)
Srinagar	5.49 (3.8)	4.78 (3.8)	2.0 (1.9)	2.1 (1.8)	1.97 (1.8)	1.97 (1.8)
All stations together	9.89 (6.64)	10.85 (6.86)	4.75 (3.74)	5.81 (5.43)	6.10 (5.33)	6.10 (5.33)

mainly based on the meteorological data from mid and high latitude regions. All the models for ZHD show poor performance for the stations Bhopal, Jodhpur, Lucknow and Patiala could be due to poor radiosonde data quality at these stations. Excluding these, the mean absolute difference for ZHD estimated using Surface model (~ 2.1 cm) is less than the other two models (~ 2.5 cm).

3.5 Variability in Zenith Tropospheric Delay and its Deviation from Model Derived Values for Different Stations

The dry and wet component of the tropospheric zenith delay shows a rather systematic annual variation, though the amplitude and phase show a variation with latitude. It would be interesting in this context to examine the distribution of these delays on a day-to-day basis for a period of one year to assess the extent of variability. Values of ZHD, ZWD and ZTD (estimated through ray tracing) on different days are grouped at small intervals and the percentage of occurrence of each group is estimated. Similarly, in order to examine the model accuracies, the deviation of model predicted values of ZHD, ZWD and ZTD from the true values estimated as above are also estimated for different days in a year and the frequency distribution of these deviations are also examined. Figure 3.8 shows the distribution of true ZHD obtained through ray-tracing and ΔZHD (true value of ZHD – ZHD derived from Unified model). Figure 3.8a and Figure 3.8b shows the plots of these distributions for different stations. Similarly Figure 3.9a and Figure 3.9b shows the distribution of ZWD and ΔZWD for these stations, while Figure 3.10a and Figure 3.10b shows the respective distributions of ZTD and ΔZTD . The distribution of ZHD is more-or-less similar for all these stations except for Srinagar (for which it is truncated in the upper half). The distribution is slightly skewed in its lower half for Bangalore while it is skewed in its upper half for Bhopal. The distribution of model deviation for the ZHD is generally sharp and symmetric for Ahmedabad and station south of it. For station north of it, the distribution peaks at the highest value. The distribution of ZWD is more-or-less symmetric for Bangalore, Portblair and Trivandrum. For other stations the distribution is rather flat indicating that all values are equally probable. For stations like Mangalore, Vishakhapatnam, Mumbai and Delhi, the distribution shows a double hump feature. The distribution of the deviation of model from true value of ZWD is more or less symmetric for

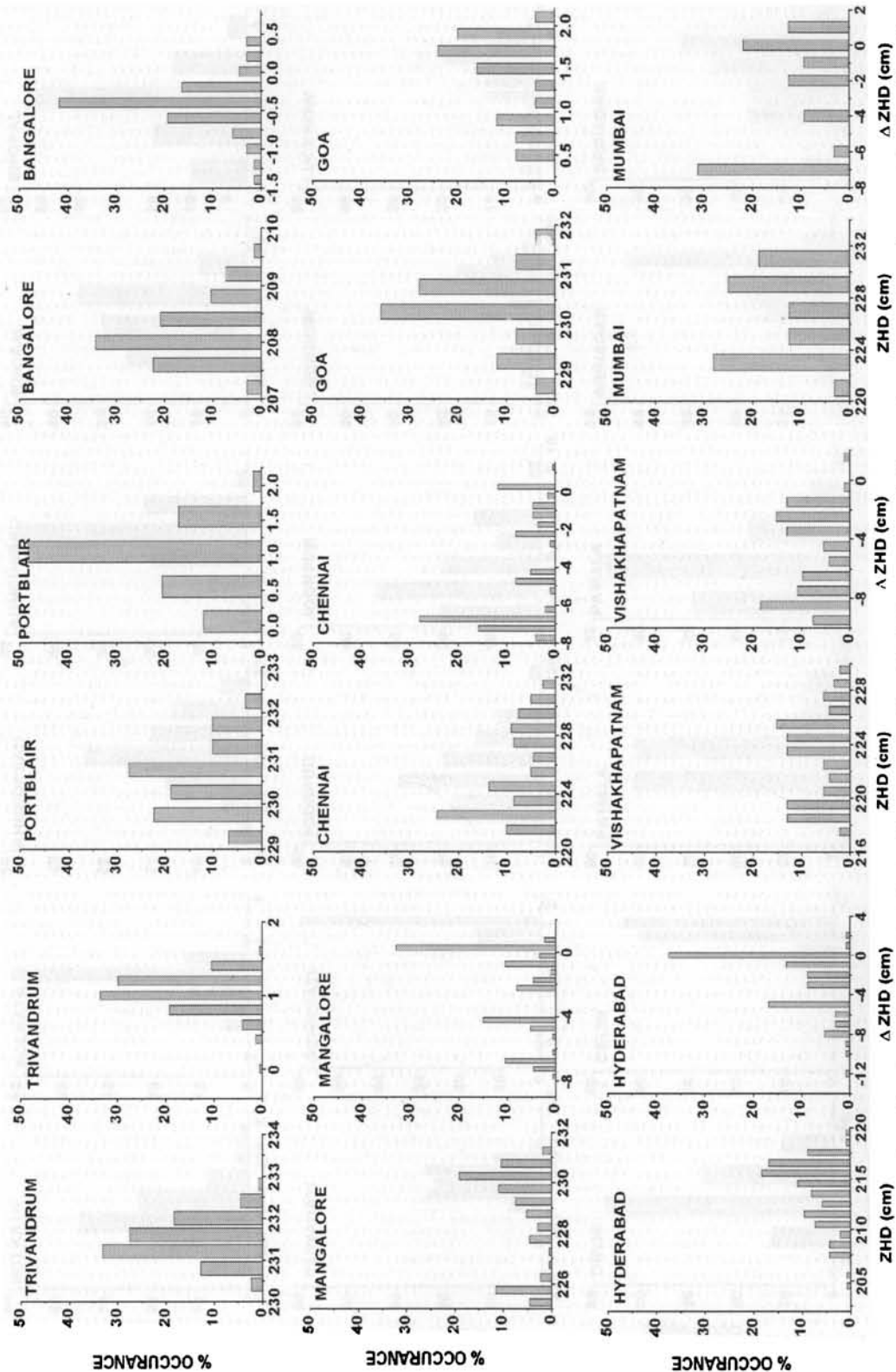


Figure 3.8a: Frequency distribution of true Zenith Hydrostatic Delay (ZHD) estimated through ray-tracing along with the distribution of the model deviations from the true value for Trivandrum, Portblair, Bangalore, Mangalore, Chennai, Goa, Hyderabad, Vishakhapatnam, and Mumbai

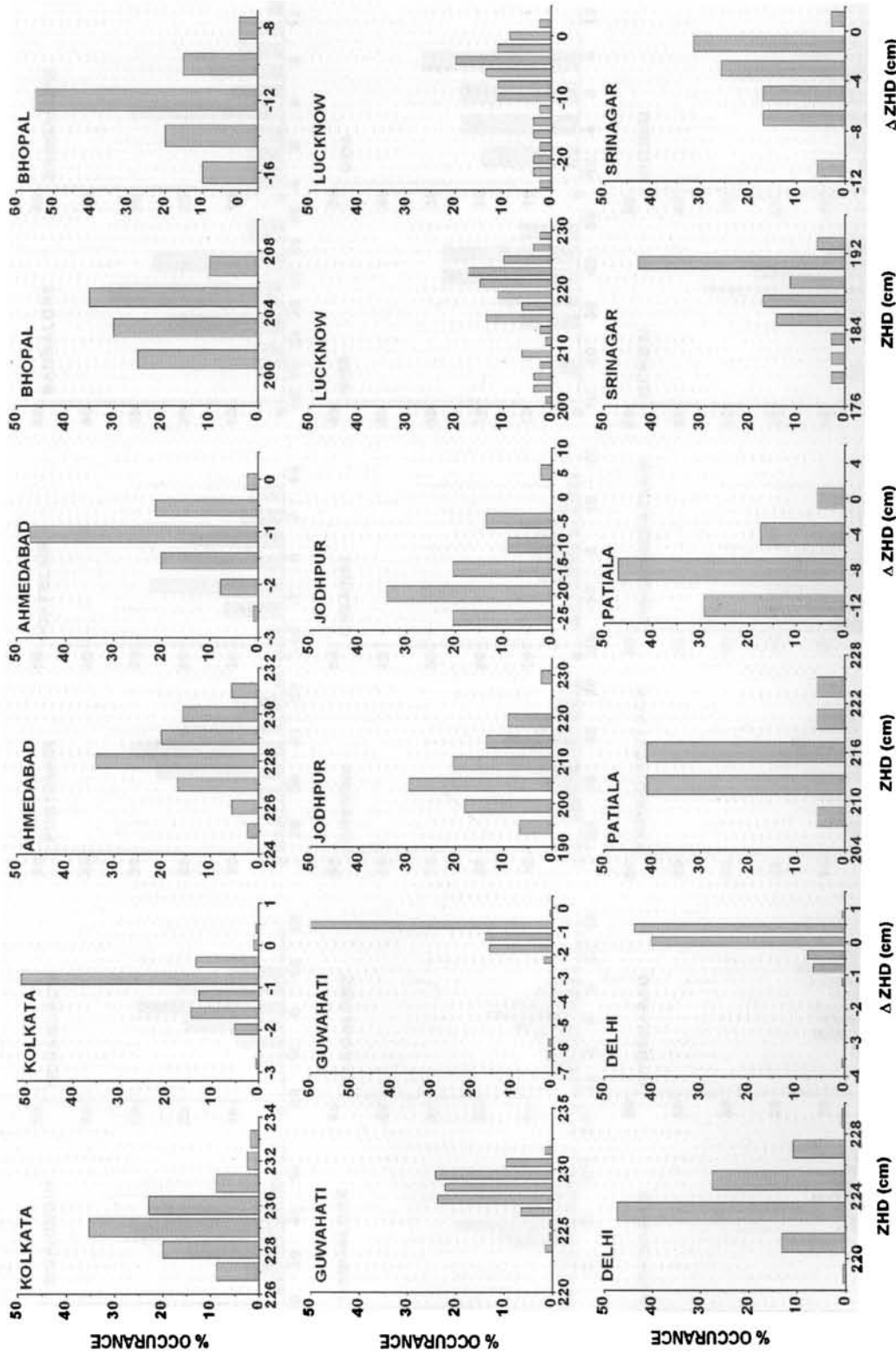


Figure 3.8b: Frequency distribution of true Zenith Hydrostatic Delay (ZHD) estimated through ray-tracing along with the distribution of the model deviations from the true value for Kolkata, Ahmedabad, Bhopal, Guwahati, Jodhpur, Lucknow, Delhi, Patiala, and Srinagar

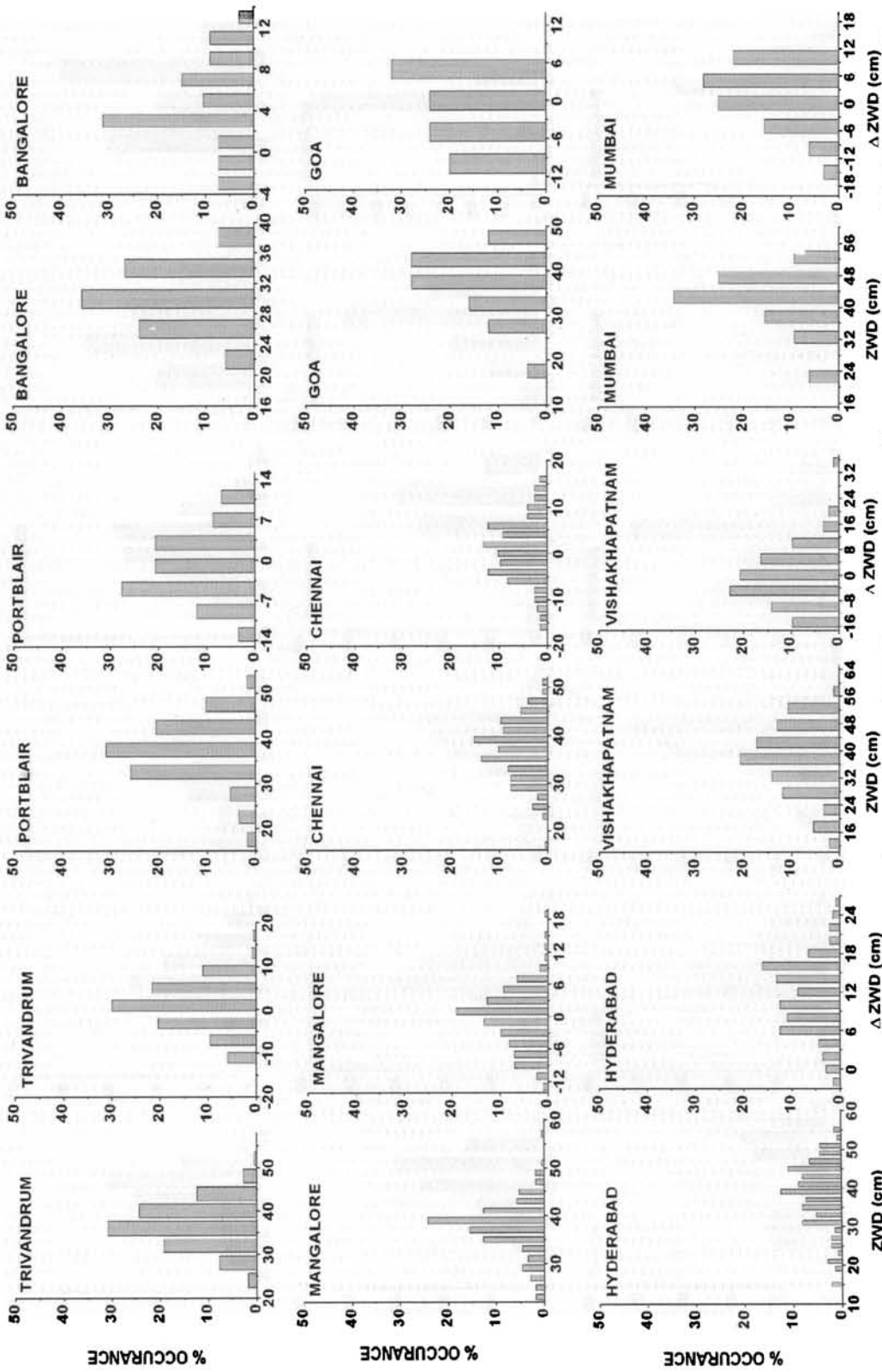


Figure 3.9a: Frequency distribution of true Zenith Wet Delay (ZWD) estimated through ray-tracing along with the distribution of the model deviations from the true value for Trivandrum, Portblair, Bangalore, Mangalore, Chennai, Goa, Hyderabad, Vishakhapatnam, and Mumbai

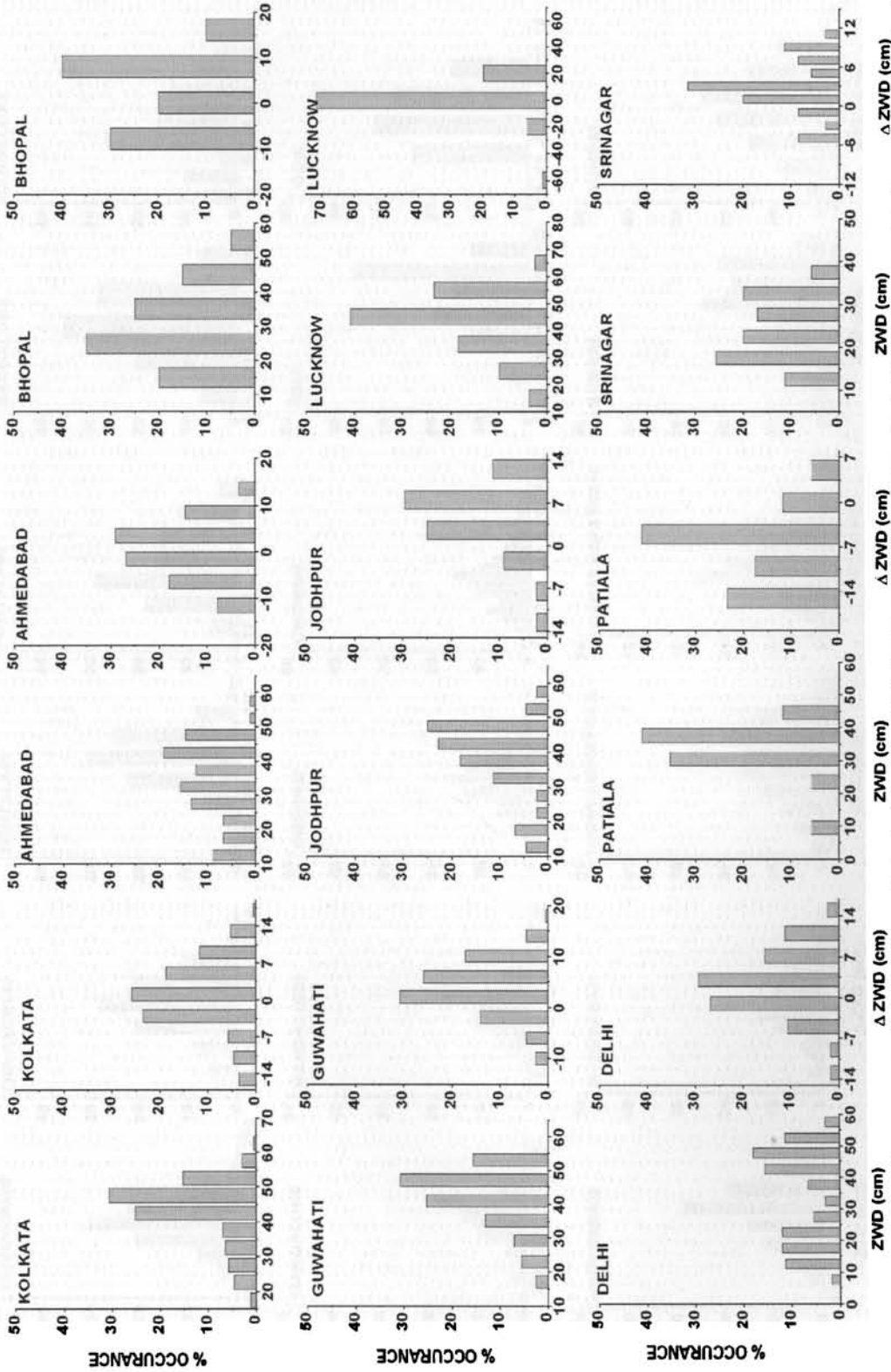


Figure 3.9b: Frequency distribution of true Zenith Wet Delay (ZWD) estimated through ray-tracing along with the distribution of the model deviations from the true value for Kolkata, Ahmedabad, Bhopal, Guwahati, Jodhpur, Lucknow, Delhi, Patiala, and Srinagar

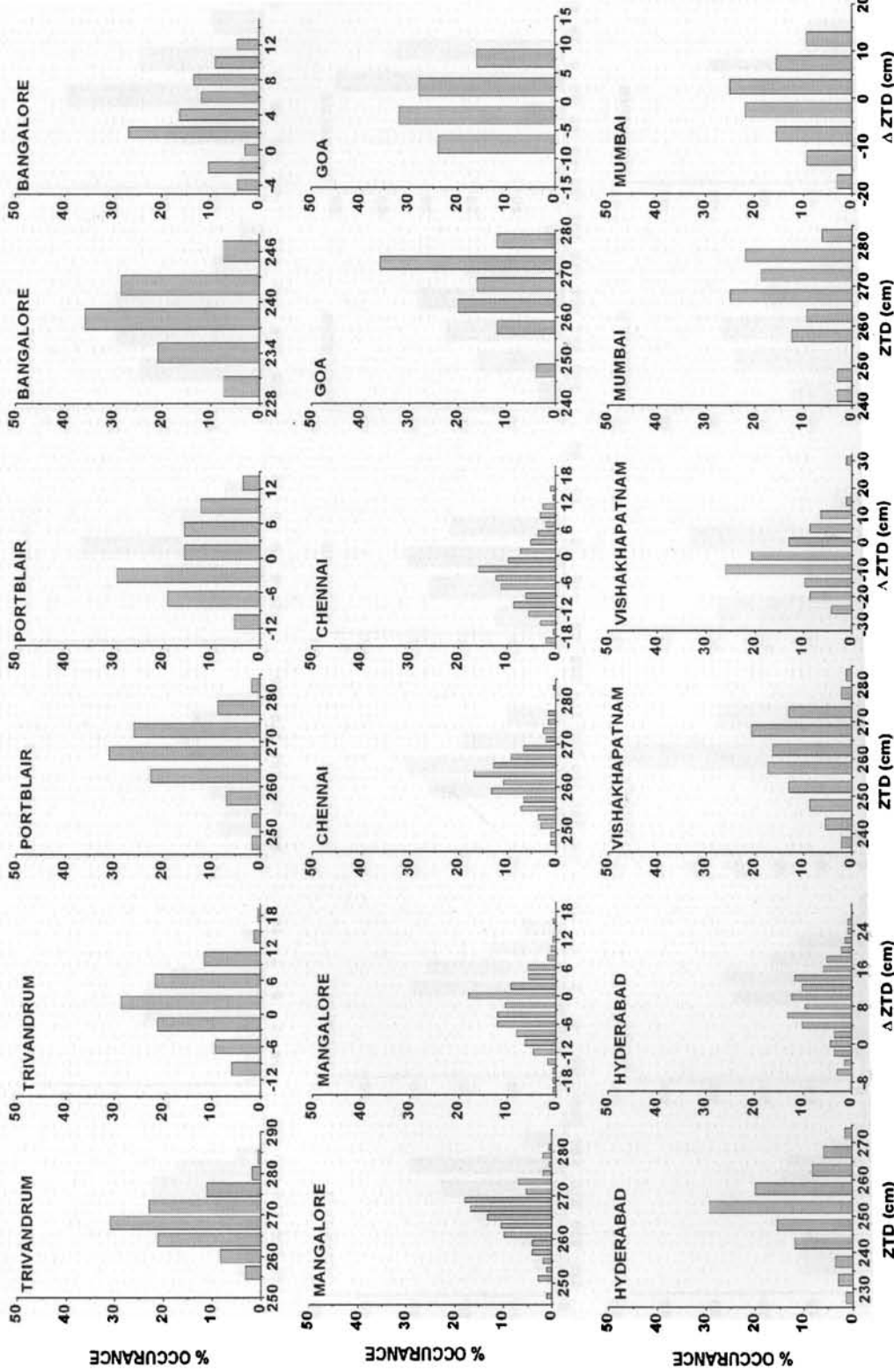


Figure 3.10a: Frequency distribution of true Zenith Tropospheric Delay (ZTD) estimated through ray-tracing along with the distribution of the model deviations from the true value for Trivandrum, Portblair, Bangalore, Mangalore, Chennai, Goa, Hyderabad, Vishakhapatnam, and Mumbai

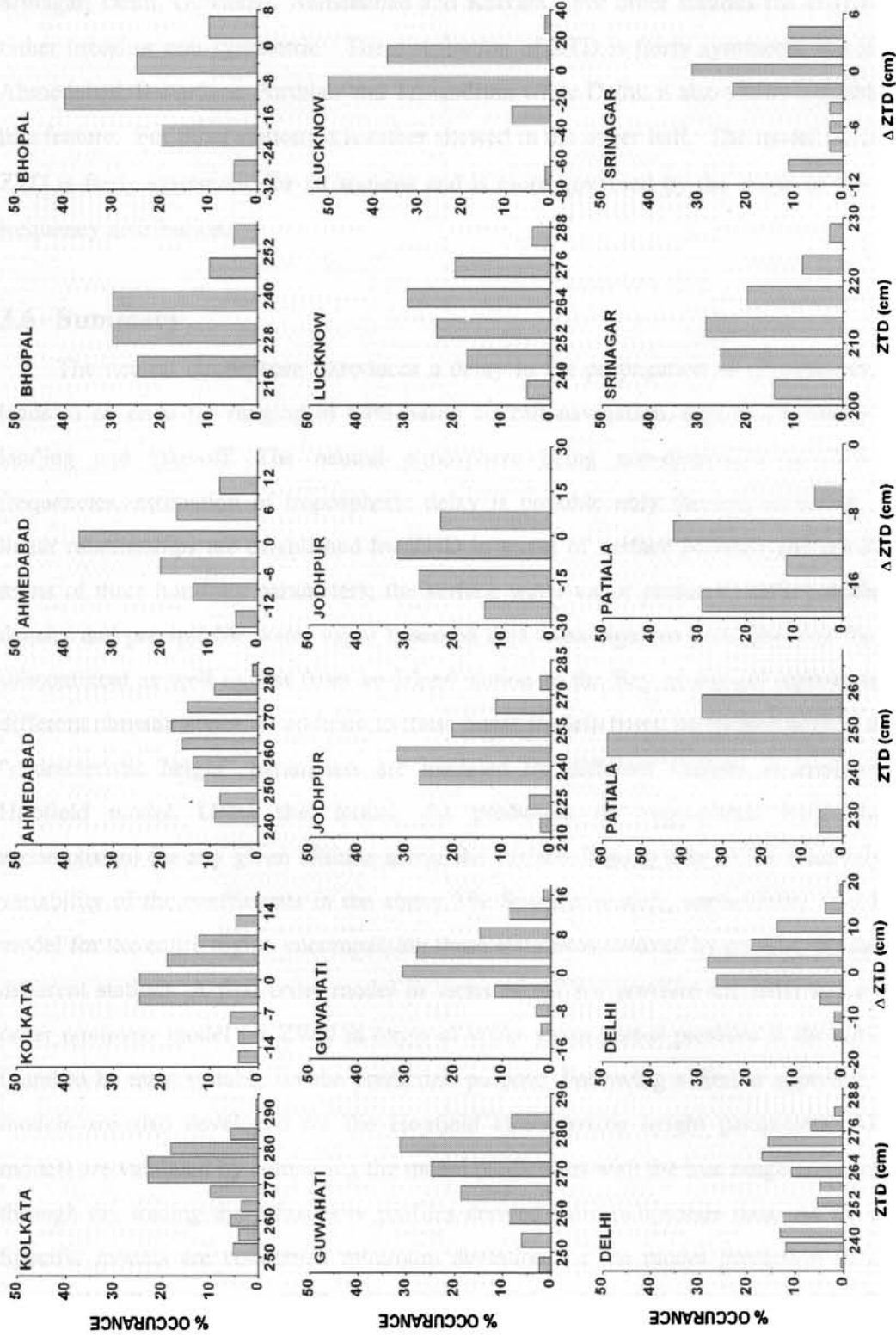


Figure 3.10b: Frequency distribution of true Zenith Tropospheric Delay (ZTD) estimated through ray-tracing along with the distribution of the model deviations from the true value for Kolkata, Ahmedabad, Bhopal, Guwahati, Jodhpur, Lucknow, Delhi, Patiala, and Srinagar

Srinagar, Delhi, Guwahati, Ahmedabad and Kolkata. For other stations the distribution is rather broad or non-symmetric. The distribution of ZTD is fairly symmetric for Srinagar, Ahmedabad, Bangalore, Portblair and Trivandrum while Delhi; it also shows a double hump like feature. For other stations it is rather skewed in the upper half. The model deviation of ZTD is fairly systematic for all stations and is more governed by the shape of the ΔZWD frequency distribution.

3.6 Summary

The neutral atmosphere introduces a delay in the propagation of microwaves, which leads to an error for ranging in GPS based aircraft navigation, significant mainly during landing and take-off. The neutral atmosphere being non-dispersive at GPS signal frequencies, estimation of tropospheric delay is possible only through modeling. Simple linear relationships are established for ZHD in terms of surface pressure and for ZWD in terms of three humidity parameters; the surface water vapor pressure, surface water vapor density and precipitable water vapor based on data from eighteen locations over the Indian subcontinent as well as that from an Island station in the Bay of Bengal representative of different climatic zones. In addition to these linear models based on meteorological data the "characteristic height" parameters are modeled for different stations to implement the Hopfield model. Using this model, the prediction of tropospheric error could be accomplished for any given altitude above the surface. Taking note of the relatively small variability of the coefficients in the above Site-Specific models, applicability of a Unified model for the entire region encompassing these stations is evolved by pooling the data from different stations. A first order model in terms of surface pressure for ZHD and a second order nonlinear model for ZWD in terms of water vapor partial pressure at the surface are found to be most suitable for the prediction purpose. Following a similar approach unified models are also developed for the Hopfield characteristic height parameters. All these models are validated by comparing the model predictions with the true range errors obtained through ray tracing the refractivity profiles derived from radiosonde data. As far as Site-Specific models are concerned minimum deviation for the model prediction of ZHD is observed at Trivandrum (~ 0.17 cm) while the maximum deviation is observed for Srinagar (~ 2 cm). The validity of the Unified Surface model is also examined by comparing modeled delay values with true ray-traced values as well as with other global models. In the case of

ZWD the deviation ($\sim 5.81 \pm 5.43$ cm) of Unified Surface model is comparable to that of site-specific model. The Unified surface model is found to be superior to the global models when applied to Indian region.

Chapter 4

A REGIONAL TROPOSPHERIC DELAY MODEL FOR TROPICS WITH EMPHASIS TO THE INDIAN REGION

4.0 Introduction

The first tropospheric delay model developed as a function of geographical latitude and longitude as well as the day of the year aiming its potential application of using GPS data in geodetic studies is the Altshuler model [Altshuler and Kalaghan, 1974]. This was further modified to suite a wider region by De Cleene, [1995]. A similar model, recommended by North Atlantic Treaty Organisation (NATO) for GPS related applications in its Standards Document [NATO, 1993], employs a three-layer atmospheric model (*viz.* 0 to 1 km, 1 to 9 km, and above 9 km) for accounting the variation in atmospheric refractivity with height. This delay model was derived from the Central Radio Propagation Laboratory (CRPL) Reference Atmosphere – 1958 (RA-1958) [Bean and Thayer, 1959], which was originally evolved from extensive radiosonde launches in and around the United States. In this model the atmospheric refractivity is assumed to decrease linearly in the first layer followed by an exponential decrease to reach a steady value of 105 N units at 9 km and continue to decrease at the same rate above. Similarly there was an attempt to include seasonal variations in Altshuler model based on world-wide surface refractivity data in different seasons from the CRPL profiles. Being derived from the Altshuler model, all the earlier models generated for this applications had similar genesis and were also specified with the same mean global surface refractivity value of 324.8 N units, although the Altshuler adjusted this to account for a seasonal and latitude dependency as well. Though both these models are specified with a constant value of surface refractivity, the NATO model employs only the user's altitude to generate the altitude profile while the Altshuler model incorporates the user altitude, latitude and time to model the variation in atmospheric refractivity. All these models were initially considered for Wide Area Differential GPS (WADGPS) also.

New methodologies for tropospheric delay correction are explored as a part of the extension of GPS applications to navigate the civil aircraft. In this process the WADGPS envisaged in providing the GPS correction over a large area, splits the total error into different components, namely the orbit error, clock error, ionospheric error, tropospheric error, *etc.* Information on these errors is broadcasted *via* a geo-stationary satellite over to a large region to enable the users to apply appropriate corrections. Because of large spatio-temporal heterogeneity of the lower atmosphere this broadcasted tropospheric delay may not be sufficiently accurate for critical applications like landing/take-off of an aircraft. In such cases the delay estimated using local model is preferred. This lead to the development of different models for estimating the tropospheric delay either through a profile-based method (ray-tracing) or by employing conventional methods based on surface atmospheric parameters [*Bock and Doerflinger, 2000; Hopfield, 1971; Saastamoinen, 1972; Bevis et al. 1992; Schüeler, 2000; Saha et al., 2007*]. Though these models are sufficiently accurate for this purpose, its development and later usage requires collocated measurements of different atmospheric parameters. This limits the applicability of these models over a particular region.

When no direct access to the measured atmospheric parameters are available, such as for the case of navigating aircraft, a second method devoid of any measured atmospheric parameters but depends on the geographical location and day of the year [*Collins and Langley, 1997*] becomes handy for direct use. In this case a periodic function is developed for representing the seasonal variation of P , T and e at MSL as a function of latitude. This model mainly depends on a look up table of mean and amplitude (of annual variation) of five parameters P , T , e , β and λ (where β and λ are, respectively, the atmospheric temperature lapse rate and atmospheric water vapor lapse rate) at discrete latitudinal intervals. This model was tested satisfactorily as a part of the WAAS system over North America. The applicability of the look-up table used in WAAS model developed primarily using the meteorological data over North America [*COESA, 1966*] was examined over Europe by *Penna et al.* [2001], as a part of Global Navigation System (GNS-I). The tropospheric correction based on both WAAS and EGNOS models comply with the International Civil Aviation Organization (ICAO) Standard and Recommended Practices (SARPS) for Satellite Based Augmentation System (SBAS) [*RTCA, 1999*]. The validity of these models is also assessed in various studies [*Collins and Langley, 1997, 1998; Dodson et*

al., 1999b; Penna *et al.*, 2001; Farah *et al.*, 2005] for demonstrating its capability in predicting the mean tropospheric delay effectively for the mid-latitude stations.

The geographical features and weather conditions that prevail over Indian subcontinent make it different from other regions where most of the tropospheric delay models are developed. While the temperature over northern region of India that lies in the temperate zone, undergoes significant seasonal variation with a large range of diurnal heating and cooling, the southern peninsular region, which lies south of the tropic of cancer, experiences a tropical climate characterized by warm and highly humid condition with less seasonal and diurnal variations. On examining the applicability of WAAS model over this region it is seen that the model deviates significantly from true values especially at region which are located relatively close to equator. Under this scenario, an Indian Region-specific Tropospheric Delay model based on the regular radiosonde data collected by the IMD from different stations located at distinctly different climatic zones over the Indian subcontinent is developed analogous to the WAAS Tropospheric Delay (WTD) model. Applicability of this model is tested by comparing with true ZTD obtained by ray-tracing the refractivity profiles, and ZTD estimated using the surface parameter based model.

4.1 The WAAS Tropospheric Delay (WTD) Model

With an aim of the most stringent tropospheric delay correction for GPS based real time aircraft navigation, a model was proposed by Collins and Langley, [1997], which has its roots from the geodetic-GPS positioning. This model named as University of New Brunswick (UNB), model has various generations indicating the evolution of this model into one of the most accepted tropospheric delay model for WAAS. The first and most primitive among them was UNB1, which uses the Saastamoinen models driven by a set of constant values to represent the mean global atmosphere. These values represent the standard surface values of pressure (P) and temperature (T) with a value for water vapor pressure (e) derived to be equivalent to the mean global surface refractivity of 324.8 N units. A global mean, spatially invariant value for the temperature lapse rate (β) and water vapor lapse rate (λ) is used in this model. The values of these mean atmospheric parameters used in UNB1 model is respectively of $P_0 = 1013.25$ hPa, $T_0 = 288.15$ K, $e_0 = 11.691$ hPa, $\beta_0 = 6.5$ K/km and $\lambda_0 = 3$. Due to the stochastic nature of water vapor, the λ value is only a representative index for the average decrease in water vapor partial pressure in a column of air. Though it is derived

from real-time measurements it is accurate only at those spatial and temporal scales with which it is derived [Schwarz, 1968; Smith, 1968]. However, the water vapor profile does exhibit a latitudinal trend. Because of this, the zenith delay model with a constant value for λ was found to perform poorly at higher latitudes [Ifadis, 1986]. Subsequently detailed investigations were carried out to improve this model by incorporating a mean annual variation of all these five parameters depending on latitudes. This led to the development of UNB2 model. This model was evolved for representing the latitudinal variation over a geographical region of 80°N to 70°S. The third generation model (referred to as UNB3) was developed subsequently by introducing a temporal variation in these parameters, applying the concepts used by the Niell mapping functions. Presently this model is used in WAAS. Hereafter this model will be referred as the WAAS Tropospheric Delay (WTD) model in the following discussions.

The WTD model [Collins and Langley, 1997] intended to surrogate the measured atmospheric parameters, employs a look-up table (Table 4.1) primarily developed using US standard meteorological data (US Standard Atmospheric Model 1966 COESA, [1966]), containing the annual mean value of the five atmospheric parameters and the amplitudes of the respective annual variations at particular latitudinal interval of 15° pertaining to the mean sea level.

Table 4.1: Look-up Table for WTD Model Showing the Annual Mean (P_o , T_o , e_o , β_o and λ_o) and Seasonal Amplitude (P' , T' , e' , β and λ')

Latitude	Mean (ξ_o)				
	P_o (hPa)	T_o (K)	e_o (hPa)	β_o (K/km)	λ_o
15	1013.25	301.70	26.31	6.50e-03	2.77
30	1017.25	298.65	21.79	6.50e-03	3.15
45	1015.75	292.40	11.66	6.50e-03	2.57
60	1011.75	281.35	6.78	6.50e-03	1.81
75	1013.00	278.90	4.11	6.50e-03	1.55
Latitude	Amplitude ($\Delta\xi$)				
	P' (hPa)	T' (K)	e' (hPa)	β (K/km)	λ'
15	0.00	0.00	0.00	0.00	0.00
30	-3.75	4.50	8.85	0.00	0.33
45	-2.25	7.75	7.24	0.00	0.46
60	-1.75	8.80	5.36	0.00	0.74
75	-0.50	9.00	3.39	0.00	0.30

The latitude-dependent mean meteorological elements for 15° to 75° latitude are taken from the table, which subsequently is denoted as ξ_o . The seasonal variability of this parameter is

taken into account by employing the corresponding amplitude values ($\Delta\xi$) along with a periodic (cosine) function (of the day number) with a phase of 28 days for northern hemisphere and 211 for the southern hemisphere. These epochs in a year are the days in which the mean sea level surface temperature is a minimum. Thus the phase is defined such that the minimum occurs on the epoch day number (d_0). Using this look-up table the value of any desired atmospheric parameter for a particular day of the year (d) is estimated as

$$\xi(\varphi, d) = \xi_o(\varphi) - \Delta\xi(\varphi) \times \cos\left[\frac{2\pi(d - d_0)}{365.25}\right] \quad (4.1)$$

where φ is the receiver's latitude. The atmospheric parameters for a particular location that lies in between the two adjacent latitudes given in Table 4.1, are obtained through a linear interpolation as

$$\xi_o(\varphi) = \xi_o(\varphi_i) + [\xi_o(\varphi_{i+1}) - \xi_o(\varphi_i)] \cdot \frac{\varphi - \varphi_i}{\varphi_{i+1} - \varphi_i} \quad (4.2)$$

and

$$\Delta\xi(\varphi) = \Delta\xi(\varphi_i) + [\Delta\xi(\varphi_{i+1}) - \Delta\xi(\varphi_i)] \cdot \frac{\varphi - \varphi_i}{\varphi_{i+1} - \varphi_i} \quad (4.3)$$

where i and $i+1$ refer to tabular latitudes below and above the receiver latitude, respectively. These values are further scaled up to the user altitude using a scaling factor derived from hydrostatic equation. The values of pressure (P_S), temperature (T_S) and water vapor pressure (e_S) at the user altitude h are estimated from the respective mean sea level values (P_o , T_o and e_o) using appropriate scaling factors as,

$$P_S = k_{hyd} \cdot P_o \quad (4.4a)$$

$$e_S / T_S = k_{wet} \cdot e_o / T_o \quad (4.4b)$$

and

$$T_S = T_o - \beta \cdot h \quad (4.4c)$$

$$\text{with } k_{hyd} = \left(1 - \frac{\beta \cdot h}{T_o}\right)^{\frac{g}{R_d \beta}} \quad \text{and} \quad k_{wet} = \left(1 - \frac{\beta \cdot h}{T_o}\right)^{\frac{(A+1)g}{R_d \beta} - 1} \quad (4.4d)$$

Employing the above relationships the values of ZHD and ZWD are estimated [Saastamoinen, 1972; Davis et al., 1985; Askne and Nordius, 1987] as

$$\text{ZHD} = \frac{10^{-6} k_1 R_d}{g_m} \left[1 - \frac{\beta h}{T} \right]^{\frac{g}{R_d \beta}} P_o = \frac{10^{-6} k_1 R_d}{g_m} P_s \quad (4.5)$$

and

$$\begin{aligned} \text{ZWD} &= \frac{10^{-6} k_2 R_d}{g_m (\lambda + 1) - \beta R_d} \left[1 - \frac{\beta h}{T} \right]^{\frac{(\lambda+1)g}{R_d \beta} - 1} \frac{e_o}{T_o} \\ &= \frac{10^{-6} k_2 R_d}{g_m (\lambda + 1) - \beta R_d} \frac{e_s}{T_s} \end{aligned} \quad (4.6)$$

where g is 9.80665 m/s^2 , h is the height (in meters) of the receiver above mean-sea level, $g_m = 9.784 \cdot (1 - 0.00266 \cdot \cos 2\varphi - 0.00028 \cdot h)$ in m/s^2 , φ is the ellipsoidal latitude and h is the height of the antenna site above the ellipsoid.

In line with the above, this model is evaluated for the Indian region using atmospheric data from 18 different locations (Figure 4.2) spread over the Indian subcontinent spanning the latitude 8°N to 32°N . The mean atmospheric model for WTD is mainly governed by the values of the coefficients in Table 4.1, which does not show any seasonal variation for all the five model parameters in the latitude region $\leq 15^\circ\text{N}$. The mean values for P_o , T_o and e_o which are 1013.25 hPa , 301.7°K and 26.31 hPa , respectively, differs from the actually observed annual mean values in this region. In order to examine the deviation of this model for the Indian stations the true annual variation of these atmospheric parameters for all the 18 stations are examined using daily data for five years from 1995 to 1999 and compared with the model values. This study revealed that the observed annual mean and its seasonal variation deviate significantly from the model values using the coefficients given in Table 4.1. The annual variations of P_s , T_s and e_s at Trivandrum and Chennai (two stations located below 15°N) are presented in Figure 4.1 along with those for Ahmedabad and Delhi which are located at 23.06°N and 28.58°N , respectively. For a comparison the values derived from WTD model is also presented (continuous curve) in Figure 4.1. As can be seen, the annual variations are relatively small at lower latitudes and increases with latitude. The most striking feature is that the values of P_s , T_s and e_s deviate significantly from the respective values obtained from WTD model. For those stations which are located at latitudes north of 15°N though the WTD model shows a systematic annual variation, its amplitude is significantly lower than that of the true values. The phase of the annual variation also shows significant deviation from the model values. Surface temperature at Delhi and Ahmedabad

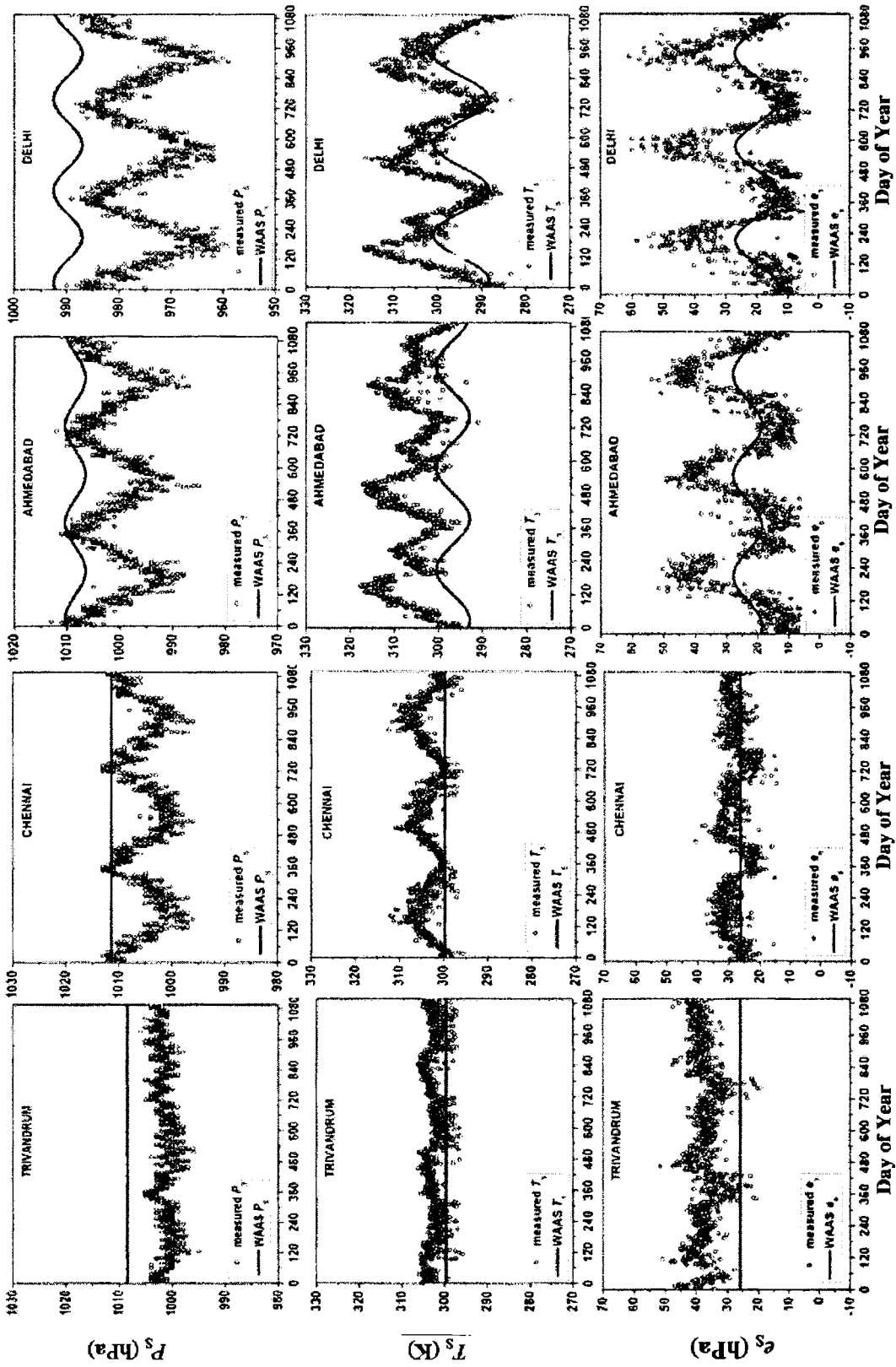


Figure 4.1: Time series plots for surface pressure (P_s), surface temperature (T_s) and surface water vapor pressure (e_s) for Trivandrum, Chennai, Ahmedabad and Delhi representative for different latitude sectors over the Indian subcontinent. Measured surface parameters are represented by open circle (o) and WTD estimate by solid line (—)

shows the prevalence of a sub-annual component also. The mean absolute deviation of the WTD model from the measured atmospheric parameters shows that the deviation in P_S and T_S increases with latitude. While the mean absolute deviation for P_S is 7 ± 2 hPa for the low latitude stations (Trivandrum and Chennai), it is of the order of 14 ± 5 hPa for the other two stations which are located north of 23°N . The maximum deviation of ~ 28 hPa for P_S is encountered at Delhi, which can lead to an error of ~ 6.5 cm in the estimated ZTD employing Saastamoinen model [Saastamoinen, 1972]. In case of e_S the mean absolute deviation ranges from 4 to 12 hPa and does not show any latitudinal trend. A maximum deviation of ~ 33.95 hPa is observed for e_S at Delhi, which can introduce an error up to ~ 44 cm in the estimated value of ZWD. This shows that the mean atmospheric model employed in WTD is not adequate for the Indian region. This prompted the development of a new model exclusively for this purpose, which is detailed in the following section.

4.2 Indian Region-specific Tropospheric Delay (IRTD) Model

An Indian Region-specific Tropospheric (IRTD) Model applicable for the latitude region 5°N to 32°N is developed using the radiosonde data for five years (1995-1999) from 18 selected IMD stations covering different climatic zones (Figure 4.2). All these IMD stations are in the proximity of the airports. The altitude profiles of P , T and e obtained from the radiosonde data are used to develop monthly mean models of these parameters for all these stations. These are used to estimate the β_0 and λ_0 (monthly mean values for β and λ). These values of β_0 and λ_0 in each month are used to scale the P_S , T_S , and e_S to the respective mean MSL values (P_{msl} , T_{msl} and e_{msl}). The day-to-day and seasonal variation of P_{msl} , T_{msl} , e_{msl} , β_0 and λ_0 are studied in detail for all these stations. The time series of these MSL values are Fourier analyzed to determine the mean (P_0 , T_0 , e_0 , β_0 and λ_0) as well as the annual amplitudes (P' , T' , e' , β and λ' , respectively) for each of these stations. Once this is accomplished the stations are arranged in different latitude sectors, by grouping stations located almost at the same latitude and assigned a mean value for these parameters by averaging. These mean values in different discrete latitude sectors are further interpolated for a constant latitudinal interval of 5° and presented in the form of a look-up table as shown in Table 4.2. The phase offset epoch (d_0) is also estimated for each of these stations and optimized for a single value of 6 days for the whole sub-continent. Similar to WTD model,

the values of these parameters at any location in between the 5° latitude interval could further be obtained through linear interpolation (eqs. 4.2 and 4.3). These values could further be scaled to the user altitude employing appropriate scaling factors k_{hyd} and k_{wet} (eq. 4.4).

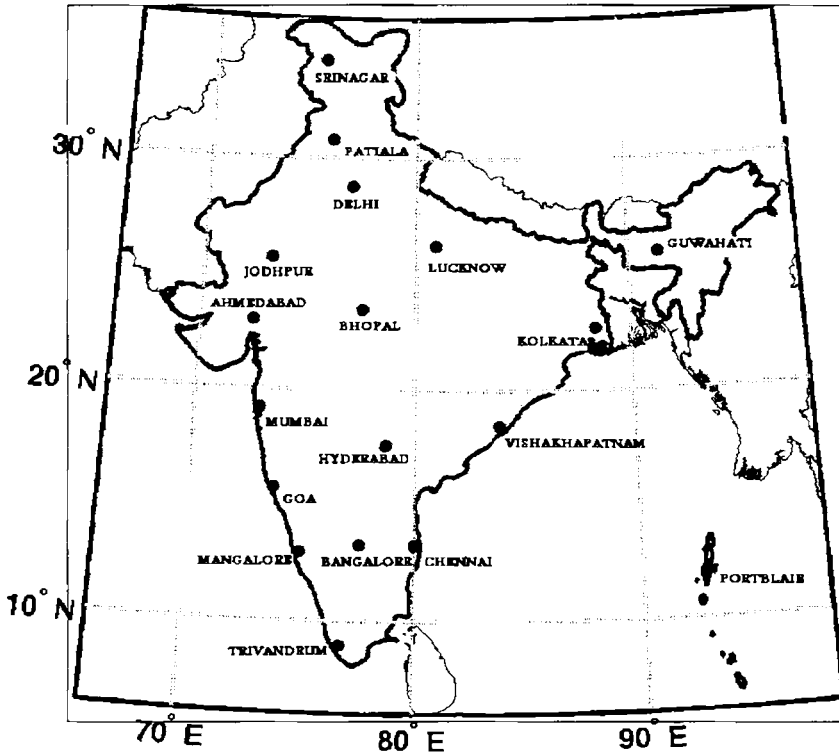


Figure 4.2: Map showing the location of 18 stations spread across the Indian sub-continent covering different climatic zone used for this study

Table 4.2: Look-up Table for IRTD Model

Latitude	Mean (ξ_0)				
	P_0 (hPa)	T_0 (K)	e_0 (hPa)	β_0 (K/km)	λ_0
5	1005.95	302.00	29.62	5.58e-03	2.73
10	1005.29	303.29	28.93	5.52e-03	2.69
15	1004.97	306.26	25.67	5.71e-03	2.50
20	1006.17	306.37	22.31	6.08e-03	2.33
25	1004.65	304.51	21.5	6.14e-03	2.39
30	1001.41	301.91	22.65	6.28e-03	2.60
Latitude	Amplitude ($\Delta\xi$)				
	P' (hPa)	T' (K)	e' (hPa)	β (K/km)	λ'
5	-1.05	1.42	1.29	0.19e-03	0.44
10	-1.85	2.02	2.89	0.26e-03	0.45
15	-4.50	3.78	6.82	0.67e-03	0.56
20	-6.95	5.11	8.89	1.17e-03	0.53
25	-8.95	6.80	10.73	1.28e-03	0.40
30	-10.3	8.72	11.69	1.17e-03	0.49

The desired atmospheric parameter for any particular day of the year (d) then is estimated incorporating the periodic function (eq. 4.1). The model parameters thus estimated for a particular location is then incorporated into the Unified Surface model [Suresh Raju *et al.*, 2007a] in which a linear relation between ZHD and surface pressure is established based on linear regression (keeping zero intercept) (eq. 3.10) and a second order regression relation (eq. 3.12) is used for estimating the non-hydrostatic component of ZTD.

4.3 Evaluation of IRTD and WTD model for the Indian Subcontinent

The accuracy of IRTD and WTD models over the Indian sub-continent is assessed by comparing the values of the hydrostatic and non-hydrostatic components of ZTD estimated from these models with those estimated using Unified Surface models employing measured atmospheric parameters (for P_S and e_S) as input. The surface meteorological data collected from different IMD stations on a daily basis are used as an input for the Unified surface models (eq. 3.10 and 3.12) to estimate both zenith hydrostatic delay (ZHD_m) and zenith wet delay (ZWD_m). Daily atmospheric parameters are also generated for the corresponding day number, using the periodic function (eq. 4.1) (suitably interpolating the coefficients from Table 4.2 using eq. (4.2)), which is used as input to the Unified Surface models (eq. 3.10 and 3.12) to derive the dry delay ($ZHD_{IRT D}$) and wet delay ($ZWD_{IRT D}$). For an explicit inter-comparison time series plots for $ZHD_{IRT D}$ and $ZWD_{IRT D}$ are generated for all these stations as shown in Figures 4.3 and 4.4 with the corresponding daily values of ZHD_m and ZWD_m superposed. Similarly the corresponding atmospheric parameters from the atmospheric model associated with WTD model (which also employs eqs. 4.1 and 4.2 but the coefficients as given in Table 4.1 with a value of 28 for d_0) is also estimated. These values are used for estimating ZHD_{WTD} and ZWD_{WTD} using the WTD model as given by eqs. 4.5 and 4.6. The time series plot of ZHD_{WTD} thus obtained is also presented in Figure 4.3a and 4.3b by dashed curves. These Figures show that, the IRTD model agrees fairly well with the ZHD_m . In most of the cases the ZHD_{WTD} is larger than ZHD_m . The difference between ZHD_{WTD} and ZHD_m increases with increase in latitude. Moreover, for those stations below $15^\circ N$, WTD model provides only a single value for the dry delay throughout the year where as in real case at these stations also the ZHD_m show a significant seasonal variation even though the amplitude is relatively small (≤ 4 cm). It may further be noted that the $ZHD_{IRT D}$ responds to the seasonal variations fairly well. Among the 18 met stations shown in the Figure 4.2,

Trivandrum, Portblair, Mangalore, Chennai, Goa, Vishakhapatnam, Mumbai and Kolkata are the coastal stations. Among these coastal stations, Trivandrum, Mangalore, Goa and Mumbai are located in the Arabian Sea side, while the rest in the Bay of Bengal (BoB) side. Portblair is an island in BoB. While Mangalore, Bangalore and Chennai are located almost at the same latitude but separated longitudinally, Bangalore is located in the plateau region which is around 930 m above MSL. Most of the low altitude coastal stations show high values of ZHD (greater than ~ 2.3 m) while that at Bangalore is ~ 2.1 m. For stations beyond 15°N the seasonal variation of ZHD_{IRTD} agrees fairly well with that estimated using measured atmospheric data. The WTD model though also shows a seasonal variation for the high latitude stations, does not account for its large amplitude as well as there is difference in the phase also. For a better quantification, the *rms* deviations and maximum absolute deviations of the ZHD_{IRTD} and ZHD_{WTD} from ZHD_m for all the stations are presented in Table 4.3. For near equatorial stations the *rms* deviation of ZHD_{IRTD} is 0.3 ± 0.2 cm while that for mid-latitude region is 0.5 ± 0.4 cm. In case of the WTD model, the *rms* deviation of ZHD_{WTD} is more than twice that of ZHD_{IRTD} . Note that, while the maximum deviation of ZHD_{IRTD} is around 3 cm for Lucknow, the corresponding deviation of ZHD_{WTD} is ~ 5 cm.

A similar time series plot of zenith wet delay estimated using the WTD and IRTD models for all the stations along with the ZWD_m are presented in Figures 4.4(a & b). The most striking feature in the figure is the ability of WTD model to estimate the seasonal variations of ZWD for the high latitude stations compared to ZHD (shown in Figure 4.3). The agreement between ZWD_{IRTD} and ZWD_m is much superior compared to that between ZWD_{WTD} and ZWD_m . For the near equatorial stations (Trivandrum and Portblair) the seasonal variation of ZWD is very small (< 20 cm) and its amplitude increases with increasing latitude. Largest annual variation (≥ 50 cm) in ZWD is observed at Delhi. The WTD model gives a single value for the wet delays for all the five near-equatorial stations all through the season even though the values of ZWD_m show significant annual variation especially for Mangalore and Chennai. Being located at higher altitude the value of ZWD_{WTD} for Bangalore is slightly low. Although it is clear from Figures 4.3 and 4.4 the WTD model improves in exhibiting the seasonal variation of ZHD and ZWD with increase in latitude but the overall *rms* deviation increases with latitude. Note that, the estimation of both ZHD and ZWD using IRTD model is always better even though it fails to capture the extremely high values.

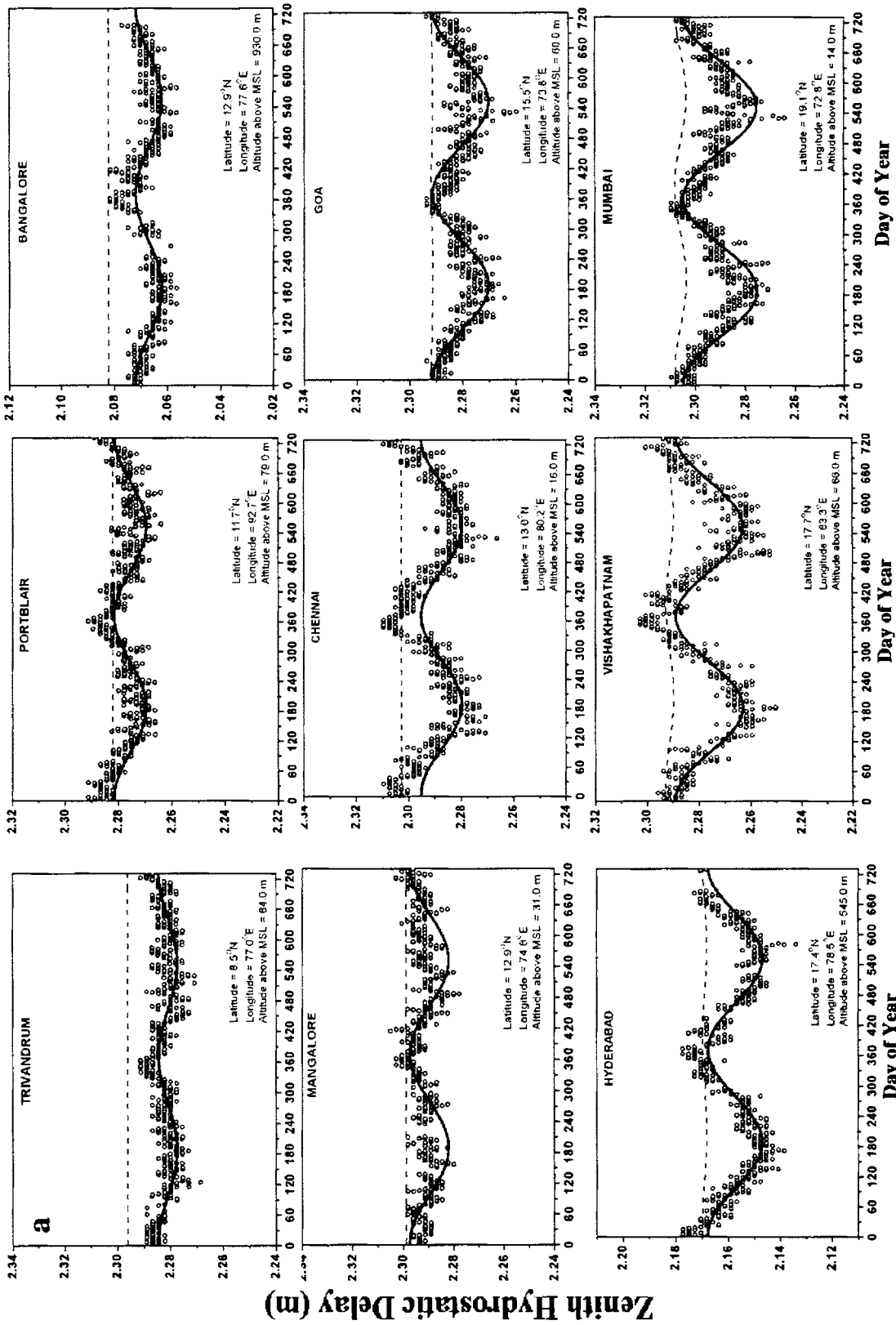


Figure 4.3 (a): Time series plots showing a comparison of ZHD estimated by IRTD (ZHD_{IRTD}) and WTD model (ZHD_{WTD}) with that obtained using measured surface parameters (ZHD_m) for Trivandrum, Portblair, Bangalore, Chennai, Goa, Hyderabad, Vishakhapatnam, and Mumbai. The ZHD_m are represented by open circle (o), ZHD_{IRTD} by solid line (—) and ZHD_{WTD} with dashed line (----)

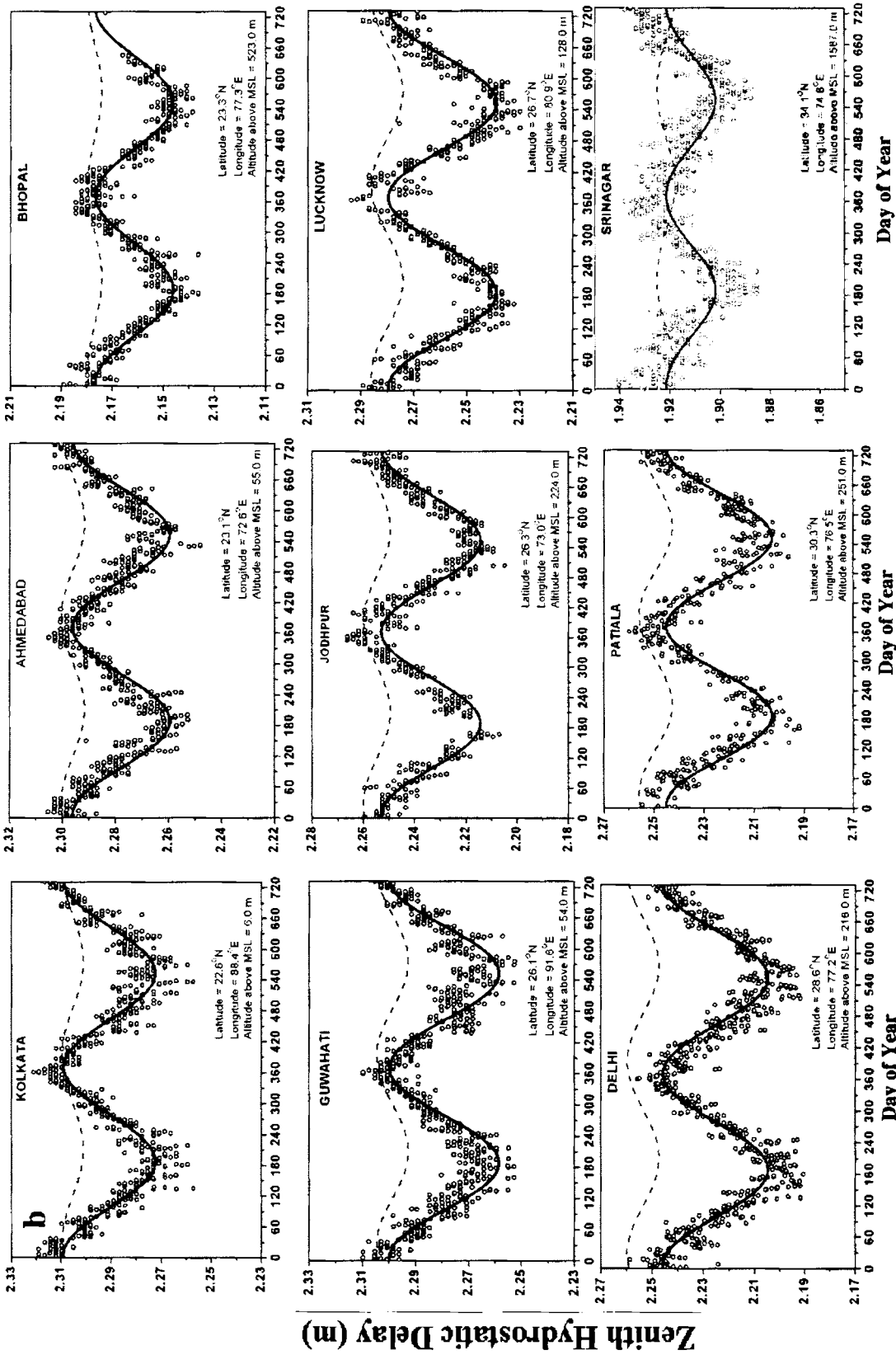


Figure 4.3 (b): Time series plots showing a comparison of ZHD estimated by IRTD (ZHD_{IRTD}) and WTD model (ZHD_{WTD}) with that obtained using measured surface parameters (ZHD_m) for Kolkata, Ahmedabad, Bhopal, Guwahati, Jodhpur, Lucknow, Delhi, Patiala, and Srinagar. The ZHD_m are represented by open circle (o), ZHD_{IRTD} by solid line (—) and ZHD_{WTD} with dashed line (----)

Table 4.3: The *rms* Deviation and Maximum Absolute Deviation of IRTD Model ($\Delta ZHD_{IRT D}$) and WTD Model (ΔZHD_{WTD}) from Unified Surface Model (ZHD_m). The Values Given with in the Bracket are Standard Deviations (σ) of the Absolute Difference

Stations	<i>rms</i> deviation ($\pm \sigma$) (cm)		Max. Abs. deviation (cm)	
	$\Delta ZHD_{IRT D}$	ΔZHD_{WTD}	$\Delta ZHD_{IRT D}$	ΔZHD_{WTD}
Trivandrum	0.3 (\pm 0.2)	1.3 (\pm 0.4)	1.4	2.8
Portblair	0.4 (\pm 0.3)	0.5 (\pm 0.4)	1.4	2.2
Bangalore	0.3 (\pm 0.2)	1.5 (\pm 0.5)	1.1	2.6
Mangalore	0.4 (\pm 0.3)	0.7 (\pm 0.4)	1.6	2.1
Chennai	0.5 (\pm 0.4)	0.9 (\pm 0.6)	1.5	2.4
Goa	0.4 (\pm 0.3)	1.0 (\pm 0.6)	1.7	3.2
Hyderabad	0.3 (\pm 0.2)	1.2 (\pm 0.8)	1.4	3.4
Vishakhapatnam	0.5 (\pm 0.3)	1.4 (\pm 1.0)	1.7	4.0
Mumbai	0.5 (\pm 0.4)	1.3 (\pm 0.7)	2.2	4.0
Kolkata	0.5 (\pm 0.4)	1.5 (\pm 1.1)	2.2	5.1
Ahmedabad	0.5 (\pm 0.4)	1.5 (\pm 1.0)	2.7	4.5
Bhopal	0.4 (\pm 0.3)	1.6 (\pm 1.0)	1.9	4.0
Guwahati	0.6 (\pm 0.5)	1.7 (\pm 1.0)	2.4	4.2
Jodhpur	0.5 (\pm 0.3)	1.8 (\pm 1.1)	1.6	4.8
Lucknow	0.5 (\pm 0.4)	2.1 (\pm 1.2)	3.2	5.0
Delhi	0.5 (\pm 0.4)	3.0 (\pm 1.3)	2.2	6.1
Patiala	0.6 (\pm 0.4)	2.1 (\pm 1.2)	2.0	5.3
Srinagar	0.6 (\pm 0.5)	1.2 (\pm 1.0)	2.5	4.2

A detailed quantitative comparison of periodic models (IRT D and WTD) for estimating ZWD with those estimated using measured surface atmospheric parameters over different stations is presented in Table 4.4. The *rms* deviation of $ZWD_{IRT D}$ from ZWD_m is 4 ± 3.1 cm for near-equatorial stations and > 5 cm for mid-latitude region, while ZWD_{WTD} deviates by 7.8 ± 4.1 cm for near-equatorial stations and > 7 cm for mid-latitude region. Larger deviations (> 25 cm) for IRT D model are observed for Guwahati, Lucknow, Delhi and Srinagar, while those for the other stations are < 20 cm. In case of WTD model the maximum deviation is of the order of ~ 50 cm. The deviation of IRT D model is quite significant (~ 30 cm) at higher latitudes, especially over Delhi during the July-September (monsoon) period, which could be attributed to the advection of large amount water vapor in the atmosphere during the Asian summer monsoon. Collins and Langley [1998] reported

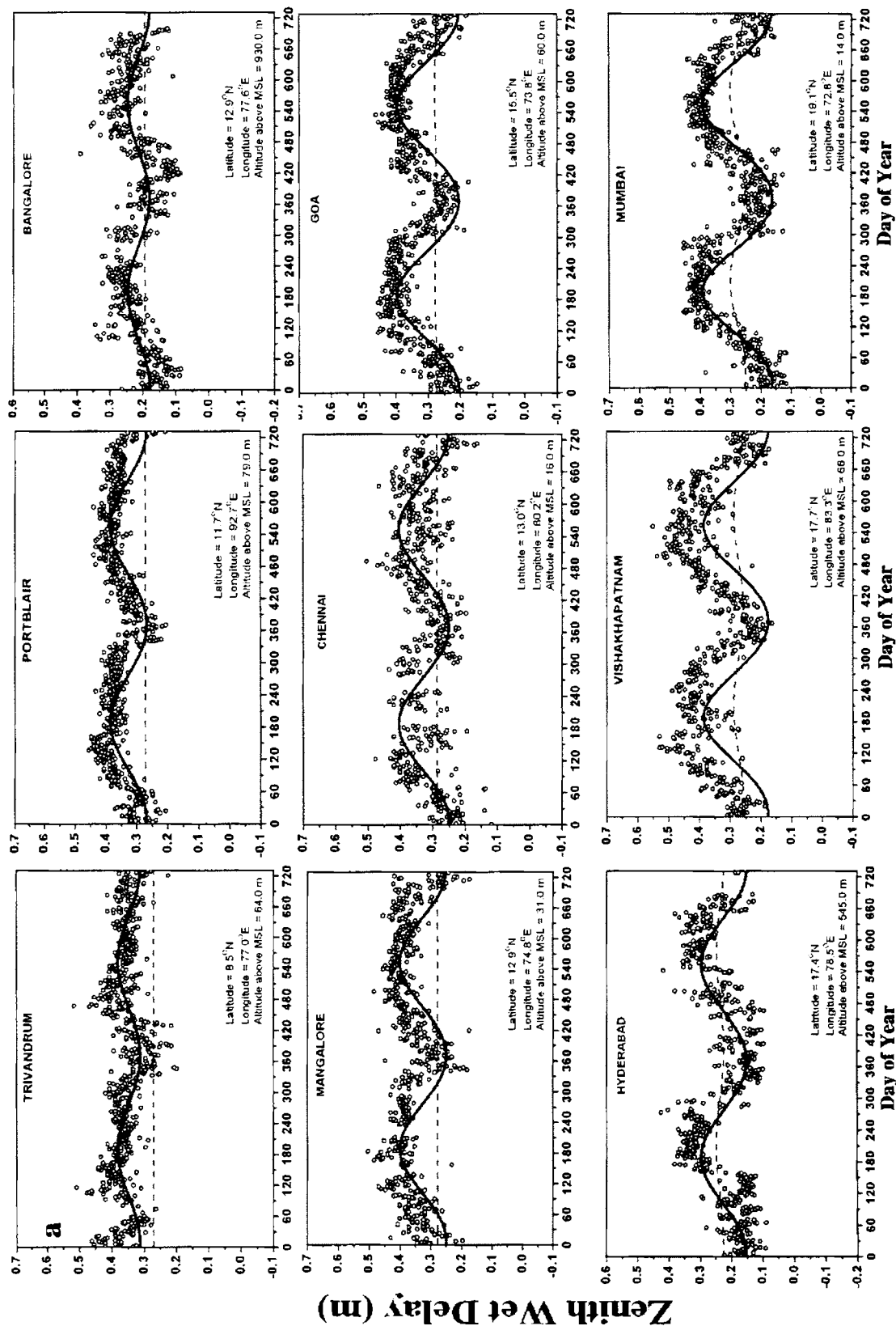


Figure 4.4 (a): Time series plots showing a comparison of ZWD estimated by IRTD (ZWD_{IRTD}) and WTD model (ZWD_{WTD}) with that obtained using measured surface parameters (ZWD_m) for Trivandrum, Portblair, Bangalore, Chennai, Goa, Hyderabad, Vishakhapatnam, and Mumbai. The ZWD_m are represented by open circle (o), ZWD_{IRTD} by solid line (—) and ZWD_{WTD} with dashed line (----)

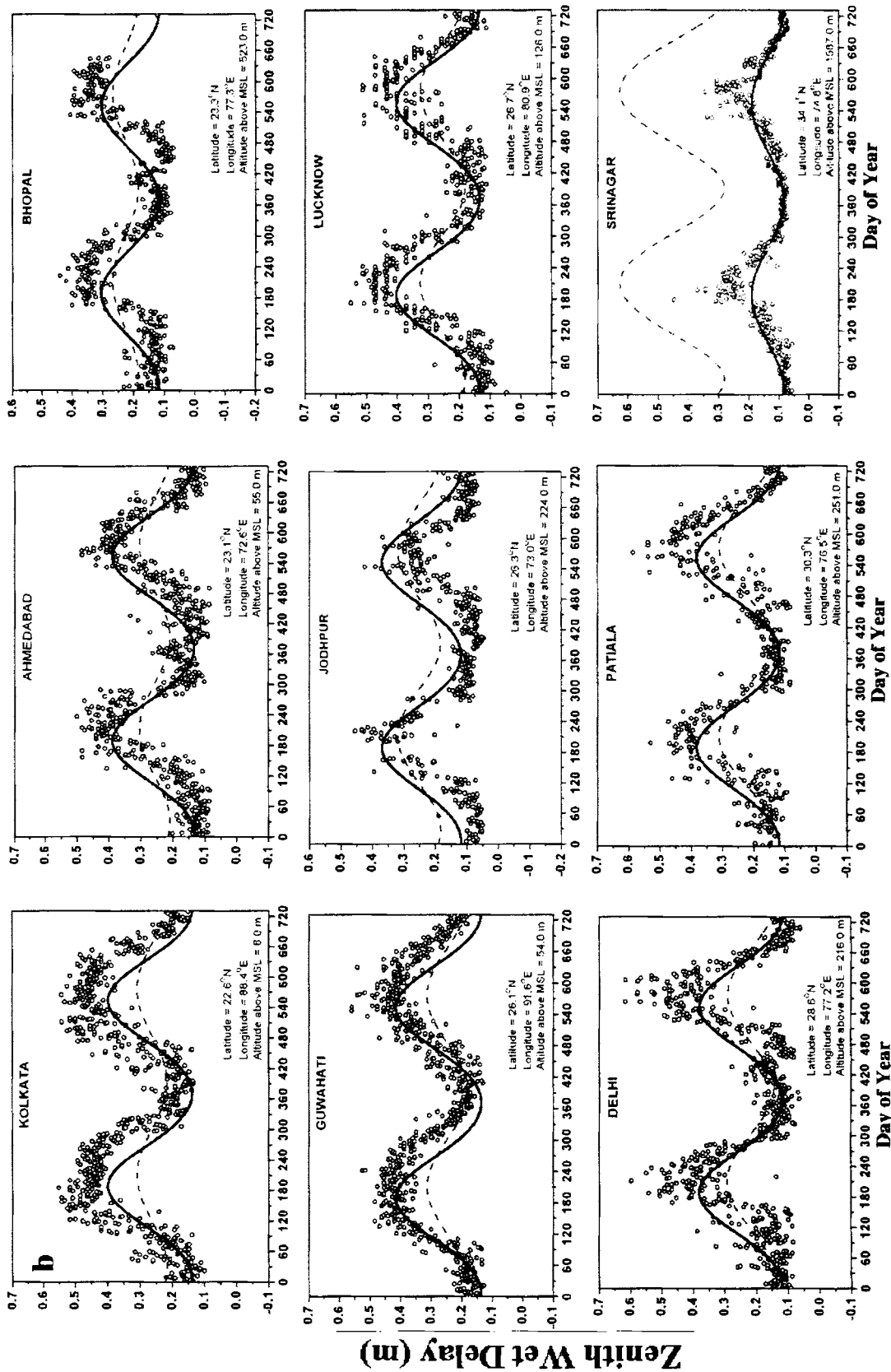


Figure 4.4 (b): Time series plots showing a comparison of ZWD estimated by IRTD (ZWD_{IRTD}) and WTD model (ZWD_{WTD}) with that obtained using measured surface parameters (ZWD_m) for Kolkata, Ahmedabad, Bhopal, Guwahati, Jodhpur, Lucknow, Delhi, Patiala, and Srinagar. The ZWD_m are represented by open circle (o), ZWD_{IRTD} by solid line (—) and ZWD_{WTD} with dashed line (---)

Table 4.4: The *rms* Deviation and Maximum Absolute Deviation of IRTD Model (ΔZWD_{IRTD}) and WTD model (ΔZWD_{WTD}) from Unified Surface Model (ZWD_m). The Values Given with in the Bracket are Standard Deviations (σ) of the Absolute Difference

Stations	<i>rms</i> deviation ($\pm \sigma$) (cm)		Max. Abs. deviation (cm)	
	ΔZWD_{IRTD}	ΔZWD_{WTD}	ΔZWD_{IRTD}	ΔZWD_{WTD}
Trivandrum	3.3 (± 2.7)	9.0 (± 3.8)	16.7	24.5
Portblair	3.8 (± 2.8)	8.2 (± 4.7)	15.6	18.2
Bangalore	3.6 (± 2.8)	5.1 (± 3.3)	17.8	19.5
Mangalore	5.2 (± 3.8)	9.4 (± 4.4)	19.7	22.7
Chennai	5.0 (± 3.6)	6.4 (± 4.3)	20.8	22.7
Goa	5.4 (± 4.0)	8.2 (± 4.5)	19.0	20.1
Hyderabad	4.8 (± 3.6)	6.2 (± 3.4)	19.6	18.4
Vishakhapatnam	9.0 (± 4.6)	10.3 (± 6.2)	21.1	26.3
Mumbai	4.4 (± 3.5)	7.4 (± 3.9)	20.0	18.4
Kolkata	7.5 (± 4.9)	9.5 (± 6.2)	23.0	26.0
Ahmedabad	5.8 (± 4.6)	8.0 (± 3.8)	22.5	20.0
Bhopal	6.3 (± 4.4)	7.2 (± 3.5)	18.1	17.4
Guwahati	5.9 (± 4.1)	7.2 (± 5.2)	24.8	26.0
Jodhpur	7.8 (± 4.8)	10.0 (± 4.7)	24.0	22.0
Lucknow	6.0 (± 4.4)	7.0 (± 4.6)	25.0	25.0
Delhi	6.3 (± 5.9)	7.0 (± 6.0)	29.5	33.6
Patiala	5.6 (± 4.7)	6.2 (± 5.0)	22.5	27.6
Srinagar	2.6 (± 3.1)	31.8 (± 7.5)	25.7	49.7

such extreme residuals (~ 42 cm) at La Paz, Mexico, due to extremely large values of wet delay (~ 70 cm) associated with the passage of a tropical cyclone (Hurricane Flossie).

Localized and short lived changes in weather systems could vary the tropospheric delay both temporally and spatially. To account for such short lived and severe variations in tropospheric delay, real-time meteorological measurements are to be incorporated in the models. Thus the periodic models (like IRTD, WTD, *etc.*) fail significantly in such situations. A detailed comparison of WTD and IRTD models on a day-to-day basis with ZHD and ZWD estimated from Unified Surface models shows that the IRTD model predicts the mean hydrostatic component fairly well for all the locations over the Indian sub-

continent for different seasons with mean absolute difference < 0.6 cm, while the deviation of the WTD (< 3 cm) is three times higher (Table 4.3). The deviation of ZWD is ~ 3 -9 cm for IRTD model and ~ 5 -11 cm for WTD model except at Srinagar, where the deviations are extremely high (~ 31.8 cm), notwithstanding the fact that the phase of the annual variation predicted by WTD leads approximately by a month. The IRTD model estimates are found to be more close to the Unified surface model estimates over the Indian subcontinent.

Table 4.5: The Mean and Standard Deviation of Absolute Difference and Maximum Absolute Deviation of IRTD Model (ZTD_{IRTD}) from Ray-traced ZTD (ZTD_{TRUE}). The Number of Good Profiles which could be Used for this Comparison is also Given in Last Column. Stations with Bold Face are the RIM Stations

Station	Abs.($ZTD_{\text{IRTD}} - ZTD_{\text{TRUE}}$)			
	Mean (cm)	Standard deviation (cm)	Maximum (cm)	No. of good profiles in 3 years
Trivandrum	5.9	4.3	18.8	216
Portblair	5.7	4.6	17.8	58
Bangalore	9.4	4.5	20.6	67
Mangalore	5.3	4.4	22.4	173
Chennai	5.5	4.3	22.0	196
Goa	6.2	4.5	17.2	25
Hyderabad	11.7	7.1	35.0	136
Vishakhapatnam	6.5	4.4	18.2	92
Mumbai	10.7	6.8	22.8	12
Kolkata	10.1	5.5	26.5	170
Ahmedabad	6.7	4.8	24.3	89
Bhopal	10.9	7.0	23.6	20
Guwahati	2.3	0.8	3.8	198
Jodhpur	10.9	7.4	29.1	44
Lucknow	8.6	5.6	24.8	80
Delhi	8.6	6.2	27.7	167
Patiala	5.4	3.6	11.1	8
Srinagar	5.4	4.4	17.4	35

4.4 Validation of IRTD Model by Comparing it with True ZTD

The IRTD model is further validated with the true value of ZTD obtained by ray-tracing the refractivity profiles obtained from regular radiosonde data. Table 4.5 summarizes the comparison between the ZTD obtained from IRTD model (ZTD_{IRTD}) and that estimated

by ray-tracing (ZTD_{TRUE}). The second column provides with the values for the mean of the absolute difference between the two estimates, along with their standard deviations in the third column. The maximum deviation of the IRTD model from the true values of ZTD is also reported in the fourth column. The last column shows the number of the available good data employed for deriving the statistics. For some stations the availability of good profiles is not enough to arrive at a better statistical conclusion (*e.g.* Patiala). For most of the stations the mean absolute deviation is <10 cm, except at Hyderabad, Mumbai, Kolkata, Bhopal and Jodhpur. The maximum value of absolute difference is as low as 3.8 cm (for Guwahati) and can be up to 35 cm (for Hyderabad).

4.5 Summary

A region specific tropospheric delay model for Indian region which is independent of any measured atmospheric parameters is developed. This model named as the IRTD model, has a 5° latitudinal interval and also accounts for the seasonal variation even below 15°N , which is significant for the stations in the Indian peninsula. The IRTD model performs much better than the currently available WTD model over the Indian subcontinent and adjoining regions. Both the periodic models (IRTD and WTD) have limitations to account for the large variations in tropospheric delay caused by extreme and severe weather conditions. Comparison of IRTD estimated ZTD with that obtained from ray-tracing the refractivity profiles shows that IRTD model predicts the delay with an accuracy of ~ 10 cm.

Chapter 5

TROPOSPHERIC DELAY FROM GROUND BASED GPS AND COMPARISON WITH MODEL ESTIMATES

5.0 Introduction

A ground based GPS receiver tracking the transmissions from a cluster of GPS satellites are successfully used in pin-pointing its co-ordinate employing appropriate triangulation and subsequent inversion of the derived range information. This technique is well established in geodetic applications to measure the continental drift. As a by-product from these studies a residual component in the range information is extracted which is attributed to the extra path length due to tropospheric delay. As may be noted, this delay is estimated based on the accurate measurement of pseudo range using network of receiver sites distributed at different locations (which includes inter-continental baselines) tracking simultaneously each orbiting satellites and subsequent inversion of their precise position. Such GPS data from different parts of the globe is freely available throughout the day from the International GPS service (IGS) stations.

The IGS stations formally established by the International Association of Geodesy (IAG) in 1993 (officially started its operations on January 1, 1994) is composed of more than 400 globally distributed permanent GPS tracking sites, three Global Data Centers, five Operational or Regional Data Centers, seven Analysis Centers, an Analysis Center Coordinator, and a Central Bureau. Each IGS site of the global network operates a dual-frequency GPS receiver that records the continuous transmission from the GPS satellite averaged at 30-second intervals. The Jet Propulsion Laboratory (JPL) serves as its Central Bureau since 1999 and the Center of Orbit Determination in Europe (CODE) serves as the Analysis Center Coordinator. There are three IGS stations in India, two are at Bangalore and one is at Hyderabad. In the present analysis the GPS data from Bangalore and Hyderabad downloaded from the IGS website are used for estimating the tropospheric delay. Analysis of this data essentially requires the GPS data processing software, which is used for high precision geodetic measurements. The GAMIT 10.2 [MIT and SIO, 2000] software package developed collectively by Massachusetts Institute of Technology (MIT) and Scripps Institute

of Oceanography (SIO) is used in the present study to estimate 3-Dimensional relative positions of ground points and satellite orbits from GPS data.

5.1 Processing of GPS Data

In general, different IGS stations use different types of GPS receivers which store the data in different binary format. To use from a common platform, it is essential to convert this data into a standard readable format. The first step involved in this analysis is to convert these binary files from different GPS receivers into a Receiver Independent Exchange (RINEX) format. The RINEX is a standard ASCII translation of the compressed receiver binary data file. The RINEX version 2.10 employed in the analyses defines six different RINEX files; (1) Observation data file, (2) Navigation message file, (3) Meteorological file, (4) GLONASS navigation message file, (5) geostationary satellite data files, and (6) satellite and receiver clock data files, each containing a header and data section. Along with RINEX data the GPS analysis also requires the broadcasted ephemeris data (BRDC files) and G-files information. The GAMIT 10.2 software, used to analyze the GPS data, estimates the orbital parameters of the satellites, solves for transmitter and receiver positions, accounts for Ionospheric delays, phase cycle ambiguities and clock errors following the differencing and double differencing techniques, in addition to solving for Tropospheric delay parameters along the line of sight up to the satellite. This tropospheric delay is then mapped to zenith direction using appropriate mapping function to yield ZTD. In solving for ZTD and other parameters using a constrained batch least-squares inversion procedure it uses different types of data files, like station coordinates, broadcast ephemeris for the satellite observed, phase and pseudo range observations, auxiliary information regarding the instrumentation. The GPS receiver data is arranged in different groups usually organized into sessions spanning 24 hour covering a single UTC day. These sessions are defined by spans in which a group of receivers simultaneously tracks the phases of two or more satellites or vice versa. The data and other information are arranged in the prescribed formats for each session and are analyzed individually or combined with other sessions to estimate the required parameters.

In order to estimate ZTD using GAMIT, both functional and stochastic models of GPS are to be properly defined. While the functional model describes the mathematical relation between the GPS measurement and the unknown parameters, the stochastic model describes

the statistical properties of the measurements, which are mainly defined by an appropriate covariance matrix indicating the uncertainty of, and the correlations between, the measurements [Rizos, 1997; Brunner *et al.*, 1999]. The linear observation model for GPS can be written as:

$$\mathcal{P} = \mathbf{A} \times \ddot{\mathbf{O}}_{xyz} + \mathcal{O} \quad (5.1)$$

where \mathcal{P} is the vector of observations in GPS phase measurements, \mathbf{A} is the observations' matrix, $\ddot{\mathbf{O}}_{xyz}$ is the vector of unknown parameters including three-dimensional station position or baseline distances, station clock offsets, tropospheric delay, satellite clock and orbits and phase ambiguities, and \mathcal{O} is the measured white noise. The most commonly used techniques in GPS analyses to estimate the parameters in $\ddot{\mathbf{O}}_{xyz}$ are either Kalman filtering or a piecewise linear least-squares (LS) solution method.

The GAMIT software parameterizes ZTD as a stochastic variation from the Saastamoinen model with a piecewise linear interpolation [King and Bock, 2000]. The variation is currently constrained to be a first-order Gauss-Markov (GM) process with a special power density (zenith parameter constraint) of 2 cm/sqrt (hour). This first-order GM process is used under the assumption that all the GPS measurements have the same variance. In some cases the baseline components may also be stochastically constrained. In standard stochastic models, it is assumed that all the carrier phases or pseudo ranges have the same variance and are statistically independent. Therefore, the observations are treated as independent and uncorrelated.

The least-squares estimation is a piecewise LS technique where the observations are divided into segments of a specified time length. The normal LS solution to eq. (5.1) is:

$$\ddot{\mathbf{O}}_{xyz} = (\mathbf{A}^T \mathbf{B}^{-1} \mathbf{A})^{-1} \mathbf{A}^T \mathbf{B}^{-1} \mathcal{P} \quad (5.2)$$

where \mathbf{B} is the measurement noise of covariance matrix. In this piecewise LS technique the observation series, \mathcal{P} , is divided in segments, \mathcal{P}_i , of a specified length. These segments are treated separately and estimation is performed for the unknown parameters using the observations for the particular segment only. The solutions are then combined to get the estimates for the whole time series. The dominant measurement errors in GPS analyses are those caused by the multipath, ionosphere and orbit effects. These errors are quite different for each satellite. Therefore, the measurements obtained from different satellites cannot have the same accuracy due to varying noise levels [Wang *et al.*, 1998]. Studies in precise GPS

positioning have shown that unrealistic stochastic models may lead to errors of up to 10-15 mm in the height components [Satirapod *et al.*, 2002]. Therefore, selection of proper stochastic model has a significant impact on precise estimation of ZTD. The GPS measurement is made along the line of sight from the ground station to the satellite. Niell mapping functions [Niell, 1996] for hydrostatic and non-hydrostatic components of the delay are used in GAMIT for mapping the measured tropospheric delay to the zenith direction. Various studies have shown that this mapping function is less sensitive to the lower limit of elevation angles compared to other mapping functions [Niell, 1996].

The GAMIT have options for manual, batch and automatic processing. In this analysis the automatic processing scheme, which enables easy handling of the data and analysis of the results is adopted. Another main reason for opting the automatic batch processing is the voluminous amount of GPS data to be processed. Figure 5.1 illustrate a schematic presentation of the GAMIT data processing scheme in a simple block diagram. On completing the processing for each day, a summary of the information regarding the number of stations used, the normalized *rms* values from the output file, the *rms* of the one way phase residuals for the best and worst stations as well as a list of any major adjustments done in the station coordinates are given as the output. This summary provides an idea about the quality of the processing and helps the user to use the GAMIT output for further analyses.

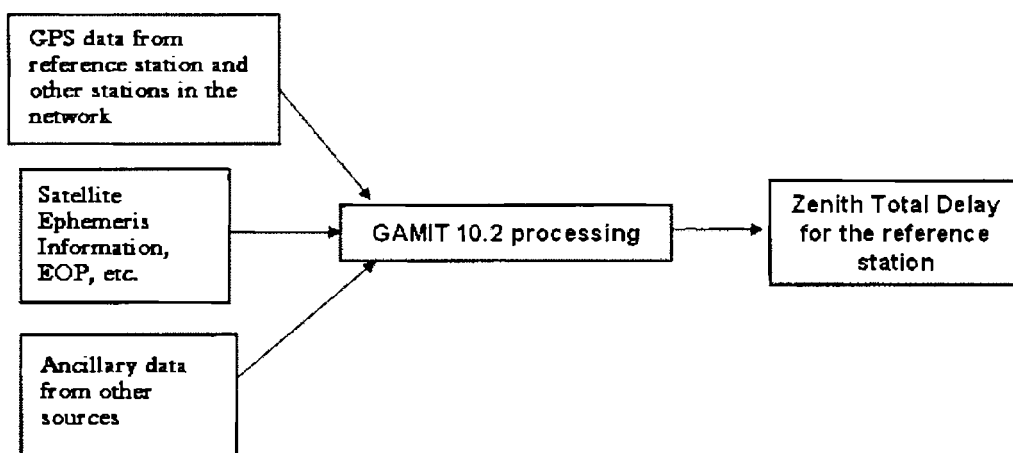


Figure 5.1: Schematic representation of GPS data processing using GAMIT

5.1.1 Optimization of IGS Stations in GAMIT Analysis

The choice of stations to be included in the network used for GPS analyses is of utmost importance because the accuracy of ZTD thus estimated strongly depends on the composition of the stations employed in the LS batch fitting process. A centered network is easy to compose and may serve a good job if the user is mainly concerned in parameters related to the particular station at which the baselines are centered. In the present study to initiate the analysis the network of stations are selected keeping the IGS stations at Bangalore and Hyderabad at the center. The other stations are selected such that they lie around the two stations. Based on this an experimental analysis is performed with GAMIT and optimization is carried out by changing the combination of other IGS stations selected which are mostly located over the Asian continent, Indian Ocean and Arabian Sea regions. In the initial phase 22 stations are selected based on availability and baseline geometry, which are presented in Table 5.1a. As the IGS station network over the Indian subcontinent is rather poor, the stations are selected keeping in mind the fact that inclusion of baseline of more than 2000 km is essential to achieve better accuracy of GPS estimation [Tregoning *et al.*, 1998].

Table 5.1a: A List of 22 Stations used in the Initial Phase of GAMIT Analysis for Optimization Study Carried on Keeping IISC (India) at the Center of the Network. The Stations are Arranged Such that the Stations which are Eliminated in Each Trial Appear Sequentially from the Lower End of this Table

S. No.	IGS Station (Country)	S. No.	IGS Station (Country)
1	HYDE (India)	12	COCO (Australia)
2	LHAS (China)	13	URUM (China)
3	KIT3 (Uzbekistan)	14	MALI (Kenya)
4	NTUS (Singapore)	15	SEY1 (Seychelles)
5	POL2 (Kyrghyzstan)	16	KUNM (China)
6	BAHR (Bahrain)	17	TEHN (Iran)
7	SELE (Kazakstan)	18	GUAO (China)
8	WUHN (China)	19	CHUM (Kazakhstan)
9	SHAO (China)	20	DGAR (Diego Garcia)
10	MALD (Maldives)	21	PIMO (Philippines)
11	BAKO (Indonesia)	22	MBAR (Uganda)

The GPS data collected from all these 22 stations are processed for seven continuous days. From the output, the stations are arranged into a set of best and worst stations based on the quality of data used to perform the analysis depending on noise and bias components embedded in the data. From this, those stations having maximum post fit *rms* residual scatter

and large number of cycle slips (bias flags) are identified and removed. The analysis is repeated using the remaining stations. This iterative removal process is continued until a combination of stations having least post-fit *rms* error < 5 mm is attained with maximum data availability (with less cycle slips) from the satellite for each session. The summary of the analysis on optimization study is presented in Table 5.1b. By systematic removal of stations having erroneous and less correlated data, the number of stations included in the processing is sequentially reduced to 9 through different steps. As can be seen from the table the residual *rms* scatter reduced from 7.2 mm to 5 mm through this elimination process. The number of double difference statistics also decreases with decrease in number of stations, mainly because of the fact that the amount of data epochs decreases with the decrease in the number of stations included in the network.

Table 5.1b: Optimization Study Results for the Selection of Stations

Number of stations used for processing	Average post-fit <i>rms</i> to and by satellite (mm)	Double difference statistics. Post-fit <i>nrms</i> values	Number of double differences
22	7.2	0.19708	54821
20	6.5	0.18916	51711
15	6.5	0.18745	41314
10	5.8	0.19960	26034
9	5.0	0.20462	21087
6	5.0	0.20449	11525

From Table 5.1b, it can be seen that processing the GPS data using either 6 or 9 stations in the network give similar results in terms of post fit *nrms* (column 3) and residual *rms* statistics (column 2). Since the data epochs are less, the number of double differences in the processing is very small in the case when 6 stations are used. The number of double difference data becomes almost double in the case when data from 9 stations are used. This is quite significant in mitigating other errors. Note that there is no significant improvement in number of double differences statistics by including data from 10 stations and in fact, the addition of one more station has actually degraded the accuracy of analysis as seen in column 2 of Table 5.1b. On the other hand, when the processing is carried out using data from 5 or 4 stations, the results are significantly inferior in terms of post-fit *rms* statistics and residual *rms* statistics. From this study it is concluded that the GAMIT analysis carried out using a combination of nine stations in the network yields results with optimum accuracy. The selected stations along with their geographical locations and their distance

from Bangalore are presented in Table 5.2. A pictorial illustration of the location of these stations is presented in Figure 5.2.

Table 5.2: A List of IGS Stations used in the Present Study Along with the Geographical Location of Each Station and Distances from Bangalore

Location	Latitude ($^{\circ}$ N)	Longitude ($^{\circ}$ E)	Ellipsoidal Height (m)	~ Distance From Bangalore (km)
IISC (India)	12.95	77.68	800.00	0.0
HYDE (India)	17.25	78.33	441.68	483.68
LHAS (China)	29.66	91.10	3622.00	2313.78
KIT3 (Uzbekistan)	39.14	66.88	640.00	3083.36
NTUS (Singapore)	1.35	103.68	79.00	3122.63
POL2 (Kyrgyzstan)	42.68	74.70	1714.20	3295.81
BAHR (Bahrain)	26.21	50.61	-17.03	3167.14
SELE (Kazakstan)	43.18	77.02	1340.00	3338.27
WUHN (China)	30.53	109.22	25.80	3739.62
SHAO (China)	31.09	121.20	22.21	4781.89

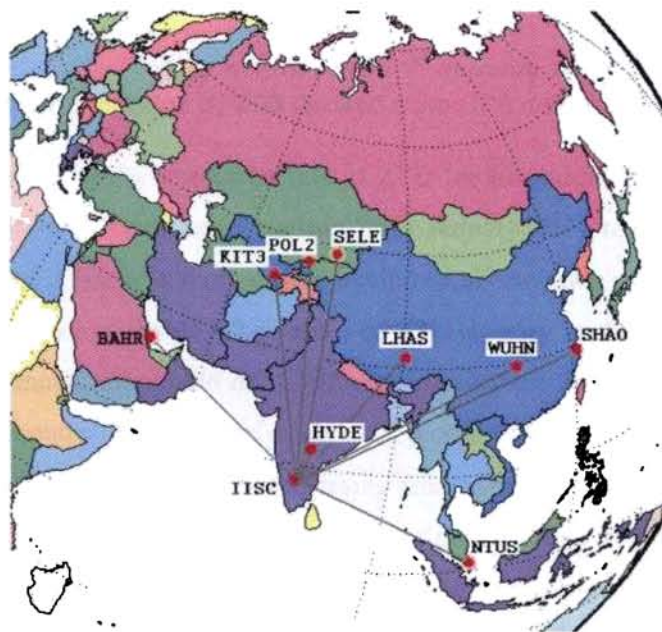


Figure 5.2: The network of IGS stations in and around Bangalore

5.1.2 Estimation of ZTD from GPS Data

In the analysis of GPS data, the GAMIT 10.2 uses the raw data in RINEX format at 30 seconds interval for a period of two hours keeping a threshold cut off of 10° for the satellite elevation angle mainly to minimize the multipath error. This shows that each data segment going in to the GAMIT analysis spans for a period of 2 hrs and the software gives one value of ZTD as output for the desired station (Bangalore or Hyderabad as the case may be). This

allows 12 values of ZTD over a day separated by a time interval of 2 hrs. This is the basic resolution of ZTD obtained from this GPS analysis.

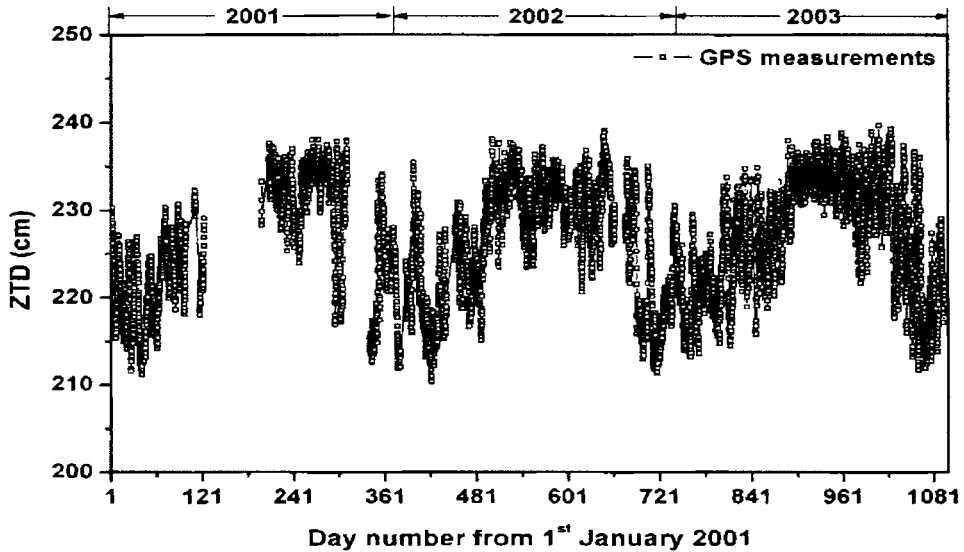


Figure 5.3: Day-to-day variation of ZTD derived from GPS data for the period 2001-2003

The Figure 5.3 shows a time series plot of ZTD for Bangalore derived from GPS data (ZTD_{GPS}) for a period of three years starting from January 2001 to December 2003. The seasonal variation of ZTD_{GPS} is more or less similar in all the three years. In May and June 2001, GPS data was not available. The values of ZTD_{GPS} vary in the range 210 cm to 240 cm amounting to annual amplitude of $\sim \pm 15$ cm. Low values of ZTD_{GPS} are encountered during the winter months (with a mean of about 220 cm). From a lowest value of < 215 cm in February the value of ZTD_{GPS} starts increasing from April reaching a mean high plateau value of about 235 cm during the summer monsoon period (June to October). The day-to-day variability in general is large during winter months compared to that during the monsoon period which then could possibly be attributed to the corresponding variation in the non-hydrostatic component of ZTD.

5.1.3 Comparison of GAMIT Derived ZTD with the IGS Operational Product

As detailed above, the accuracy of ZTD retrieved from GPS data depends on the data quality as well as the network of stations used in the analysis. In order to evaluate the accuracy of the present analysis the values of ZTD_{GPS} estimated using the GAMIT (ZTD_{GAMIT}) is compared with those reported by IGS on their sites at SOPPAC/CSRC

archive available at <http://garnet.ucsd.edu/pub/troposphere/>. Two hourly values of ZTD_{GAMIT} for Bangalore for the year 2002 is used along with the corresponding values of

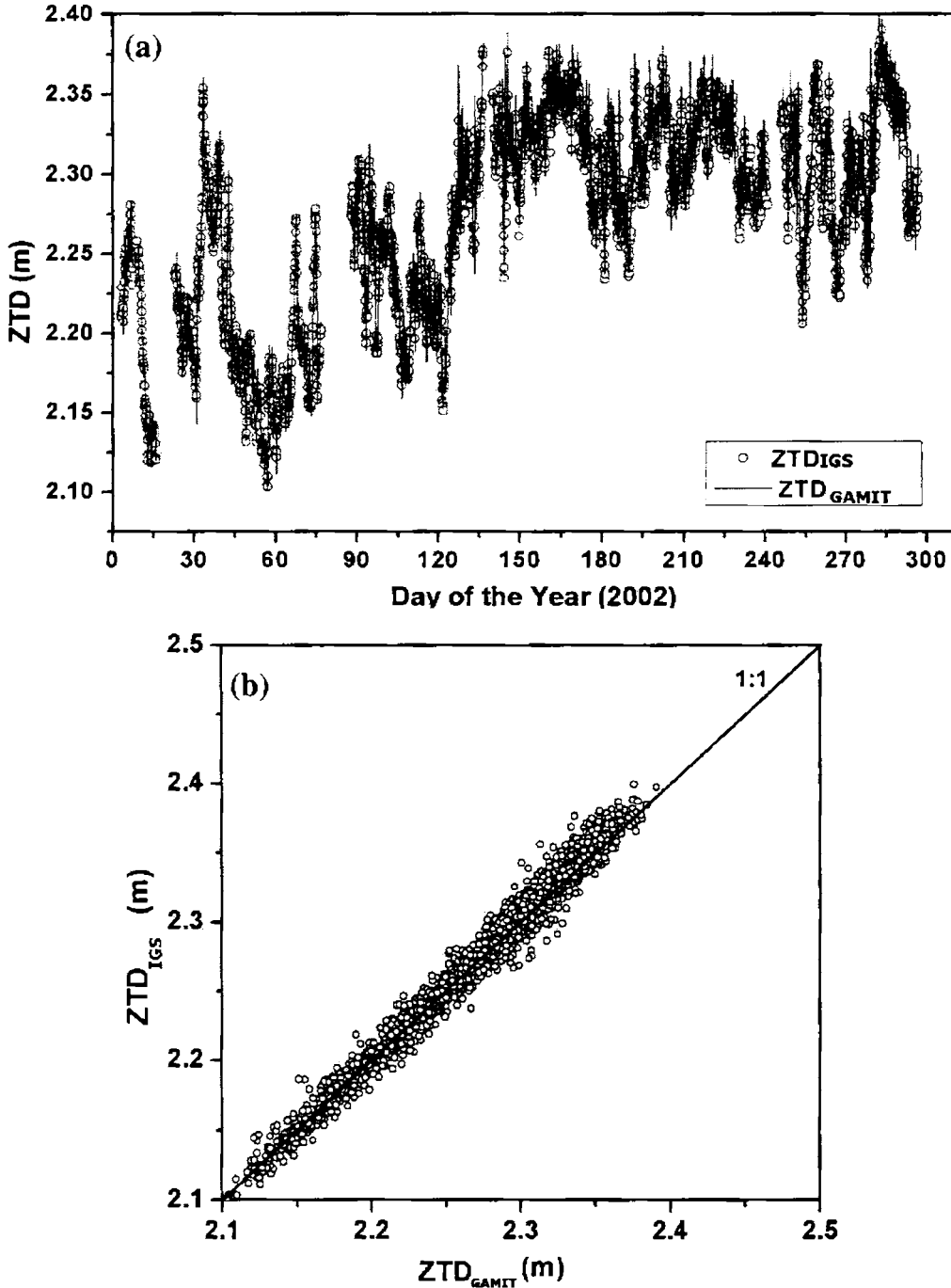


Figure 5.4 (a & b): A comparison of zenith delay estimated using GAMIT 10.2 (ZTD_{GAMIT}) for Bangalore with that estimated by IGS (ZTD_{IGS}) downloaded from the IGS web site. A time-series comparison for different days in 2002 (a), and a value-by-value comparison for the same data (b). The unit-slope line also is shown in the base panel to illustrate the amount of deviation between the two

ZTD downloaded from the IGS website (ZTD_{IGS}) is used for this purpose. Figure 5.4a shows a time series plot of the two on a day-to-day basis in which two different colors are used to distinguish the two curves. The values of ZTD_{GAMIT} are plotted with continuous curve (grey) without symbols and the corresponding values obtained from IGS site are plotted (in red) with symbols but no lines to join them. As can be seen from the figure the deviation of these symbols from the curve is almost insignificant through out the period. For a more quantitative comparison, a scatter plot of the two generated by plotting the ZTD_{IGS} against corresponding values of ZTD_{GAMIT} is presented in Figure 5.4b along with the unit slope line. As can be seen the points are mostly aligned to the unit slope line, a very small scatter indicating a fairly good agreement between the two. The mean absolute difference between the two is < 8 mm. This small difference between the two could mostly be attributed to the difference in the software used for processing the data in the two cases and/or due to the difference in the IGS stations incorporated (in the network) for the analysis of GPS data. Difference in the operating system (UNIX/LINUX) could also be one of the factors responsible for this small deviation. However, within these constraints the difference between the two can be treated as insignificant.

5.2 Comparison of ZTD Derived from GPS Measurements with those Estimated using Unified Models

In order to assess the accuracy of the Unified models the values of ZTD estimated based on relevant surface meteorological parameters is compared with the corresponding values derived from GPS measurements. Figure 5.5 shows a time-series plot of daily ZTD values derived from GPS measurements at Bangalore along with the corresponding values estimated using the Unified Surface model (eq. 3.10 and eq. 3.12) and Unified Hopfield model (eq. 3.14) for a period of 2 years starting from January 2003 as a typical example. Both these models though agree fairly well with the GPS measurements in most of the days, in an average the model values are slightly larger than the ZTD derived from GPS measurements. This indicates that in most of the cases both the models overestimate ZTD, which is particularly common during the winter season. A direct comparison of the two is accomplished by plotting the model-derived ZTD against the corresponding values obtained from GPS measurements. A scatter plot thus obtained for surface model with GPS measurement is shown in Figure 5.6a and that obtained for the Hopfield model with the GPS

measurement is shown in Figure 5.6b along with the unit slope line to illustrate the deviations.

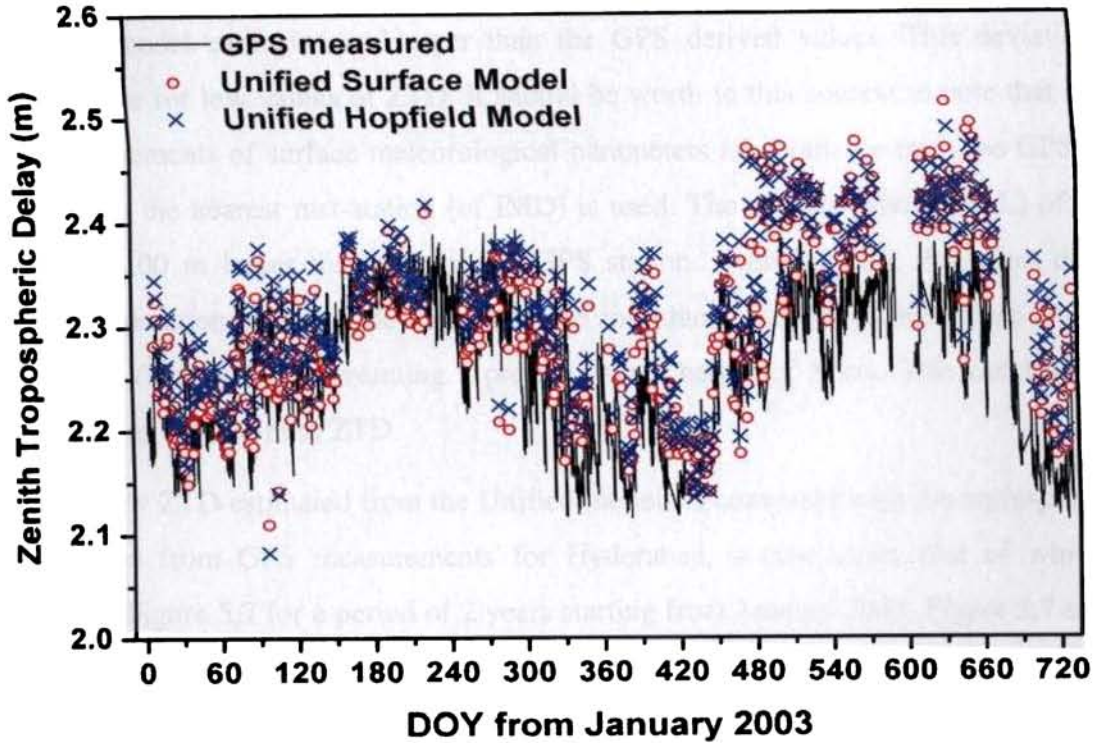


Figure 5.5: A time series plot of daily ZTD derived from GPS data for Bangalore along with the corresponding plots of ZTD derived using the two unified models (Unified Surface model and Unified Hopfield model)

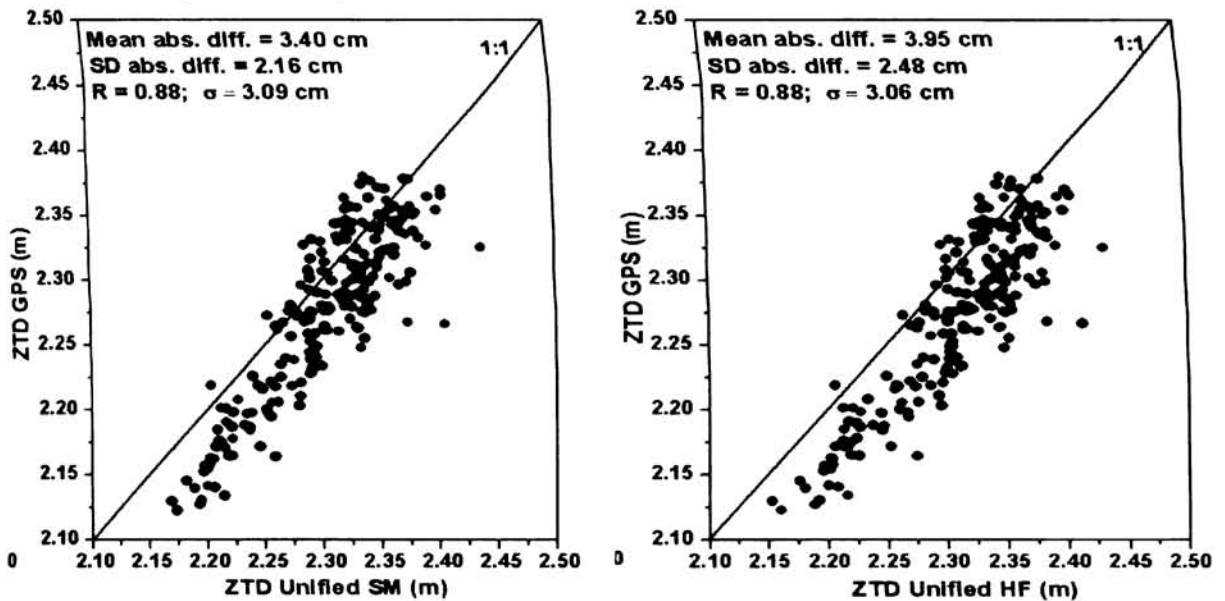


Figure 5.6: Scatter plots of GPS derived ZTD verses model derived values for Bangalore on different days during the period January 2001 to October 2002, a time series of which is shown in Figure 5.5; Unified Surface model verses GPS derived values (a) and Unified Hopfield model verses GPS derived values (b). The diagonal is the unit slope line

The mean absolute difference is of the order of 3.4 to 4.0 cm with a standard deviation of ~ 2 cm. More numbers of points are aligned below the unit slope line indicating that in general the model estimates are larger than the GPS derived values. This deviation is relatively large for low values of ZTD. It should be worth in this context to note that as no direct measurements of surface meteorological parameters are available from the GPS site, the data from the nearest met-station (of IMD) is used. The altitude (above MSL) of IMD station is ~ 100 m larger than that of the GPS station. Even ignoring the effect due to horizontal separation, this altitude difference can introduce a difference in surface pressure by ~ 10 hPa (less at IMD) assuming a pressure scale height of 8 km. This can lead to a positive bias of ~ 0.023 m in ZTD.

Similarly ZTD estimated from the Unified models is compared with the corresponding value derived from GPS measurements for Hyderabad, a time-series plot of which is presented in Figure 5.7 for a period of 2 years starting from January 2003. Figure 5.7 shows that the annual mean of the ZTD is ~ 2.4 m, which is higher than that at Bangalore.

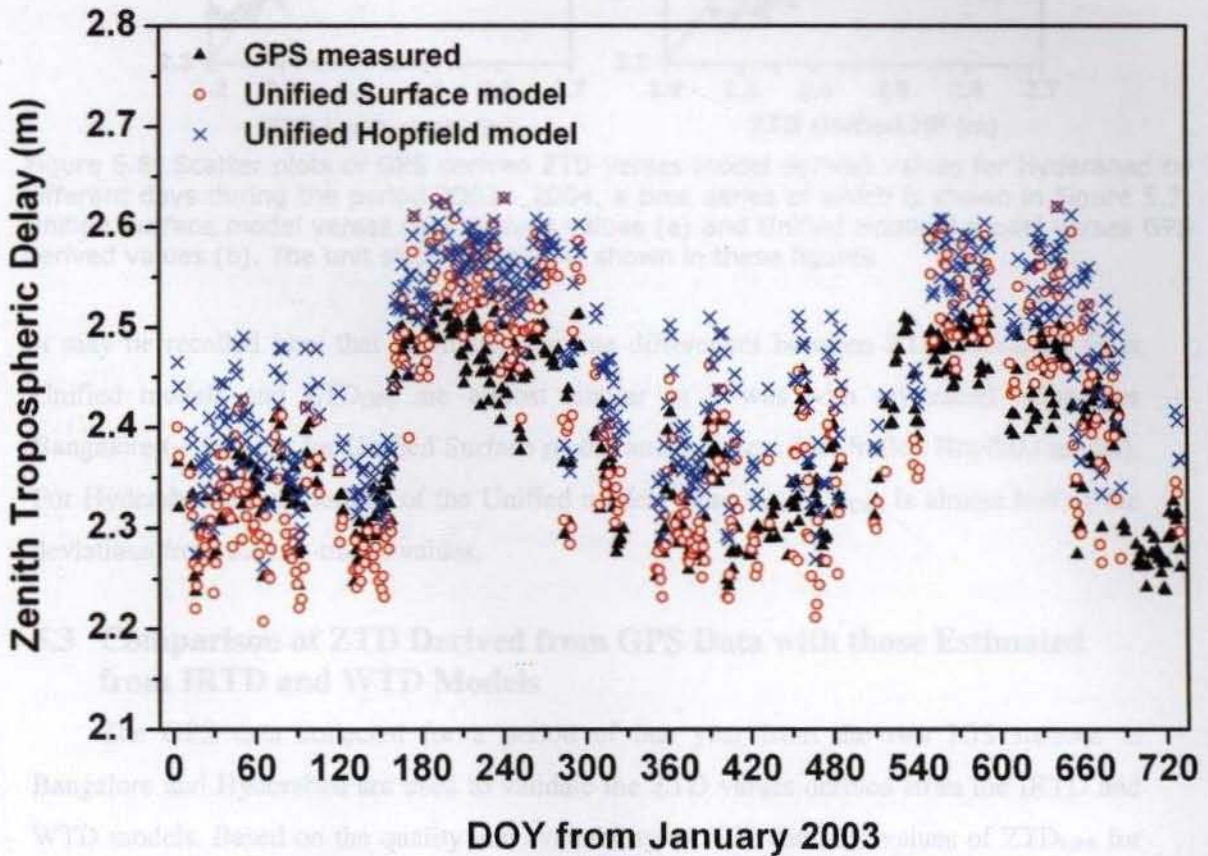


Figure 5.7: A time series plot of daily ZTD derived from GPS data for Hyderabad along with the corresponding plots of ZTD derived using the Unified Surface model and Unified Hopfield model

Figure 5.8 shows scatter plots of ZTD estimated from GPS data with the two Unified models. This shows that for Hyderabad the Unified Surface model estimates better than the Unified Hopfield model. The mean absolute difference is 4.37 ± 3.25 cm for Unified Surface model and 7.4 ± 3.7 cm for Unified Hopfield model. Moreover, the ZTD values estimated using Unified Hopfield model is biased throughout the period.

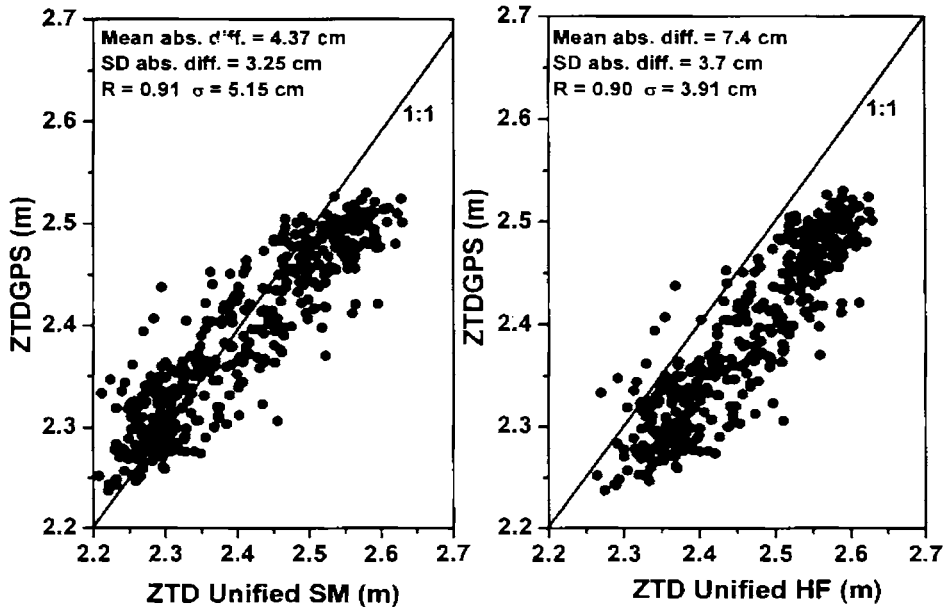


Figure 5.8: Scatter plots of GPS derived ZTD verses model derived values for Hyderabad on different days during the period 2003 - 2004, a time series of which is shown in Figure 5.7; Unified Surface model verses GPS derived values (a) and Unified Hopfield model verses GPS derived values (b). The unit slope line also is shown in these figures

It may be recalled here that the mean absolute differences between ZTD estimated from Unified models and ZTD_{GPS} are almost similar as it was with ray-traced values for Bangalore (~ 4.75 cm for Unified Surface model and ~ 4.5 cm for Unified Hopfield model). For Hyderabad the deviations of the Unified models from the ZTD_{GPS} is almost half of the deviations from the ray-traced values.

5.3 Comparison of ZTD Derived from GPS Data with those Estimated from IRTD and WTD Models

The GPS data collected for a period of one year from the two IGS stations at Bangalore and Hyderabad are used to validate the ZTD values derived from the IRTD and WTD models. Based on the quality and availability of GPS data, the values of ZTD_{GPS} for Bangalore are estimated from January 2002 while that for Hyderabad from January 2003. A

time series plot of ZTD obtained from GPS data (ZTD_{GPS}) along with those obtained from IRTD (ZTD_{IRTD}) and WTD model (ZTD_{WTD}) for Bangalore and Hyderabad are presented in Figure 5.9 (a-b). As the GPS data is processed at 2 hr interval all the 12 values of ZTD_{GPS} derived from this data on each day are averaged and the mean value is plotted in this figure. The vertical bars representing the standard deviations indicating the amplitude of diurnal variability, while the models give only one mean value for each day. As can be seen from the figure for Bangalore, the WTD model does not show any seasonal variation for ZTD as depicted by the respective value derived from GPS data. The IRTD model could provide the seasonal variation of ZTD_{IRTD} to a large extent notwithstanding the fact that the annual amplitude is slightly less (while the annual amplitude of ZTD_{GPS} is > 20 cm that for ZTD_{IRTD} is around 7 cm). For Hyderabad, which is located $\sim 5^\circ$ north of Bangalore and also at a lower altitude (~ 500 m above MSL) the values of ZTD in general are larger than that for Bangalore. The amplitude of the annual variations also is large for Hyderabad. Being located at a latitude $> 15^\circ N$, the WTD model depicts a small seasonal variation for ZTD with an amplitude of ~ 2.5 cm. The IRTD model shows significant improvement in representing the seasonal variations of ZTD (with amplitude of ~ 15 cm) while the ZTD_{GPS} shows an annual amplitude of ~ 25 cm. Quantitatively, from Figure 5.9, the *rms* deviations of the ZTD_{IRTD} from ZTD_{GPS} , for Bangalore and Hyderabad are $\sim 4.7 (\pm 3.2)$ cm and $\sim 5.2 (\pm 3.3)$ cm, respectively, while the *rms* deviations of ZTD_{WTD} are $\sim 6.0 (\pm 3.6)$ cm and $\sim 7.0 (\pm 3.6)$ cm. A detailed comparison of WTD and IRTD models on a day-to-day basis with ZTD estimated from GPS data shows that the latter model predicts the ZTD fairly well for both the IGS stations over the Indian sub-continent for different seasons. The *rms* deviation of ZTD is 4-5 cm for IRTD and 6-7 cm for WTD. But, the phase of the annual variation predicted by WTD leads approximately by a month. The IRTD model is at par if not better than the WTD model as far as the Indian sub-continent is considered.

It would be worth in this context to note that since all these region specific models (WTD, EGNOS, IRTD, *etc.*) are derived based on the mean annual variation of surface atmospheric parameters and they could deviate more from real values under abnormal climatic conditions like prolonged drought, as well as during short-term weather changes like cyclones, cloud burst, strong thunder showers *etc.* A typical example of this is observed at Hyderabad during May-June of 2003, when the region experienced an abnormal drought for a prolonged period of about 2 months. As can be seen from Figure 5.9b, the models

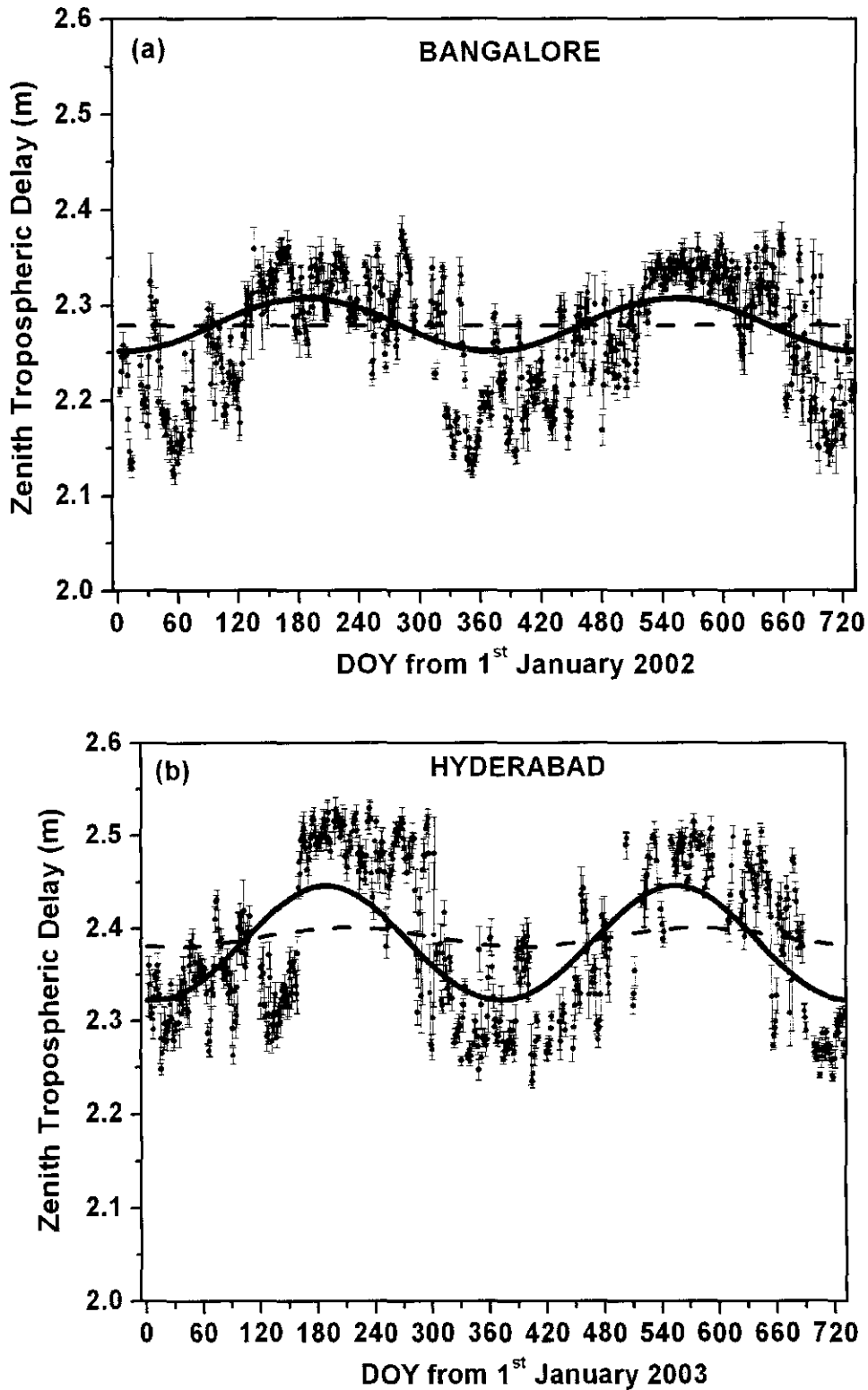


Figure 5.9: The time series plots of ZTD derived from GPS data (ZTD_{GPS}) and that estimated from IRTD (ZTD_{IRTD}) and WTD models (ZTD_{WTD}) for a period of two years for Bangalore (a) and Hyderabad (b). The ZTD_{GPS} are represented by filled circle (\bullet), ZTD_{IRTD} by solid line ($—$) and ZTD_{WTD} with dashed line ($----$)

significantly overestimate the delay at Hyderabad during these months while no such abnormality is observed at Bangalore. In this context, the surface meteorological data at Hyderabad during 2003-04 is examined. Figure 5.10 shows the day-to-day variation of P_s , T_s and e_s for Hyderabad for the years 2003 and 2004, which shows abnormally low values of e_s and high values of T_s during May-June of 2003 (compared to those during the same period in a normal year as 2004). Low water vapor content in the atmosphere has significantly reduced the wet component of the zenith delay thereby resulting in an overestimate for the model. The maximum error in ZTD estimated from IRTD model for Hyderabad during this 45 day period is ~ 15 cm. A 'rule of thumb' [MacMillan and Ma, 1994] states that an equivalent zenith atmospheric error will imply an error 3-4 times larger for the vertical coordinate. In this case 15 cm error in the ZTD means approximately 0.5 m error in the vertical positioning. For an aircraft flying above its intended height, given an unfavorable satellite constellation and unusual weather conditions, vertical position biases of up to 4 m are possible for wide-area differential users, solely due to mis-modeled tropospheric delays [Collins and Langley, 1998]. However, in such situation, the regional tropospheric delay models like Unified surface models with near real time atmospheric parameters as input is a good option.

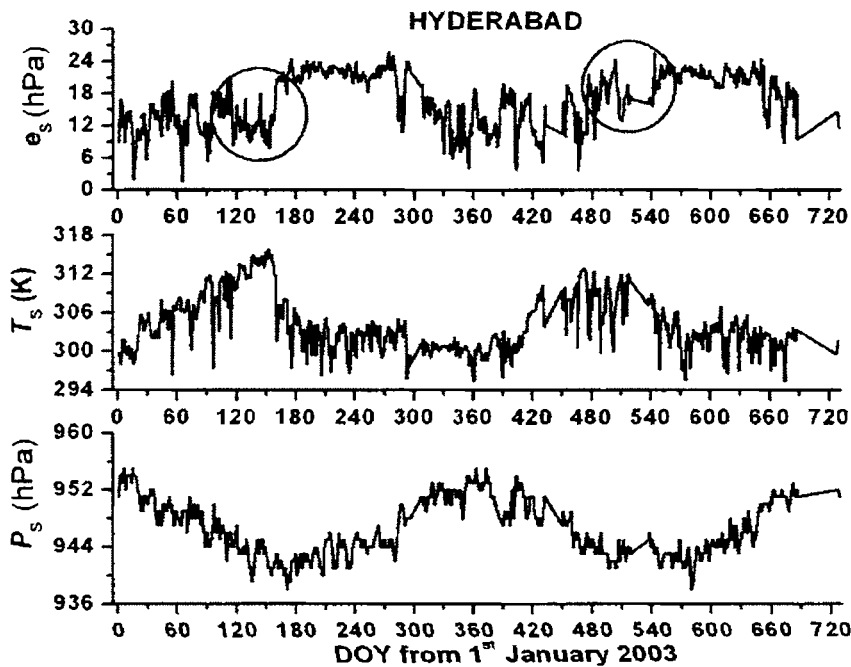


Figure 5.10: day-to-day variation of P_s , T_s and e_s for Hyderabad for the years 2003 and 2004

But when such direct measurements at that location are not available another option available for this purpose would be the NCEP/NCAR reanalysis data. So as an alternate measure the applicability of the Unified surface model with NCEP/NCAR predicted surface values (P_S and e_S) as inputs for estimating ZTD is examined. Figure 5.11 shows a time series plot for the ZTD estimated using six-hourly NCEP/NCAR reanalysis data for P_S , T_S and e_S as input to the Unified surface model along with the ZTD estimated from GPS data for different days at Hyderabad for the year 2003. On an average the agreement is fairly good especially during the extreme weather condition prevailed during May-June 2003. However, there is a general bias throughout the year, which amounts to 7 ± 4.5 cm. This bias could be attributed to the overestimation in the P_S and e_S values from NCEP/NCAR reanalysis, compared to real measurements near the surface at the GPS site. This shows that in case when measured surface meteorological data are not readily available the reanalysis data from NCEP/NCAR could be a good option. However, further routines to provide the NCEP/NCAR prediction in real-time is to be developed for this purpose.

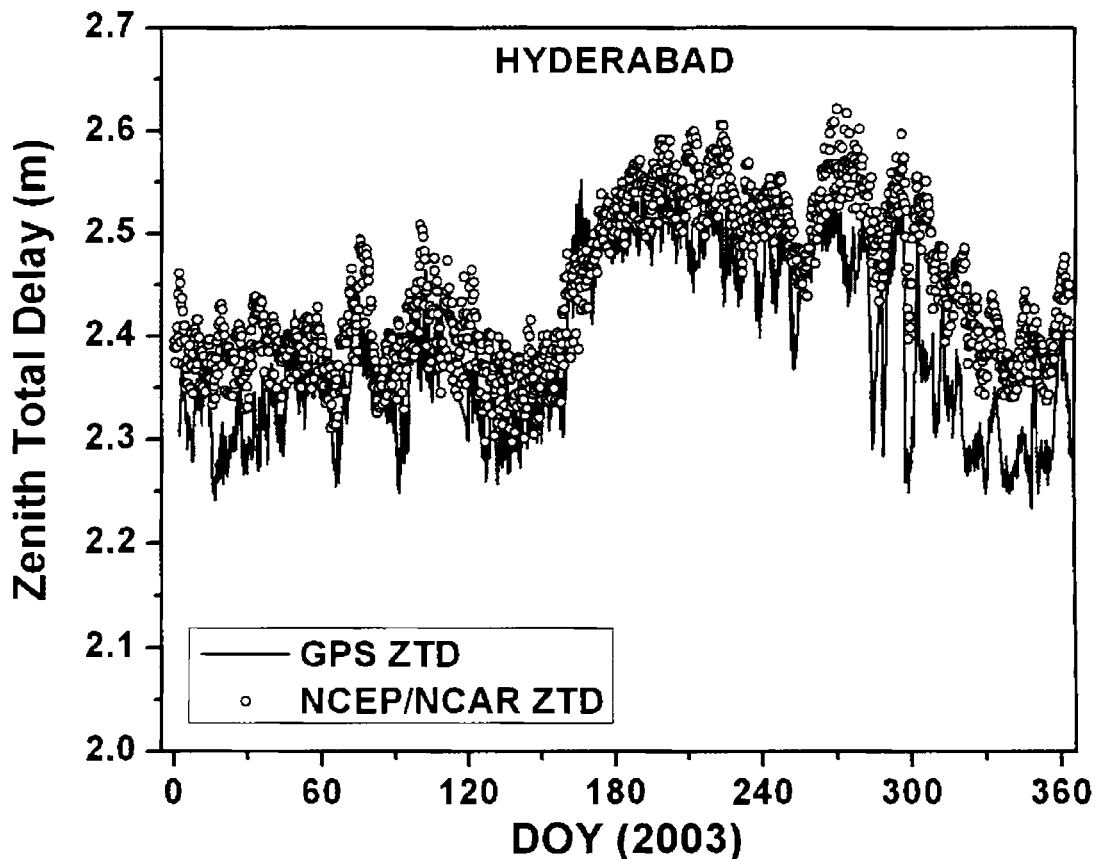


Figure 5.11: A time series plot of ZTD for the year 2003, estimated using the Unified surface model and using six-hourly NCEP/NCAR reanalysis data for P_S and e_S as input, along with that estimated from GPS data for Hyderabad

5.4 Periodic Variations in ZTD

The zenith tropospheric delay estimated from GPS measurements (as detailed in Section 5.1.2) with a temporal resolution of 2 hrs, for Bangalore and Hyderabad are examined in detail to study the associated periodic variations. This would help to understand and estimate the variability in ZTD values due to the various atmospheric oscillations. This will be important information for improving the accuracy of the periodic models (*e.g.* IRTD, WTD *etc.*). As a typical sample the temporal variation of ZTD at Bangalore for a few days in the year 2002 (starting from day number 161 to day number 171, corresponding to the month of June) is presented in Figure 5.12. This data in fact is zoomed from Figure 5.3 to illustrate the nature and amount of temporal variability. The mean value of ZTD_{GPS} during this period is ~ 235.3 cm with a standard deviation of 1.18 cm. These values are relatively small in the morning hours and increases in the afternoon. These temporal variations in ZTD_{GPS} could be attributed to corresponding changes in different atmospheric parameters (such as pressure, temperature and humidity). The amplitude of diurnal variation shows a significant variation from day-to-day (1-4 cm). As these ten days belong to June, when the South West monsoon is quite active over this region, the day-to-day variability in mean ZTD_{GPS} is rather small. A close examination of Figure 5.12 shows that the value of ZTD_{GPS} shows a peak around 18:00 UTC (corresponding to 23:30 IST) on almost all the days. The time series plots in Figures 5.3 and 5.12 show that the conspicuous components in the

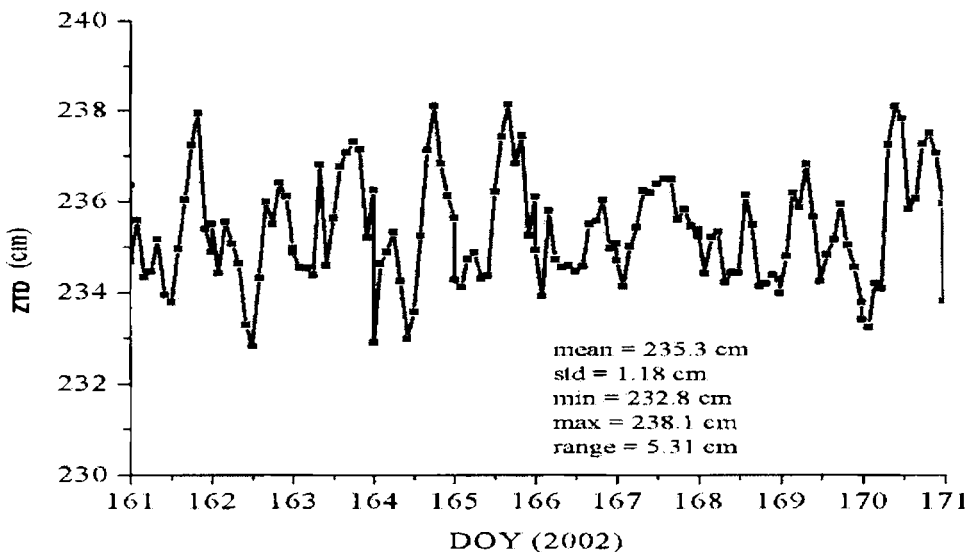


Figure 5.12: Day-to-day and diurnal variation of ZTD derived from GPS data for 10 days (DOY 161 to 171 in the year 2002)

temporal variations of ZTD_{GPS} are the diurnal, seasonal and annual oscillations. In the following a detailed analysis of these periodicities are carried out for Bangalore and Hyderabad.

5.4.1 Mean Diurnal Variations of ZTD in Different Months for Bangalore and Hyderabad

To study the mean diurnal pattern of ZTD and its month-to-month variations at Bangalore and Hyderabad (IGS stations over Indian region), the two hourly values on different days in a month are grouped, averaged and a time series plot is generated. A set of such plots generated for the year 2002 for Bangalore is presented in Figure 5.13 and that for Hyderabad is presented in Figure 5.14. Examining the diurnal variation of ZTD for Bangalore it can be seen that the diurnal amplitude is very small with its maximum value not exceeding 4 cm. This shows a pronounced variation with season. In general, the prominent peak in ZTD is observed close to midnight (22:00 IST) with a small secondary peak around 10:00 IST. Interestingly in April the diurnal variation of ZTD is almost negligible and shows a small dip close to 16:00 IST which is in contrast to other months. The diurnal amplitude is very small during the January to April period (which are mostly the dry months) and maximum amplitude is observed during June - November period. On comparing the diurnal variation of ZTD in different months for Hyderabad (Figure 5.14), it is observed that in general these diurnal patterns are more or less similar to the corresponding curves for Bangalore. A prominent peak in ZTD is observed around 22:00 IST with a small secondary peak around 10:00 IST. The amplitude of the diurnal variation is very small during the December to March period and high in June (beginning of SW monsoon) and October (beginning of NE monsoon).

This study reveals that the magnitude of the diurnal variation at these two sites depends on the availability of water vapor in the atmosphere. At both these stations, the diurnal amplitude is large during the monsoon period with minimum day-to-day variations (indicated by vertical lines) when the atmospheric water vapor content is fairly large. This indicates that the diurnal variation in ZTD could mainly be contributed by corresponding variation in the ZWD.

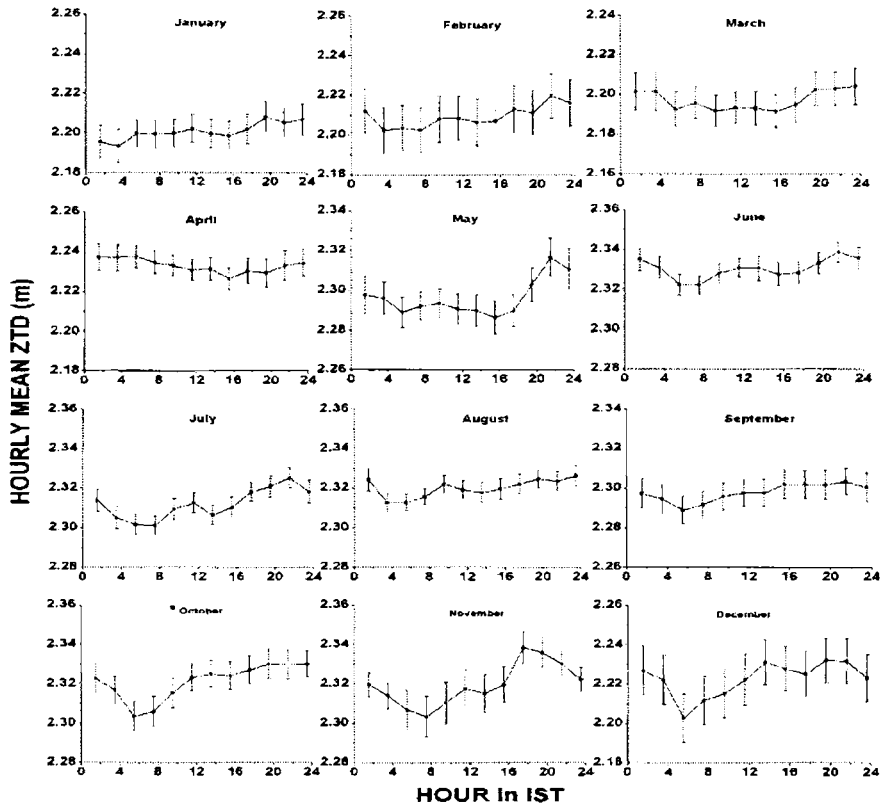


Figure 5.13: Mean diurnal variation of tropospheric zenith delay in different months for Bangalore estimated from GPS data with vertical bars showing the standard error

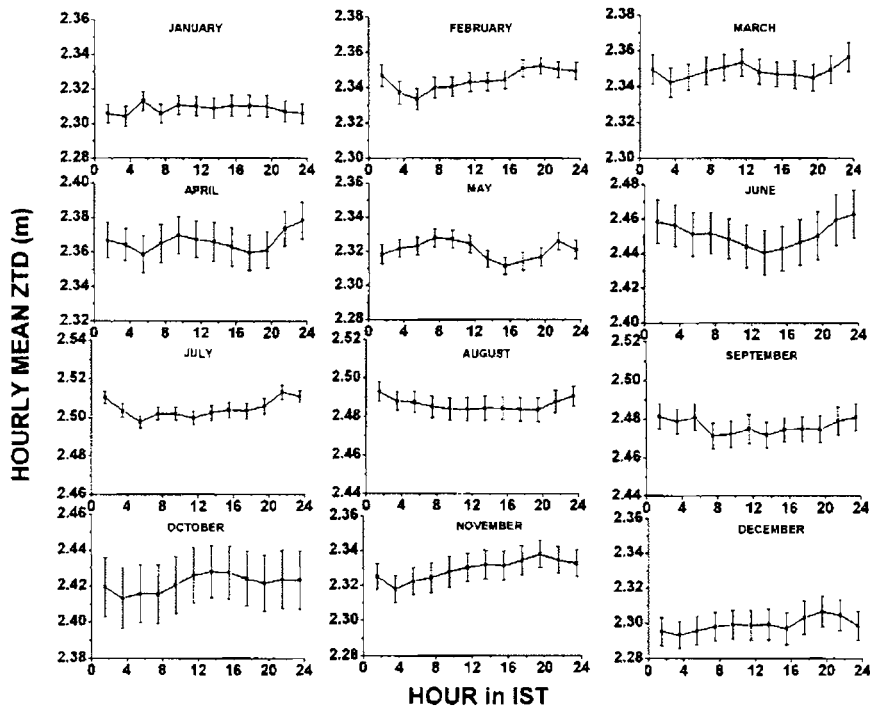


Figure 5.14: Mean diurnal variation of tropospheric zenith delay in different months for Hyderabad estimated from GPS data with vertical bars showing the standard error

5.4.2 Month-to-month (Seasonal) Variation in ZTD

To study the mean month-to-month variation of ZTD, the values of ZTD_{GPS} for a particular standard time (17:30 IST in the present case) in each month are grouped and averaged to get a mean value for that month. This is repeated for different months for Bangalore and Hyderabad. Figure 5.15 shows a plot of the month-to-month variation of mean ZTD at 17:30 IST for 2003 at Bangalore and Figure 5.16 shows the same for 2003 and 2004 at Hyderabad. A lowest value of 2.2 m is encountered at Bangalore during February and highest value of 2.33 m during the period June to November, while at Hyderabad low values of ZTD (~ 2.3 m) are encountered during December with a peak (~ 2.5 m) during July. In the year 2003 there is a dip (in ZTD) in May for Hyderabad. As detailed in Section 5.3, the year 2003 Hyderabad had an abnormally severe drought in May which lead to abnormally low values of ZTD. Except for this, the annual pattern of ZTD for the year 2003 matches fairly well with that for 2004. As seen from Figure 5.9b, 2004 is a normal year, and hence the annual variation of ZTD for this year presents the general feature of the annual variation of ZTD at Hyderabad. The net annual amplitude of ZTD for Bangalore is $\sim \pm 7.5$ cm while that for Hyderabad is $\sim \pm 10$ cm. As can be seen from these two figures, the seasonal patterns of ZTD differ at these two locations. While the value of ZTD at Bangalore

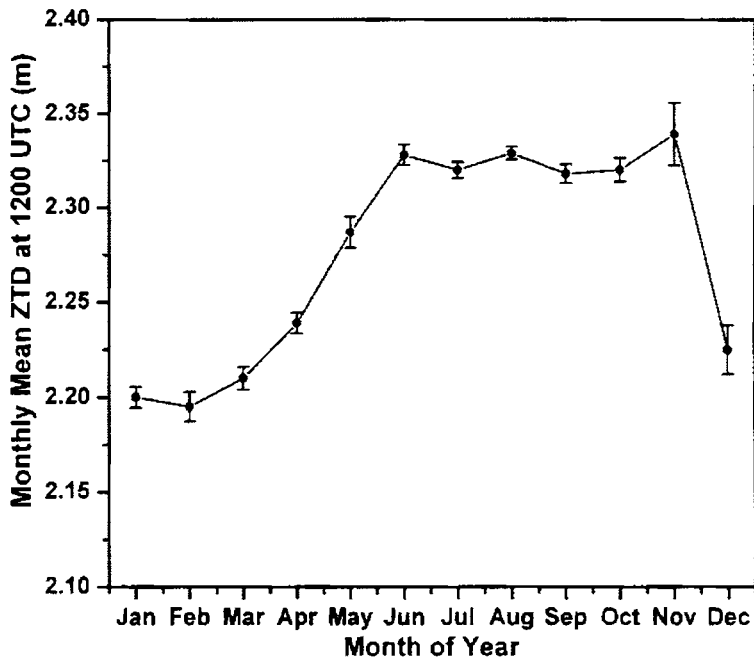


Figure 5.15: Mean annual variation of tropospheric zenith delay at 17:30 IST for Bangalore derived from GPS data (vertical bars showing the standard error)

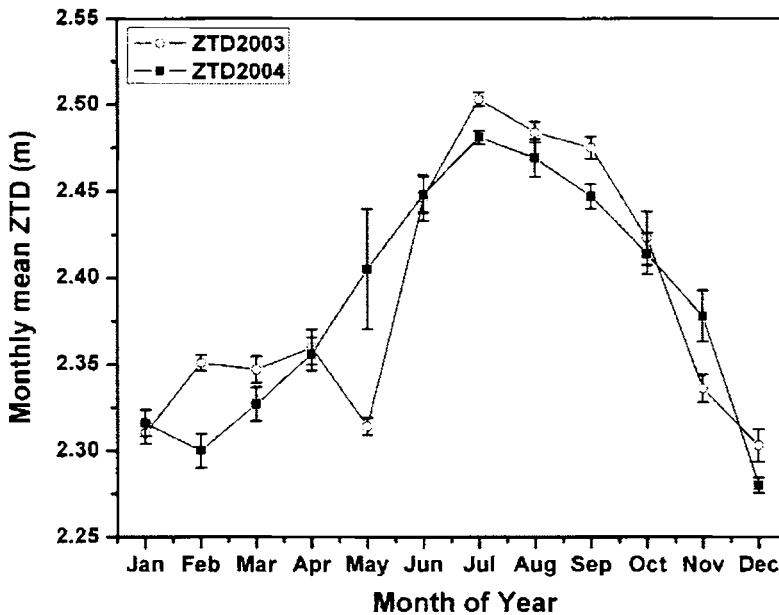


Figure 5.16: Mean annual variation of tropospheric zenith delay at 17:30 IST for Hyderabad derived from GPS data (vertical bars showing the standard error)

remains low during the December-February period and shows a broad peak during June to November with a steady increase during the March to May, the month-to-month variation of ZTD at Hyderabad shows a prominent well defined peak during July (with relatively high values from May to November) and low during December-January. A small secondary peak is observed during February-April in 2003, which could be an abnormal variation. The prominent difference in the annual variations of ZTD at the two sites could mainly be attributed to the difference in seasonal pattern of the columnar water vapor content, which is examined in detail in the following section.

5.4.3 Atmospheric Oscillations in GPS Derived ZTD

Since the ZTD derived from GPS measurements is a function of both the pressure and water vapor in the atmosphere it should show the oscillations at tidal frequencies [Humphreys *et al.*, 2005]. Atmospheric tides are the persistent global oscillations that are observed in all types of atmospheric fields, including wind, temperature, pressure, density, geo-potential height and water vapor. The periods of tidal oscillations are integer fraction of a solar or lunar day. The solar diurnal (S1) and semi-diurnal (S2) tides have 24 hr. and 12 hr. periods, respectively, while the Lunar diurnal period (M1) and semi-diurnal period (M2) are of the order of 24.8 hr. and 12.4 hr. These tidal oscillations are further characterized by their

sources. The moon's gravity forces the lunar atmospheric tides, while solar atmospheric tides can be excited in several ways, including absorption of solar radiation, large-scale latent heat release associated with deep convective clouds in the troposphere, and the gravitational pull of sun. The wavelet analysis of the two-hourly values of ZTD_{GPS} during the year 2002 at Bangalore is carried out to study the tidal oscillations. Wavelet analysis is the breaking up of a signal into shifted and scaled versions of the original (or mother) wavelet. In this process, a signal is split into an approximation and a detail. The approximation is further split into a second-level approximation and detail. This process is repeated for a number of times. For n -level decomposition, there are $n+1$ possible ways to decompose or encode the signal. This analysis is capable of revealing different aspects of data (like trends, breakdown points, discontinuities in higher derivatives, and self-similarity) which the other conventional signal analysis techniques generally miss. In this study, the wavelet analysis shows a prominent S1 (24-hours) and S2 (12-hours) oscillations. The Morlet wavelet function is used (as a mother wavelet) because localization of signal characteristics in time and frequency domains can be accomplished very efficiently with this wavelet function. Figure 5.17 shows the tidal oscillations seen in the ZTD_{GPS} for the four

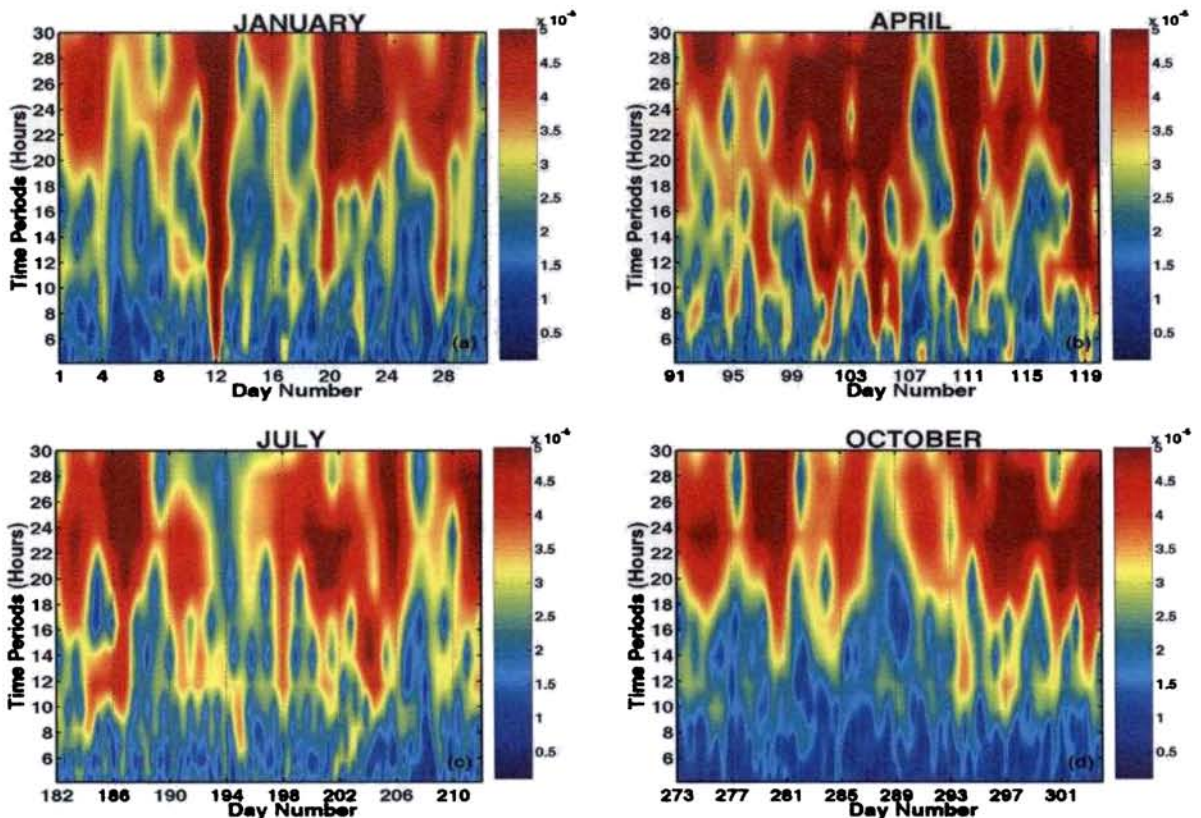


Figure 5.17: wavelet analysis carried out on ZTD_{GPS} over Bangalore showing all the tidal oscillations for four months (a) January (winter), (b) April (pre-monsoon), (c) July (SW monsoon) and (d) October (NE monsoon)

months (representing four seasons) over Bangalore. The amplitudes of these variations are large during the period June to October and low during the winter period. The surface pressure (P_S) is also subjected to similar wavelet analysis to extract the tidal oscillations. Figure 5.18 shows the wavelet analysis of the P_S obtained every three hour from the IMD observations for the same four months, representing the winter, pre-monsoon and the monsoon seasons. Both the S1 and S2 oscillations are very prominently observable in these

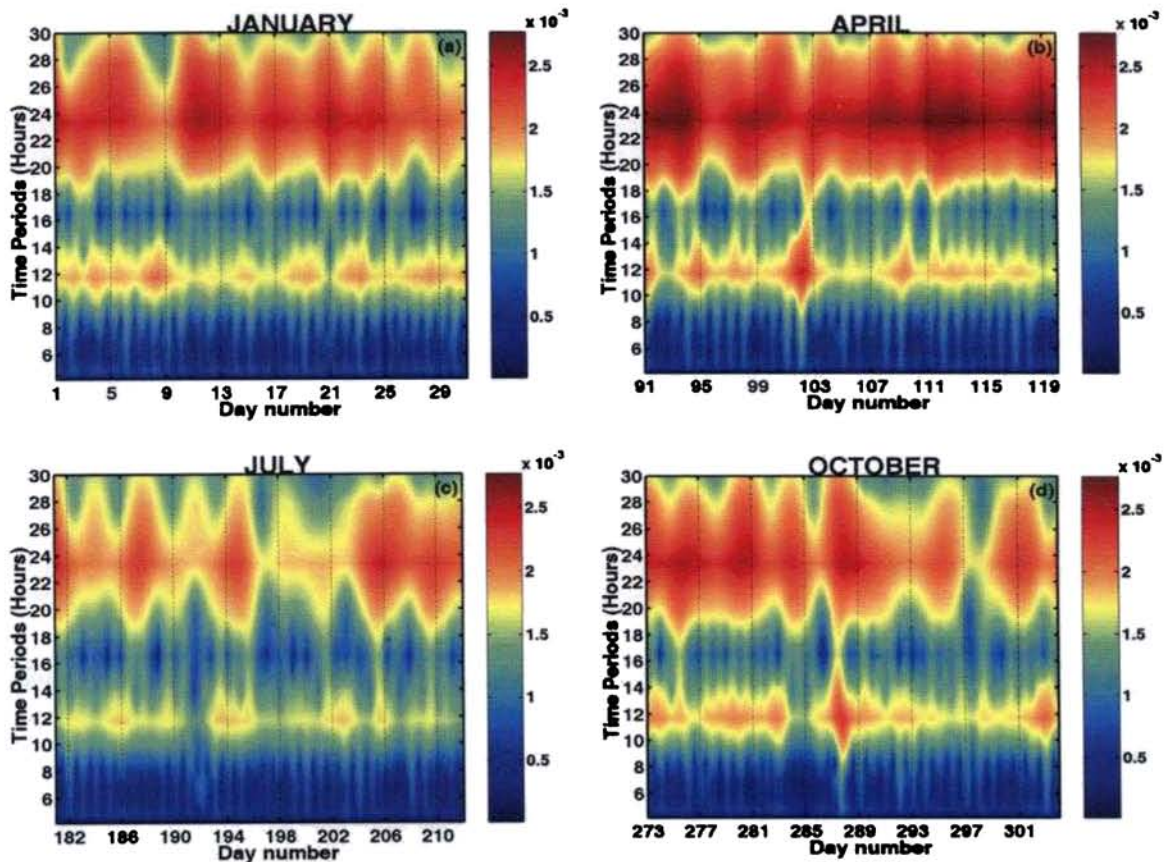


Figure 5.18: wavelet analysis carried out on P_S over Bangalore (showing tidal oscillations) for four months (a) January (winter), (b) April (pre-monsoon), (c) July (SW monsoon) and (d) October (NE monsoon)

figures. The manifestation of the prominent tidal oscillations (S1 and S2) revealed in P_S is observed in ZTD_{GPS} also. Over and above, a few other harmonics are also observed in ZTD which could be due to the atmospheric water vapor. To account for these oscillations the hydrostatic component of ZTD is estimated from the P_S (using eq. (3.10)) and subtracted from the ZTD_{GPS} to estimate the ZWD_{GPS} . A wavelet analysis is performed on ZWD_{GPS} and the results for the same four months are presented in Figure 5.19. This analysis clearly

indicates that the periodicities associated with ZTD_{GPS} are modulated by the periodicities prevailed both in atmospheric pressure and water vapor.

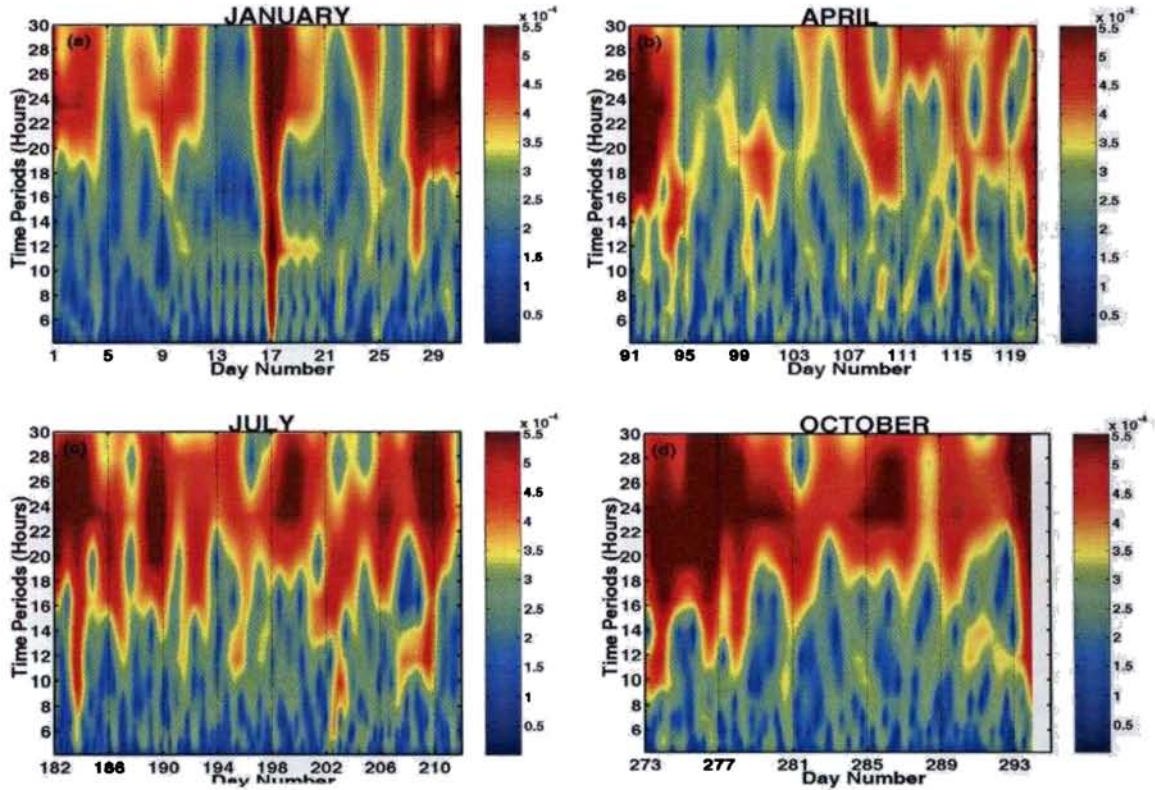


Figure 5.19: wavelet analysis carried out on ZWD_{GPS} over Bangalore (showing tidal oscillations) for four months (a) January (winter), (b) April (pre-monsoon), (c) July (SW monsoon) and (d) October (NE monsoon)

5.4.4 ISO and other Planetary Oscillations in ZTD_{GPS}

The Intra Seasonal Oscillations (ISO) is a topic of significant interest in meteorology and atmospheric science mainly because of its complexity as well as a wide range of processes with which they interact with the atmosphere. During the Northern Hemisphere winter, the westerly oscillation (30-60 days) is generally referenced as the Madden-Julian Oscillation (MJO) [Madden and Julian, 1994]. Strong ISOs are also observed over the monsoon regions during summer, where the dominant mode is the northward propagation or sudden northward shift of convection and rainfall, associated with the onset and break monsoon [Webster et al., 1998]. The physical basis for the existence of ISOs and their role in monsoon dynamics is a subject of great interest. In this context the wavelet analysis is carried out to study the intra-seasonal oscillations in ZTD_{GPS} (Figure 5.20). The prominent

oscillations seen are the semi-annual oscillations, 120 days, 90-100 days, 30-90 days (MJO). The 60-90 days oscillations are prominent throughout the year however the intensity decreases in the monsoon season. The 90-100 days periodicities are visible for winter season only. In addition to ISOs various planetary scale waves (with periodicities of 27 days, 16 days, and 5 – 10 days) are also observable in Figure 5.20c. The 16 day oscillation is well pronounced during pre-SW monsoon (March-April) and pre-NE monsoon season (September). The 5-10 days oscillation is prominent almost through out the year except during the summer monsoon (June-September) period. A better understanding of these prevailing oscillations will help to improve the periodic models used for the estimation of ZTD.

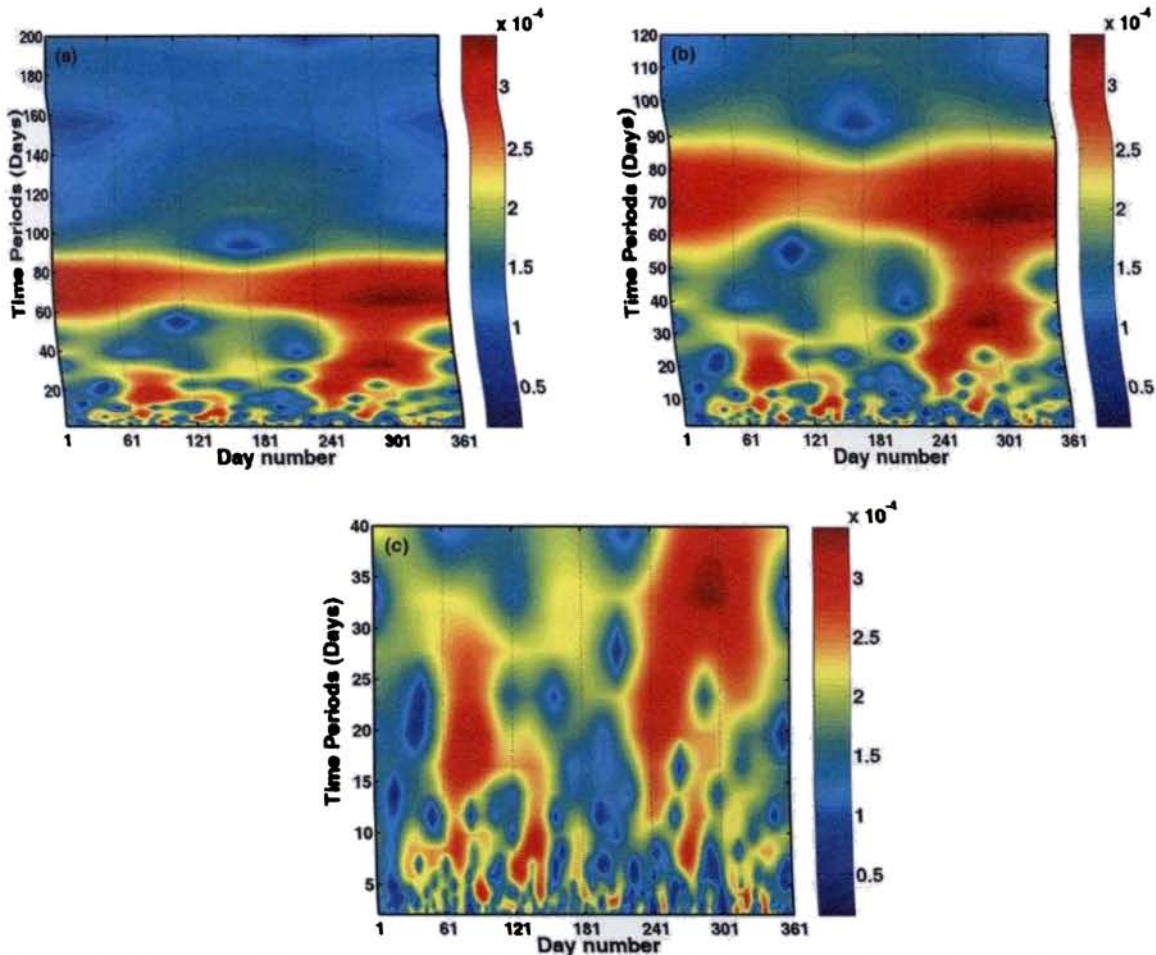


Figure 5.20: wavelet analysis carried out on ZTD_{GPS} over Bangalore showing seasonal oscillations

5.5 Summary

The tropospheric delay is derived from the GPS data collected at Bangalore and Hyderabad using GAMIT 10.2 software package. The diurnal variation of ZTD is also

studied with GPS measurements. The GPS derived ZTD values over Bangalore and Hyderabad are compared with those estimated from the Unified models. The Unified Surface model estimates agree fairly well with the GPS derived values with in ~ 3.4 cm for Bangalore and ~ 4.34 cm for Hyderabad. In case of Unified Hopfield model the attainable accuracy is ~ 3.9 cm for Bangalore and ~ 7.4 cm for Hyderabad.

In a few practical applications when the measured surface parameters are not readily available the Unified models cannot be used for the estimation of ZTD. In such cases, a conventional method devoid of any measured atmospheric parameters but depending on the geographical location and day of the year (*e.g.* IRTD model) becomes handy. The present study shows that on an average the IRTD model developed based on Indian atmospheric conditions could be incorporated for aircraft navigation within the acceptable error limits. This model performs much better than the currently available WTD model over the Indian subcontinent and adjoining regions. A comparison of the model derived ZTD with GPS derived values from the two IGS stations, Bangalore and Hyderabad, shows a fairly good agreement, with a mean absolute difference of ~ 5 cm and a maximum difference of ~ 15 cm, which corresponds to a maximum ~ 0.5 m error in vertical position coordinate in aircraft navigation considering the lowest satellite elevation of 5° . This model works out to be a better alternate for the GPS based navigation over the locations where directly measured surface atmospheric data is not available, even though like all other globally used periodic models this model also fails to respond to sudden and abnormal weather conditions. The potential of using NCEP/NCAR reanalyzed surface atmospheric data to estimate the ZTD appears to be a better substitute in this context.

The various periodicities in the GPS derived ZTD are studied to account for the variability in ZTD due to the atmospheric oscillations, which could improve the existing periodic models for ZTD. The potential of GPS derived ZTD data to study tidal, intra seasonal oscillations and various planetary waves are also illustrated in this study. The GPS estimated ZTD shows the signatures of prominent periodicities that are quintessentially present in the lower atmosphere (which is the source region).

Chapter 6

MAPPING FUNCTION FOR TROPOSPHERIC DELAY

6.0 Introduction

The tropospheric delay along the line of sight of the satellite is estimated by multiplying the zenith delay with a geometric factor [Davis *et al.*, 1985], known as "mapping function (MF)". This function describes the angular dependence of the delay assuming an azimuthal symmetry for the atmospheric parameters. Very Long Baseline Interferometry (VLBI) employed for geodetic applications uses the zenith tropospheric delay calculated a priori from the surface atmospheric parameters [Herring *et al.*, 1990 and Ma *et al.*, 1990] as described in Chapters 2, 3, and 4 and projects it in to the satellite direction. One of the major factors which limits the accuracy of this slant projection, particularly at very high zenith angle ($> 75^\circ$), is the uncertainty associated with the MF (due to the horizontal inhomogeneities in atmospheric parameters employed in modeling the MF). For a static station this error influences the geodetic results as (1) an additional scatter on timescales from sub-daily to annual and (2) a bias which depends on the maximum observed zenith angle. The latter effect which was examined in detail by Davis *et al.*, [1985] observed to have a systematic change in the estimated parameters, primarily the local vertical coordinate of the GPS receiver antenna position leading to the estimated baseline length when data at maximum zenith angle are used. In water vapor estimation the GPS data recorded at large zenith angles ($\sim > 85^\circ$) are used mainly to achieve a longer path length (and hence to intercept a higher amount of water vapor). In GPS based navigation some high zenith angle measurements is essential mainly for maintaining a good GDOP [Ramjee and Ruggieri, 2005].

For convenience the MF is separated into two components, one for the hydrostatic delay and the other for the non-hydrostatic (wet) component [Davis *et al.*, 1985]. These mapping functions, which are independent of the azimuth angle are formulated by fitting coefficients a , b , and c in the form of continued fraction [Marini, 1972] as described in Chapter 1 (Section 1.7.1) separately for hydrostatic and wet components. However, as the

hydrostatic delay contributes $\sim 90\%$ of the total delay, development of a mapping function for this component becomes more vital. In this chapter the global MFs, detailed in Section 1.7 is examined for different stations. Along with this an attempt is made to modify the Chapman's grazing incidence function [Chapman, 1931], $Ch(X, \chi)$, to suit this purpose. This "Chi" function is mainly used to describe the attenuation of solar radiation by the atmosphere in which the density is decreasing with increase in altitude (z), as function of zenith angle (χ), atmospheric scale height (H). The results obtained by using this modified Chi function is compared with that obtained using other global MFs is presented in this chapter.

6.1 Slant Tropospheric Delay and True Mapping Function

Applying ray-trace technique described in Chapter 2 to monthly mean refractivity profiles obtained from radiosonde measured profiles of P , T and e , the slant delay is estimated for different zenith angles ranging from 0° to $\sim 90^\circ$. The variation of the slant delay with zenith angle for Trivandrum is presented in Figure 6.1 along with its hydrostatic and wet components. Note that, the ray-tracing also assumes horizontal stratification of the atmosphere. The tropospheric delay, which is around 2.5 m in the zenith direction increases up to ~ 90 m for zenith angles close to 90° ($\chi = 89.8^\circ$).

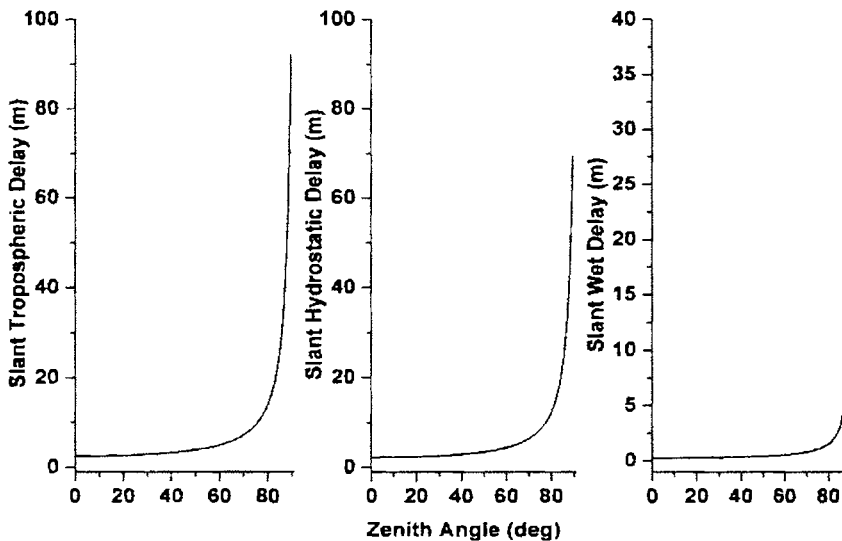


Figure 6.1: Ray-traced values of ΔR , SHD and SWD for 8947 angles between 0° to 90° zenith angle for Trivandrum (8.47° N).

The corresponding variation in the slant hydrostatic delay component (SHD) is from 2.3 m to 70 m while that for the slant wet delay component (SWD) is ~ 0.2 m in the zenith direction and ~ 15 m when zenith angles approaches to 90° . The mapping function is usually defined as the ratio of the delay ΔR in oblique and the zenith direction (eq. 1.41), estimated from Figure 6.1 (the true mapping function) is presented for the dry and wet components in

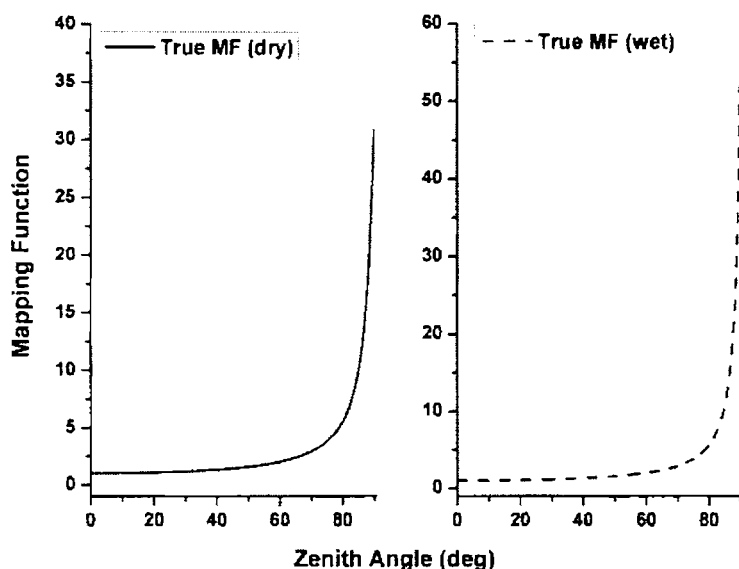


Figure 6.2: True mapping function estimated using Ray-trace Technique over Trivandrum (8.47° N).

Figure 6.2. Both these components show an exponential increase with zenith angle. Increase in the wet component of MF is slightly larger than that of the dry component especially for zenith angles beyond $\sim 80^\circ$. Note that, as the above MF is derived using the altitude profile of atmospheric refractivity through ray-tracing in the appropriate direction, it can be taken to be a more realistic value subject to the assumption of horizontal stratification. But in practical application it may become necessary to use an analytical function for estimating the MF without adopting a complex ray-tracing through realistic atmosphere. In the earlier attempts by *Saastamoinen* [1972] the zenith hydrostatic delay is estimated using surface pressure and further mapped in slant direction using a simple $1/\cos(\chi)$ function. As in these efforts he used $\chi < 70^\circ$, this simple function was reasonably adequate for the estimation of slant delay. Subsequently, a number of mapping functions were developed to estimate the function at larger zenith angles [*Marini*, 1972; *Ifadis*, 1986; *Herring*, 1992; *Niell*, 1996; *Boehm et al.*, 2006a]. The commonly used MFs and the required input parameters are

Table 6.1: Parameterization of Mapping Function coefficients. Abbreviations are χ - zenith angle, P - total pressure; e - water vapor pressure; T - temperature; λ - latitude; h - height of the station above geoid; DOY - time in UTC days since the beginning of the year.

Mapping Function	Reference	Maximum zenith angle	Required input	
			Hydrostatic	Wet
True MF	Section 6.1	-	χ, P, T profiles	χ, e, T profiles
HMF	Herring [1992]	85°	χ, T, λ, h	χ, T, λ, h
NMF	Niell [1996]	87°	$\chi, \text{DOY}, \lambda, h$	χ, λ
GMF	Boehm et al. [2006a]	88°	ERA40 data at 15° × 15°	ERA40 data at 15° × 15°

presented in Table 6.1 for a quick comparison. These MFs also uses look-up tables and periodic functions to compute their respective inputs based on day-of-year and latitudes. A detailed discussion of these mapping functions is presented in Section 1.7. Of these functions, the GMF developed by Boehm et al. [2006a] can be used up to a zenith angle of 88°, even though the deviation from true value increases with increase in zenith angle. This function however, utilizes the ERA40 data as input while NMF employs only day-of-year (*doj*), latitude (λ) and altitude (h) of the station.

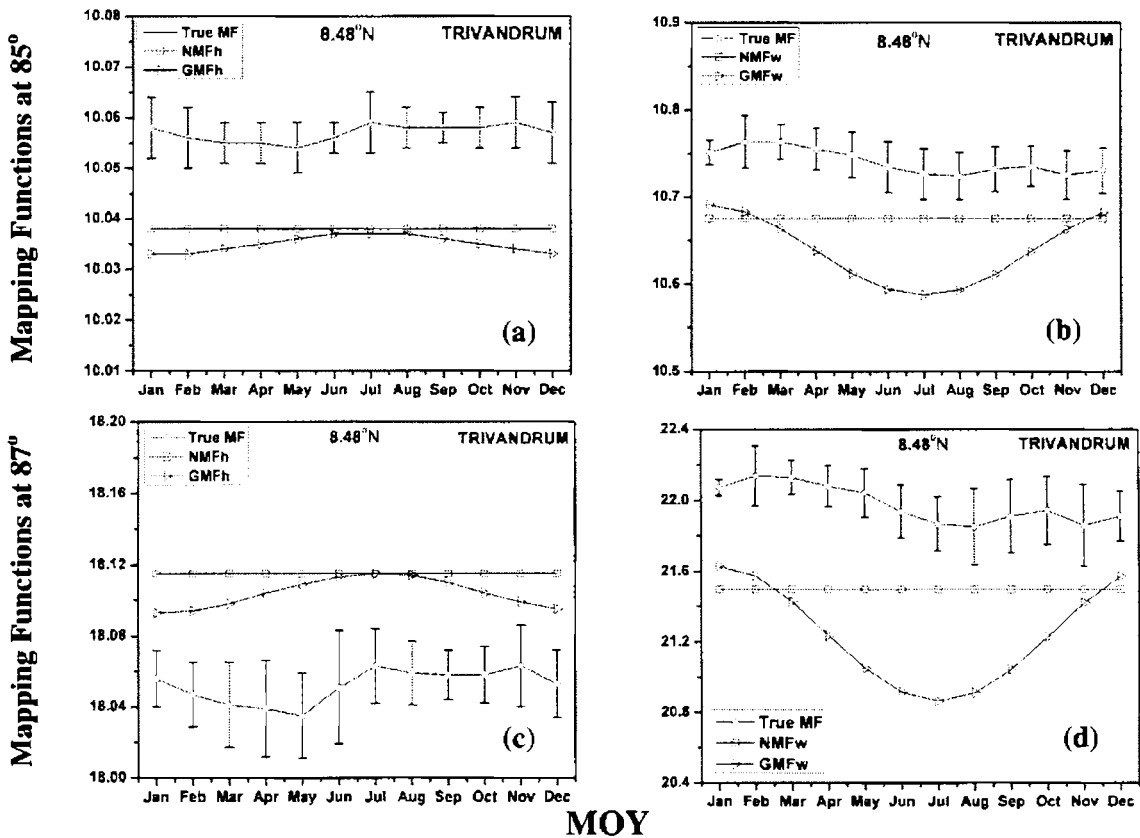


Figure 6.3(a-d): The month-to-month variation of hydrostatic MF (a & c) and wet MF (b & d) for Trivandrum at $\chi = 85^\circ$ (a & b) and 87° (c & d)

For a typical illustration of the accuracy achievable by these mapping functions the (mean) month-to-month variation of these mapping functions estimated for Trivandrum for $\chi = 85^\circ$ and 87° are presented in Figure 6.3(a-d), along with true value (of MF) estimated from the mean altitude profiles of refractivity separately for the dry and wet components. The hydrostatic component of NMF (NMF_h) and wet component of NMF (NMF_w) does not account for the seasonal variation of MF and provides a constant value through out the year for any station below 15° latitude. The mean bias of the NMF_h is ~ 0.02 (for $\chi = 85^\circ$) and ~ 0.06 (for $\chi = 87^\circ$). In case of NMF_w the bias increases to ~ 0.1 (for $\chi = 85^\circ$) and ~ 0.6 (for $\chi = 87^\circ$). Although GMF does show seasonal variation but it also has a bias throughout the year.

However, in the present study an attempt is made to use the Chapman grazing incidence function with some modification as a MF for the hydrostatic component of tropospheric delay. This new function is found to be better than the other available functions up to 87° . An attempt to develop a similar MF for the non-hydrostatic component could not yield a satisfactory result and hence dropped. In the following sections a detailed description of this new MF developed for hydrostatic component is presented.

6.2 Modified Chi Function for Troposphere

A new mapping function for the hydrostatic delay is developed by modifying the Chapman grazing incident function [*Chapman*, 1931; 1953], which is generally used for studying the attenuation of solar radiation in ionosphere. An analytical solution of this function is used and then modified to use it as a hydrostatic mapping function for the troposphere. The attenuation of solar radiation along the path depends on the absorption of radiation as described by the Beer-Lambert's law as

$$dI = -I \sigma_{\text{abs}} dz \quad (6.1)$$

$$\text{or, } I = I_\infty \exp(-\int \sigma_{\text{abs}} \rho dz) = I_\infty \exp(-\zeta) \quad (6.2)$$

where σ_{abs} is the absorption cross-section, ρ is the density, I_∞ is the un-attenuated flux at the top of the atmosphere (TOA) and ζ is the atmospheric column depth, which is the optical path traversed by the ray in the medium (atmosphere). Following *Rees* [1989], ζ of a species of density $n(z)$ from a point at an altitude of z_0 to the sun at solar zenith angle of χ can be written as

$$\zeta(\chi, z_0) = \int_{z_0}^{\infty} n(z) \left[1 - \left(\frac{r_e + z_0}{r_e + z} \right)^2 \sin^2 \chi \right]^{-1/2} dz \quad (6.3)$$

for $\chi \leq \pi/2$. Here r_e is the radius of the Earth and for an exponential atmosphere the density of any species varies as $n(z) = n(z_0) \exp[-(z - z_0)/H]$, with a constant scale height, H . The column depth of the species can thus be represented by the Chapman function, $\text{Ch}(X, \chi)$ through the relation

$$\zeta(\chi, z_0) = H n(z_0) \text{Ch}(X, \chi) \quad (6.4)$$

where $X = (r_e + z_0)/H$ is a dimensionless ratio with typical values ranging from 200 to 1300 for terrestrial atmosphere. Here the Chapman function relates the actual column depth with the same for a vertical sun. Figure 6.4 shows the spherical geometry for the evaluation of

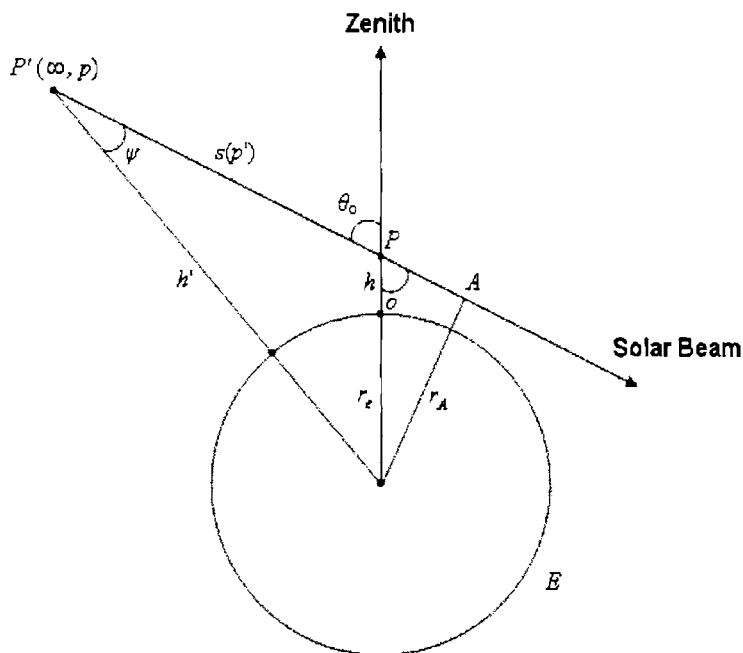


Figure 6.4: A schematic diagram depicting the spherical geometry and evaluation of the Chapman function: θ_0 = solar zenith angle, r_e = earth's radius, r_A = AE , h = PO , h' = $P'O'$, $s(p')$ = The path length from p' to A .

Chapman function, with the objective of calculating the absorption at point ' p ', which is at height ' h ' above the earth's surface, based on the actual path length $s(p')$. One of the basic assumptions in this is that there is no bending effect on the solar beam due to the intervening atmosphere. An analogy is drawn between the altitude variation of the species density and

that of refractivity given by $N(z) = N(z_0) \exp[-(z)/H]$. Moreover, as ζ for solar radiation extinction is estimated by integrating the density profile similarly the total delay in microwave propagation also estimated by integrating (eq. 2.25) the refractivity profiles, only difference being there is an extra term in the latter which denotes the bending of the ray.

Using eq. 6.3 and eq. 6.4 the Chapman function can be written as

$$\text{Ch}(X, \chi) = \frac{1}{H} \int_{z_0}^{\infty} \exp[-(z - z_0)/H] \left[1 - \left(\frac{r_e + z_0}{r_e + z} \right)^2 \sin^2 \chi \right]^{-1/2} dz \quad (6.5)$$

By making the substitution $y = [r_e + z/r_e + z_0] - 1$ and $X = (r_e + z_0)/H$ one obtains

$$\text{Ch}(X, \chi) = X \int_0^{\infty} \exp(-Xy) \left[1 - \left(\frac{\sin \chi}{1+y} \right)^2 \right]^{-1/2} dy \quad (6.6)$$

Further substituting for $s = (1+y)/\sin \chi$ and $s_0 = 1/\sin \chi$ gives

$$\text{Ch}(X, \chi) = X \sin \chi e^X \int_{s_0}^{\infty} \exp[-(X \sin \chi)s] s (s^2 - 1)^{-1/2} dy \quad (6.7)$$

If $s = 1/\sin \lambda$ then

$$\text{Ch}(X, \chi) = X \sin \chi \int_0^{\chi} \exp[X(1 - \sin \chi \csc \lambda)] \csc^2 \lambda d\lambda \quad (6.10)$$

Following *Chapman* [1931] the Chapman function can be written as

$$\text{Ch}(X, \pi/2) = X e^X B_1(X) \quad (6.11)$$

with B_1 being a well-known Bessel function. Expanding the square root in eq. 6.6 and then substituting $[\sin \chi/(1+y)]^2 = \sin^2 \lambda$, one arrives at a new form of eq. 6.10 without numerical singularities. Using a simple convergence condition $\text{Ch}(0, \chi) = \text{Ch}(X, 0) = 1$, the function can be written as

$$\text{Ch}(X, \chi) = 1 + X \sin \chi \int_0^{\chi} \exp[X(1 - \sin \chi \csc \lambda)] / (1 + \cos \lambda) d\lambda \quad (6.12)$$

Alternatively, on substituting $t^2 = y + t_0^2$, with $t_0^2 = 1 - \sin \chi$, in eq. 6.6 gives

$$\text{Ch}(X, \chi) = 2X \int_{t_0}^{\infty} \exp[-X(t^2 - t_0^2)] f(t, \chi) dt \quad (6.13)$$

where $f(t, \chi) = (t^2 + \sin \chi) / (t^2 + 2 \sin \chi)^{1/2} = (t^2 - t_0^2 + 1) / (t^2 - t_0^2 + 1 + \sin \chi)^{1/2}$. In this analysis an arbitrarily accurate analytical evaluation for the Chapman Function is used. As

reported by *Huestis* [2001] this is a first analytical method to achieve good accuracy for small X values, which generally is the case for lower atmosphere. So an explicit analytical representation, valid for all values of X and χ , based on differential equation satisfied by $\text{Ch}(X, \chi)$.

6.2.1 The Asymptotic Expansion for $\text{Ch}(X, \chi)$

As stated above the value of X generally ranges from 200-1300. This means that only a limited range of t -values contribute significantly to the integral (eq. 6.13), i.e. $t^2 - t_o^2 < 0.1$. This suggests a construction of an asymptotic power series based on the expansion

$$f(t, \chi) = \sum_n C_n(\chi)(t^2 - t_o^2)^n \quad (6.14)$$

that is nominally convergent only for $(t^2 - t_o^2)/(1 + \sin \chi) < 1$. Here

$$\begin{aligned} C_0 &= (1 + \sin \chi)^{-1/2}, \\ C_1 &= (1 + 2 \sin \chi) / [2(1 + \sin \chi)^{-3/2}], \\ C_2 &= -(1 + 4 \sin \chi) / [8(1 + \sin \chi)^{-5/2}], \\ C_3 &= (1 + 6 \sin \chi) / [16(1 + \sin \chi)^{-7/2}]. \end{aligned} \quad (6.15)$$

Thus, for $\chi \leq \pi/2$ the Chapman function can be represented as

$$\text{Ch}(X, \chi) \approx 2X \sum_{n=0}^3 C_n I_n \quad (6.16)$$

where $I_n = \int_0^{\infty} \exp[-X(t^2 - t_o^2)](t^2 - t_o^2)^n dt$. Evaluating these integrals in terms of gamma

functions [*Abramowitz and Stegun*, 1964] gives

$$\begin{aligned} I_n &= 1 / (X^{(n+1/2)}) \exp(y_o^2) \sum_{j=0}^n \frac{n!}{j!(n-j)!} (-y_o^2)^j \int_0^{\infty} \exp(-y^2) y^{2(n-j)} dy \\ &= 1 / (2X^{(n+1/2)}) \exp(y_o^2) \sum_{j=0}^n \frac{n!}{j!(n-j)!} (-y_o^2)^j \Gamma(n-j+1/2, y_o^2) \end{aligned} \quad (6.17)$$

with $y_o^2 = X t_o^2 = X(1 - \sin \chi)$. For small values of y_o^2 , i.e. as $\chi \rightarrow \pi/2$,

$$\Gamma(1/2, y_o^2) = \sqrt{\pi} \operatorname{erfc}(y_o) \quad (6.18)$$

and calculate $\Gamma(k + 1/2, y_o^2)$ by upward recursion [*Abramowitz and Stegun*, 1964] as

$$\Gamma(k + 3/2, y_o^2) = (k + 1/2) \Gamma(k + 1/2, y_o^2) + y_o^{2k+1} \exp(-y_o^2) \quad (6.19)$$

For large values of y_0^2 the asymptotic expansion of the incomplete gamma function [Abramowitz and Stegun, 1964] is used to get

$$\begin{aligned}
 I_0 &= [1/(2X^{1/2}y_0)][1 - (1/2)/y_0^2 + (3/4)/y_0^4 - (15/8)/y_0^6 + (105/16)/y_0^8 - \dots] \\
 I_1 &= [1/(2X^{3/2}y_0)][1 - 1/y_0^2 + (9/4)/y_0^4 - (15/2)/y_0^6 + (525/16)/y_0^8 - \dots] \\
 I_2 &= [1/(2X^{5/2}y_0)][2 - 3/y_0^2 + 9/y_0^4 - (75/2)/y_0^6 + (1575/8)/y_0^8 - \dots] \\
 I_3 &= [1/(2X^{7/2}y_0)][6 - 12/y_0^2 + 45/y_0^4 - 225/y_0^6 + (11025/8)/y_0^8 - \dots]
 \end{aligned} \tag{6.20}$$

6.2.2 Development of Mapping Function using the Chi Function

The analytical solution (eq. 6.15, 6.16, and 6.20) for the Chi function is used to estimate $\text{Ch}(X, \chi)$ for different values of χ ranging from 0° to $\sim 90^\circ$ for all the eight RIM stations. These values are further compared with the true MF values estimated by ray-tracing. The deviation of the $\text{Ch}(X, \chi)$ function from the true value of MF for zenith angle $> 60^\circ$ is shown in Figure 6.5 for all the RIM stations. The Chi function agrees well with the true hydrostatic MF for angles $< 70^\circ$ while it overestimates the MF values in an exponential form with significant deviations for zenith angle $> 80^\circ$. The deviation ranges from 0.0 to 2.0 for all the stations with lower values for Bangalore, Delhi and Srinagar. In order to account for this deviation for each station it is fitted to evolve an exponential function of the form

$$Y = a \times \exp [b/(x + c)] \tag{6.21}$$

Table 6.2: Fitting Coefficients for the Modified Chi Function

Station	Latitude $^\circ(\text{N})$	Altitude (m)	$a (\times 10^{-5})$	b	c
Trivandrum	8.48	64.0	0.2 (0.014)	-198.1 (2.24)	-103.9 (0.09)
Portblair	11.66	79.0	2.0 (0.105)	-122.7 (1.19)	-100.2 (0.06)
Bangalore	12.96	921.0	0.006 (0.0007)	-280.2 (4.42)	-105.8 (0.14)
Kolkata	22.65	6.0	4.0 (0.144)	-115.9 (0.91)	-100.1 (0.05)
Ahmedabad	23.06	55.0	4.0 (0.148)	-115.0 (0.87)	-100.1 (0.04)
Guwahati	26.10	54.0	4.0 (0.150)	-114.5 (0.85)	-100.1 (0.04)
Delhi	28.58	216.0	4.0 (0.888)	-70.1 (0.47)	-97.4 (0.03)
Srinagar	34.08	1587.0	1.0 (0.083)	-121.7 (1.44)	-99.8 (0.07)

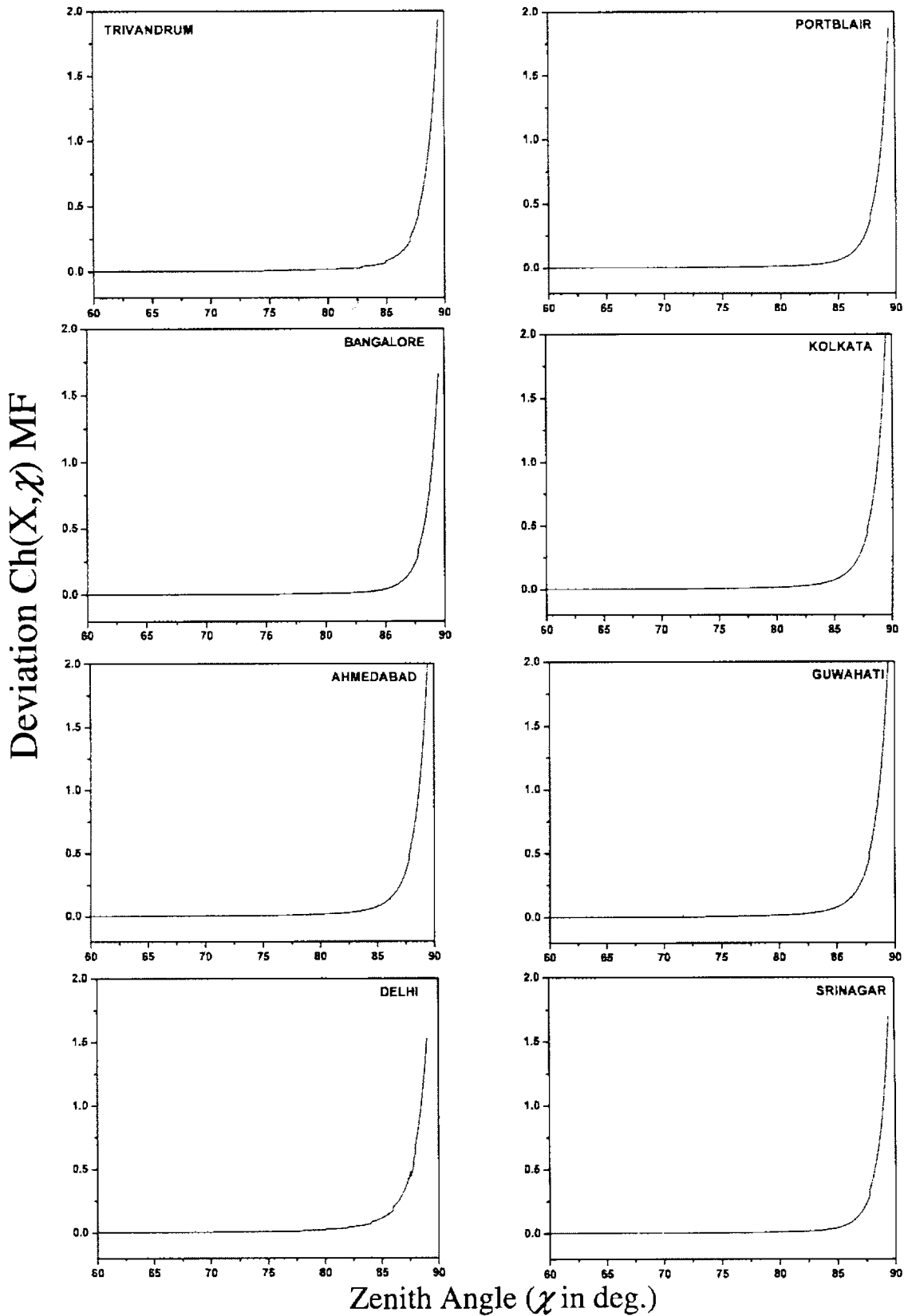


Figure 6.5: Deviation of $Ch(X, \chi)$ function from true MF at $\chi > 60^\circ$ for different RIM Stations

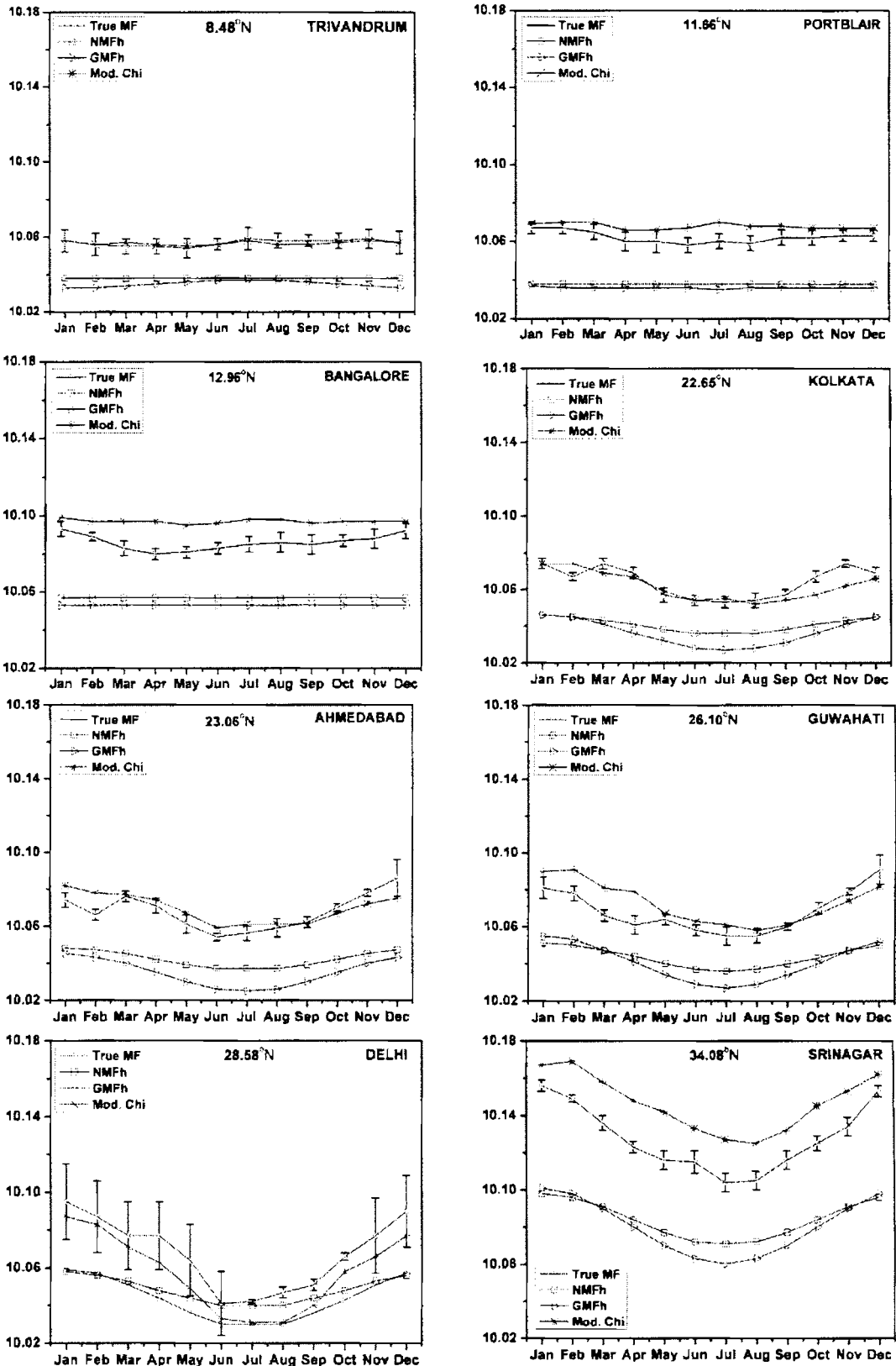
and the coefficients a , b , and c are evaluated for all RIM stations. These values are presented in Table 6.2 along with their standard deviations within the parenthesis. The non-linear empirical fitting is used with the Chapman function to make modified Chi function of the form

$$Ch_m(X, \chi) = 2X \int_{t_0}^{\infty} \exp[-X(t^2 - t_0^2)] f(t, \chi) dt - [a \times \exp\{b/(x+c)\}] \quad (6.22)$$

6.3 Validation and Comparison of Modified Chi Function

The modified Chi function is validated by comparing it with the true MF obtained by ray tracing the refractivity profile up to 100 km. This is further inter-compared with the other well established global mapping functions such as NMF and GMF. Since all the mapping functions agrees fairly well for zenith angle $< 75^\circ$ with deviations which are generally less significant (≤ 0.000051), the comparison and validation of the MF presented here is focused for a vacuum (outgoing) zenith angle $\geq 75^\circ$. This comparison is carried out for all the eight RIM stations (from 8°N to 34°N). Figure 6.6 shows the mean month-to-month variation of the modified Chi function ($Ch_m(X, \chi)$), the hydrostatic components of NMF, GMF along with the true MF estimated from radiosonde data for a zenith angle of 85° . The vertical bars represent the amount of day-to-day variability due to corresponding changes in the atmospheric parameters. The day-to-day variations which are relatively small at the tropical stations (Trivandrum, Portblair, Bangalore) increases with increase in latitude. The mean value of MF at high latitude stations (Kolkata, Ahmedabad, Guwahati, Delhi, Srinagar) also show significant seasonal variation. This seasonal variation is largest for Delhi. Among all the modeled MFs, the agreement with true values is the best for modified Chi function. The global models (NMF, GMF) show a consistent bias (underestimation) for all the stations through out the year, while the modified Chi function marginally over estimates (except at Delhi). Note that, this deviation is relatively small considering the day-to-day variability of true MF. The hydrostatic component of true MF at $\chi = 85^\circ$ for different stations are in the range 10.02 to 10.10, except for Srinagar where it is in the range 10.10 to 10.16. This shows that the slant delay at $\chi = 85^\circ$ is ~ 10 times of the zenith delay. A seasonal variation of 0.06 in hydrostatic MF can produce an error in delay of the order of ~ 14 cm. Figure 6.7 shows the annual variation of the non-hydrostatic (wet) components of NMF, GMF and the true MF at a zenith angle of 85° . As mentioned earlier the NMF_w does not

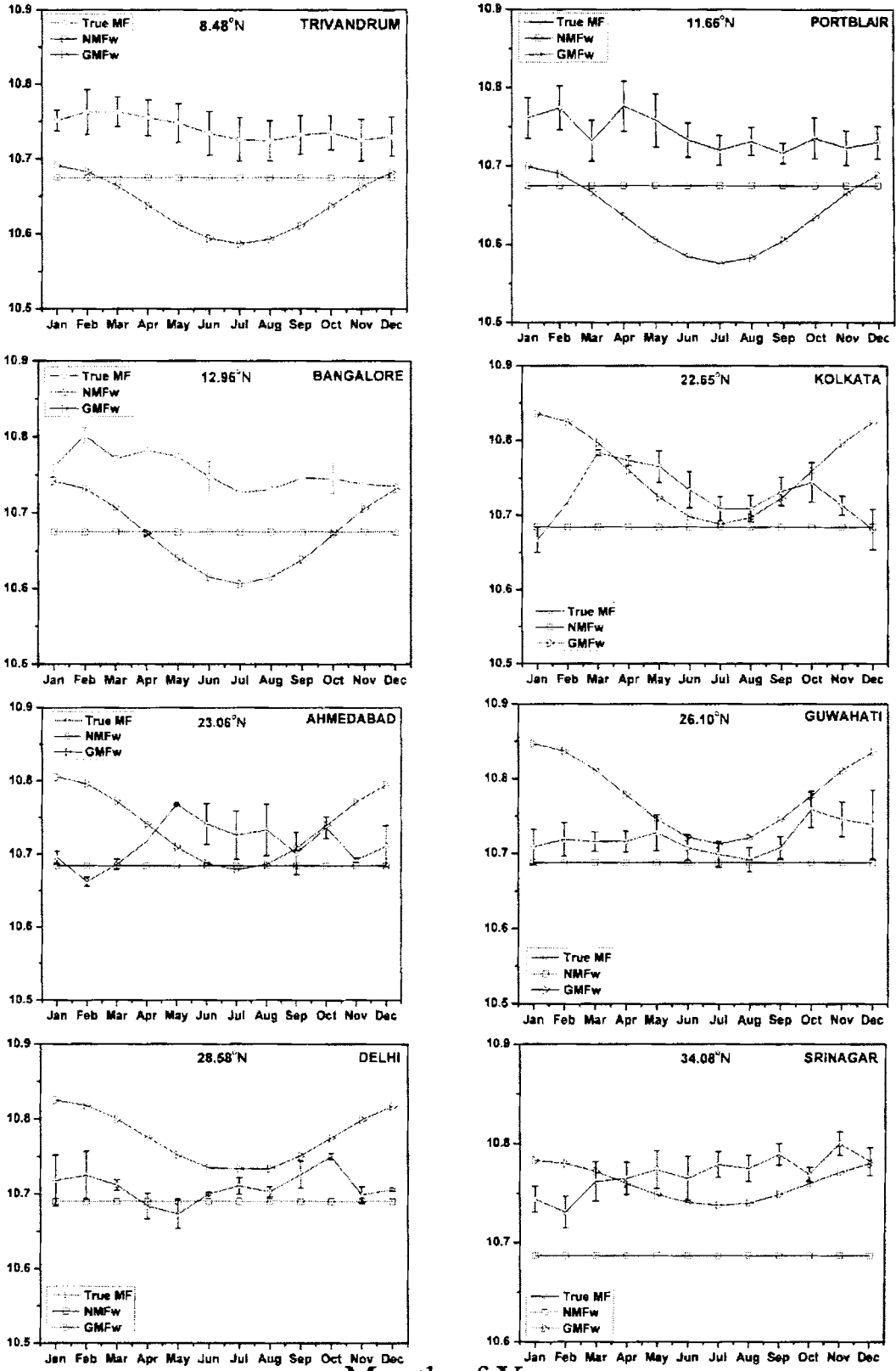
Hydrostatic Mapping Function



Month of Year

Figure 6.6; Month-to-month variation of the hydrostatic MF for different RIM stations at $\chi = 85^\circ$ based on different analytical functions (NMF_h, GMF_h, Mod. Chi) along with the true value (True MF)

Non-Hydrostatic Mapping Function



Month of Year

Figure 6.7: Month-to-month variation of the Wet MF for different RIM stations at $\chi = 85^\circ$ based on different analytical functions (NMF_w, GMF_w) along with the true value (True MF)

account for the seasonal variation of wet MF. It provides only a single value throughout the year. Though GMF_w reproduces a seasonal variation, it deviates significantly from the true value during the summer monsoon period especially for the low latitude stations, and during the winter months for the high latitude stations. For a quantitative comparison, the annual mean absolute difference of all the modeled MF values from the true value at 85° and 88° are shown in Table 6.3. The respective standard deviations, representative of the seasonal variations, are presented within parenthesis. It is clear from the analysis that the mean absolute deviations of modified Chi function are one order less than those of the existing global hydrostatic MFs for $\chi = 85^\circ$. For the non-hydrostatic component the performance of both the existing global MFs are comparable.

Table 6.3: Annual-mean Absolute Difference of all the Mapping Functions from the True MF Values

RIM stations	Zenith angle 85°					Zenith angle 88°				
	Mean abs. diff MFh			Mean abs. diff MFw		Mean abs. diff MFh			Mean abs. diff MFw	
	Mod Chi	NMF	GMF	NMF	GMF	Mod Chi	NMF	GMF	NMF	GMF
Trivandrum	0.001 (0.0007)	0.02 (0.002)	0.02 (0.002)	0.06 (0.015)	0.10 (0.03)	0.008 (0.004)	0.06 (0.01)	0.05 (0.01)	0.5 (0.11)	0.7 (0.24)
Portblair	0.006 (0.002)	0.02 (0.003)	0.03 (0.003)	0.06 (0.02)	0.10 (0.04)	0.02 (0.015)	0.02 (0.016)	0.02 (0.012)	0.5 (0.17)	0.8 (0.33)
Bangalore	0.010 (0.003)	0.03 (0.004)	0.03 (0.004)	0.08 (0.02)	0.08 (0.05)	0.016 (0.01)	0.015 (0.01)	0.018 (0.016)	0.6 (0.19)	0.6 (0.32)
Kolkata	0.004 (0.003)	0.02 (0.005)	0.03 (0.004)	0.05 (0.03)	0.05 (0.05)	0.02 (0.02)	0.04 (0.02)	0.02 (0.01)	0.4 (0.25)	0.4 (0.4)
Ahmedabad	0.005 (0.003)	0.03 (0.006)	0.03 (0.005)	0.03 (0.02)	0.06 (0.04)	0.02 (0.01)	0.02 (0.02)	0.03 (0.02)	0.3 (0.2)	0.5 (0.3)
Guwahati	0.007 (0.005)	0.02 (0.007)	0.03 (0.005)	0.03 (0.02)	0.06 (0.04)	0.02 (0.01)	0.03 (0.01)	0.01 (0.01)	0.2 (0.15)	0.5 (0.33)
Delhi	0.01 (0.004)	0.02 (0.012)	0.02 (0.01)	0.02 (0.015)	0.06 (0.036)	0.04 (0.025)	0.04 (0.03)	0.02 (0.01)	0.2 (0.12)	0.5 (0.33)
Srinagar	0.02 (0.005)	0.04 (0.01)	0.05 (0.005)	0.08 (0.005)	0.02 (0.005)	0.12 (0.025)	0.06 (0.04)	0.08 (0.02)	0.5 (0.14)	0.2 (0.14)

The significance of these differences in MF on the accuracy of positioning is assessed by converting the MF difference values to an equivalent vertical position error (VPE). A 'rule of thumb' [MacMillan and Ma, 1994] followed for this conversion, states that for azimuthally symmetric delay errors and observations down to approximately 85° , the height error is approximately one fifth of the error in delay estimation at the highest zenith angle, such that

$$VPE = \frac{[True\ Delay(85^\circ)] - [ZHD \times Modeled\ MF(85^\circ)]}{5} \quad (6.23)$$

Figure 6.8 shows the VPE due to the difference between true hydrostatic MF and all other

Height change w.r.t. Radiosonde (mm) at $\chi = 85^\circ$

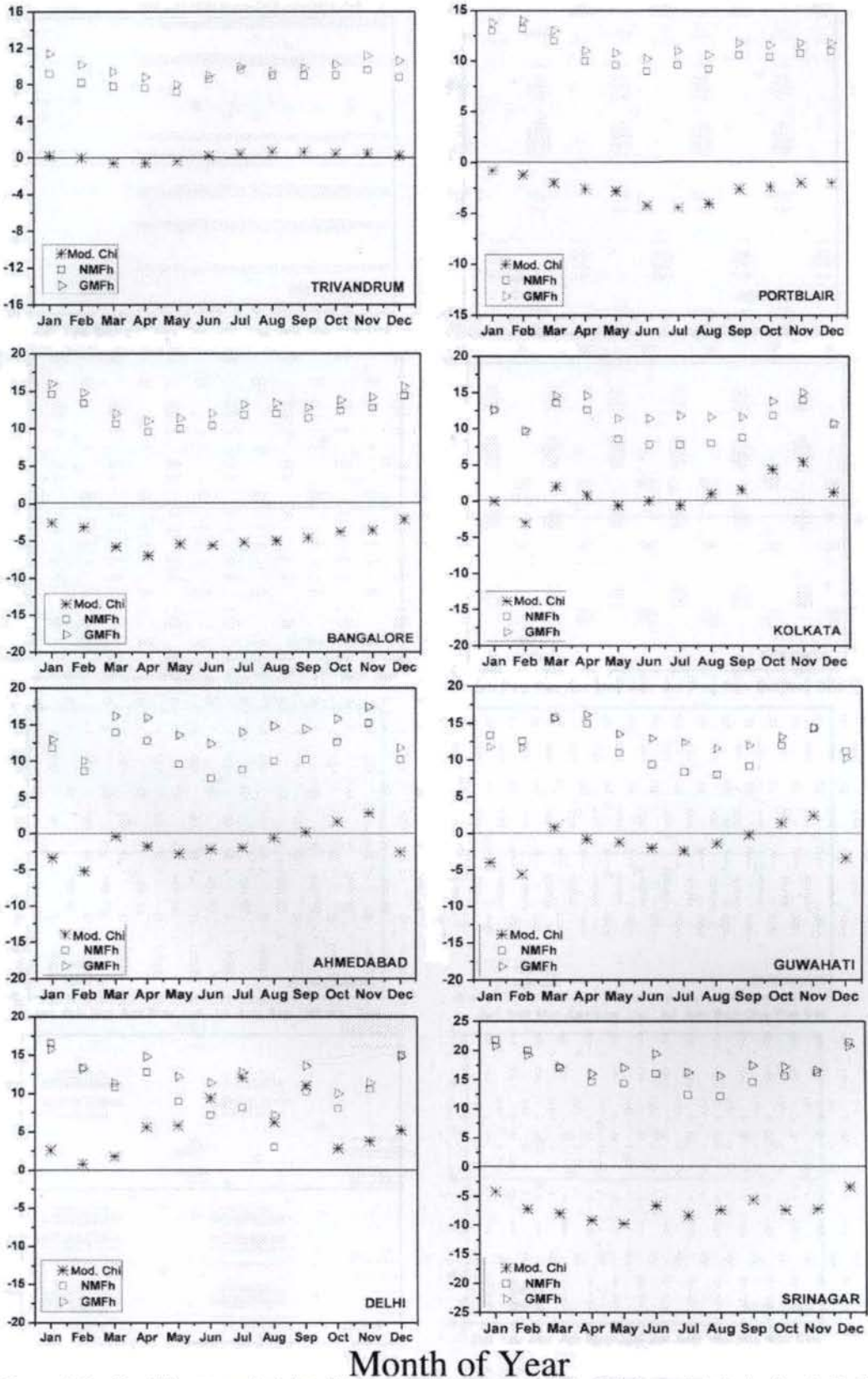


Figure 6.8: Monthly mean height differences in mm for Mod. Chi (asterisks), hydrostatic NMF (squares), and GMF (triangles) relative to radiosonde based True MF

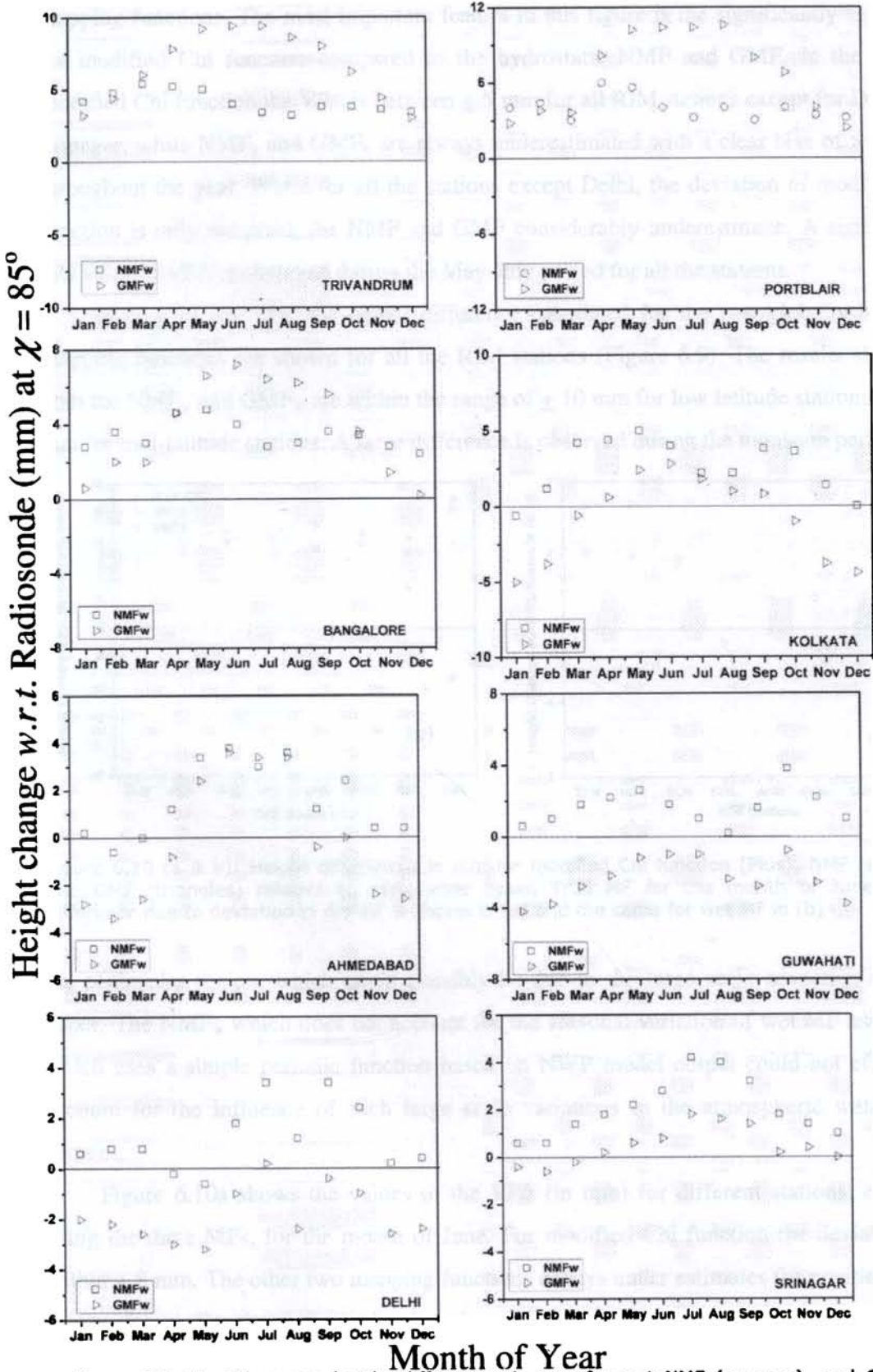


Figure 6.9: Monthly mean height differences in mm for wet NMF (squares), and GMF (triangles) relative to radiosonde based True MF

mapping functions. The most important feature in this figure is the significantly small bias for modified Chi function compared to the hydrostatic NMF and GMF. In the case of modified Chi function the *VPE* is between ± 5 mm for all RIM stations except for Delhi and Srinagar, while NMF_h and GMF_h are always underestimated with a clear bias of > 10 mm, throughout the year. While for all the stations except Delhi, the deviation of modified Chi function is only marginal, the NMF and GMF considerably underestimate. A significantly low value of *VPE* is observed during the May-July period for all the stations.

In case of wet MF, the height difference calculated for the two globally used wet mapping functions are shown for all the RIM stations (Figure 6.9). The results show that both the NMF_w and GMF_w are within the range of ± 10 mm for low latitude stations and ± 6 mm for mid-latitude stations. A large difference is observed during the monsoon period over

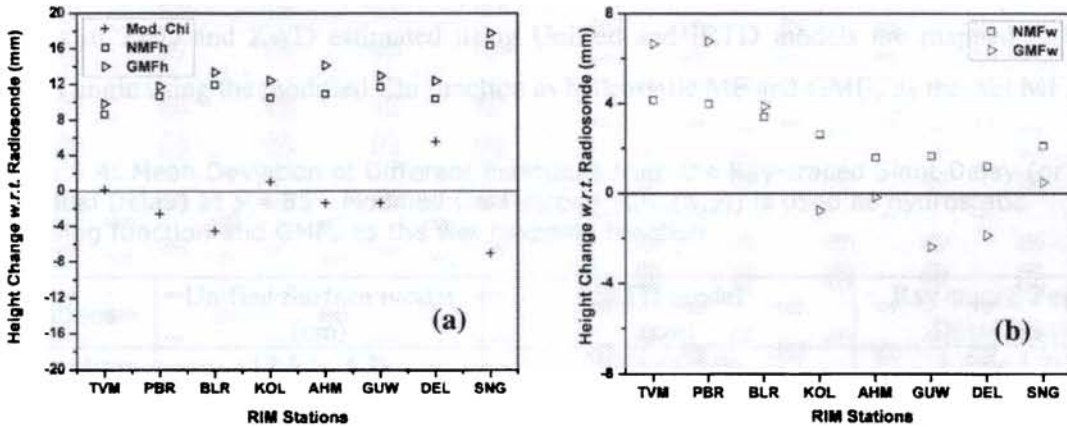


Figure 6.10 (a & b): Height differences in mm for modified Chi function (Plus), NMF (squares), and GMF (triangles) relative to radiosonde based True MF for the month of June. Height difference due to deviation in dry MF is shown in (a) and the same for wet MF in (b)

the peninsular region, which could possibly be due to the large scale advection of water vapor. The NMF_w which does not account for the seasonal variation of wet MF and GMF_w which uses a simple periodic function based on NWP model output could not effectively account for the influence of such large scale variations in the atmospheric water vapor content.

Figure 6.10a shows the values of the *VPE* (in mm) for different stations, estimated using the three MFs, for the month of June. For modified Chi function the deviations are within ± 8 mm. The other two mapping functions always underestimate the position with a bias > 10 mm. For the wet mapping functions (Figure 6.10b) the *VPE* is within ± 8 mm. At

higher latitudes (like Delhi and Srinagar) this difference decreases up to ± 2 mm. It would be worth in this context to note that the influence of the wet component is less pronounced in GPS and VLBI analyses compared to the hydrostatic mapping functions mainly because of the fact that the magnitude of wet delay is much smaller (by a factor of ~ 10) than the hydrostatic delay [Boehm *et al.* 2006a].

6.4 Assessment of the Estimated Tropospheric Delay using Various Models and Mapping Functions for Navigation Purpose

As per the basic requirement projected in Table 1.3, the residual Tropospheric delay should be ~ 20 cm (for 1σ level). It will be interesting in this context to examine the accuracies up to which the models developed in this study satisfy this requirement. The values of ZHD and ZWD estimated using Unified and IRTD models are mapped to 85° zenith angle using the modified Chi function as hydrostatic MF and GMF_w as the wet MF.

Table 6.4: Mean Deviation of Different Estimates from the Ray-traced Slant Delay (or Residual Delay) at $\chi = 85^\circ$. Modified Chi function ($\text{Ch}_m(X, \chi)$) is used as hydrostatic mapping function and GMF_w as the wet mapping function

Stations	Unified Surface model (cm)	IRTD model (cm)	Ray-traced Zenith Delay (cm)
Trivandrum	17.5 (+ 4.3)	18.8 (+ 4.0)	3.5 (+ 1.2)
Portblair	18.8 (+ 6.7)	18.4 (+ 5.4)	4.7 (+ 2.2)
Bangalore	14.2 (+ 2.8)	21.2 (+ 4.8)	4.2 (+ 2.0)
Kolkata	18.0 (+ 3.0)	36.6 (+ 5.0)	2.0 (+ 1.7)
Ahmedabad	17.8 (+ 5.2)	29.3 (+ 13.8)	2.2 (+ 1.3)
Guwahati	17.9 (+ 5.0)	36.2 (+ 5.0)	2.3 (+ 1.4)
Delhi	13.8 (+ 3.0)	29.8 (+ 10.9)	3.8 (+ 2.3)
Srinagar	18.3 (+ 2.8)	25.3 (+ 5.6)	3.9 (+ 1.2)

The values of slant delay for $\chi = 85^\circ$ estimated employing the MFs are compared with the true slant delay obtained by ray-tracing. The second and third columns of Table 6.4 show the 1σ values of residual tropospheric delay, which is the mean absolute deviation of the modeled delays from the ray-traced delay, for different RIM stations. The last column represents the same but uses the true value of ZHD and ZWD, estimated by ray-tracing profiles of the atmospheric parameters, along with the modified Chi function and GMF_w , respectively, as hydrostatic and wet MFs. This table clearly shows that for all the stations residual tropospheric delay using the Unified model is within the specified limits. However,

the best option is to have the true value of ZHD and ZWD in real time which is rather difficult. The Unified model which depends on real time measured surface parameters, is sufficiently accurate to provide the required residual value.

6.5 Summary

To estimate the delay in slant direction, the zenith delay is mapped along the line of sight of the satellite using appropriate mapping functions. The existing global mapping functions as well as a new mapping function developed by modifying the Chapman function are examined for this purpose. These MFs are validated by comparing them with the true value estimated by ray-tracing. The analysis is further extended by examining the error in vertical positioning due to the deviation of the MFs from the true MF values at 85° zenith angle. This study concludes that the modified Chi function agrees much better than the other mapping functions for the hydrostatic component, through out the Indian region, with a positioning error < 5 mm. The Unified model along with the modified Chi function and GMF_w endow with required residual error of ≤ 20 cm at 1σ level.

Chapter 7

RETRIEVAL OF ATMOSPHERIC COLUMNAR WATER VAPOR CONTENT FROM GROUND BASED GPS

7.0 Introduction

As the wet delay derived from the GPS data (ZWD_{GPS}) depends primarily on the atmospheric water vapor content, this parameter could be used for estimating the columnar water vapor or precipitable water vapor (PW) in the atmosphere. Since the quantity of water vapor in the atmosphere is temperature dependent and both these parameters vary with altitude, accounting the effect of temperature profile in the estimation of PW is rather complicated. This problem is attempted by many investigators to arrive at a parameter called the weighted mean temperature (T_m), which is the water vapor weighted vertically averaged temperature [Davis *et al.*, 1985]. While some of these models are simple linear types, some others take care of the periodic variations in T_m also. Most of the linear models [Mendes *et al.*, 2000; Bevis *et al.*, 1992; 1994; Solbrig, 2000; Schüeler, 2000] are based on surface temperature (T_s), developed using the altitude profiles of atmospheric water vapor and temperature obtained from different parts of the globe. These linear models, considered as the global models, had a variability of about $\pm 20\%$ [Bevis *et al.*, 1994], which could be significant for many applications. Schüeler [2000] also proposed a pair of harmonic models for T_m , accounting for its seasonal variation through a periodic function. Ross and Rosenfeld [1997] after an extensive study on T_m based on the meteorological data from 53 global stations (covering a wide latitudinal region) concluded that site-specific model would be superior to the geographically and globally invariant regression relationship used for T_m . But in tropics where the correlation between T_m and T_s decreases significantly this superiority is not very prominent. This could be due to the fact that the range of T_s variations over the tropics would be rather small. In such cases it would be better to generate a region specific model. This prompted examining the potential of a Bevis-type regional model for the Indian meteorological conditions. A statistical relationship for T_m in terms of T_s is established considering different stations spread over the Indian subcontinent from where good

atmospheric data is available through the regular radiosonde measurements conducted by the IMD. Using this model the PW is retrieved from the GPS data of the IGS stations Bangalore and Hyderabad. However, the possibility of developing T_m -based site-specific regression models for these stations and its applicability both at Bangalore and Hyderabad are examined. Over and above these T_m -based models, the possibility of arriving a simple site-specific model for PW directly in terms of the ZWD [Saha *et al.* 2007], and use it for the estimation of PW from GPS data, is also examined for both the stations. The accuracies of these models are examined by comparing the retrieved PW with that obtained by integrating the water vapor density profile estimated from radiosonde measured altitude profiles of temperature and dew point temperature. The values of ZWD_{GPS} estimated using the GAMIT, is used to test the validity of the models by estimating the PW using the models and comparing it with those obtained from radiosonde data.

7.1 Linear Model of PW in terms of ZWD

The altitude profile of water vapor density (ρ_w , in kg m^{-3}) estimated from the e and T profiles employing the equation of state ($e = \rho_w R_v T$) for water vapor, is integrated up to its highest altitude and the columnar (integrated) water vapor (IWV) or Precipitable water vapor (PW) are estimated as

$$IWV = \int_{z_{ant}}^{z_{TOA}} \rho_v dz \quad (7.1)$$

$$PW = \frac{IWV}{\rho_l} \quad (7.2)$$

where ρ_l (kg m^{-3}), is the density of liquid water, which is approximated as 10^3 kg m^{-3} for the present study. Often PW is expressed in “mm” to avoid small decimal values. In order to establish an empirical relation connecting PW with ZWD, the mean value of ZWD is plotted against the corresponding value of PW; both estimated using the mean altitude profile of water vapor and temperature (eq. 2.27 and eq. 7.1). A scatter plot thus obtained is presented in Figure 7.1. As can be seen from this figure the points are mostly aligned along the straight line. The empirical relations for Bangalore and Hyderabad [Sureshraj *et al.*, 2007b], respectively, connecting PW and ZWD obtained through regression analysis, yielding a correlation coefficient of 0.999 are

$$PW = (0.153 \pm 0.00016) \times ZWD \quad (7.3)$$

$$PW = (0.156 \pm 0.00014) \times ZWD \tag{7.4}$$

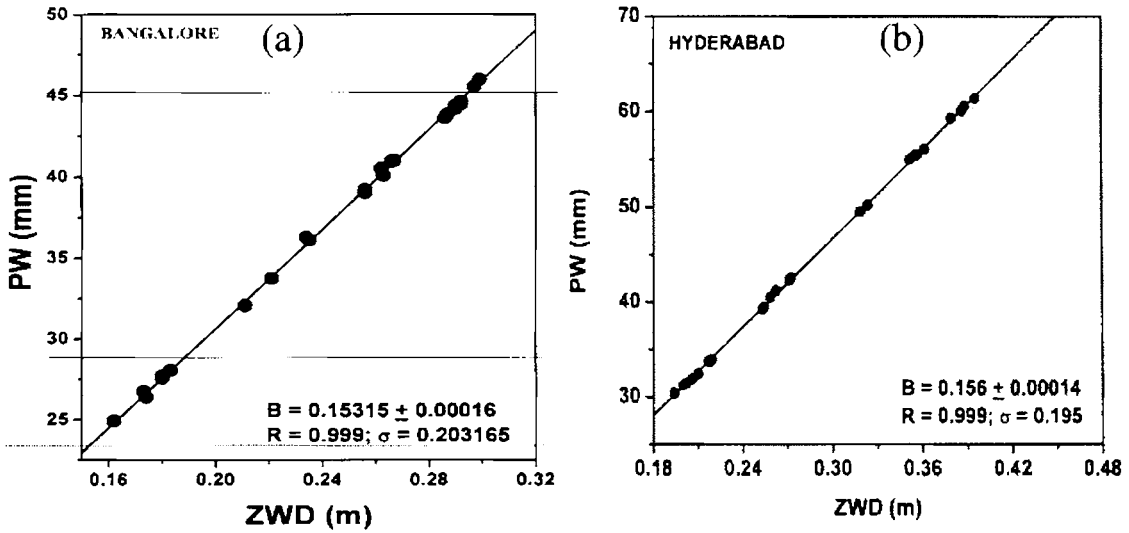


Figure 7.1: Dependence of Precipitable Water vapor (PW) on ZWD derived using monthly mean values of ZWD and PW for Bangalore (a) and Hyderabad (b)

The accuracy of the model is further examined by studying the absolute difference of model prediction from the true estimate (from daily radiosonde measurements) for the period 2001-2002. The mean absolute difference in PW was found to be ~1.6 mm.

7.2 Adaptation of Bevis Model for Indian Region

The wet component of zenith delay depends on the altitude profiles of e and T , but the amount of water vapor present in air itself is related to temperature, which complicates the modeling. This prompted many investigators to account for the altitude variation of temperature through a term called weighted mean temperature (T_m) and use it along with PW to relate the later with ZWD. *Askne and Nordius* [1987] attempted to relate the PW and ZWD through a linear relation given as:

$$PW = \Pi \times ZWD \tag{7.5}$$

Π is the proportionality coefficient related to T_m [*Askne and Nordius*, 1987; *Bevis et al.*, 1992; *Liou et al.*, 2001] as

$$\Pi = \frac{10^8}{\rho_l R_v [(k_3/T_m) + k'_2]} \tag{7.6}$$

Note that, this relationship is similar to that presented through eqs. (7.3) and (7.4) except for the fact that in eq. (7.5) the variation of the proportionality coefficient (Π) with temperature is taken into account through the weighted mean temperature T_m (in Kelvin) defined as [Bevis *et al.*, 1994]

$$T_m = \frac{\int (e(z)/T(z)) dz}{\int (e(z)/T^2(z)) dz} \quad (7.7)$$

The vertical distribution of water vapor pressure thus acts as a weighting factor in defining T_m . As seen from eq. (7.6), Π is non-linearly related to T_m . Though the typical value of Π is ~ 0.15 , it varies from place to place and also depends on season. Being a function of T_m , Π varies as much as 20% with latitude, altitude and time of the year [Bevis *et al.*, 1994]. Using the altitude profiles of e and T from various mid-latitude stations (27° to 65°N) Bevis *et al.* [1992] arrived an empirical relation connecting T_m and T_s of the form

$$T_m = 70.2 + 0.72 \times T_s \quad (7.8)$$

This relation was arrived after analyzing about 8718 radiosonde ascends spanning approximately for a period of two years from different sites in the United States of America with a latitude range of 27° to 65° , a height range of 0 to 1.6 km and an *r.m.s.* deviation of 4.74 K, hereafter will be referred to as “**Bevis model**”, for convenience. A similar empirical model for T_m based on radiosonde measurements from eight locations (Table 7.1) over the Indian subcontinent employing about 4104 good radiosonde profiles with humidity measurements extending up to or above 10 km during the period 1995 to 1997 is attempted. The value of T_m estimated for different surface temperatures are presented in a scatter plot shown in Figure 7.2. A linear relationship, established between the two following regression analysis and the best-fit straight line, is also shown in this figure. This yields an empirical relation between T_m and T_s in the following form

$$T_m = (62.6 \pm 1.67) + (0.75 \pm 0.006) \times T_s \quad (7.9)$$

This figure shows that the values of T_m vary in the range 265 to 295 K for a corresponding variation of 265 to 315 K in T_s . There is a high density of points for $T_s > 290$ K and low density of points for $T_s < 273$ K (mostly belong to Srinagar (32.67°N) located at ~ 1600 m above MSL).

In Bevis *et al.* [1992], there were quite a few cases with estimated T_m values being larger than T_s , which was attributed to strong temperature inversions near the surface, a

Table 7.1: Mean value of T_m and Π along with their range of variability at different Indian stations.

Station	Latitude (°N)	Longitude (°E)	Mean T_m (K)	Range T_m (K)	Mean Π	Range Π
Trivandrum	8.5	76.9	287.8	4.1	0.164	0.002
PortBlair	11.6	92.5	287.6	3.6	0.164	0.002
Bangalore	12.9	77.7	284.1	6.0	0.162	0.003
Kolkata	22.6	88.5	287.3	12.0	0.164	0.007
Ahmedabad	23.1	72.6	287.3	12.4	0.164	0.007
Guwahati	26.1	91.6	285.3	11.8	0.163	0.007
Delhi	28.6	77.1	284.6	17.3	0.162	0.010
Srinagar	34.1	74.8	274.3	24.6	0.156	0.014

phenomenon usually encountered at high-latitudes. However, such cases seldom encountered in our analysis. It would be worth in this context to note that similar attempts to relate T_m with T_s were pursued by various investigators at different contexts, a consolidation of which is provided by *Jade et al.* [2005]. They arrived at different values for the coefficients in eq. (7.9). While the intercept varied in the range 50.4 K to 86.9 K, the slope varies in the range 0.65 to 0.79. It would be more meaningful to compare the end product, T_m , for the range of T_s values usually encountered than examining the agreement in coefficients of “Bevis” and “**Bevis Adapted for Indian region (BAI) regional model**” [eq. (7.9)]. For the range of T_s from 282 to 312 K, which is usually encountered over the study region (Figure 7.2), the values of T_m obtained from Bevis model ranges from 273 to 295 K, while that from eq. (7.9) ranges from 274 to 297 K, resulting in a net difference of 1-2 K, which is not very significant. However, for a more quantitative comparison, the PW was estimated for different days (about 605 days) during 2001-2002 employing both these equations and the *r.m.s* deviation between the two is found to be < 0.18 mm, which is insignificant considering the regional differences amounting $\sim 20\%$ as reported by *Jade et al.*, [2005].

Based on the eq. (7.9) the mean values of Π and T_m as well as their month-to-month variability is examined for eight different Indian stations. These are summarized in Table (7.1). The features are quite obvious. The range of variability is small for the low latitude stations, and increases with increasing latitude. For Bangalore the mean value of Π is about 0.0162, which is marginally larger than the typical value reported for American stations [*Bevis et al.*, 1994; *Ross and Rosenfeld*, 1997] based on Bevis model. Further eight stations

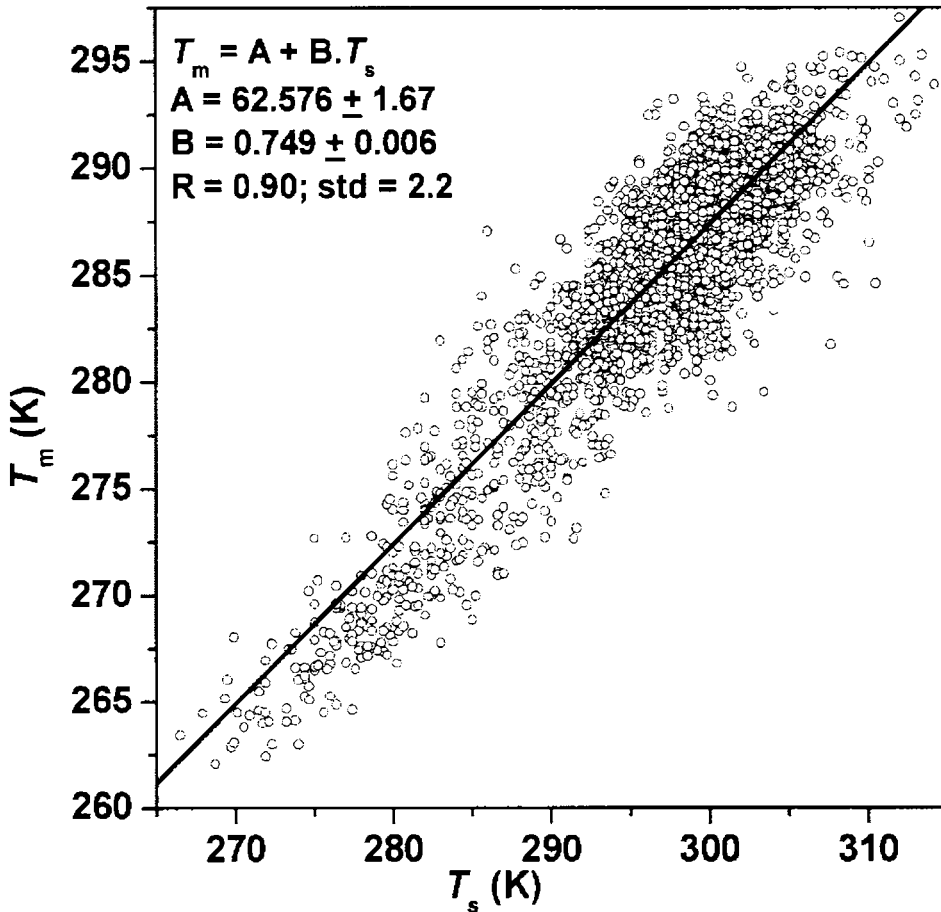


Figure 7.2: Variation of T_m with T_s based on upper air data for the period 1995-1997 for eight selected met-stations spread over Indian subcontinent ($8.5^\circ\text{N} - 34.1^\circ\text{N}$)

spread over the Indian subcontinent extending from tropical to mid-latitudes are considered for establishing the relationship between T_m and T_s . But as noted earlier, *Ross and Rosenfeld* [1997] recommended for a site-specific model as superior to geographically invariant regression. This aspect also is examined in the Indian scenario. Figure 7.3 shows a scatter plot of T_m with T_s separately for the eight stations considered for the analysis along with the best-fit regression line in each case. The regression coefficients thus obtained is also shown in the respective frames. This model hereafter will be referred to as “**BAI site-specific model**”. As can be seen from this figure, for the tropical stations the points are mostly clustered around a small region because the range of T_s variations is small. The spread of the points increases with increase in latitude. For the tropical stations the derived coefficients deviate significantly from that of eq. (7.9), while those for the mid-latitude stations tend to become closer. On comparing the values of T_m obtained from the “BAI regional” model and

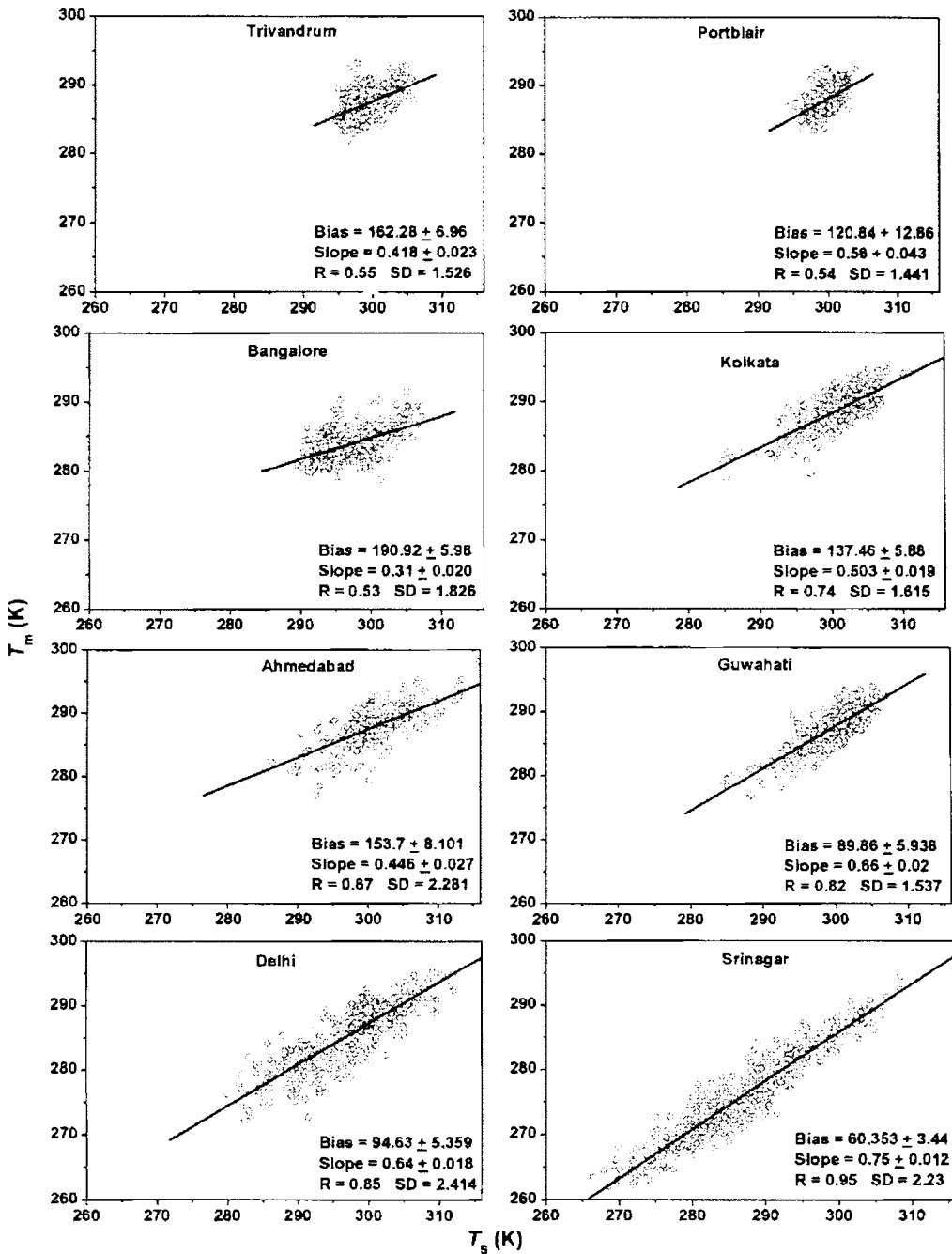


Figure 7.3: Variation of T_m with T_s for the eight stations located over Indian sub-continent based on upper air data for the period 1995-1997. The geographical locations of these stations are furnished in Table 2.1. The dynamical range of T_m and T_s and the correlation of T_m with T_s increase with increase in latitude

“BAI site-specific” model for the range of T_s values encountered at Bangalore (287-307 K), it can be seen that while the former yields T_m in the range 277.9 to 292.9 K, the latter yields T_m in the range 279.9 to 286.1 K, resulting a deviation of around 2 to 6 K depending on T_s .

Note that the difference between “Bevis” and “BAI regional” models in this case is only around 1 K.

7.3 Estimation of PW from GPS Data at Bangalore

The zenith tropospheric delay (ZTD_{GPS}) is estimated from the GPS data at 2-hr interval for different days during the period 2001-2002 for Bangalore using GAMIT. The hydrostatic component of zenith tropospheric delay is estimated, employing eq. (3.1) using the appropriate value of P_s , and subtracted it from the ZTD_{GPS} to obtain the ZWD_{GPS} for different days during the study period. The values of P_s measured at the IMD site and corrected for the elevation difference as mentioned in Chapter 5, are used for this purpose. The values of ZWD_{GPS} at 00:00 UTC and 12:00 UTC are used for estimating PW, employing the site-specific linear model (eq. (7.3)), as well as the regional model (“BAI regional”) established based on T_m (eqs. (7.5), (7.6), (7.9)) and site-specific T_m -based model (“BAI site-specific” refer Figure 7.3). The basic difference between the linear and BAI models is that while the latter models account for the effect of temperature variations the former does not.

In order to establish the general applicability of the model, PW was estimated from the GPS data (PW_{GPS}) for 22 months during the period January 2001 to October 2002, a time-series plot of which is presented in Figure 7.4 (blue curve). The top panel in this figure shows the values of PW retrieved for 00:00 UTC and the base panel those for 12:00 UTC. For a direct comparison, the value of PW derived from radiosonde profiles (red curve) at the respective timings is also plotted along the same estimated from the GPS data. The values of PW is relatively low during the period December-February (<25 mm) with a day-to-day variation of ~4 mm. It shows a gradual increase during the March-April period and reaches its peak during June, when the southwest monsoon sets over the southern part of Indian peninsula. It remains fairly high, with mean value >32 mm, up to September and starts decreasing thereafter. It may also be noted that the atmospheric water vapor content is relatively large during the evening hours (~12:00 UTC).

A close examination of Figure 7.4 shows that the values of PW estimated from GPS data agrees fairly well with that derived from radiosonde data. In a few cases, the value of PW estimated from radiosonde data is lower than that derived from GPS data. This could probably be due to the fact that though in most of the cases the profiles of water vapor

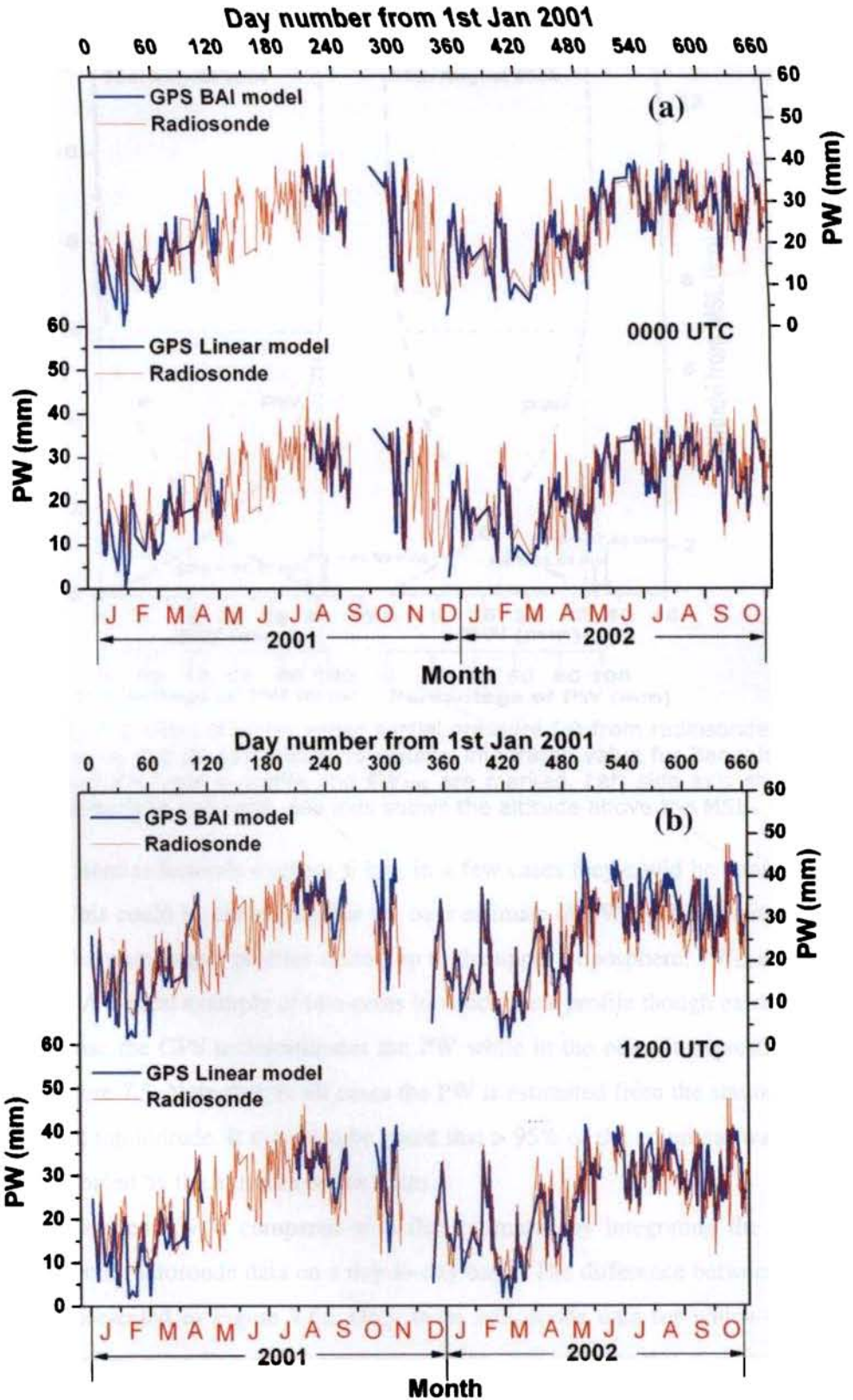


Figure 7.4: Daily Precipitable water vapor estimated from GPS data for Bangalore using BAI regional model and site-specific linear model along with those derived from radiosonde data at 00:00 UTC (a) and 12:00 UTC (b) for the period January 2001 to October 2002

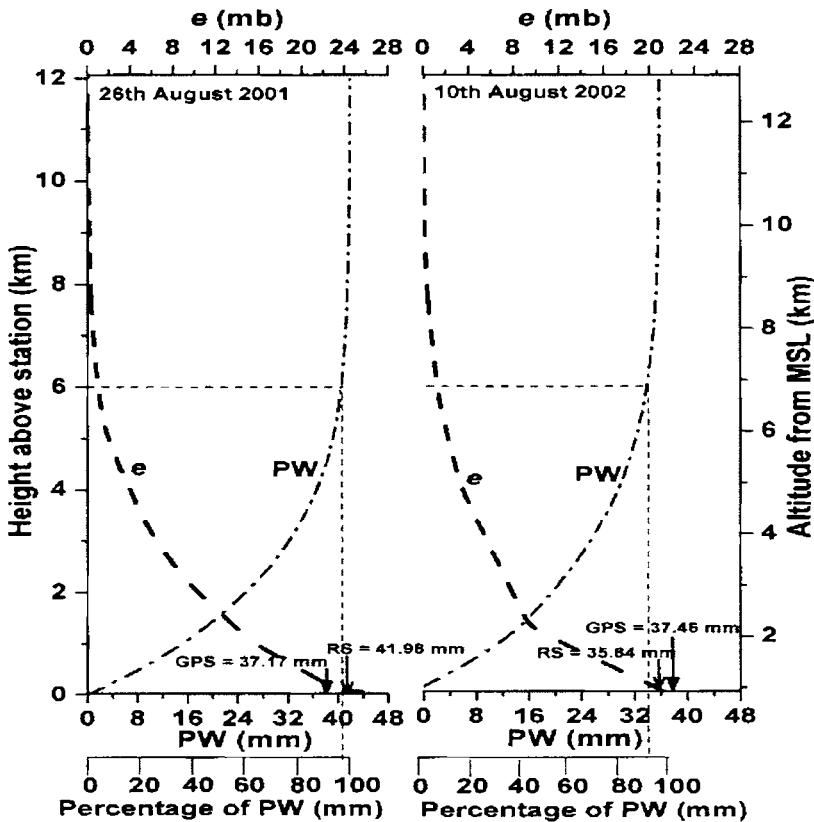


Figure 7.5: Altitude profiles of water vapor partial pressure (e) from radiosonde, PW up to different altitudes and its percentage to column integrated value for Bangalore. The column integrated PW from e profile and PW_{GPS} are marked. Left side axis shows the height above the surface and right side axis shows the altitude above the MSL

density derived from radiosonde exceeds 6 km, in a few cases they could be confined to a lower altitude. This could be one reason for the over estimate of PW_{GPS} . But even for those cases in which the water vapor profiles extend up to the upper troposphere, PW_{GPS} could be an overestimate. A typical example of two cases in which the e profile though extent up to ~ 13 km, in one case the GPS underestimates the PW while in the other it overestimates, is presented in Figure 7.5. Note that, in all cases the PW is estimated from the station altitude up to the relevant top-altitude. It may also be noted that > 95% of the columnar water vapor (or PW) is contributed by the altitudes below 6 km.

The GPS derived PW is compared with that estimated by integrating the humidity profile derived from radiosonde data on a day-to-day basis. The difference between the two on each day is presented in Figure 7.6a. Only those radiosonde data for which the water vapor density profiles extending up to upper troposphere, are used for this purpose. The top panel shows a plot of this difference at 00:00 UTC and the base panel the same for 12:00

UTC. In most of the cases the deviation is less than ± 10 mm. Deviations exceeding ± 10 mm are mostly observed during April-May and September-November period which could partly be due to large spatial heterogeneity in water vapor distribution associated with short range convective systems. It is also interesting to note that compared to 12:00 UTC, the number of cases in which the deviations exceed ± 10 mm is very small at 00:00 UTC.

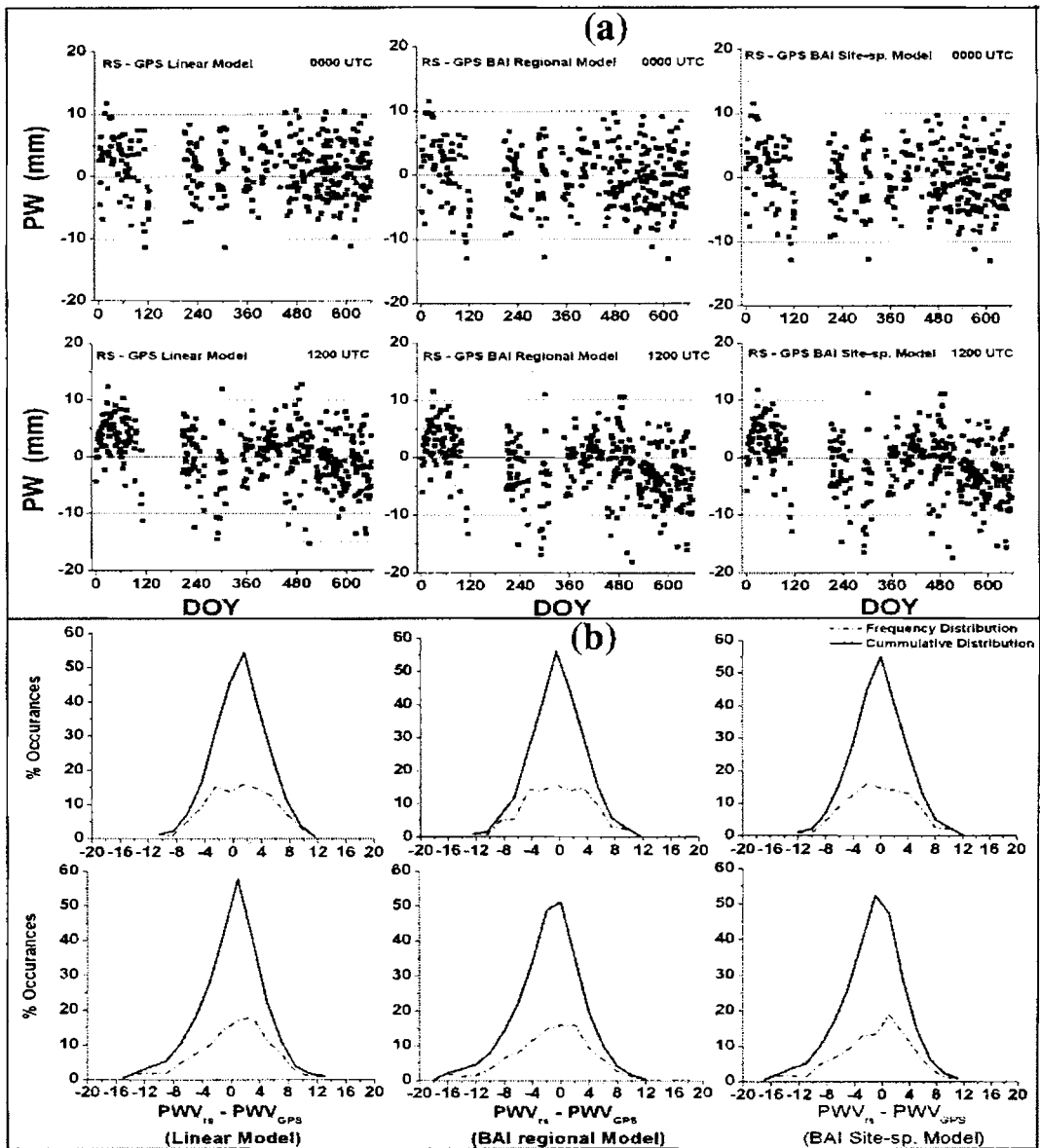


Figure 7.6(a & b): Difference between Radiosonde derived PW and GPS derived PW for 00:00 UTC and 12:00 UTC for Bangalore. The left-hand side panels show the deviation of PW_{GPS} estimated employing the linear model from radiosonde derived values, while the middle and right-hand side panels show the same for BAI regional model and BAI site-specific model (a). Percentage distribution and cumulative percentage distribution of the deviations (b)

Moreover, on examining the relative merits of the three models based on deviations it is seen that large deviations exceeding ± 10 mm is very small for the case of linear model compared to the other two. A plot of the frequency distribution of these deviations along with its cumulative percentage distribution (number of occurrences above a particular value in the case of positive deviations and number of occurrences below a particular value in the case of negative deviations) for the three cases is presented in Figure 7.6b. The cumulative distribution is relatively sharp in the case of linear model indicating that the large deviations are less probable. While the probability of positive deviations is more for linear model, in around 30% cases the deviation exceeds ± 6 mm. For linear model in $< 5\%$ cases the deviations exceed ± 10 mm while for the other models it is between 5 to 10%. For 00:00 UTC while the mean absolute difference for the linear model is ~ 3.76 mm, the BAI regional and BAI site-specific models shows deviations of ~ 3.82 mm. For 12:00 UTC, while the mean deviation for linear model is 3.93 mm that for the BAI regional and site-specific models are, respectively, 4.22 mm and 4.14 mm. Figure 7.7 shows the scatter plot of the day-to-day values of PW_{GPS} data at Bangalore using the site-specific linear model, BAI regional model and BAI site-specific model verses the corresponding values estimated from radiosonde.

The mean absolute difference, correlation coefficient, slope and bias of the best-fit line are also listed in respective frames. While the mean difference is small for 00:00 UTC, the bias is very small and the slope is more close to unity for 12:00 UTC. Examining the mean differences, it is seen that the linear model gives equally good values of PW_{GPS} , if not better, as those from BAI model which reveals that incorporation of temperature influence through Π could not significantly improve the accuracy of PW estimation from GPS data. It may be noted here that the radiosonde sites and GPS sites are not collocated. To study whether these biases have been generated because of the altitude difference in the PW measurements from the GPS and the Radiosonde site, the water vapor profile from radiosonde is extrapolated using proper scaling technique to the GPS site altitude. The cumulative frequency of the deviation of GPS estimated and radiosonde estimated (after extrapolating the water vapor) PW is presented in Figure 7.8. The top and the middle panels are, respectively, for 00:00 and 12:00 UTC and the base panel represent the composite distribution combining the data for 00:00 and 12:00 UTC. It is found that after accounting for the height difference (~ 100 m in this case) between the GPS and radiosonde sites, the mean deviation in PW is ~ 4.0 mm for

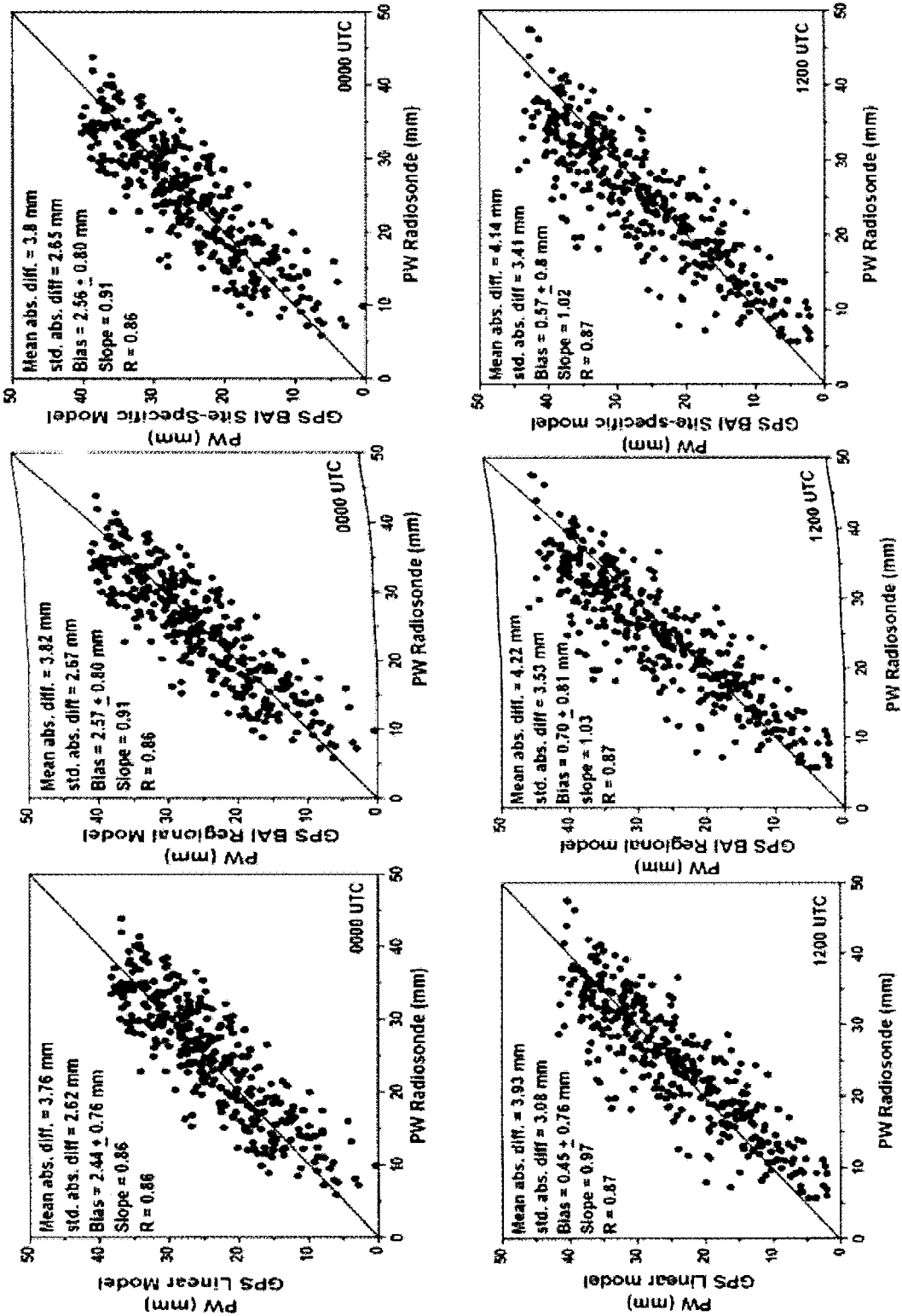


Figure 7.7: A scatter plot of PW_{GPS} estimated using linear model and BAI models versus the PW derived from the altitude profiles of water vapor estimated from radiosonde data for Bangalore. Scatter plot generated from the time-series data of PW_{GPS} and PW derived from radiosonde for the period January 2001 to October 2002

all the three models. While the probability of positive deviations is more for linear model, in around 35% cases the deviation exceeds ± 6 mm. For linear model in $\sim 80\%$ cases the deviations are between ± 2 mm while for the other models it is between 60 to 70%.

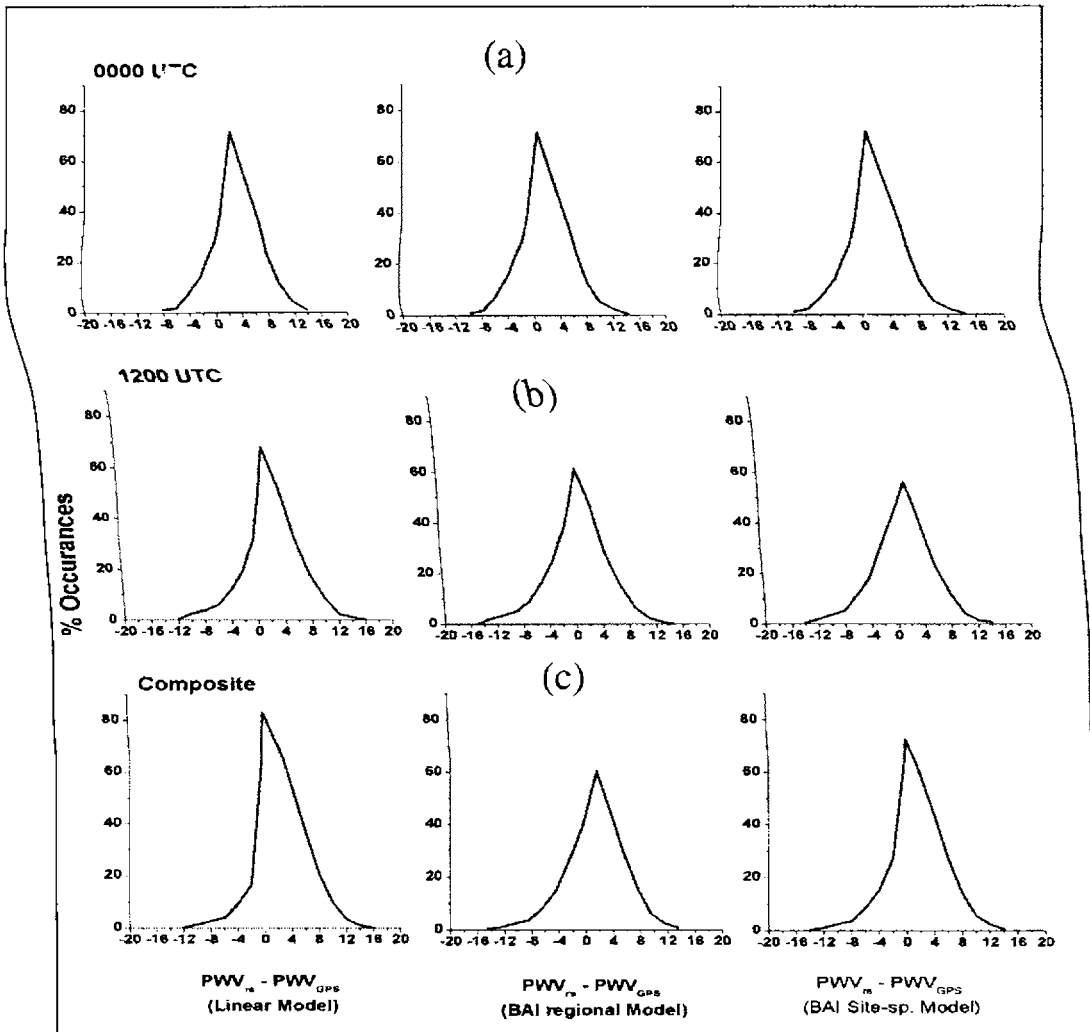


Figure 7.8: Cumulative percentage distribution of the deviations shown on different panels of Figure 7.6a after accounting for the height correction in water vapor profile at 00:00 UTC (a), 12:00 UTC (b) and combining both 00:00 & 12:00 UTC (c)

It would be worth in this context to compare the PW estimates from different models with radiosonde derived values on a monthly mean scale. The Figure 7.9 shows a bar-chart presenting the monthly mean values of PW for the year 2001, obtained from radiosonde data along with those estimated from GPS data employing the two models described above and those reported by *Jade et al.* [2005] who used the Bevis model. The seasonal variation in

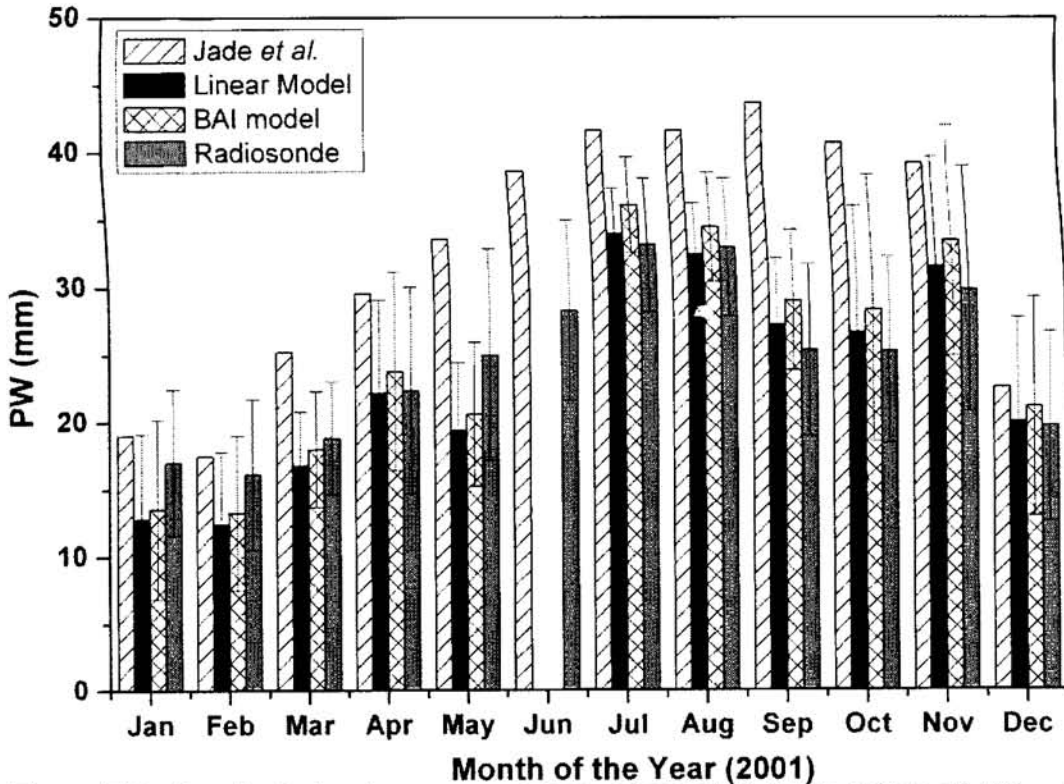


Figure 7.9: Bar-chart showing a comparison of monthly mean values of PW_{GPS} at Bangalore using site-specific linear model and BAI regional model for the year 2001 along with corresponding values of PW derived from radiosonde data and those reported by *Jade et al.* [2005]

PW is well depicted in all the estimations. Standard deviations amounting to ~ 10 mm in each month indicate large day-to-day variability. While the GPS underestimates the PW in the first half of the year (January-May), it overestimates in the later part. The deviations are ≤ 4 mm during the winter period and ≤ 2 mm during the summer/monsoon period. However, it would be worth in this context to note that typical accuracies associated with radiosonde measurements [Bisagni, 1989] can lead to an error of approximately 2.0 mm in PW estimation [Elgered, 1993].

7.4 Estimation of PW from GPS Data at Hyderabad

The applicability of these models for another location over the subcontinent is examined using the GPS data from Hyderabad (17.45°N , 78.46°E); a station located 5° north of Bangalore. As the GPS station at Hyderabad started operation since November 2002, in this analysis continuous good quality data for a period of one year from January 2003 is used. In order to accomplish a direct comparison, the GPS data from Bangalore for the same

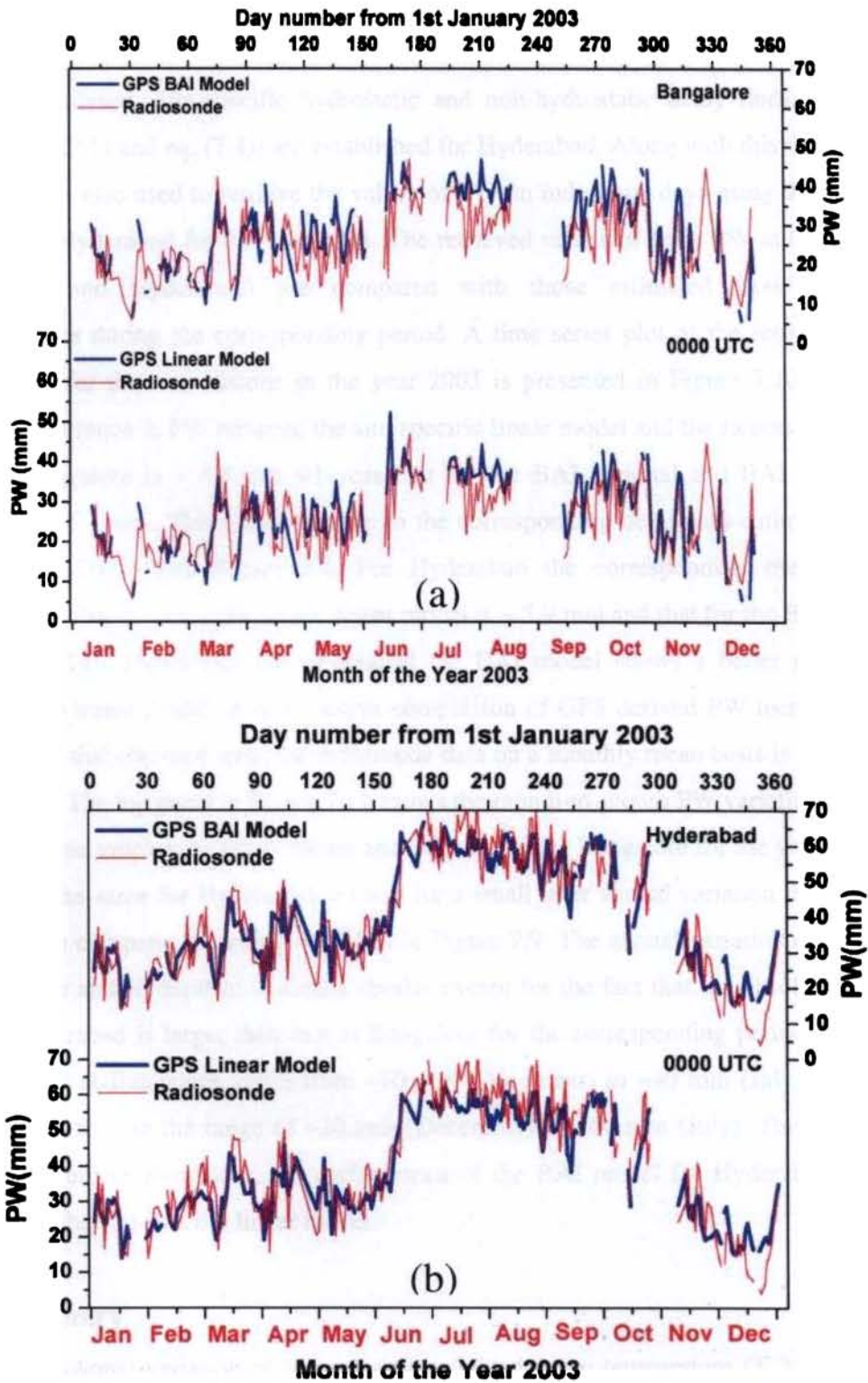


Figure 7.10: Daily PW estimated from GPS data for the year 2003 using BAI regional model and site-specific linear model along with those derived from radiosonde data at 00:00 UTC, for Bangalore (a) and same for Hyderabad (b)

period is analysed. Site-specific hydrostatic and non-hydrostatic delay linear regression models (eq. (3.1) and eq. (7.4)) are established for Hyderabad. Along with this the T_m -based BAI model is also used to retrieve the values of PW on individual days using the GPS data recorded at Hyderabad for the year 2003. The retrieved values of daily PW at the two sites (Bangalore and Hyderabad) are compared with those estimated from radiosonde measurements during the corresponding period. A time series plot of the retrieved PW at 00:00 UTC for the two stations in the year 2003 is presented in Figure 7.10. The mean absolute difference in PW between the site-specific linear model and the radiosonde derived PW for Bangalore is ~ 4.4 mm whereas that for the BAI regional and BAI site-specific models is ~ 5.1 mm. This is comparable to the corresponding deviations estimated for the period 2001-2002 from Figure 7.4. For Hyderabad the corresponding mean absolute difference in PW for the site-specific linear model is ~ 5.9 mm and that for the BAI model is ~ 5.2 mm. This shows that for Hyderabad the BAI model shows a better performance compared to linear model. A quantitative comparison of GPS derived PW using these two models with that obtained from the radiosonde data on a monthly mean basis is presented in Figure 7.11. The top panel in Figure 7.11 shows the month-to-month PW variation estimated from GPS data employing linear model and BAI model for Bangalore for the year 2003 and base panel the same for Hyderabad. Except for a small inter annual variation the pattern in Figure 7.11a compares favorably with that in Figure 7.9. The annual variation of mean PW at Bangalore and Hyderabad is almost similar except for the fact that the absolute value of PW at Hyderabad is larger than that at Bangalore for the corresponding period. The mean value of PW at Bangalore varies from ~ 10 mm (December) to ~ 40 mm (July) and that at Hyderabad varies in the range of ~ 20 mm (December) to ~ 60 mm (July). This figure also shows that, unlike Bangalore, the performance of the BAI model for Hyderabad is better than that of the site-specific linear model.

7.5 Summary

The seasonal variation of water vapor weighted mean temperature (T_m) used in PW retrieval from GPS data is studied over the Indian subcontinent (lat 8°N to 34°N) following the Bevis model. An empirical model for T_m based on surface temperature adapting the Bevis model is developed for the Indian zone. A simple site-specific linear model relating the ZWD with ground measured integrated water vapor is further established. The utility of

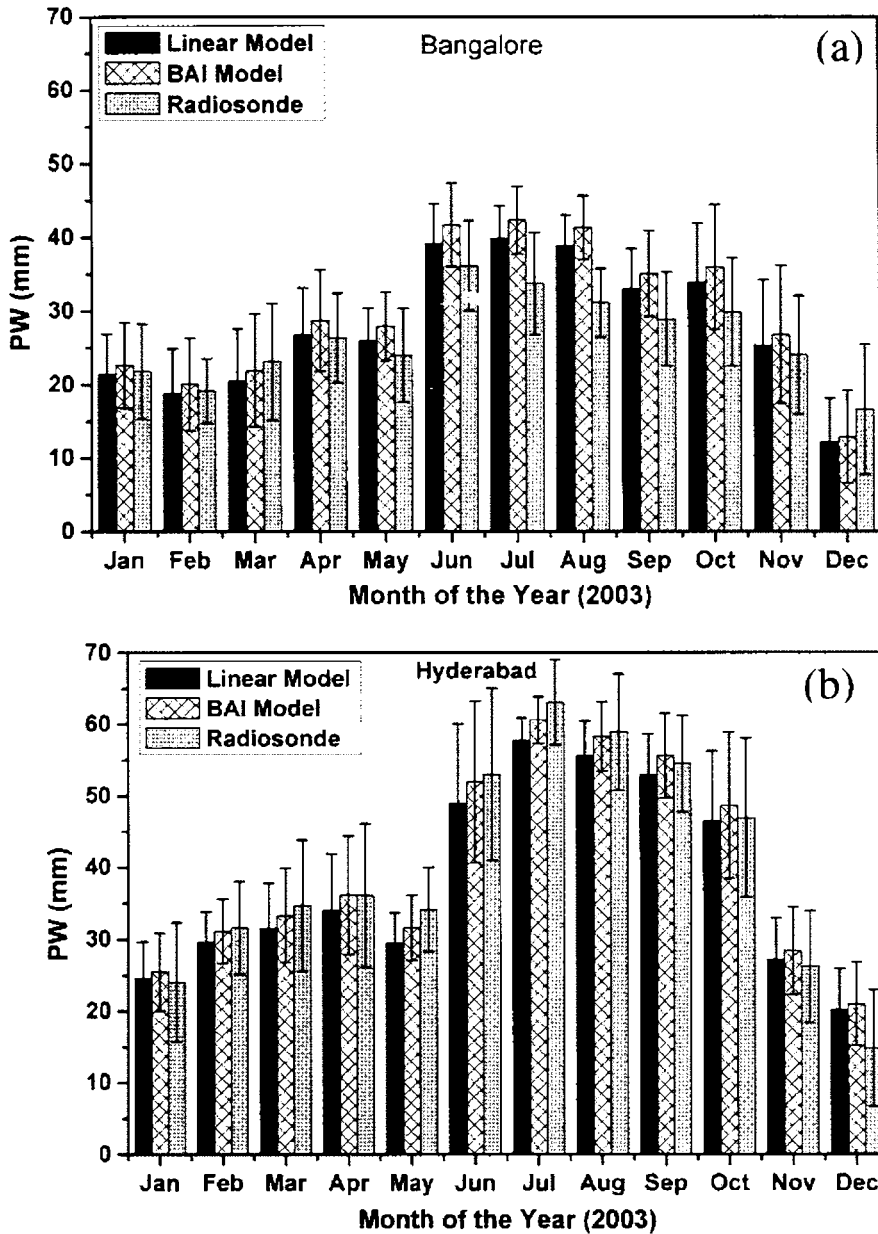


Figure 7.11: The bar-chart showing a comparison of monthly mean values of PW_{GPS} using the temperature independent site-specific linear model and BAI regional model for the year 2003 along with corresponding values of PW derived from radiosonde data at Bangalore (a); and same for Hyderabad (b)

these models for a tropical station is examined using the GPS data from Bangalore. The simple linear model though does not make use of the effect of the variation in atmospheric temperature is well suited for PW estimation (with locally derived coefficients) for the tropical region. However, a station specific T_m -based model is not found to be superior to

the regional model especially over the tropics mainly because of the fact that at these locations the range of variability in T_S (over a year) is rather small. The seasonal variability of Π is significant for mid-latitude region. The region specific T_m -based model is found to be in par with if not better than a similar site-specific T_m -based model for the near equatorial station, Bangalore. In case of Hyderabad a station located at slightly higher latitude, the deviation for the linear model is found to be larger than that of the T_m -based model. This shows that the temperature independent site-specific linear model, which is quite satisfactory for the equatorial stations, is not quite adequate for higher latitudes and in such cases the performance of T_m -based model is better than that of the linear model.

Chapter 8

SUMMARY AND FUTURE SCOPE

Summary

Being non-dispersive in nature, the propagation delay for microwaves due to the neutral atmosphere could be circumvented only through appropriate modeling. This delay has two components. While the hydrostatic (dry) component, which depends primarily on atmospheric pressure and temperature, accounts for approximately 90% of the total delay, the remaining 10% which is represented by the wet component, depends purely on the moisture content of the atmosphere. A true estimate of the tropospheric delay could be accomplished through ray-tracing the altitude structure of atmospheric refractivity profile which can be derived from the altitude profiles of P , T , and e . As a prelude to developing empirical models, the true value of the zenith tropospheric delay (ZTD) is estimated for a few selected Indian stations to study its spatial and temporal variability. This study showed that the hydrostatic component (ZHD) and non-hydrostatic component (ZWD) of ZTD show pronounced day-to-day variation (~ 4.0 cm to ~ 8.5 cm for ZHD and ~ 7.0 cm to ~ 15.8 cm for ZWD), which is much larger than the month-to-month variation of the respective mean values. This shows that for accurate prediction of ZTD it is essential to have the real time information on the altitude structure of P , T , and e at respective location. This may not be possible always. In such cases it becomes essential to develop appropriate models either based on geographical location and day of the year or based on more easily available atmospheric parameters at the surface.

Simple linear relationships are established for ZHD in terms of surface pressure and for ZWD on the basis of different surface humidity parameters such as surface water vapor pressure, surface water vapor density and the Precipitable Water vapor (PW) through regression analysis for eighteen stations representing different climatic zones over Indian region. In addition to this, the widely used Hopfield model was also adapted for the Indian condition by establishing appropriate model for the dry and wet characteristic heights in terms of surface temperature. Based on these analyses and taking note of the fact that the variability of the model parameters within these stations in general, are small, a single

Unified model is developed pooling the data from all these stations which hence will be applicable for the entire Indian subcontinent. These models are further validated by comparing the model predictions with the true range errors estimated through ray-tracing. While for ZHD the deviation of Site-Specific ranges from ~ 0.17 cm (for Trivandrum) to ~ 2 cm (for Srinagar) that for the Unified model is within ~ 2.9 cm. Similarly for ZWD, the deviation of Unified surface model ($\sim \pm 5.8$ cm) is comparable to that of the Site-Specific models (at the respective locations). The applicability of all these models for the Indian region is found to be much superior to the currently available global models employed for this purpose.

A Region specific Tropospheric Delay model (*IRTD*), which is independent of any measured atmospheric parameters but depends only on the geographical location and day of the year is developed specifically for the tropical region (with special reference to Indian zone) using the atmospheric data from different locations over the subcontinent. The performance of this model for the Indian region was found to be much superior to the currently available global (*WTD*) model widely used in satellite based navigations. A validation of these models is accomplished by comparing the model derived tropospheric delay with that estimated from ground based GPS receivers located at the two IGS sites, Bangalore (*IISC*) and Hyderabad (*HYDE*).

The tropospheric delay which is estimated in the zenith direction is projected to the desired slant direction (along the line-of-sight of the satellite) using appropriate mapping functions. Applicability of the existing global mapping functions along with a new mapping function developed by modifying the Chi function is examined for this purpose. On comparing the capabilities of different types of mapping functions along with the newly developed modified Chi function, it is found that the modified Chi function behaves much better than the other functions.

The potential of using GPS data to estimate the PW in the atmosphere is demonstrated using the data from two IGS stations over the Indian subcontinent. In this context a simple site-specific linear model relating the ZWD with ground measured integrated water vapor is established. An empirical model for water vapor weighted mean temperature (T_m) based on surface temperature is developed for the Indian zone, adapting the Bevis model, and its applicability for the Indian region is examined along with the linear model. The simple linear model though does not make use of the effect of the variation in atmospheric

temperature is found to be well suited for the PW estimation (with locally derived coefficients) for the near equatorial station (Bangalore). For station located at a slightly higher latitudes (Hyderabad and beyond) the T_m -based model is found to be better suited. The seasonal variability of the proportionality constant connecting PW with ZWD is quite significant for these stations.

Future Scope

Following are some of the important points on which more in depth studies are to be carried out in the near future: (1) The IRTD model proposed in the present study contains only one harmonic component for representing the temporal variation of ZTD at any location. A subsequent analysis of ZTD derived from ground based GPS indicates the presence of more periodicities in its temporal variations. There is a scope for improving the accuracy of IRTD model by incorporating a few more dominant periodicities associated with ZTD. (2) The GPS derived ZTD could be used to delineate periodicities associated with dry and humid atmospheric parameters and its possible application in Meteorology. (3) At present two separate mapping functions are used for projecting the hydrostatic and non-hydrostatic component of zenith delay in a slant direction. In place of this a composite mapping function taking account of the angular variation of both the components together, is to be developed for directly applying to the zenith total delay (ZTD). (4) A network of ground based GPS, which would become operational as a part of various application oriented programs, could form a suitable network (spaced at ~ 100 km) to monitor continuously the atmospheric columnar water vapor. This could yield a spatial map of PW over the subcontinent and its variations in different time scales, which is an important input for numerical weather prediction models. (5) A low-earth orbiting satellite receiving the signal from GPS satellites during its occultation can be used for measuring the atmospheric bending angle. This can be used to derive the vertical refractivity profile in the stratosphere and the upper troposphere, which will be very important not only in numerical weather predictions but also in various areas of atmospheric research including atmospheric structure and dynamics. As quite a few such low earth orbiting (LEO) satellites are either operational or planned, it will be quite realistic to hope that the radio occultation (an important tool for atmospheric research) will become a reality in the near future.

REFERENCES

- Abramowitz, M., I. A. Stegun, 1964: Handbook of Mathematical functions, Vol. NBS AMS 55, Washington, DC: USGPO.
- Altshuler, E. E., and P. M. Kalaghan, 1974: Tropospheric range error corrections for the NAVSTAR system. AFCRL-TR-74-0198, *Interim Scientific Report*, Air Force Cambridge Research Laboratories, Bedford, Mass., 16 April, 13 pp.
- Askne, J., and H. Nordius, 1987: Estimation of tropospheric delay for microwave from surface weather data. *Rad. Sci.*, **22**, 379-386.
- Baby, H. B., P. Gole, and J. Lavernat, 1988: A model for the tropospheric excess path length of radio waves from surface meteorological measurements. *Rad. Sci.*, **23**, 1023-1038.
- Barry, R. G., and R. J. Chorley, 1998: *Atmosphere, Weather, and Climate*. 7th Ed., Routledge, London.
- Bean, B. R., and G. D. Thayer, 1959: Models of the atmospheric radio refractive index. *Proceedings of the IRE*, **47(5)**, May, 740-755.
- Berman, A. L., 1976: The prediction of zenith refraction from surface measurements of meteorological parameters. *Rep. JPL TR 321602*. Calif. Inst. of Technol. Jet Propul. Lab., Pasadena, California.
- Bevis, M., S. Businger, T. A. Herring, C. Rocken, R. A. Anthes, and R. H. Ware, 1992: GPS meteorology: Remote sensing of atmospheric water vapor using the Global Positioning system. *J. Geophys. Res.*, **97**, 15787-15801.
- Bevis, M., S. Businger, S. Chiswell, T. A. Herring, R. Anthes, C. Rocken, and R. H. Ware, 1994: GPS meteorology: Mapping Zenith wet delays onto precipitable water. *J. Appl. Meteor.*, **33**, 379-386.
- Bisagni, J. J., 1989: Wet tropospheric range corrections for satellite altimeter-derived dynamic topographies in the western North Atlantic. *J. Geophys. Res.*, **94(C3)**, 3247-3254.
- Bock, O., and E. Doerflinger, 2000: Atmospheric processing methods for high accuracy positioning with Global Positioning System. COST Action 716 Workshop, "Towards Operational GPS meteorology", July 10-12, 2000, Norway.
- Boehm, J., A. Niell, P. Tregoning, and H. Schuh, 2006a: Global Mapping Function (GMF): A new empirical mapping function based on numerical weather model data. *Geophys. Res. Lett.*, **33**, L07304 (1-4).
- Boehm, J., B. Werl, and H. Schuh, 2006b: Tropospheric mapping functions for GPS and very long baseline interferometry from European Centre for Medium-Range Weather Forecasts operational analysis data. *J. Geophys. Res.*, **111**, B02406 (1-9).
- Braun, J., C. Rocken, and R. Ware, 2001: Validation of line-of-sight water vapor measurements with GPS. *Rad. Sci.*, **36**, 459-472.

- Brunner, F. K., H. Hartinger, and L. Troyer, 1999: GPS signal diffraction modeling: The stochastic SIGMA- Δ model. *J. Geod.*, **73**, 259-267.
- Businger, S., S. R. Chiswell, M. Bevis, J. Duan, R. Anthes, C. Rocken, R. H. Ware, T. M. Exner, T. Vanhove, and F. Solheim, 1996: The promise of GPS in atmospheric monitoring. *Bull. Amer. Meteor. Soc.*, **77**, 5-18.
- Chao, C. C., 1972: A model for Tropospheric calibration from daily surface and radiosonde balloon measurements. *Tech. Memo Calif. Inst. of Technol. Jet Propul. Lab.*, 17.
- Chapman S., 1931: The absorption and dissociative or ionizing effect of monochromatic radiation in atmosphere on a rotating earth. *Proc. Phys. Soc. (London)*, **43**, 483.
- Chapman S., 1953: Note on the grazing-incidence integral for monochromatic radiation in an exponential atmosphere. *Proc. Phys. Soc. B (London)*, **66**, 710.
- CIRA, 1986: Part I Middle atmosphere models, D. Rees (ed.). *Adv. Space. Res.*, **8(5-6)**, 1988.
- COESA, 1966: U.S. Standard Atmosphere Supplements, 1966. U.S. Committee on Extension to the Standard Atmosphere. Sponsored by Environmental Science Services Administration, National Aeronautics and Space Administration, United States Air Force and published by the Superintendent of Documents, U.S. Government Printing Office, Washington, D.C.
- Cohen, C., B. Pervan, D. Lawrence, H. S. Cobb, J. D. Powell, and B. Parkinson, 1994: Real time flight testing using integrity beacons for GPS Category III precision landing. *Navigation*, **41(2)**, 145-157.
- Collins, J. P., and R. B. Langely, 1997: A Tropospheric Delay Model for the User of the Wide Area Augmentation System. Final contract report prepared for Nav Canada Department of Geodesy and Geomatics Engineering Technical Report No. 187, University of New Brunswick, Fredericton, N.B., Canada.
- Collins, J. P., and R. B. Langley, 1998: The residual tropospheric propagation delay: How bad can it get? *Proceedings of ION GPS-98*, The 11th International Technical Meeting of the Satellite Division of The Institute of Navigation, Nashville, Tenn., September 15-18, 729-738.
- Dabberdt, W. F., H. L. Cole, N. Chamberlain, T. Hock, E. Korn, D. Lauritsen, K. Norris, and S. Stenslund, 1995: A Reference Radiosonde, Preprints, Ninth Symposium on Meteorological Observations and Instrument. *Amer. Meteor. Soc.*, Boston, Mass., 55-59.
- Davis, J. L., T. A. Herring, I. I. Sharipo, A. E. E. Rogers, and G. Elgered, 1985: Geodesy by radio interferometry: effects of atmospheric modeling errors on estimates of baseline length. *Rad. Sci.*, **20(6)**, 1593-1607.
- Debye, P., 1957: Polar molecules. *Dover Publishing Co.*, New York, 89-90.
- De Cleene, B. 1995: Scientific Report submitted to *Federal Aviation Administration*, May.
- Dodson A. H., R. M. Bingley, N. T. Penna, and M. H. O. Aquino, 1999a: A national network of continuously operating receivers for the UK. *Geodesy beyond 2000: The challenges of the first decade, International Association of Geodesy Symposia*, **121**, 367-372.

- Dodson, A. H., W. Chen, H. C. Baker, N. T. Penna, G. W. Roberts, J. Westbrook, and R. Jeans, 1999b: Assessment of EGNOS Tropospheric correction model. *Proceedings of IONGPS 99*.
- Duan, J., M. Bevis, P. Fang, Y. Bock, S. Chiswell, S. Businger, C. Rocken, F. Solheim, and T. Van Hove, 1996: GPS meteorology: direct estimation of the absolute value of precipitable water. *J. Appl. Meteor.*, **35**, 830-838.
- Elgered, G., J. L. Davis, T. A. Herring, and I. I. Shapiro, 1991: Geodesy by radio interferometry: water vapor radiometry for estimation of the wet delay. *J. Geophys. Res.*, **96**, 6541-6555.
- Elgered, G., 1992: Refraction in the troposphere, in Symposium on refraction of transatmospheric signals in geodesy. J. C. de Munck and T. A. Th Spoelstra (eds.), Netherlands Geod. Comm., Delft.
- Elgered, G., 1993: Tropospheric radio-path delay from ground-based microwave radiometry, in Atmospheric Remote Sensing by Microwave Radiometry, Janssen, M. (Ed.) John Wiley, New York, 215-258.
- Elliott, W. P., and D. J. Gaffen, 1991: On the Utility of Radiosonde Humidity Archives for Climate Studies. *Bull. Am. Meteorol. Soc.*, **72**, 1507.
- Elrod B. D., and A. J. Van Dierendonck, 1993: Testing and evaluation of GPS augmented with pseudolites for precision landing applications. *Proc. DSNS 93*, Amsterdam, The Netherlands, March.
- Elrod B. D., K. J. Barltrop, and A. J. Van Dierendonck, 1994: Testing of GPS augmented with pseudolites for precision approach applications. *Proc. ION-GPS 94*, Salt Lake City, UT, September.
- Emardson, T. R., G. Elgered, and J. Johansson, 1998: Three months of continuous monitoring of atmospheric water vapor with a network of GPS receivers. *J. Geophys. Res.*, **103**, 1807-1820.
- Farah, A., T. Moore, and C. J. Hill, 2005: High Spatial Variation Tropospheric Model for GPS-Data Simulation. *The Journal of Navigation*, **58**, 459-470.
- Fleming, E. L., S. Chandra, M. R. Shoerberl, and J. J. Barnett, 1988: Monthly mean global climatology of temperature, wind, geopotential height and pressure for 0-120 km, *National Aeronautics and Space Administration, Technical Memorandum 100697*, Washington, D.C.
- Flores, A., G. Ruffini, and A. Rius, 2000: 4D tropospheric tomography using GPS slant wet delay. *Ann. Geophys.*, **18**, 223-234.
- Hein, G. W., J. A. Rodriguez, S. Wallner, B. Eissfeller, T. Pany, and P. Hartl, 2007: Envisioning a Future GNSS system of systems, working papers. *InsideGNSS*, January-February.
- Herring, T. A., J. L. Davis, and I. I. Shapiro, 1990: Geodesy by radio interferometry: The application of Kalman filtering to the analysis of very long baseline interferometry data. *J. Geophys. Res.*, **95**, 12561-12581.
- Herring, T. A., 1992: Modeling Atmospheric Delays in the Analysis of Space Geodetic Data, de Munck, J. C. and Spoelstra, T. A. Th (eds.), *Refraction of Transatmospheric Signals in Geodesy*, Proceedings of the Symposium, Netherlands Geodetic Commission, Publications on Geodesy, New Series, No. 36, The Hague, The Netherlands, May 19-22.

- Hopfield, H. S., 1969: Two-quartic tropospheric refractivity profile for correcting satellite data. *J. Geophys. Res.*, **74**, 4487-4499.
- Hopfield, H. S., 1971: Tropospheric effect on electromagnetically measured range: Prediction from surface weather data. *Rad. Sci.*, **6**(3), 357-367.
- Huestis, D. L., 2001: Accurate evaluation of the Chapman function for atmospheric attenuation. *J. Quant. Spec. & Rad. Trans.*, **69**, 709-721.
- Humphreys, T. E., M. C. Kelley, N. Huber, and P. M. Kintner Jr., 2005: The semidiurnal variation in GPS-derived zenith neutral delay. *Geophys. Res. Lett.*, **32**, L24801 (1-4).
- ICG, 2006: Report on the Meeting of the International Committee on Global Navigation Satellite Systems, Vienna, 1-2 November (A/AC.105/879, *United Nations publication*, sales No. V.06-59640(E)).
- Ichikawa, R., 1995: Estimation of atmospheric excess path delay based on three-dimensional numerical prediction model data. *J. Geod. Soc. Jap.*, **41**, 379-408.
- Ifadis, I., 1986: The atmospheric delay of radio waves: Modeling the elevation dependence on a global scale. In: *Technical Report No. 38L*, School of Electrical and Computer Engineering, Chalmers University of Technology, Göteborg, Sweden.
- Jade, S., M. S. M. Vijayan, V. K. Gaur, T. P. Prabhu, and S. C. Sahu, 2005: Estimates of Precipitable water vapor from GPS data over the Indian subcontinent. *J. Atmos. Solar Terr. Phys.*, **67**, 623-635.
- Janes, H. W., R. B. Langley, S. P. Newby, 1991: Analysis of tropospheric delay prediction models: comparisons with ray-tracing and implications for GPS relative positioning. *Bull. Géodés.*, **65**, 151-161.
- Kaplan, E. D. and C. J. Hegarty, 2006: *Understanding GPS Principles and applications*, II Ed. Artech House, Boston. ISBN -10; 1-58053-894-0.
- Kibe, S. V., 2003: Indian plan for satellite-based navigation systems for civil aviation. *Curr. Sci.*, **84**(11), 1405-1411.
- King, R. W., and Y. Bock, 2000: Documentation for the GAMIT GPS analysis software, Department of Earth, Atmospheric, and Planetary Sciences, Massachusetts Institute of Technology, Scripps Institute of Oceanography, University of California at San Diego.
- Ku, H. H., 1966: Notes on the use of propagation of error formulas. *Journal of Research Engineering and Instrumentation*, **NBS-C 70C(4)**, 263-273.
- Kuo, Y.-H., X. Zou, and Y.-R. Guo, 1996: Variational assimilation of precipitable water using a nonhydrostatic mesoscale adjoint model, Part I: Moisture retrieval and sensitivity experiments. *Mon. Weather Rev.*, **124**, 122-147.
- Kuo, Y.-H., Y.-R. Guo, and E. R. Westwater, 1993: Assimilation of precipitable water into a mesoscale numerical model. *Mon. Weather Rev.*, **121**, 1215-1238.

- Kursinski, E. R., 1997: The GPS radio occultation concept: Theoretical performance and initial results. *PhD. Thesis*, California Institute of Technology, Pasadena.
- Labitzke, K., J.J. Barnett, and B. Edwards (eds.), 1985: Middle Atmosphere Program, MAP Handbook, Volume 16, University of Illinois, Urbana.
- Liou, Y. -A., Y. -T. Teng, T. Van Hove, and J. C. Liljegren, 2001: Comparison of precipitable water observations in the near tropics by GPS, Microwave Radiometer, and Radiosondes. *J. Appl. Meteor.*, **40**, 5-15.
- Ma, C., J. M. Sauber, L. J. Bell, T. A. Clark, D. Gordon, W. E. Himwich, and J. W. Ryan, 1990: Measurement of horizontal motions in Alaska using very long baseline interferometry. *J. Geophys. Res.*, **95**, 21991-22011.
- MacDonald, A., and Y. Xie, 2000: On the use of slant observations from GPS to diagnose three dimensional water vapor using 3DVAR. Preprints, *Fourth Symposium on Integrated Observing Systems*, Long Beach, CA, *Amer. Meteor. Soc.*, 62-73.
- MacMillan, D. S., and C. Ma, 1994: Evaluation of very long baseline interferometry atmospheric modeling improvements. *J. Geophys. Res.*, **99**, 637-652.
- Madden, R. A., and P. R. Julian, 1994: Observations of the 40-50 day tropical oscillation: A review. *Mon. Weather Rev.*, **112**, 814-837.
- Marini, J. W., 1972: Correction of satellite tracking data for an arbitrary tropospheric profile, *Rad. Sci.*, **7(2)**, 223-231.
- Marini, J. W., and C. W. Murray, 1973: Correction of Laser Range Tracking Data for Atmospheric Refraction at Elevations above 10 Degrees. *NASA report X-591-73-351*, Goddard Space Flight Center.
- Mendes, V. B., and R. B. Langley, 1998: Tropospheric Zenith Delay prediction accuracy for airborne GPS high-precision positioning. *Proceedings of the Institutes of Navigation 54th Annual meeting*, Denver, CO, U.S.A., 1-3 June, 337-347.
- Mendes, V. B., G. Prates, L. Santao, and R. B. Langley, 2000: An evaluation of the accuracy of models for the determination of weighted mean temperature of the atmosphere. *Proc. Of ION 2000*, National Technical Meeting, Anaheim, CA, USA, 433-438.
- Middleton, W. E. K., and A. F. Spilhaus, 1953: Meteorological Instruments. *University of Toronto Press*, Toronto, Ont., Canada.
- Misra, P. and P. Enge, 2001: Global Positioning System Signals, Measurements, and Performance. *Ganga-Jamuna Press*, Lincoln, Massachusetts.
- MIT and SIO, 2000: Documentation for the GAMIT GPS analysis software, Department of Earth, Atmospheric, and Planetary Sciences, Massachusetts Institute of Technology, and Scripps Institute of Oceanography, University of California at San Diego.
- NATO, 1993: Standardisation Agreement (STANAG) Doc. 4294 EL (Edition 1), Appendix 6 to Annex A. pp. A-6-34 – A-6-37. *North Atlantic Treaty Organisation*, Brussels.

- Niell, A. E., 1996: Global Mapping Functions for the atmospheric delay at radio wavelengths. *J. Geophys. Res.*, **101**, 3227-3246.
- Niell, A. E., 2000: Improved atmospheric mapping functions for VLBI and GPS. *Ear. Plan. Spa.*, **52**, 699-702.
- Oltmans, S. J., and D. J. Hofmann, 1995: Increase in Lower-Stratospheric Water Vapor at a Mid-Latitude Northern Hemisphere Site from 1981 to 1994. *Nature*, **374**, 146.
- Cort, A.H., 1983: Global Atmospheric Circulation Statistics 1958-1983, National Oceanic and Atmospheric Administration, Professional Paper 14, 180 pp, U.S. Government Printing Office, Washington, D.C.
- Parameswaran, K., B. V. Krishna Murthy, 1990: Altitude profiles of tropospheric water vapor at low latitudes. *J. App. Meteor.*, **29(8)**, 665-679.
- Parkinson, B. W., and J. J. Spilker Jr., (eds.), 1996: Global Positioning System: Theory and Applications. *Progress in Astronautics and Aeronautics*, **164**, American Institute of Aeronautics and Astronautics.
- Penna, N., A. Dodson, and W. Chen, 2001: Assessment of EGNOS Tropospheric Correction Model. *The Journal of Navigation*, **54**, 37-55.
- Petty, G. W., 2004: A first course in atmospheric radiation. *Sundog Publishing*, Madison, Wisconsin.
- Ramjee, P., and M. Ruggieri, 2005: Applied satellite navigation using GPS, GALILEO and augmentation systems. *Boston, Artech House*. Artech House mobile communications series.
- Rees, M. H., 1989: Physics and chemistry of the upper atmosphere. Cambridge: *Cambridge University Press*.
- Rind, D., E. -W. Chiou, W. Chu, S. Oltmans, J. Lerner, J. Larsen, M. P. McCormick, and L. McMaster, 1993: Overview of the Stratospheric Aerosol and Gas Experiment II Water Vapor Observations: Method, Validation, and Data Characteristics. *J. Geophys. Res.*, **98**, 4835.
- Rizos, C., 1997: Principles and Practice of GPS Surveying Monograph 17. *School of Geomatic Engineering*, University of New South Wales, 555.
- Rocken, C., R. Ware, T. Van Hove, F. Solheim, C. Alber, J. Johnson, M. Bevis, S. Chiswell, and S. Businger, 1993: Sensing atmospheric water vapor with the global positioning system. *Geophys. Res. Lett.*, **20**, 2631-2634.
- Rocken, C., T. Van Hove, J. Johnson, F. Solheim, R. Ware, M. Bevis, S. Chiswell, and S. Businger, 1995: GPS/STORM – GPS sensing of atmospheric water vapor for meteorology. *J. Atmos. Oceanic Technol.*, **12**, 468-478.
- Rocken, C., T. Van Hove, and R. Ware, 1997: Near real-time GPS sensing of atmospheric water vapor. *Geophys. Res. Lett.*, **24**, 3221-3224.

- Rocken, C., S. Slokolovskiy, J. M. Johnson, and D. Hunt, 2001: Improved Mapping of Tropospheric Delay. *J. Atmos. Oceanic Technol.*, **18**, 1205 – 1213.
- Rosenthal, G., 2007: The European position determination system (EUPOS); Goals, status and activities. Report to the: *International Committee on Global navigation satellite system (ICG)*, second meeting and related events at ISRO, Bangalore, India, September 4-7.
- Ross, R. J., and S. Rosenfeld, 1997: Estimating mean weighted temperature of the atmosphere for Global Positioning System applications, *J. Geophys. Res.*, **102(D18)**, 21719-21730.
- RTCA, 1999: Minimum operational performance standards for Global Positioning System Wide Area Augmentation System airborne equipment. *RTCA DO-229B*, Issued 10 June 1999.
- Saastamoinen, J., 1972: Atmospheric correction for the troposphere and stratosphere in radio ranging of satellites, in *The Use of Artificial Satellites for Geodesy*. In: *Geophys. Monogr. Ser.*, 15: Henrikson, S.W., A. Mancini, and B. H. Chovitz, (Eds.) AGU, Washington D. C., 247-251.
- Saha, K., K. Parameswaran, and C. Suresh Raju, 2007: Tropospheric delay in microwave propagation for tropical atmosphere based on data from the Indian subcontinent. *J. Atmos. Solar Terr. Phys.*, **69**, 875–905.
- Sasi, M. N. and A.K. Sen Gupta, 1986: A reference atmosphere for Indian equatorial zone from surface to 80 km – 1985, Scientific Report, *SPL:SR:006:85*.
- Satirapod, C., 2002: Improving the GPS data processing algorithm for precise static relative positioning. *PhD. Thesis, School of Surveying and Spatial Information Systems, The University of New South Wales, Sydney, Australia*.
- Satirapod, C., and P. Chalermwattanachai, 2005: Impact of different tropospheric models on GPS baseline accuracy: case study in Thailand. *Journal of Global Positioning Systems*, **4(1-2)**, 36-40.
- Schuchman, L., B. D. Elrod, and A. J. Van Dierendonck, 1989: Applicability of an augmented GPS for navigation in the national airspace system. *Proc. IEEE*, **77(11)**, 1709-1727.
- Schüeler, T., 2000: Die Dissertation wurde am 18. Oktober 2000 bei der Universität der Bundeswehr München, Werner-Heisenberg-Weg 39, D-85577 Neubiberg eingereicht.
- Schwarz, F. K., 1968: Comments on “Note on the relationship between total Precipitable Water and surface dew point”. *J. App. Meteor.*, **7**, 509-510.
- Smith, W. L., 1968: Reply to Note on the relationship between total precipitable water and surface dew point. *J. Appl. Meteor.*, **7**, 510.
- Smith, E. K., and S. Weintraub, 1953: The constants in the equation for atmospheric refractive index at radio frequencies. *Proc. IRE* **41**, 1035-1037.
- Solbrig, P., 2000: Untersuchungen über die Nutzung numerischer Wettermodelle zur Wasserdampfbestimmung mit Hilfe des Global Positioning Systems. *Diploma Thesis, Institute of Geodesy and Navigation, University FAF Munich, Germany*.

- Starr, D. O., and S. H. Melfi (eds.), 1991: The Role of Water Vapor in Climate: A Strategic Research Plan for the Proposed GEWEX Water Vapor Project (GVaP). *NASA Conf. Publ., CP-3120*, pp. 50.
- Suresh Raju, C., K. Parameswaran, and Korak Saha, 2007a: A summary report on tropospheric correction model for GAGAN in: *Scientific Report*, Space Physics Laboratory, VSSC, Trivandrum, India.
- Suresh Raju, Korak Saha, Bijoy V. Thampi and K. Parameswaran, 2007b: Remote Sensing of Precipitable Water Vapor Using Ground Based GPS Measurements. *Ann. Geophys.*, **25**, 1935 – 1948.
- Susskind, J., J. Rosenfeld, D. Reuter, and M. T. Chahine, 1984: Remote Sensing of Weather and Climate Parameters from HIRS2/MSU on TIROS-N. *J. Geophys. Res.*, **89**, 4677.
- Thayer, D., 1974: An improved equation for the radio refractive index of air. *Rad. Sci.*, **9**, 803-807.
- Tregoning, P., R. Boers, D. O'Brien, and M. Hendy, 1998: Accuracy of absolute precipitable water vapor estimates from GPS observations. *J. Geophys. Res.*, **103**, 28701-28710.
- Van Dierendonck, A. J., 1990: The role of Pseudolites in the implementation of Differential GPS. *Proc. PLANS 90*, Las Vegas, NV, March.
- Wang, J., M. Stewart, and M. Tsakiri, 1998: Stochastic modeling for static GPS baseline data processing. *J. Surv. Eng.*, **124**, 171-181.
- Ware, R., C. Alber, C. Rocken, and F. Solheim, 1997: Sensing integrated water vapor along GPS ray paths. *Geophys. Res. Lett.*, **24**, 417-420.
- Warren, D. L. M., and J. F. Raquet, 2002: Broadcast vs. Precise GPS Ephemerides: A Historical Perspective. *Proc. ION National Technical Meeting*, San Diego, CA, January 28-30.
- Webster, P. J., V. O. Magana, T. N. Palmer, J. Shukla, R. T. Tomas, M. Yanai, and T. Yasunari, 1998: Monsoon: processes, predictability, and the prospects for prediction. *J. Geophys. Res.*, **103**(C7), 14451-14510.
- Wübbena, G., 1991: Zur Modellierung von GPS-Beobachtungen für die hochgenaue Positionsbestimmung. *Wissenschaftliche Arbeiten der Fachrichtung Vermessungswesen der Universität Hannover*, Nr. 168, Hannover 1991.
